Ultraquantitative Raman Spectral Cytometry to Measure the Cargo Capacity of Individual Macrophages

by

Vernon L. LaLone

A dissertation submitted in partial fulfillment
of the requirements for the degree of
Doctor of Philosophy
(Pharmaceutical Sciences)
in The University of Michigan
2019

Doctoral Committee:

Professor Gustavo R. Rosania, Co-Chair
Professor Kathleen A. Stringer, Co-Chair
Professor James T. Dalton
Professor Theodore J. Standiford

Vernon LaLone
laloneve@umich.edu
ORCID iD: 0000-0001-6043-8993

To eternal creation

And simply being;

When facing the void,

May you always find meaning.

ACKNOWLEDGEMENTS

First, my thanks go to our Creator for providing the chance to exist. Then, to those who forged the foundations of human knowledge and wisdom: the philosophers of our past – especially Marcus Aurelius, Friedrich Nietzsche, and Carl Jung – who have contributed to my personal growth as a philosopher and a human being. I thank those who directly helped me along my path and contributed to my past growth, specifically as a scientist: Nara Parameswaran at Michigan State University (for having the faith to employ me during my undergraduate studies) and Carol Bergh at Perrigo (for her fierce mentorship and friendship). A massive thank you goes out to my dissertation committee: Ted Standiford, Jim Dalton, and especially my advisors, Gus Rosania and Kathleen Stringer, who have provided me with scientific and philosophical training, the likes of which exceeded my wildest imagination; I also thank them for their patience, support, understanding, and flexibility during my times of trouble. They made this research endeavor possible and I am eternally grateful for the opportunity to be part of it.

I could not have endured the struggle or completed the trials of this dissertation without the educational guidance of my past, and for that I thank all those who have ever taught me. I also thank everyone at the College of Pharmacy – especially Patrina Hardy, Antoinette Hopper, Cherie Dotson, Beth Talbot, Jan Mitchell, and Larisa Yeomans – for their invaluable administrative and emotional support throughout the course of my graduate studies. I also thank all my classmates, co-workers, colleagues, and collaborators for sharing this journey and helping me along the way, specifically my former lab mates Rahul Keswani, Gi Yoon, Tehetina Woldemichael, Phil Rzeczycki, Misha Murashov, and Jen Diaz-Espinosa: no human is an island. Another massive thank you goes out to Steve and Anna Schwendeman, who helped me find the right path for my

career and personal life; I cannot thank them enough for the profound impact they have had on my life.

I want to thank my friends, from all stages of my life, for their positive influence and for making my time on this Earth enjoyable. I have deep appreciation for my loving partner Sarah, for her courageous support and willingness to embark on the adventure of a lifetime with me, and for her ability to serve as a spiritual beacon when I have drifted astray. A special thank you goes out to the ER boys – Sam Naples, Dan DeRosha, Max Bauer, Devon Morrison, and Ryan Sundberg – and Allie Cross for sharing a plethora of incredible experiences with me: may we one day return from whence we came. I thank Robbie Pemberton and Luke Barnes for their comradery, in work and in play, and for looking out for me throughout our college years. I also thank Cora McHugh and Thomas Flott for their willingness to listen to my work-related ramblings, their general excitement, kindness, and appreciation for science; they made graduate school a lot more fun.

Next, I want to thank my family, who have always supported and believed in me to the greatest imaginable extent. From the moment of my birth, my Mom and Dad provided a life enriched with creative activities and liberties which allowed me to grow; without them I certainly would not be the man I am. I thank my brother Ben for his unwavering friendship, acceptance, and love for me despite my endless tricks. I also thank my grandparents, aunts, uncles, and cousins for helping me understand the value of family and for always welcoming me home with open arms, regardless of how long I've been away.

I owe society a thanks for financially supporting science; despite present difficulties in funding acquisition, we had the chance to peer into the vast unknown. I see great value in scientific pursuits and so hope to advocate and inspire further support for the creative exploration of nature and humanity's place in it. Finally, I want to thank the future souls who will follow in our footsteps, however briefly; may the trails we blaze forever lead towards the light. When the forthcoming philosophers find themselves at the forefront of human knowledge and wisdom, I pray they look back on us fondly.

TABLE OF CONTENTS

LIST OF FIGURES

LIST OF TABLES

LIST OF APPENDICES

ABSTRACT

This dissertation demonstrates the usefulness of Raman microscopy as a multipurpose, 'high content' cytometric analysis tool for characterizing the phenotype of diverse macrophage populations in terms of their molecular contents, in absolute quantitative terms. Experimentally, the results indicate how a Raman microscope can be used to map the spatial distribution of drug cargo contents of macrophages at a single cell level; to ascertain the charged state of drug molecules and their location within single cells; to determine different phospholipidosis phenotypes in terms of lipid and protein contents or the associated lipid/protein ratios within individual cells; and, to determine the existence of different macrophage subpopulations in terms of lipid, protein, DNA or (drug) cargo contents and their spatial distribution within the cell. Furthermore, the thesis argues for Raman cytometry as having distinct advantages in relation to flow cytometry or other semi-quantitative indirect cytometric analysis, especially by allowing for an absolute approach to the characterization of cellular phenotypes using limited number of cells. In terms of its broader applicability, Raman microscopy can demonstrably be used to obtain insights from macrophages obtained from bronchoalveolar lavages; for comparative analysis of the biomolecular composition of different cell types at the level of the individual cells (e.g. macropahges vs. fibroblasts); and for assessing drug distribution in complex tissue samples. Direct quantitation of total cellular contents reveals how drug exposure and accumulation interplays with the accumulation of phospholipids in alveolar “foam cell” macrophages. Since airway and alveolar macrophages are readily accessible in humans, this methodology could potentially be used to assess amiodarone exposure in the lungs, in a minimally invasive manner. Lastly, in terms of its relevance to pharmaceutical sciences, the Raman technique was also used to obtain insights into microscopic drug transport pathways and the function of controlled-release drug delivery devices, in a

manner that could be used for optimizing a specific drug formulation. We envision this microanalysis calibration platform as the foundation for many future biomedical applications, ranging from diagnostic assays to pathological analysis to advanced pharmaco/toxicokinetic research studies. The findings from this study represent a significant advancement in the cytometry field and open the doors of quantitative scientific perception to the entirety of the intracellular biomolecular matrix without artificial chemical tags, providing an approach by which scientists and clinicians may holistically explore the unadulterated biochemical realm within single cells: the building blocks of life.

CHAPTER 1

Introduction

1.1 Background and Significance

1.1.1 Adverse Drug Reactions, Phospholipidosis, and Organ Toxicity

An adverse drug reaction (ADR) is defined by the World Health Organization as, “one that is noxious, is unintended, and occurs at doses normally used in man” (1); it is important to note that this definition does not include therapeutic failures, drug abuse, errors in drug administration, or complications arising from patient non-compliance. As evidenced by their high frequency of occurrence in hospitals and general practices, ADRs are an important clinical issue and a major healthcare concern; they were conservatively estimated to represent the sixth leading cause of death in the United States (2, 3) with an estimated economic impact of up to 30.1 billion dollars per year (4). For the healthcare service industry, ADRs result in increased hospitalization rates, prolonged hospital stays, and sometimes clinical investigations; to the drug development industry, ADRs are a challenging obstacle to bring a drug product to the market. During drug development, randomized controlled trials serve as the gold standard for determining the efficacy and safety of compounds but often fall short in the detection of ADRs. These clinical trials are performed in standardized settings on test subject groups that may not be representative of the real-world patient population; reports have suggested females and elderly patients are often underrepresented in some trials and individuals undergoing concomitant drug therapy may even be restricted from participation. Another major limitation of clinical trials stems from the duration of drug treatment; many ADRs manifest only after continuous

long-term drug exposure, something which many trials do not adequately account for with their relatively short follow-up times (4, 5).

One specific response induced by continuous long-term exposure to certain drugs, termed drug-induced phospholipidosis (PLD), has proven to be especially difficult to characterize via conventional clinical trials. Reported for the first time in 1948 as the occurrence of foamy alveolar macrophages from chloroquine-fed rats (6, 7), PLD has historically been defined by morphological and supramolecular changes within certain cell types of specific organs; specifically, lipids begin accumulating within cells in the form of lamellated membranous inclusions which are most commonly detected by electron microscopy. Although the exact mechanism driving PLD progression is currently unknown, it has been shown to occur concurrently with intracellular accumulation of PLD-inducing drugs (Figure 1-1). Another notable feature of PLD is the reversibility of the disorder following cessation of drug treatment (8-11).

PLD has been reported as a dose-dependent process by which the extent of lipid accumulation is directly related to the extent of drug accumulation and duration of exposure in cells and tissues (12). It is believed that most, if not all, species, genders, and age groups are susceptible to induction of PLD following long-term exposure to certain drugs. In addition, the specific anatomical locations (i.e., tissues and/or cells) affected, the degree of accumulation, and the types of accumulating lipids all differ between species for different PLD-inducing drugs (7, 13, 14). *As such, the relevance of animal models is often questionable and not adequately predictive of clinical findings, making the study of actual human subjects particularly important.*

Since the mechanistic link between the accumulation of phospholipids and organ toxicity has yet to be identified, PLD is considered an adaptive response by the host experiencing drug exposure rather than a direct toxic effect (7). Regardless, the induction of PLD is predictive of drug accumulation in ADR-affected tissues and is therefore believed to be associated with the manifestation of organ toxicity. *Since specific organ toxicities may be associated with increased drug concentrations in the local tissues or cells, a quantitative assessment of drug and lipid accumulation at the single cell level*

would help to further elucidate the functional consequences of this mysterious phenomenon (Figure 1-1.).

1.1.2 Physicochemical Basis for Drug-Induced Phospholipidosis

There are currently over fifty marketed drugs reported to induce PLD and nearly 400 reported incidences of PLD-positive compounds in the FDA database (NDAs, INDs, pharmaceutical companies, and literature) (15). The ability to induce PLD is believed to be unrelated to the pharmacologic activity of the drug because PLD-inducing drugs are associated with every pharmacological class; some of the more publicized examples are amiodarone, chloroquine, gentamicin, tamoxifen, and fluoxetine. Many of these compounds share similar structural and physicochemical properties, specifically hydrophobic ring structures with side chains containing one or more weakly basic amines (12, 13, 15, 16). In addition, the presence of amine groups with pKa values greater than 8 were reported to result in greater intracellular accumulation of drug (and increased lipid content) compared to amines with lower pKa values (4).

If a compound has high lipophilicity, typically measured as the partition coefficient (LogP), it may preferentially partition into biological membranes and lipid-rich vesicles from the extracellular or cytoplasmic fluids. Furthermore, the weakly basic amine group allows for ionization of the compound ($D \rightarrow DH^+$) in low pH environments, such as the lysosome, and promotes electrostatic interactions between positively charged drug molecules and negatively charged phospholipid head groups (Figure 1-2). Dependent on the structure and degree of accumulation, intercalation of drugs into biological membranes can also alter the dynamics of membrane fluidity; cholesterol (LogP ~ 7) is an endogenous example of a lipophilic molecule that alters membrane biophysics. Another structural feature that influences induction of PLD is the presence of halogen groups, which, when present increase the membrane fluidizing effect and enhance induction of PLD (11).

Although the underlying biochemical mechanism governing PLD induction has not been directly proven, the prevailing theory involves inhibition of lysosomal phospholipases; either electrostatic interactions between the drug and phospholipid prevent enzymatic degradation of lipids by physically blocking access to the enzyme's active site or the drug is thought to directly inhibit phospholipase enzymes (7-9, 11). In addition to inhibition of phospholipid degradation, the upregulation of phospholipid and cholesterol biosynthesis genes have been reported (15). Increased levels of lipids in certain organs have also been shown to increase the affinity of PLD-inducing drugs for those organs, thus further enhancing drug bioaccumulation (11). *In this way, it may be suggested that organisms develop an 'expanded volume of distribution' following long-term exposure to certain drugs; when the compartments reach maximum capacity, the drug must redistribute, resulting in high local drug concentrations, ADRs, and potentially cell and/or organ toxicity.*

1.1.3 Macrophages, Drug Exposure, and Bioaccumulation

Serving as the frontline of the innate immune response, macrophages sequester and digest nonspecific foreign matter, essentially acting as metaphorical vacuum cleaners and residing throughout most tissues and organs of animals. Foreign particulate matter (cellular debris, bacteria, inhaled dust, nanoparticles, etc.) are phagocytosed (16) while lipophilic small molecule xenobiotics (e.g., drugs, environmental toxins, food additives, etc.) may passively diffuse directly through cellular membranes and accumulate within specific organelles. As the primary phagocytic cells of an animal's immune system, macrophages have highly active endosome/lysosome systems by which they sequester, acidify, and digest foreign matter (17, 18). Compared to other cell types, they have been shown to express elevated levels of vacuolar H^+-ATPase, the membrane proton transporter responsible for acidifying endocytic compartments, making macrophages especially well-suited for digestion of foreign matter (17).

Upon ingestion of foreign matter, the size and total mass of a macrophage (with phagocytosed contents) increases. Likewise, intracellular accumulation of drug molecules also increases total cell mass and may accompany a shift in biochemical composition as observed with PLD-inducing compounds (Figure 1-1). *This cell-by-cell shift in chemical composition is hypothesized to serve as a potential biomarker for changes in cellular physiology (i.e., induction of PLD) and/or xenobiotic accumulation and could be related to functional changes observed at the cellular, organ, and whole organism levels.*

As mentioned, macrophages throughout many organ systems have been reported to sequester and accumulate specific drugs following continuous exposure (19-25). Some example compounds that are known to accumulate in lysosomes include amiodarone, clofazimine, chloroquine, azithromycin, nilotinib, and imatinib; although many of these compounds are different classes of pharmaceuticals, they share similar structural and physicochemical properties. The highly lipophilic (logP > 3) and weakly basic (pKa > 8) archetype of such compounds gives rise to their increased propensity for lysosomal accumulation (26, 27). As illustrated in Figure 1-2, a thermodynamic equilibrium model has been proposed to describe the lysosomal accumulation of weakly basic xenobiotics via passive diffusion; the bioaccumulation of lipophilic weak bases is driven by pH differences between the extracellular fluid, cytoplasm, and the lysosomal compartments.

Molecules with high lipophilicity (logP > 3) can readily diffuse through biological membranes when in non-ionized form (neutral net charge). When a weakly basic small molecule encounters the acidic environment of lysosomes, it may become protonated (depending on pKa). Once protonated, a weakly basic amine group becomes ionized (positively charged) and can no longer diffuse through lipid membranes, thereby becoming trapped within the lysosome. The term for this phenomenon is “ion trapping” and it is the basis for lysosomal bioaccumulation of weakly basic molecules. The positively charged drug molecules also enable electrostatic interactions with negatively charged phospholipids, thereby facilitating induction of PLD.

Lysosomal accumulation of lipophilic weak bases has been shown to occur linearly over time (with no apparent steady-state) until the solubility of the compound is exceeded; once exceeded, there are two likely possibilities: *1) excess drug molecules spill over into the cytoplasm, achieving potentially cytotoxic intracellular concentrations or, 2) the drug precipitates and an additional solubility equilibrium increases the rate of accumulation* (28). Lysosomes typically contain ~140 mM of chloride anion which can promote intracellular drug precipitation as a hydrochloride salt. Precipitation allows a cell to sequester massive amounts of drug and facilitates a phase transition from liquid to solid as observed in the case of clofazimine (29) and suggested for nilotinib (28).

Lysosomal bioaccumulation has been reported to occur concurrently with the induction of PLD for some drug molecules (as previously discussed in "Physicochemical basis for drug-induced phospholipidosis") and has also been linked to functional consequences such as suppression of the inflammatory immune response (e.g., clofazimine, chloroquine, azithromycin, and amiodarone) (30-34). In some cases, such as treatment of leprosy with clofazimine and chronic obstructive pulmonary disease with azithromycin, these anti-inflammatory consequences are considered favorable. *Perhaps PLD following lysosomal bioaccumulation of xenobiotics is an adaptive physiological response to long-term drug exposure; macrophages protect the organs and tissues via sequestration of the drug which is made possible by a lipid-mediated expansion of the subcellular volume of distribution.*

1.1.4 Amiodarone, Pulmonary Toxicity, and Alveolar Macrophages

Amiodarone is a highly lipophilic (logP ~ 7.5) weak base (pKa = 8.47) and is the most widely used and effective antiarrhythmic medication available for the treatment of ventricular arrhythmias; unfortunately, the benefits of amiodarone therapy are accompanied by the risk of potentially life-threatening ADRs (35, 36). The most severe side effect is pulmonary toxicity. Manifestations include chronic, subacute, and acute complications such as pulmonary fibrosis, pneumonitis, and acute respiratory distress

syndrome (37-40). In the past, the prevalence of pulmonary toxicity was reported to be 15% but more recent trials indicate that rate is now 5% or less (35). The current clinical testing recommendations for patients prescribed amiodarone include biannual liver and thyroid function tests, yearly chest x-rays, ophthalmologic evaluation, pulmonary function tests (with diffusion capacity of carbon monoxide - D_LCO), and high-resolution CT scan when there is suspicion of pulmonary toxicity (35). Most patients on amiodarone are being treated for an underlying cardiovascular disease which can further complicate the diagnosis of pulmonary toxicity (38).

Robust attempts to understand the relationship between amiodarone exposure and adverse reactions began in 1983 following the development of an analytical assay sensitive enough to measure the low plasma concentrations of drug and enable pharmacokinetic profiling (38, 41). The pharmacokinetic parameters were experimentally determined in humans, each given three 400mg doses as IV infusion or oral formulation (Cordarone or Cordarone X) and relevant results are summarized as follows (Mean ± SD and Range respectively for each category): steady-state volume of distribution (L) = 4936 ± 3290 and 1375-11081, total plasma clearance (L/hr) = 8.6 ± 1.9 and 6.5-11.1, and terminal elimination half-life (days) = 24.8 ± 11.7 and 9.3-44.1. The large volume of distribution indicates significant distribution and bioaccumulation of amiodarone into tissue compartments, specifically the liver, lung, and lymph nodes. The major metabolite, desethylamiodarone, accumulates to much greater concentrations in tissue compartments compared to the parent drug. Consistent with reports of amiodarone-induced PLD, amiodarone and desethylamiodarone exhibited extensive accumulation in lung tissue. Following cessation of long-term dosage (400mg/day for 25 months) in a human patient, amiodarone and desethylamiodarone plasma levels both maintained therapeutic concentrations (>1.0 mg/L) for ~120 days.

This pharmacokinetic behavior is consistent with predictions of lysosomal bioaccumulation of lipophilic weak bases and is believed to be a result of a ‘slowly effluxable drug pool’ within the lysosomal phospholipid inclusions (lamellar bodies) previously described (26). BAL cells (>90% alveolar macrophages) from amiodarone-

treated patients showed significant intracellular accumulation of parent compound and the metabolite; pooled population analysis suggested up to 100 picograms of total xenobiotic per cell which equates to an estimated 25% of biochemical mass for typical eukaryotic cells (see table 1-1 in for context). Additionally, both amiodarone and desethylamiodarone concentrations directly correlated with phospholipid accumulation in BAL cells (42). Although the relationship between bioaccumulation and pulmonary toxicity has not yet been elucidated, the intracellular bioaccumulation of drug, metabolite, and phospholipid is observed in almost all clinical cases of pulmonary toxicity (42); perhaps the ability to quantitatively analyze drug-induced shifts in the biochemical composition of single cells and cell populations will enable the characterization of this 'slowly effluxable pool'. *By quantitatively defining the expansion limits of an organism's volume of distribution at the cellular level, a toxicity threshold could be identified and utilized to facilitate intelligent clinical decision-making and better understand the risk-benefit properties of amiodarone.*

1.1.5 Raman Micro-Spectroscopy for the Analysis of Clinical Biospecimens

Raman scattering was discovered in 1928 by Indian physicists C.V. Raman and K.S. Krishnan and was described as, "a modified scattered radiation of degraded frequency" (43). Since then, the phenomenon has been utilized to perform chemical characterization via spectroscopic analysis. Raman spectroscopy employs a monochromatic excitation light source (e.g., laser) to induce molecular vibrations within a sample; depending on the molecular bonds present in the sample, inelastic scattering of light occurs by which light emitted back off the sample is shifted to lower energy wavelengths. Nowadays, the intensity of scattered, or emitted, light can be collected and measured across a range of wavelengths using a CCD detector which converts the number of scattered photons at each wavelength into an electrical signal that can be interpreted computationally. The relative changes in light energy (between excitation and emission wavelengths) are known as Raman shifts and are measured in units of wavenumbers (cm^{-1}). The physical nature of the phenomenon allows for quantitative

interpretation of the spectral data as the number of Raman-active bonds in a molecule is directly related to the number of scattered Raman photons.

Raman micro-spectroscopy (aka micro-Raman spectroscopy, Raman microscopy, Raman microanalysis, etc.) involves the coupling of a Raman spectrometer to a confocal microscope, enabling chemical analysis of samples with sub-micron spatial resolution (Figure 1-3). Over the past two decades, Raman microscopy has been successfully utilized to quantitatively study the chemical composition of biological specimens at the tissue, single cell, and subcellular levels; some might even suggest the technique is a "magic bullet" for biomedical analysis applications (28, 44-50). Modern advances in Raman microscope technology have enabled faster, more accurate, repeatable, and robust quantitative analyses of the biotic and abiotic chemical constituents comprising individual eukaryotic cells. *Biomedical Raman spectroscopy is an emerging field which offers new avenues for the chemical analysis of biological specimens; the non-destructive and label-free methodology allows for quantitative characterization of the natural distribution and sequestration patterns of colorless molecules within biological matrices such as single cells or tissues.* Due to the inherent chemical complexity of biological specimens, a measured Raman spectrum represents a mixture of molecular species differentially contributing to overall signal. As such, acquired Raman spectra may be modeled as a mixture of reference spectra representing the most abundant biochemical species present in a sample (Figure 1-4). To serve as a preliminary theoretical foundation, the approximate chemical composition of a typical eukaryotic cell was calculated based on cell population average values from bulk measurements (of homogenized cell populations) and provided in table 1-1. Since water does not interfere with Raman scattering, proteins and lipids comprise the majority of a cell's chemical mass and the majority of acquired Raman signals.

Proteins are all constructed from the same 20 amino acids and thus give rise to similar Raman signals; the predominant vibrational modes arise from amide bonds in the polypeptide backbone (52). As the second-most abundant chemical component of biological systems, lipids are readily detectable via Raman analysis. Lipids have a

relatively strong and unique vibrational signal occurring at 2850 cm^{-1} due to fatty hydrocarbon chains (C-H), and are easily distinguished from other biochemical components; furthermore, specific spectral differences can be used to discriminate between diverse types of lipids present in a biological sample (53). Metabolites represent a heterogeneous population of small molecules, all of which have unique Raman spectra and are likely undetectable unless present at levels significantly greater than the physiological baseline. Polysaccharides may be detectable; in certain cell types (e.g., muscle cells, hepatocytes) cytosolic granules of glycogen exist and could give rise to a detectable Raman signal. Nucleic acids, DNA and RNA, make up the final population of biomolecules of interest. Their Raman signals are comprised of contributions from the five nucleobases (cytosine, guanine, adenine, thymine, and uracil) and the sugar-phosphate backbone. *Proteins, lipids, polysaccharides, and nucleic acids have all been successfully detected in single eukaryotic cells, confirming the feasibility of Raman micro-spectroscopy for chemical analysis of biological specimens.*

Compared to spectra of cellular components, amiodarone's major Raman peak occurs at a unique wavenumber and can therefore feasibly be distinguished from endogenous biomolecules and quantified within a biological matrix. Despite this, there appears to be very little published information regarding Raman analysis of amiodarone; the most relevant study for our purposes involved the development of a Raman-based assay for amiodarone in Angoron® concentrated injectable solutions (51). Based on the reported Raman spectra, the major peak of the solid amiodarone HCl powder occurred at ~1640 cm^{-1} while the major peak of the soluble drug occurred at 1568 cm^{-1} (Figure 1-4). By exploiting these spectral differences, Raman microanalysis will enable the characterization of the phase transitions that amiodarone is most likely to experience within the lysosomal compartments. As described in the previous section, macrophage lysosomes maintain low-pH environments with ~140mM chloride ion concentration; under these conditions, the precipitation of amiodarone as a HCl salt crystal is completely feasible. This precipitation phenomenon has been previously reported to occur with other lipophilic weakly basic compounds, specifically clofazimine and nilotinib (28, 29). As such,

the scope of this research endeavor was expanded beyond just amiodarone to include a multitude of bioaccumulating compounds in a variety of cell types from an assortment of species, namely mice, pig, and humans.

As the robustness of Raman bioanalytical methodology advances, the clinical application of this technology is emerging as a powerful and reliable research tool. The coupling of a Raman spectrometer with an endoscope has enabled diagnostic Raman endoscopy for detection of oral, esophageal, and gastric cancers (54-56). Raman spectroscopy has also been utilized for breast cancer detection purposes to study acquired drug resistances in cancer cell lines (57, 58). The feasibility of *in vivo* Raman spectroscopy as a noninvasive biomedical imaging modality for chemical analysis of tissues within living organisms has also been demonstrated in small animal models (59). Raman microscopy has been successfully employed to quantitatively study the uptake and distribution of a multitude of small molecules (drugs, vitamins, lipids, glycogen, etc.) within individual cells (28, 49, 50, 60-62). Biochemical characterization of single cells has also been extensively explored to assess drug-induced changes in composition or to discriminate and classify different cell populations; these techniques often require advanced multivariate statistical interpretations to extract the relevant information for each major biochemical component (46, 47, 63-66).

1.1.6 Computational Preprocessing and Statistical Analysis of Raman Datasets

Due to the inherent chemical complexity of biological systems, acquired spectra are composed of a multiplicity of features from which the relevant information must be extracted. In addition to the Raman peaks of interest, there are three major artifacts that contribute to a measured Raman spectrum: cosmic ray spikes, autofluorescense background, and detector noise (44, 67-72). To accurately interpret the actual Raman spectra, these side effects must be effectively removed; this is achieved via optimization of experimental acquisition parameters and computational preprocessing of the acquired raw spectrum. The preprocessing procedures may be performed manually on individual

spectra but this allows for greater chance of analyst error and raises questions regarding the objectivity of the analysis, so for Raman hyperspectral images, which often consist of thousands of spectra (Figure 1-5), there is a necessity for robust computational algorithms to quickly pre-process spectra and extract the relevant information of interest. Once the pure Raman spectra have been computationally extracted from the acquired raw spectra, they are typically normalized to account for differences in sample preparation or acquisition parameters. All subsequent analysis of Raman data is heavily dependent on spectral preprocessing and so error minimization is a necessity.

Once preprocessed, the Raman spectra must be decoded appropriately to obtain the relevant information of interest (Figure 1-5). There are many straightforward approaches that have been utilized to measure analytes of interest using the acquired Raman spectra (e.g., Raman peak intensity at a given wavenumber, integrated peak intensity, peak intensity ratios, etc.). Owing to their inherent chemical complexity, biological specimens often require advanced multivariate statistical approaches to generate accurate models from acquired Raman datasets (44, 73). There are many statistical approaches that allow for more detailed extraction of chemical information contained within acquired Raman spectra; in the case of single cell Raman imaging, multivariate approaches enable the distinction and identification of subcellular compartments such as the nucleus, organelles, and other cytoplasmic inclusions (73). It is worth noting that different results can be obtained from the same Raman dataset depending on the statistical approach employed. In addition to statistical interpretation, the color shading schemes utilized during construction of the final Raman images must be carefully chosen in order to display the most appropriate information to address the scientific question of interest (74).

Between pre-processing, statistical interpretation, and resulting image construction, Raman spectral analysis algorithms are extremely detailed processes. *As such, it is imperative to confirm the validity of spectral preprocessing algorithms and employ checkpoints to confirm confidence and accuracy throughout the process.* In addition to spectral preprocessing, the validity of employed statistical analysis

approaches must be confirmed; to do this, *the statistical model for any given set of experimental conditions must be rationally refined to account for most of the spectral variance observed in control samples.*

1.2 Innovation

Historically, transmission electron microscopy (TEM) has served as the "gold standard" for diagnosis of PLD and has been described as the most sensitive method for confirming the presence of PLD. Since the defining morphological feature of PLD is the presence of membranous lamellar inclusions, a diagnosis can be made via TEM but no quantitative information is deduced regarding the extent or degree of drug or phospholipid accumulation. Perhaps quantitative (bio)chemical characterization of cell populations affected by PLD would allow for the identification of an accumulation threshold after which organ toxicity manifests. *As such, a novel analytical methodology to study drug-induced PLD in the clinical setting by concurrently quantifying drug and lipid accumulation within individual alveolar macrophages obtained via BAL would be of significant value.*

There are currently a multitude of ongoing research initiatives attempting to investigate and address drug-induced PLD during drug development phases and following post-market approval of drugs. In 2004, the U.S. Food and Drug Administration established the Phospholipidosis Working Group to address the regulatory challenges associated with this poorly understood adverse effect (7). There are two main approaches this group is pursuing to study PLD: 1) computational QSAR *in silico* modeling to predict a drug's potential to induce PLD based on molecular structure properties and 2) identification of a plasma or urine metabolite to serve as a reliable clinical biomarker for PLD (13, 14, 75, 76). Another group looked into drug-induced transcriptional responses which they related to the structural features of the drugs under study; the results suggested transcription factor EB (TFEB) which is involved with regulation of lysosomal biogenesis and autophagy, as a transcriptional signature of drug-induced PLD (77). Although these approaches are somewhat capable of predicting and confirming the

presence of PLD, they do not offer insight into the manifestation of resulting organ toxicity. Therefore, these studies will likely serve to refine the drug development process for new compounds rather than improving the safety and usage of existing drugs in the clinical setting. A more recent approach employed the use of correlative NanoSIMS and electron microscopy, allowing for secondary ion mass spectrometric analysis with nanoscale resolution and specifically measuring phospholipid and amiodarone accumulation in alveolar macrophages (78). This study served to detect amiodarone-induced PLD in alveolar macrophages and showed a significant degree of colocalization between phospholipids and amiodarone, believed to occur within lysosomal compartments.

1.3 Rationale

In 1538, before the invention of the first microscope and the subsequent discovery of cells, the founding father of modern pharmacology - Paracelsus, expressed the following concept which has become a foundational principle in the field of modern pharmacological sciences: “All things are poison, and nothing is without poison, the dosage alone makes it so a thing is not a poison” (79). Over the past 500 years, significant advances in medical sciences have been made but ADRs still represent a major healthcare concern for individual patients and clinicians as well as an economic burden on hospitals and pharmaceutical companies attempting to develop new drug candidates (2, 4). ADRs are an inherent risk of any drug therapy regimen, each of which is differentially governed by specific factors such as genotype and health status of a patient, the compound’s pharmacokinetic parameters (e.g., volume of distribution, clearance, half-life, etc.), dose and frequency of administration. A compound may give rise to adverse effects when concentrations exceed the toxic exposure limit. Furthermore, a compound may preferentially co-localize with endogenous biomolecules and, in some cases, even sequester within specific subcellular compartments, depending on its physicochemical properties, achieving intracellular concentrations much greater than those measured in the organism’s extracellular fluids, such as blood and urine.

Bioaccumulation of xenobiotics (e.g., drug molecules, environmental toxins, food additives, etc.) has been reported for a multitude of compounds and in many cases, has been linked with the concurrent accumulation of phospholipids, termed PLD, within various organs and cell types (23-25, 27, 28, 80). The lungs and liver are the tissues in which PLD is most frequently detected during preclinical *in vivo* studies and the presence of foamy, lipid-laden, macrophages has historically served as the histopathological hallmark (10, 11, 26, 80). Despite an abundance of research endeavors surrounding PLD over the past 30 years, the relationship between drug exposure, lipid accumulation, and observed organ toxicity has yet to be firmly established (7-9, 15). Since pulmonary alveolar macrophages are readily accessible in humans and animals via bronchoalveolar lavage, we believe these cells could feasibly serve as a clinical correlate between drug-induced PLD and the observed organ toxicity (9, 18, 81). Raman micro-spectroscopy enables quantitative chemical characterization at the single-cell level without the need for artificial molecular tags, ultimately providing insight into the unadulterated composition of individual cells. The long-term goal of this project is the clinical implementation of a robust Raman-based cytoanalytical methodology; by directly relating acquired Raman signals to the actual number of Raman-active molecular bonds present in a sample, we aim to quantitatively characterize drug and lipid accumulation at the single-cell and cell population levels.

A typical 75kg human occupies a volume of approximately 75L; within that finite amount of space, resides a finite number of cells and mass of material (biological and xenobiotic). Serving as the foundation of our innate immune systems, macrophage populations exhibit seemingly unbounded sequestration and accumulation of certain xenobiotics to protect us, their human hosts, from toxic exposure. Though robust and adaptable, perhaps these cells have a limit to how much material they can carry. If so, then quantitative characterization of this system and its limits would surely serve to improve our understanding of the risk-benefit properties for a multitude of clinically effective compounds. Raman micro-spectroscopy offers a novel approach for the study of drug-induced bioaccumulation phenomena and could thus enable elucidation of the

mysterious relationship between drug exposure, PLD, and organ toxicity currently burdening the drug development industry and clinicians.

1.4 Central Hypothesis and Specific Aims

Central Hypothesis. The appropriate interpretation of Raman signals enables quantitative physio-chemical cytometry by relating intracellular xenobiotic accumulation and chemical composition of cells to the health status of a patient, potentially yielding actionable results that will help facilitate clinical decision making and improve patient outcomes.

Specific Aim 1. Development of robust computational algorithms will automate spectral preprocessing and statistical translation of Raman signals into chemically-relevant information at the single-cell level, enabling measurement of intracellular drug accumulation and precipitation in relation to protein, lipid, and nucleic acid on a per-pixel basis.

Specific Aim 2. Ultraquantitative confocal Raman micro-spectroscopy will enable the absolute quantification of the most abundant endogenous biomolecular components and sequestered xenobiotics within a single eukaryotic cell; cell-sized micro-calibration standards of known absolute mass and composition may be fabricated via controlled deposition of biomolecular ink formulations in picoliter-volume droplets to form microarrays across sample substrates that serve as calibration standards for quantitative interpretation of Raman spectral data.

Specific Aim 3. Bioanalytical micro-Raman spectropathology will provide new information about the structure, function, and role of alveolar macrophage phenotype in the context of pulmonary disease pathogenesis and will enable measurement of cellular cargo (i.e., lipids) at the single cell level, providing new perspectives by which to

quantitatively assess cellular storage disorders *in vivo* and ultimately facilitating the translation of this analytical technology to the clinical setting.

1.5 Figures

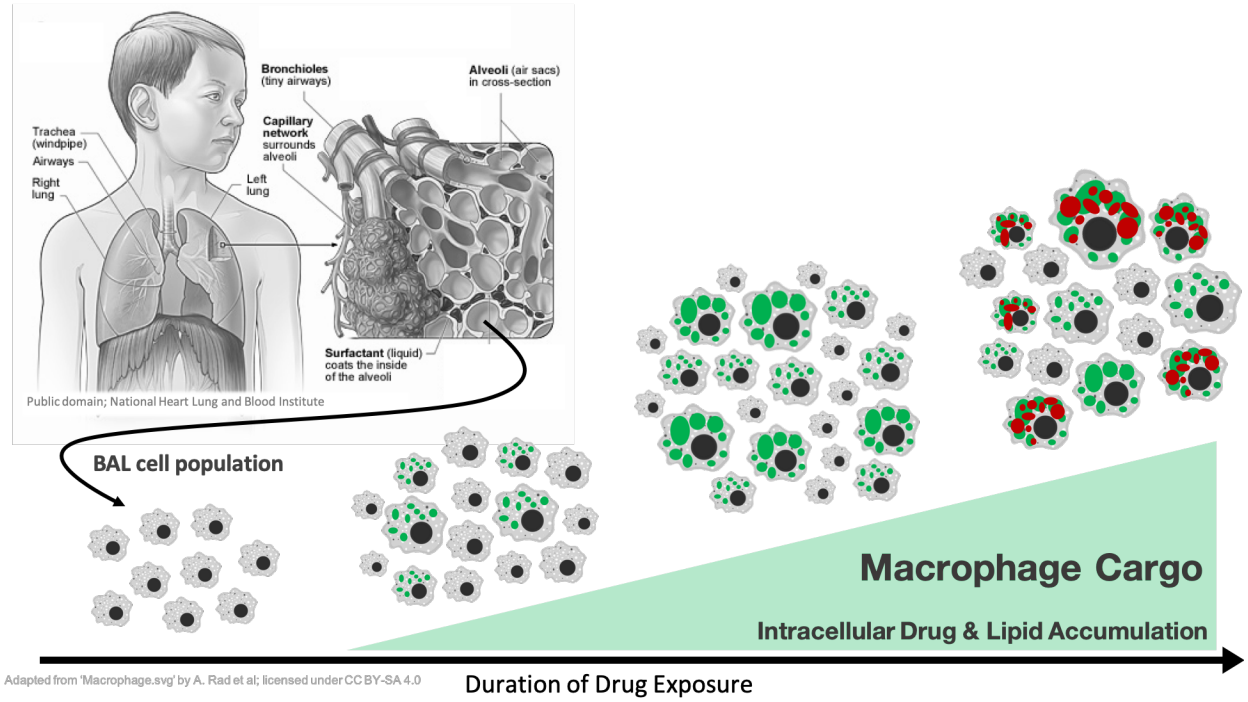

Figure 1-1. Schematic illustration for alveolar macrophage cargo loading and PLD.

Alveolar macrophages are accessible in the clinical setting via bronchoalveolar lavage; these cells are reported to sequester drugs and lipids – which may more generally be referred to as macrophage "cargo" – in response to extended periods of drug exposure.

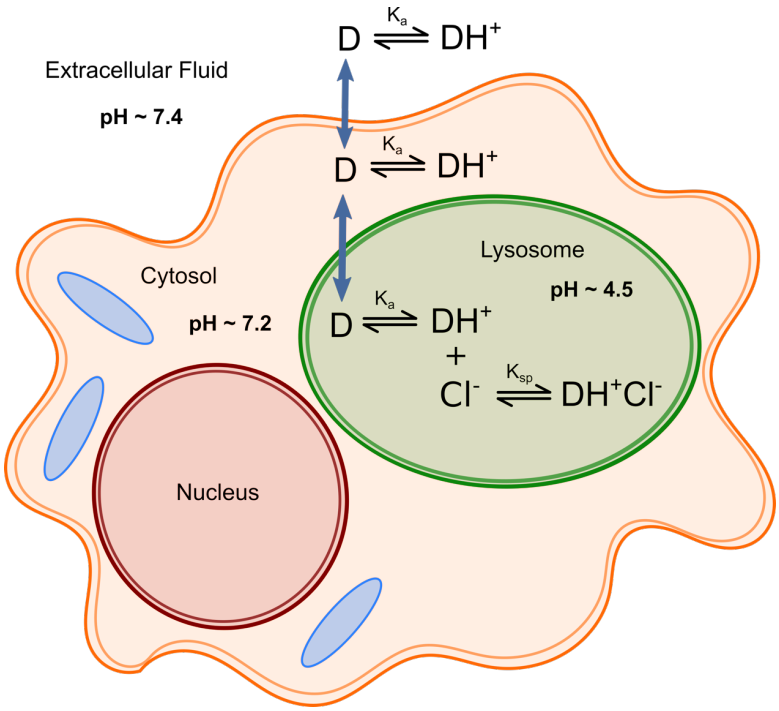

Figure 1-2. Proposed thermodynamic equilibrium model for the lysosomal accumulation of weakly basic lipophilic small molecules.

The non-ionized form of a lipophilic drug molecule (D) may passively diffuse through the lipid membranes of a biological cell; depending on the pKa of the compound and the pH of the cellular compartment, the drug may become protonated (DH^+), or ionized. The ionized form of the molecule becomes trapped because it cannot diffuse through the membranes, causing the drug to accumulate. As the drug concentration increases, depending on the molecule's K_{sp} with chloride counter-ion (Cl^-), it may precipitate as the HCl salt crystal, as observed in the case of clofazimine.

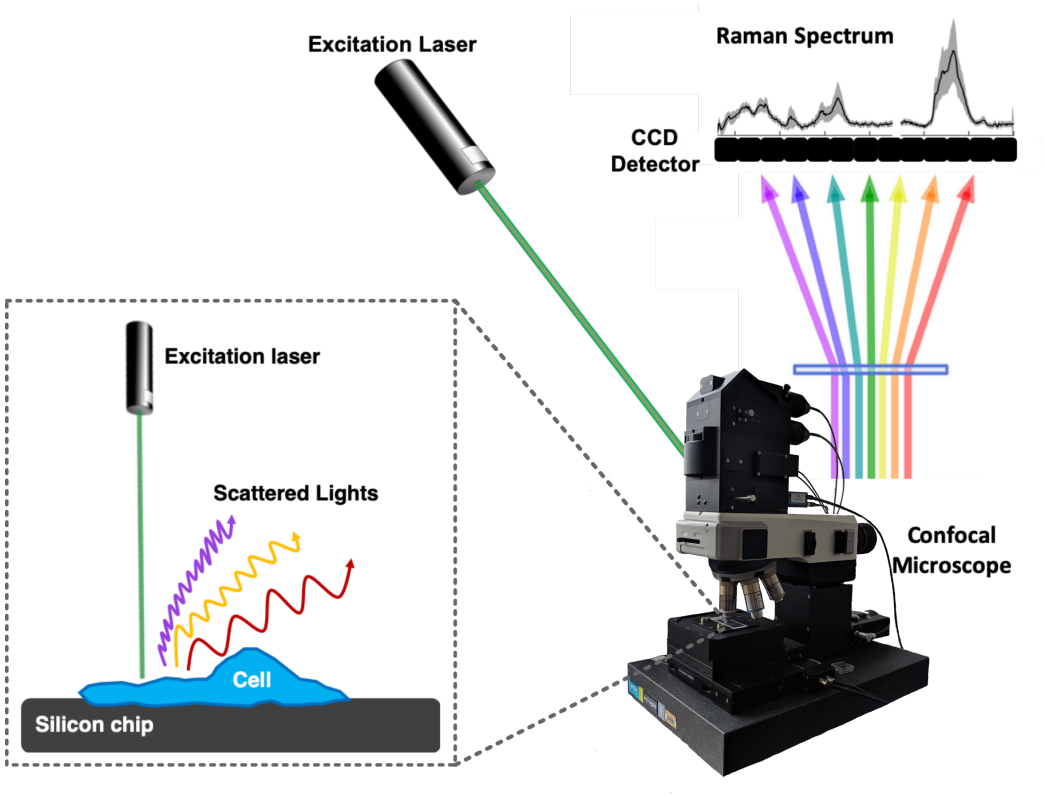

Figure 1-3. Schematic of micro-Raman spectroscopy experimental setup.

An excitation laser is coupled to a confocal microscope via a fiber-optic cable. The microscope objective lens focuses the laser down onto a cell preparation on silicon chip substrate, inducing molecular vibrations within the cell sample which scatter a multitude of different colored lights up off the sample. The reflected/scattered lights are collected by the microscope objective, separated by a diffraction grating, and directed across a CCD detector which converts the photons of light at each wavelength into an electrical signal (CCD counts), thereby forming a Raman spectrum.

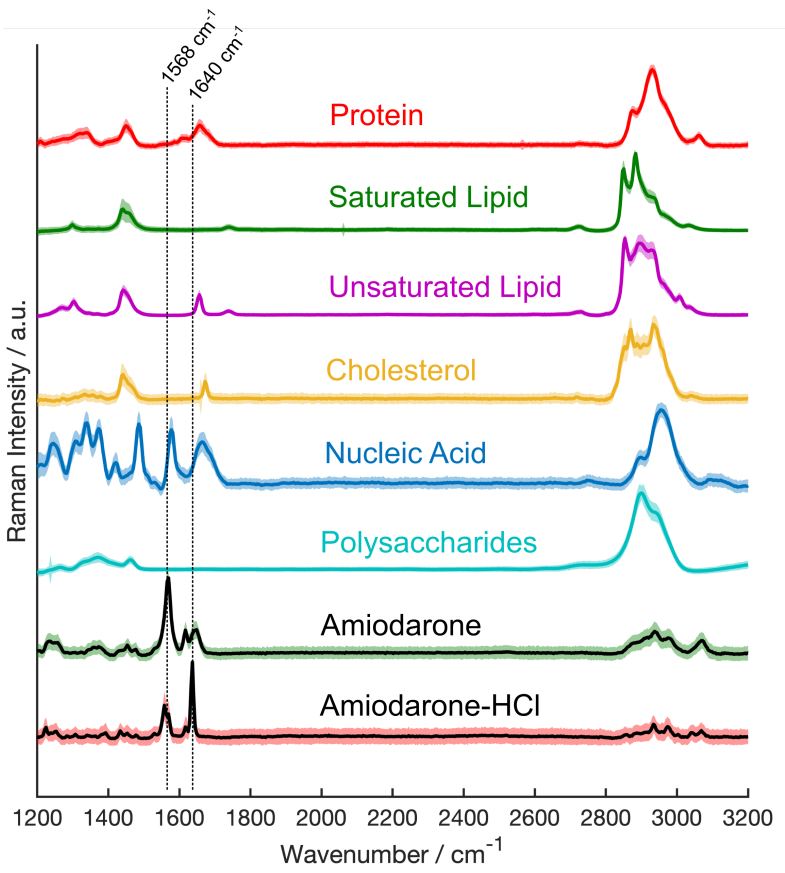

Figure 1-4. Raman reference spectral library of biomolecular components overlaid with amiodarone and amiodarone-HCl.

All reference spectra were collected with 532nm excitation laser. Amiodarone and amiodarone-HCl can theoretically be distinguished from each other and other major biomolecular components of interest in typical eukaryotic cells, by their characteristic Raman signals at 1568cm^{-1} and 1640cm^{-1}, respectively.

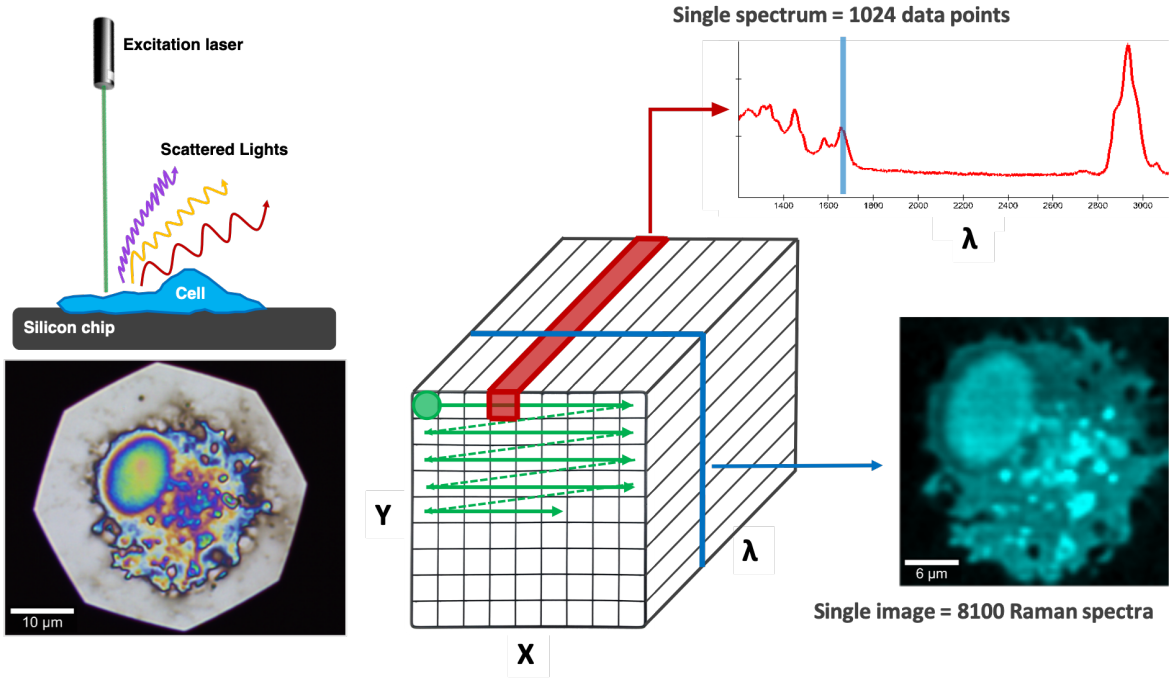

Figure 1-5. Schematic of Raman hyperspectral data acquisition and format.

The excitation laser scans across the area of interest (X-Y plane), collecting Raman spectra at every pixel of the area scan (z-plane, λ). A single image may consist of thousands of individual spectra and a single spectrum consists of 1024 data points. As shown here, a Raman image may be formed by plotting the intensity (CCD counts) for a specific wavenumber (λ) at each pixel of the image.

1.6 Tables

Table 1-1. Compositional estimates for a typical eukaryotic cell.

Data was adapted from Lodish H, Berk A, Zipursky SL, Matsudaira P, Baltimore D, Darnell J. Molecular cell biology 4th edition. National Center for Biotechnology Information Bookshelf. 2000.

Component	Water	Proteins	Lipids	Metabolites	Polysaccharides	Nucleic Acids		Inorganic Ions
						RNA	DNA	
% total cell (w/w)	70	18	5	3	2	1.1	0.25	1
Estimated mass in typical cell (pg)	700	180	50	30	20	11	2.5	10
Subcellular Location	Removed - dried samples	Throughout	Membranes, organelles	Metabolite-specific	Cytoplasmic granules	Cytoplasm, nucleus	Nucleus, mitochondria	Cytoplasm, organelles
Detectable via Raman?	-	+	+	-	+	+	+	-

1.7 References

1. Organization WH. International drug monitoring: the role of national centers. Technical Report No 498. Geneva, Switzerland: Geneva: World Health Organization; 1972.

2. Lazarou J, Pomeranz BH, Corey PN. Incidence of adverse drug reactions in hospitalized patients: A meta-analysis of prospective studies. JAMA. 1998;279(15):1200-5. doi: 10.1001/jama.279.15.1200.

3. Lacoste-Roussillon C, Pouyanne P, Haramburu F, Miremont G, Bégaud B. Incidence of serious adverse drug reactions in general practice: A prospective study. Clinical Pharmacology & Therapeutics. 2001;69(6):458-62. doi: 10.1067/mcp.2001.116145.

4. Sultana J, Cutroneo P, TrifirÚ G. Clinical and economic burden of adverse drug reactions. Journal of Pharmacology and Pharmacotherapeutics. 2013;4(5):73-7. doi: 10.4103/0976-500x.120957.

5. Martin K, Bégaud B, Latry P, Miremont-Salamé G, Fourrier A, Moore N. Differences between clinical trials and postmarketing use. British Journal of Clinical Pharmacology. 2004;57(1):86-92.

6. Nelson A, Fitzhugh O. Chloroquine (SN-7618) pathologic changes observed in rats which for 2 years had been fed various proportions. Archives of Pathology. 1948;45(4):454.

7. Sadrieh N. The Regulatory Challenges of Drug-Induced Phospholipidosis - Presented in part at the FDA Advisory Committee for Pharmaceutical Science and Clinical Pharmacology meeting. 2010.

8. Reasor MJ, Kacew S. Drug-induced phospholipidosis: are there functional consequences? Experimental Biology and Medicine. 2001;226(9):825-30.

9. Anderson N, Borlak J. Drug-induced phospholipidosis. FEBS Letters. 2006;580(23):5533-40. doi: 10.1016/j.febslet.2006.08.061.

10. Halliwell WH. Cationic Amphiphilic Drug-Induced Phospholipidosis. Toxicologic Pathology. 1997;25(1):53-60. doi: 10.1177/019262339702500111.

11. Kodavanti UP, Mehendale HM. Cationic amphiphilic drugs and phospholipid storage disorder. Pharmacological Reviews. 1990;42(4):327-54.

12. Reasor MJ, Ogle CL, Walker ER, Kacew S. Amiodarone-induced Phospholipidosis in Rat Alveolar Macrophages. American Review of Respiratory Disease. 1988;137:510-8.

13. Baronas ET, Lee J-W, Alden C, Hsieh FY. Biomarkers to monitor drug-induced phospholipidosis. Toxicology and Applied Pharmacology. 2007;218(1):72-8. doi: http://dx.doi.org/10.1016/j.taap.2006.10.015.

14. Liu N, Tengstrand EA, Chourb L, Hsieh FY. Di-22:6-bis(monoacylglycerol)phosphate: A clinical biomarker of drug-induced phospholipidosis for drug development and safety assessment. Toxicology and Applied Pharmacology. 2014;279(3):467-76. doi: http://dx.doi.org/10.1016/j.taap.2014.06.014.

15. Chatman LA, Morton D, Johnson TO, Anway SD. A Strategy for Risk Management of Drug-Induced Phospholipidosis. Toxicologic Pathology. 2009;37(7):997-1005. doi: doi:10.1177/0192623309352496.

16. Araki N, Johnson MT, Swanson JA. A role for phosphoinositide 3-kinase in the completion of macropinocytosis and phagocytosis by macrophages. The Journal of Cell Biology. 1996;135(5):1249-60. doi: 10.1083/jcb.135.5.1249.

17. Wang S-P, Krits I, Bai S, Lee BS. Regulation of enhanced vacuolar H+-ATPase expression in macrophages. Journal of Biological Chemistry. 2002;277(11):8827-34.

18. Fels AO, Cohn ZA. The alveolar macrophage. Journal of Applied Physiology. 1986;60(2):353-69.

19. Stamler DA, Edelstein M, Edelstein PH. Azithromycin pharmacokinetics and intracellular concentrations in Legionella pneumophila-infected and uninfected guinea pigs and their alveolar macrophages. Antimicrobial Agents and Chemotherapy. 1994;38(2):217-22.

20. Gladue R, Bright G, Isaacson R, Newborg M. In vitro and in vivo uptake of azithromycin (CP-62,993) by phagocytic cells: possible mechanism of delivery and release at sites of infection. Antimicrobial Agents and Chemotherapy. 1989;33(3):277-82.

21. Baik J, Rosania GR. Molecular imaging of intracellular drug–membrane aggregate formation. Molecular Pharmaceutics. 2011;8(5):1742-9.

22. Baik J, Stringer KA, Mane G, Rosania GR. Multiscale distribution and bioaccumulation analysis of clofazimine reveals a massive immune system-mediated xenobiotic sequestration response. Antimicrobial Agents and Chemotherapy. 2013;57(3):1218-30.

23. Antonini JM, Reasor MJ. Accumulation of amiodarone and desethylamiodarone by rat alveolar macrophages in cell culture. Biochemical Pharmacology. 1991;42:S151-S6. doi: http://dx.doi.org/10.1016/0006-2952(91)90405-T.

24. Morissette G, Ammoury A, Rusu D, Marguery MC, Lodge R, Poubelle PE, et al. Intracellular sequestration of amiodarone: role of vacuolar ATPase and macroautophagic transition of the resulting vacuolar cytopathology. British Journal of Pharmacology. 2009;157(8):1531-40. doi: 10.1111/j.1476-5381.2009.00320.x.

25. Zheng N, Zhang X, Rosania GR. Effect of phospholipidosis on the cellular pharmacokinetics of chloroquine. Journal of Pharmacology and Experimental Therapeutics. 2011;336(3):661-71.

26. Macintyre AC, Cutler DJ. The potential role of lysosomes in tissue distribution of weak bases. Biopharmaceutics & Drug Disposition. 1988;9(6):513-26. doi: 10.1002/bod.2510090602.

27. Logan R, Kong AC, Krise JP. Time-Dependent Effects of Hydrophobic Amine-Containing Drugs on Lysosome Structure and Biogenesis in Cultured Human Fibroblasts. Journal of Pharmaceutical Sciences. 2014;103(10):3287-96. doi: 10.1002/jps.24087.

28. Fu D, Zhou J, Zhu WS, Manley PW, Wang YK, Hood T, et al. Imaging the intracellular distribution of tyrosine kinase inhibitors in living cells with quantitative hyperspectral stimulated Raman scattering. Nature Chemistry. 2014;6(7):614-22.

29. Keswani RK, Baik J, Yeomans L, Hitzman C, Johnson AM, Pawate AS, et al. Chemical analysis of drug biocrystals: a role for counterion transport pathways in intracellular drug disposition. Molecular Pharmaceutics. 2015;12(7):2528-36.

30. Nujić K, Banjanac M, Munić V, Polančec D, Haber VE. Impairment of lysosomal functions by azithromycin and chloroquine contributes to anti-inflammatory phenotype. Cellular Immunology. 2012;279(1):78-86.

31. Liu Y, Kam WR, Ding J, Sullivan DA. One man's poison is another man's meat: using azithromycin-induced phospholipidosis to promote ocular surface health. Toxicology. 2014;320:1-5.

32. Yoon GS, Keswani RK, Sud S, Rzeczycki PM, Murashov MD, Koehn TA, et al. Clofazimine biocrystal accumulation in macrophages upregulates interleukin 1 receptor antagonist production to induce a systemic anti-inflammatory state. Antimicrobial Agents and Chemotherapy. 2016;60(6):3470-9.

33. Halici Z, Dengiz GO, Odabasoglu F, Suleyman H, Cadirci E, Halici M. Amiodarone has anti-inflammatory and anti-oxidative properties: an experimental study in rats with carrageenan-induced paw edema. European Journal of Pharmacology. 2007;566(1):215-21.

34. Wilson BD, Clarkson CE, Lippmann ML. Amiodarone causes decreased cell-mediated immune responses and inhibits the phospholipase C signaling pathway. Lung. 1993;171(3):137-48.

35. Epstein AE, Olshansky B, Naccarelli GV, Kennedy JI, Murphy EJ, Goldschlager N. Practical Management Guide for Clinicians Who Treat Patients with Amiodarone. The American Journal of Medicine. 2016;129(5):468-75. doi: http://dx.doi.org/10.1016/j.amjmed.2015.08.039.

36. Hrudikova Vyskocilova E, Grundmann M, Duricova J, Kacirova I. Therapeutic monitoring of amiodarone: pharmacokinetics and evaluation of the relationship between effect and dose/concentration. 2017.

37. Teerakanok J, Tantrachoti P, Chariyawong P, Nugent K. Acute Amiodarone Pulmonary Toxicity After Surgical Procedures. The American Journal of the Medical Sciences. 352(6):646-51. doi: 10.1016/j.amjms.2016.08.013.

38. Heger JJ, Prystowsky EN, Zipes DP. Relationships between amiodarone dosage, drug concentrations, and adverse side effects. American Heart Journal. 1983;106(4):931-5. doi: http://dx.doi.org/10.1016/0002-8703(83)90018-2.

39. Martin WJ, Rosenow EC. Amiodarone pulmonary toxicity. Recognition and pathogenesis (Part I). Chest. 1988;93(5):1067-75. doi: 10.1378/chest.93.5.1067.

40. Ott MC, Khoor A, Leventhal JP, Paterick TE, Burger CD. Pulmonary toxicity in patients receiving low-dose amiodarone. Chest. 2003;123(2):646-51.

41. Holt DW, Tucker GT, Jackson PR, Storey GCA. Amiodarone pharmacokinetics. American Heart Journal. 1983;106(4):840-7. doi: http://dx.doi.org/10.1016/0002-8703(83)90006-6.

42. Martin WJ, Standing JE. Amiodarone pulmonary toxicity: biochemical evidence for a cellular phospholipidosis in the bronchoalveolar lavage of human subjects. Journal of Pharmacology and Experimental Therapeutics. 1988;244(2):774-9.

43. Raman CV, Krishnan KS. A new type of secondary radiation. Nature. 1928;121(3048):501-2.

44. Bocklitz TW, Guo S, Ryabchykov O, Vogler N, Popp J. Raman Based Molecular Imaging and Analytics: A Magic Bullet for Biomedical Applications!? Analytical Chemistry. 2016;88(1):133-51. doi: 10.1021/acs.analchem.5b04665.

45. Palonpon AF, Sodeoka M, Fujita K. Molecular imaging of live cells by Raman microscopy. Current Opinion in Chemical Biology. 2013;17(4):708-15.

46. Fu D, Lu F-K, Zhang X, Freudiger C, Pernik DR, Holtom G, et al. Quantitative chemical imaging with multiplex stimulated Raman scattering microscopy. Journal of the American Chemical Society. 2012;134(8):3623-6.

47. Schie IW, Kiselev R, Krafft C, Popp J. Rapid acquisition of mean Raman spectra of eukaryotic cells for a robust single cell classification. Analyst. 2016;141(23):6387-95.

48. Kann B, Offerhaus HL, Windbergs M, Otto C. Raman microscopy for cellular investigations—From single cell imaging to drug carrier uptake visualization. Advanced Drug Delivery Reviews. 2015;89:71-90.

49. Beattie JR, Maguire C, Gilchrist S, Barrett LJ, Cross CE, Possmayer F, et al. The use of Raman microscopy to determine and localize vitamin E in biological samples. The FASEB Journal. 2007;21(3):766-76.

50. Galler K, Requardt RP, Glaser U, Markwart R, Bocklitz T, Bauer M, et al. Single cell analysis in native tissue: Quantification of the retinoid content of hepatic stellate cells. Scientific Reports. 2016;6.

51. Orkoula MG, Kontoyannis CG, Markopoulou CK, Koundourellis JE. Validation of a direct non-destructive quantitative analysis of amiodarone hydrochloride in Angoron® formulations using FT-Raman spectroscopy. Talanta. 2007;73(2):258-61. doi: http://dx.doi.org/10.1016/j.talanta.2007.03.033.

52. Rygula A, Majzner K, Marzec KM, Kaczor A, Pilarczyk M, Baranska M. Raman spectroscopy of proteins: a review. Journal of Raman Spectroscopy. 2013;44(8):1061-76.

53. Czamara K, Majzner K, Pacia MZ, Kochan K, Kaczor A, Baranska M. Raman spectroscopy of lipids: a review. Journal of Raman Spectroscopy. 2015;46(1):4-20. doi: 10.1002/jrs.4607.

54. Bergholt MS, Zheng W, Lin K, Ho KY, Teh M, Yeoh KG, et al. Characterizing variability in in vivo Raman spectra of different anatomical locations in the upper gastrointestinal tract toward cancer detection. Journal of Biomedical Optics. 2011;16(3):037003-10.

55. Bergholt MS, Zheng W, Huang Z. Characterizing variability in in vivo Raman spectroscopic properties of different anatomical sites of normal tissue in the oral cavity. Journal of Raman Spectroscopy. 2012;43(2):255-62. doi: 10.1002/jrs.3026.

56. Zhou X, Dai J, Chen Y, Duan G, Liu Y, Zhang H, et al. Evaluation of the diagnostic potential of ex vivo Raman spectroscopy in gastric cancers: fingerprint versus high wavenumber. Journal of Biomedical Optics. 2016;21(10):105002-.

57. Haka AS, Volynskaya Z, Gardecki JA, Nazemi J, Lyons J, Hicks D, et al. In vivo margin assessment during partial mastectomy breast surgery using Raman spectroscopy. Cancer Research. 2006;66(6):3317-22.

58. Bi X, Rexer B, Arteaga CL, Guo M, Mahadevan-Jansen A. Evaluating HER2 amplification status and acquired drug resistance in breast cancer cells using Raman spectroscopy. Journal of Biomedical Optics. 2014;19(2):025001-.

59. Keren S, Zavaleta C, Cheng Z, de La Zerda A, Gheysens O, Gambhir S. Noninvasive molecular imaging of small living subjects using Raman spectroscopy. Proceedings of the National Academy of Sciences. 2008;105(15):5844-9.

60. Konorov SO, Schulze HG, Atkins CG, Piret JM, Aparicio SA, Turner RF, et al. Absolute quantification of intracellular glycogen content in human embryonic stem cells with Raman microspectroscopy. Analytical Chemistry. 2011;83(16):6254-8.

61. van Manen H-J, Kraan YM, Roos D, Otto C. Single-cell Raman and fluorescence microscopy reveal the association of lipid bodies with phagosomes in leukocytes. Proceedings of the National Academy of Sciences of the United States of America. 2005;102(29):10159-64.

62. Stiebing C, Matthäus C, Krafft C, Keller A-A, Weber K, Lorkowski S, et al. Complexity of fatty acid distribution inside human macrophages on single cell level using Raman micro-spectroscopy. Analytical and Bioanalytical Chemistry. 2014;406(27):7037-46.

63. Schie IW, Alber L, Gryshuk AL, Chan JW. Investigating drug induced changes in single, living lymphocytes based on Raman micro-spectroscopy. Analyst. 2014;139(11):2726-33.

64. Lu F-K, Basu S, Igras V, Hoang MP, Ji M, Fu D, et al. Label-free DNA imaging in vivo with stimulated Raman scattering microscopy. Proceedings of the National Academy of Sciences. 2015;112(37):11624-9.

65. Pijanka JK, Stone N, Rutter AV, Forsyth N, Sockalingum GD, Yang Y, et al. Identification of different subsets of lung cells using Raman microspectroscopy and whole cell nucleus isolation. Analyst. 2013;138(17):5052-8.

66. Farhane Z, Bonnier F, Casey A, Maguire A, O'Neill L, Byrne HJ. Cellular discrimination using in vitro Raman micro spectroscopy: the role of the nucleolus. Analyst. 2015;140(17):5908-19.

67. Ryabchykov O, Bocklitz T, Ramoji A, Neugebauer U, Foerster M, Kroegel C, et al. Automatization of spike correction in Raman spectra of biological samples. Chemometrics and Intelligent Laboratory Systems. 2016;155:1-6. doi: http://dx.doi.org/10.1016/j.chemolab.2016.03.024.

68. Guo S, Bocklitz T, Popp J. Optimization of Raman-spectrum baseline correction in biological application. Analyst. 2016;141(8):2396-404.

69. Morháč M. An algorithm for determination of peak regions and baseline elimination in spectroscopic data. Nuclear Instruments and Methods in Physics Research Section A: Accelerators, Spectrometers, Detectors and Associated Equipment. 2009;600(2):478-87.

70. Savitzky A, Golay MJ. Smoothing and differentiation of data by simplified least squares procedures. Analytical Chemistry. 1964;36(8):1627-39.

71. Emry JR, Olcott Marshall A, Marshall CP. Evaluating the Effects of Autofluorescence during Raman Hyperspectral Imaging. Geostandards and Geoanalytical Research. 2016;40(1):29-47.

72. Zhao J, Lui H, McLean DI, Zeng H. Automated autofluorescence background subtraction algorithm for biomedical Raman spectroscopy. Applied Spectroscopy. 2007;61(11):1225-32.

73. Hedegaard M, Matthäus C, Hassing S, Krafft C, Diem M, Popp J. Spectral unmixing and clustering algorithms for assessment of single cells by Raman microscopic imaging. Theoretical Chemistry Accounts. 2011;130(4):1249-60. doi: 10.1007/s00214-011-0957-1.

74. Ashton L, Hollywood KA, Goodacre R. Making colourful sense of Raman images of single cells. Analyst. 2015;140(6):1852-8.

75. Choi SS, Kim JS, Valerio LG, Sadrieh N. In silico modeling to predict drug-induced phospholipidosis. Toxicology and Applied Pharmacology. 2013;269(2):195-204. doi: http://dx.doi.org/10.1016/j.taap.2013.03.010.

76. Kruhlak NL, Choi SS, Contrera JF, Weaver JL, Willard JM, Hastings KL, et al. Development of a Phospholipidosis Database and Predictive Quantitative Structure-Activity Relationship (QSAR) Models. Toxicology Mechanisms and Methods. 2008;18(2-3):217-27. doi: 10.1080/15376510701857262.

77. Sirci F, Napolitano F, Vaquero SP, Carrella D, Medina DL, di Bernardo D. Integrated Structure-Transcription analysis of small molecules reveals widespread noise in drug-induced transcriptional responses and a transcriptional signature for drug-induced phospholipidosis. bioRxiv. 2017:119990.

78. Jiang H, Passarelli MK, Munro PM, Kilburn MR, West A, Dollery CT, et al. High-resolution sub-cellular imaging by correlative NanoSIMS and electron microscopy of amiodarone internalisation by lung macrophages as evidence for drug-induced phospholipidosis. Chemical Communications. 2017;53(9):1506-9.

79. Paracelsus: Four Treatises. (Seven Defensiones, translated by C.L. Temkin). Baltimore, MD: Johns Hopkins University Press; 1996.

80. Kaufmann AM, Krise JP. Lysosomal sequestration of amine-containing drugs: Analysis and therapeutic implications. Journal of Pharmaceutical Sciences. 2007;96(4):729-46. doi: 10.1002/jps.20792.

81. Hocking WG, Golde DW. The pulmonary-alveolar macrophage. New England Journal of Medicine. 1979;301(11):580-7.

CHAPTER 2

Qualitative Study of Macrophage-Synthesized Drug Biocrystals and Microcrystalline Drug Formulations using Raman Microscopy

2.1 Relevance to Thesis

Clofazimine (CFZ) is a small molecule drug that has been reported to accumulate to massive extents, even crystallizing, inside tissue macrophages throughout most organs of a treated subject, be it mice or human patients. This compound's intracellular distribution and crystallization behavior has served as a robust model for the study of drug bioaccumulation and provides clear evidence for the degree to which small molecules may be stably sequestered inside macrophages. CFZ conveniently exhibits a red-orange color that can be clearly observed via conventional brightfield microscopy, thereby providing clear and obvious evidence of massive bioaccumulation inside individual cells; brightfield images of CFZ-containing macrophages provide dramatic qualitative examples of the drug cargo carrying capacity of these cells. The Rosania research group has extensively studied CFZ and characterized its distribution and bioaccumulation using a robust *in vivo* mouse model where the drug is delivered at relevant dosage via oral administration with food over extended periods of time (mimicking the actual administration and dosage in human patients). The lab has developed many techniques over the years to quantitatively and qualitatively study CFZ bioaccumulation and for this reason I have chosen it as a model compound for initial development of micro-Raman methodology used throughout all three specific aims of my dissertation research endeavor.

Preliminary Raman experiments with CFZ revealed it exhibited an extremely strong Raman signal, presumably due to its enhanced interaction with the visible spectrum of light (i.e., its red color); unfortunately, this made the Raman-based quantitation of intracellular CFZ concentrations nearly impossible because the signals acquired from cells were completely "swamped" by the strong signal emitted from CFZ. Although quantitation was unlikely, I was able to effectively study the solid-state forms of the compound from a qualitative standpoint using micro-Raman spectroscopy. I collaborated with nearly every member of the Rosania lab on a multitude of CFZ-focused projects and contributed valuable insight regarding the crystalline forms of the drug which were published in three peer-reviewed research articles and summarized in this chapter of my dissertation. This work is also the first introduction of the alveolar macrophage sample preparation as dry dispersions on the surface of silicon chips that I used for all cell samples reported in this dissertation. Furthermore, I developed the first calibration methodology for quantitative deconvolution of Raman spectra (into relative mass values – w/w%) using stoichiometric mixtures of CFZ and 1,2-dipalmitoylphosphatidylcholine (DPPC, C16:0) as thin (<1μm) dry dispersions across the surface of silicon chips; mimicking the sample preparation of all the actual biological cells herein analyzed.

2.2 Abstract

Supramolecular crystalline assembly constitutes a rational approach to bioengineer intracellular structures. Here, biocrystals of clofazimine (CFZ) that form *in vivo* within macrophages and a biomimetic microcrystalline CFZ drug formulation were studied and characterized using micro-Raman spectroscopy. A quantitative calibration approach was also developed and reported but CFZ accumulation inside alveolar macrophages of drug-treated mice far-exceeded the linear range of the method, making intracellular drug quantitation infeasible. Biomimetic CFZ hydrochloride (CFZ-HCl) crystals were synthesized and their ability to elastically deform was studied. Consistent with the ability of biocrystals to elastically deform, the inherent crystal structure of molecular CFZ-HCl has a corrugated packing along the (001) face and weak dispersive

bonding in multiple directions; These characteristics were previously found to be linked to the elasticity of other organic crystals. We propose that elastic intracellular crystals can serve as templates to construct functional microdevices with different applications. Furthermore, we developed a stable and biocompatible formulation of CFZ-HCl microcrystals that mimics the predominant form of the drug that bioaccumulates in macrophages, following long term oral CFZ administration; the formulation was characterized via a multitude of analytical techniques, including micro-Raman spectroscopy which was reported here.

2.3 Introduction

Clofazimine is a weakly basic, red-pigmented, FDA-approved, phenazine antibiotic that is included in the World Health Organization's (WHO) List of Essential Medications as part of the antibiotic cocktail used for the standard treatment for leprosy. It has been in clinical use since the 1960s and has contributed to the cure of more than 16 million people worldwide (1-4). Due to its potent activity against Mycobacterium tuberculosis, the WHO now recommends CFZ as a second line agent against multi-drug resistant tuberculosis (5-8). In humans, CFZ exhibits atypical pharmacokinetic properties; in mice, following long-term (i.e., weeks) oral administration, solid drug precipitates accumulate in tissue macrophages, forming red crystal-like drug inclusions that are most abundant in the liver and spleen (9-11). This phenomenon has also been reported in humans treated with CFZ (12). Interestingly, these biocrystals display robust stability inside macrophages and remain in the body long after discontinuation of treatment (>8 weeks) (9). The preliminary analysis of isolated biocrystals from spleen and liver of CFZ-treated mice revealed their identity as the hydrochloride salt form of drug (CFZ-HCl), which is stabilized by the acidic and high chloride concentrations present in macrophage lysosomes, while the orally-administered form of the drug is the free base (13). Remarkably, in Kupffer cells, splenocytes, alveolar macrophages, and peritoneal macrophages, the amount of intracellular CFZ-HCl typically exceeds that of every other cellular component except water (9). Known factors that contribute to this massive bioaccumulation and self-

assembly phenomenon include the drug's high oral bioavailability, coupled with large daily doses, prolonged treatment regimens, low clearance, and long elimination half-life (14).

The observed self-assembly, mechanical, and optical properties of CFZ-HCl, which can function as drug depots and photoacoustic contrast agents in macrophages, inspired our thinking about reverse engineering this weakly basic, small molecule chemical agent as a molecular building block for constructing other kinds of functional mechanopharmaceutical devices. Such devices could be used to influence the mechanical properties of cells. They could also be exploited as bio-responsive pharmaceutical or imaging agents by capitalizing on both physical and chemical interactions between cells and the self-assembled biocrystalline structures, *in vivo*. In macrophages, CFZ-HCl forms elastic structures, which bend and relax in response to biomechanical forces. Furthermore, the presence of these mechanopharmaceutical devices inside macrophages is associated with augmented anti-inflammatory activity (4, 15): upon phagocytosis, they lead to changes in cellular function, which include alterations in signal transduction pathways that affect the cell's inflammatory response. Unlike soluble CFZ, which tends to be cytotoxic, the phagocytosis of the self-assembled mechanopharmaceutical device does not lead to toxicity (13, 16). Furthermore, abnormal morphology of crystals has been a subject of significant study over the last century (17-22). Particularly, crystalline growth and distribution within living organisms such as cells, tissues and clinically in humans has allowed an understanding of how solid-state crystal chemistry can modulate biological and biophysical environments (23-28). Specifically, the interaction of crystalline matter with cells such as macrophages within clinical microenvironments has garnered much attention (29-31).

Raman microscopy enables molecular analysis at the single-cell level without the need for artificial chemical tags, offering an analytical approach by which we may characterize CFZ accumulation and crystal formation *in vivo* (32-34). Using stoichiometric mixtures of CFZ and phospholipid at known mass ratios, the range of quantitation may be experimentally determined (Figure 2-1); because of CFZ's strong interactions with visible light (evidenced by its red color and fluorescent properties) the drug yields a

significantly stronger Raman signal than endogenous biomolecules, such as lipid and protein, giving CFZ an extremely narrow linear range of quantitation (Figure 2-2). Although quantitation above the linear range is infeasible, we herein report micro-Raman analytical methodologies for the *qualitative* study of intracellular CFZ biocrystals and synthetic biomimetic CFZ crystals; synthetic crystals were grown and utilized for bending/flexibility analyses and micronized/sterilized for parenteral administration in mouse model. Raman microscopy was utilized to characterize *in vivo* intracellular distribution of CFZ in mouse alveolar macrophages, to analyze synthetic crystals during bending/flexibility analysis, and to confirm the identity of synthetic biomimetic microcrystals (for parenteral administration) throughout the manufacturing process.

2.4 Materials and Methods

2.4.1 Animal Experiments

Mice (4 week old, male C57BL/6J) were purchased from the Jackson Laboratory (Bar Harbor, ME) and acclimatized for 1 week in a specific-pathogen-free animal facility. Clofazimine (CFZ) (C8895; Sigma, St. Louis, MO) was dissolved in sesame oil (Shirakiku, Japan) to achieve a concentration of 3 mg/mL, which was mixed with Powdered Lab Diet 5001 (PMI International, Inc., St. Louis, MO) to produce a 0.03% drug to powdered feed mix, which was orally administered *ad libitum* for up to eight weeks. A corresponding amount of sesame oil was mixed with chow for vehicle treatment (control). Mice were euthanized via CO_2 asphyxiation and exsanguination. Animal care was provided by the University of Michigan's Unit for Laboratory Animal Medicine (ULAM), and the experimental protocol was approved by the Committee on Use and Care of Animals (Protocol PRO00005542). All animal experiments were done according to the protocol guidelines.

2.4.2 Alveolar Macrophage Isolation and Preparation

Following euthanasia, the trachea was surgically exposed and cannulated with a 20 G needle, and the lungs were lavaged by instilling 1 mL DPBS (Life Technologies) containing 0.5 mM EDTA (Sigma) six times. Approximately 90% of the instilled bronchoalveolar lavage (BAL) was retrieved. BAL was centrifuged (10 min at 400 × g, 4 °C), the supernatant removed, and the cell pellet was resuspended in RPMI 1640 media (Life Technologies) with 5% FBS (Life Technologies) and Penicillin/Streptomycin (Thermofisher) at a cell concentration of ~50,000 cells/mL. 15µL of each cell suspension was transferred onto pre-sterilized 5x5mm silicon chips (16008; Ted Pella, Inc., Redding, CA) and incubated for 1 h (@ 37 °C and 5% CO_2) to allow adherence to chip. The cell-containing chips were washed by brief submersion into isotonic NaCl (0.9%) solution followed by deionized (DI) water, then allowed to air-dry, thereby depositing all non-volatile molecular contents (biologic and xenobiotic) as thin dry dispersions across the surface of the silicon chips.

2.4.3 Stoichiometric Calibration Methodology for Quantitation of CFZ-HCl

Calibration samples were intelligently designed to result in thin dispersions of CFZ-HCl and phospholipid (in known mass ratios) that most closely represented the dimensions and conditions of the drug-treated cell samples under investigation. Formulated as stoichiometric mixtures of CFZ and DPPC dissolved in a solution of methanol and 0.05mM HCl solution (5:1 respective volumetric ratio), a known volume of solution was transferred to the surface of a silicon chip where the solvent then evaporated. Reference and calibration samples were analyzed by the WITec alpha300R confocal Raman microscope using large area scan methodology and average spectra from each scan were reported. Initial data preprocessing was performed in WITec Project FOUR software to remove cosmic ray interference and perform spectral smoothing. The data were then exported to Matlab® (Natick, MA USA) and the remainder of preprocessing and analysis were performed using algorithms developed in-house. The spectral regions

of interest were excised from the dataset between the wavenumbers 1200-3200 (cm^{-1}) and used for all subsequent preprocessing. Background subtraction was performed via baseline estimation within multiple shifted windows across the spectra followed by regression of the varying baseline to window points via spline approximation. The spectra were then normalized by the maximum peak height. Spectral region of interest 1200-3200 cm^{-1} was then interpreted via linear combination modelling.

Linear combination spectral modelling (aka least squares regression) was used to deconvolute the acquired spectra into the % signal for CFZ in each calibration sample; using pure component reference spectra, measured Raman spectra were deconvoluted to determine the relative signal contributions from each component of interest according to the following model:

$$I_{\tilde{\nu}} = N_1 k_{\tilde{\nu}_1} + N_2 k_{\tilde{\nu}_2} + \varepsilon_{\tilde{\nu}}$$

Where:

$\tilde{\nu}$ = relative wavenumber or Raman shift (cm^{-1})

$I_{\tilde{\nu}}$ = measured sample spectrum

$k_{\tilde{\nu}_n}$ = component “n” reference spectrum

N_n = component “n” regression estimate

$\varepsilon_{\tilde{\nu}}$ = residual spectrum

The relative signal contribution for each component was calculated using the regression estimators; the following example calculation was provided for clarity:

$$\%\ \text{Component 1 Signal} = \frac{N_1}{N_1 + N_2} * 100$$

In this case, the two components were CFZ and phospholipid (DPPC). Linear correlation of % CFZ signal with the actual mass in phospholipid provided linear range of quantitation for measuring the extent of drug accumulation in discrete lipid inclusions.

2.4.4 Raman Analysis of Cytoplasmic Drug Inclusions and Single-Cell Imaging

Raman measurements were acquired with the WITec alpha300R confocal Raman microscope (WITec, Ulm, Germany) equipped with two excitation lasers: a 532 nm solid-state sapphire and a 785 nm wavelength-stabilized diode (0–55 mW and 0–88 mW tunable intensity ranges, respectively). A 100X air objective (Zeiss Epiplan-NEOFLUAR, NA (numerical aperture) = 0.9) coupled to a CCD detector via a multi-mode fiber of 100 μm diameter serving as the confocal pinhole, produced 0.72 μm and 1.06 μm illumination spots (for 532 nm and 785 nm lasers respectively). To minimize fluorescence background from pure CFZ and CFZ-HCl reference crystals, samples were excited with 785 nm. The 532 nm laser was utilized for excitation of biological samples due to its elicitation of a stronger Raman signal from the microscopic inclusions of interest. Point spectra were acquired ($n \geq 40$ cells/group) by focusing a laser spot on cytoplasmic inclusions or pure reference crystals: at each point, the laser was tuned to optimum intensity, and acquired point spectra over an integration time of 25 seconds. Individual raw spectra were baseline-subtracted and normalized using a MATLAB® processing algorithm developed in-house. For single-cell Raman imaging, the 532 nm excitation laser was raster-scanned across a 50×50μm area with a step-size of 0.5 microns, yielding spectral datasets consisting of 10,000 spectra per cell. Exploiting the dramatic spectral differences arising from fluorescence of different CFZ forms, the un-processed Raman spectra were linearly deconvoluted via WITec ProjectFOUR software's basis component analysis using representative un-processed reference spectra obtained from untreated cells, pure free base CFZ crystals, pure CFZ-HCl crystals, and the silicon substrate. Dataset acquisition, processing, and image display parameters were performed equivalently for each cell specimen.

2.4.5 Synthesis of CFZ-HCl Biomimetic Crystals

To grow biomimetic crystals (CFZ-HCl) for bending/flexibility analyses, HCl was added to a 2mM CFZ (Sigma-Aldrich, St. Louis, MO, USA) in methanol solution until the

HCl concentration was 0.1M. After the solution sat for 5 minutes, water was added to double the solution volume. Within minutes, thin dark red crystals were observed. For bulk synthesis of CFZ-HCl crystals for parenteral formulation purposes, 10g of CFZ free base was placed in 2 L of 1 M HCl in an Erlenmeyer flask with a magnetic stir bar. After the addition of CFZ, the reaction was sealed with parafilm and stirred in the dark for 72 h. After 72 h, the stirring was turned off and CFZ salt crystals were allowed to precipitate. Following crystal precipitation, the HCl reactant was decanted and discarded. The residual acid containing the CFZ salt crystals was centrifuged (2000× g, 10 min, 4 ◦C), the supernatant was discarded, and the pellet was washed thrice with declining concentrations of HCl (100 mM, 10 mM, and 1 mM) to reduce the amount of chloride present in the solution. In between washing steps, samples were centrifuged (2000× g, 10 min, 4 ◦C). After the last wash, crystals were resuspended in MiliQ water and immediately snap frozen in liquid nitrogen and then freeze-dried.

2.4.6 Qualitative Analysis of Biomimetic Crystal Bending/Flexibility

Crystals that were about 2mm long and ~20μm thick were isolated from the crystallization solution and manipulated to demonstrate the crystal's elasticity. Crystals were placed on a microscope slide in a small amount of water to prevent the crystal from moving off the slide. A pair of tweezers and a crystallization probe were used to manipulate the crystals. Video images of this procedure were taken with a Leica M205 C stereo microscope. For analysis of bent crystals via Raman microscopy, bent crystals were snap-frozen over dry ice and imaged on silicon wafers.

2.4.7 Micronization and Sterilization of CFZ-HCl Biomimetic Crystals

A SepSol, Sturtevant Inc. (Separation Solutions; SepSol Process Solutions, Kalamazoo, MI, USA) air jet mill was used to micronize the bulk synthesized CFZ-HCl crystals and CFZ free base crystals (control) to a particle size distribution within the

desired range (0.5–5 μm). Following the company's specifications, the air jet mill was set at 50 psi grind pressure and 100 psi feed pressure. Filtered, dried, compressed air was used as the air source for the mill. Altogether, four batches of CFZ-HCl microcrystals (net weight ~40 g) and three batches of CFZ free base microcrystals (net weight ~20 g) were produced with ~80–90% yield from milling. Both types of micronized CFZ crystals were stored at −20 ◦C until the time of experimentation. Before each experiment, CFZ microcrystals were sterilized by dry heat at 170 ◦C for 1.5 h, using a bench top vacuum oven at 5 psi (Model 5831; National Appliance Co., Portland, OR, USA).

2.4.8 Formulation Diluent for Stabilized Suspension of Biomimetic Microcrystals

The diluent for the IV injectable formulation was made using polysorbate 80 (59924 Sigma-Aldrich, St. Louis, MO, USA), sodium chloride (BP358, Fisher Scientific, Fair Lawn, NJ, USA), and Milli-Q water. To coat, disperse, and adjust the size of the lipophilic CFZ-HCl microcrystals, varying concentrations of polysorbate 80 (0–0.5%) were used. Sodium chloride was added to maintain isotonicity. The pH was adjusted to pH 5 using 0.01 M HCl or 0.01 M NaOH to ensure the stability of CFZ-HCl microcrystals in the formulation. For experiments, the diluent was sterilized by sterile filtration with a syringe filter (09-719A; 0.22 μm, MCE, Sterile; Fisher Scientific, Fair Lawn, NJ, USA).

2.4.9 Particle Size Distribution Analysis

The CFZ microcrystals particle size after synthesis and after micronization were analyzed using Zeta-Sizer (Malvern Instruments, Nano-ZS90, Malvern, UK) and brightfield microscopy using Nikon Eclipse Ti inverted microscope (Nikon Instruments, Melville, NY, USA).

2.4.10 Proton Nuclear Magnetic Resonance Spectroscopy Analysis

Proton (1H) nuclear magnetic resonance (NMR) spectroscopy was performed as previously described [16]. Briefly, one-dimensional 1H-NMR spectra of micronized CFZ-HCl crystals at different stages of manufacturing were acquired using an 11.74 T (500 MHz) NMR spectrometer with a VNMRS console and a 7510-AS autosampler system operated by host software VNMRJ 3.2 and equipped with a 5 mm Agilent One NMR probe with Z-axis gradients. The samples were dissolved in dimethyl sulfoxide-D6 (D, 99.9%) (DMSO-d6; Cambridge Isotope Laboratories, Inc., Andover, MA, USA). The NMR data were acquired at room temperature and processed using MestreNova 9.0 software (MestreLab, Santiago de Compostela, Spain).

2.4.11 Powder X-ray Diffraction Analysis

Powder X-ray diffraction (pXRD) spectra of micronized CFZ-HCl crystals at different stages of manufacturing were taken by Rigaku Miniflex X-ray diffractometer (Rigaku-USA Inc., Danvers, MA, USA) using Cu Kα radiation, a tube voltage of 30 kV, and a tube current of 15 mA. Measurements were taken from 5◦ to 40◦ at a continuous scan rate of 2.5◦/min.

2.4.12 Single-Crystal Raman Analyses of CFZ-HCl Manufacturing Process

For crystal bending analysis, confocal Raman microscopy was performed using a WITec alpha300R microscope (WITec, Ulm, Germany) equipped with a near-IR 785nm excitation laser to minimize clofazimine's fluorescence signal. Samples were positioned on the stage for spectral data acquisition and were observed using the reflectance illumination mode of the microscope. Once positioned, the ~4μm diameter laser illumination spot was directed onto the sample, and the Raman spectrum was acquired. Raw data were background subtracted from the signal obtained from the pure silicon wafers and further baseline-corrected using Origin® (Origin Labs, Northhampton, MA).

For single-crystal analysis of manufacturing process, Raman spectra were acquired with a WITec alpha300R confocal Raman microscope (WITec, Ulm, Germany) equipped with a 532nm solid-state sapphire excitation laser and charge coupled device (CCD) detector. The laser was focused on the sample acquiring each Raman spectrum with an integration time of 75 s, using Zeiss EC EPIPLAN 50X objective (N.A. = 0.75). Cosmic rays were removed from all spectra using the WITec Project FOUR software. A MATLAB® processing algorithm developed in-house [22] was used to baseline-subtract, normalize, and overlay spectra to qualitatively identify the collected micronized sample spectra by comparing them to both CFZ-HCl and CFZ free base reference spectra.

2.4.13 Brightfield and Fluorescence Microscopy

Microscopy was performed using a Nikon Eclipse Ti inverted microscope (Nikon Instruments, Melville, NY, USA) as previously described. Briefly, brightfield images were captured using the Nikon DS-3 camera (Nikon Instruments, Melville, NY, USA) and fluorescence imaging in FITC channel (490/510nm, green) and Cy5 channel (640/670nm, far-red) was performed with the Photometrics CoolSnap MYO camera system (Photometrics, Tuscon, AZ, USA) under the control of Nikon NIS-Elements AR software (Nikon Instruments, Melville, NY, USA). Illumination for fluorescence imaging was provided by the X-Cite 120Q Widefield Fluorescence Microscope Excitation Light Source (Excelitas Technology, Waltham, MA, USA).

2.5 Results and Discussion

2.5.1 Intracellular Organization of the Self-Assembled CFZ Biocrystals

Prolonged administration of CFZ results in its accumulation in both human and animals as microscopic, insoluble, and membrane-bound aggregates, known as Crystal Like Drug Inclusions (CLDIs), which are primarily found within tissue macrophages (9). CLDIs are primarily comprised of a protonated, hydrochloride salt of CFZ, which forms

faceted structures possessing three orthogonal cleavage and multiple fracture planes with lamellar spacing of 6 nm to 14 nm (11). Furthermore, Raman reference spectra of pure CFZ and CFZ-HCl identified characteristic Raman peaks for clear distinction between the two forms (Figure 2-3). Spectra obtained from cytoplasmic regions of untreated mouse alveolar macrophages were typical of biological specimens with no apparent contributions from drug. However, spectra obtained from cytoplasmic regions of 4- and 8-week CFZ-fed mouse alveolar macrophages revealed the presence of CFZ-HCl, which dominated any Raman signal associated with biological specimens, and exhibited unique peak intensities and peak widths, which attribute to the geometric organization of the supramolecular structures: peaks generally become narrower and more intense with higher degree of order in samples, which suggests that by 8 weeks, the macrophages have organized the accumulated drug into supramolecular crystalline packages of CFZ-HCl salt. Moreover, Raman imaging of single-cells revealed cytoplasmic accumulation of both forms of the drug after just 1 week and continuing through 4 weeks; at 8 weeks CLDI formation was apparent and clearly distinguishable from free base CFZ, as evidenced by non-overlapping Raman signals in the biocrystal regions of Raman image (Figure 2-4).

2.5.2 Synthesis and Analysis of Biomimetic CFZ-HCl Crystals

First, biomimetic CFZ-HCl crystals were synthesized and their fluorescence and Raman spectral properties were compared to CFZ-HCl biocrystals formed *in vivo*. For fluorescence analysis, image data were acquired with the standard FITC and Cy5 excitation/emission channels of an epifluorescence microscope; for Raman spectral data, single crystals were analyzed and compared to spectra of isolated biocrystals (from mouse model). By visual inspection, biocrystals and synthetic crystals exhibited almost identical fluorescence and Raman spectra, sharing the CFZ-HCl signature peak at 1400 cm^{-1}. To scale the synthesis of CFZ-HCl to multigram and larger quantities for manufacturing of a pharmaceutical-grade formulation for clinical trials, a synthesis scheme was developed using hydrochloric acid for transforming clofazimine free base to hydrochloride salt crystals directly, without dissolving the free base in organic solvents.

For free base particles of ~100 μm diameter or less, direct conversion hydrochloride crystals were complete by 72 h, as determined using microscopy, ^{1}H-NMR, and Raman (Figure 2-5). Thus, synthetic CFZ-HCl crystals closely mimicked the optical properties of CFZ-HCl biocrystals that form *in vivo*.

2.5.3 Investigating Biomimetic CFZ-HCl Crystal Bending and Flexibility

As the primary component of the biocrystals is CFZ-HCl, we hypothesized that the inherent crystal structure of CFZ-HCl plays a role in the flexibility (being able to adopt non-linear morphologies) and elasticity (being able to return to linear conformations upon removal of force) of the biocrystals. The synthetic CFZ-HCl crystals form dark red rectangular plates that closely resemble the crystal habit and color of the biocrystals as observed with brightfield microscopy. The CFZ-HCl crystals can grow to be much larger than the biocrystals allowing for optimal structural characterization. X-ray diffraction (XRD) was also performed to determine the crystal structure of CFZ-HCl. The CFZ-HCl crystals grow in an orthorhombic *Pbca* space group with unit cell parameters; a=10.266 Å, b=19.828 Å, and c=24.156 Å, $\alpha=\beta=\gamma=90°$ and Z=8 (CCDC number: **1497722**). One CFZ and one HCl molecule make up the asymmetric unit (Figure 2-6). Cl3 (the Cl associated with the HCl) associates with the CFZ through two N−H···Cl hydrogen bond interactions between N3−H···Cl3 and N4−H···Cl3 (D, d, θ: 3.172 Å, 2.376 Å, 166.45°, and 3.104 Å, 2.243 Å, 174.51°). The data set was solved to 99.8 % completeness. Water was incorporated into the crystal structure at an occupancy of 0.13, and there was some disorder in the isopropyl group. The presence of water likely caused a change in the orientation of the isopropyl group, thereby contributing to the observed disorder (Figure S-1). A summary of the unit cell parameters and diffraction data can be found in Table S-1.

Interestingly, while harvesting CFZ-HCl crystals for XRD, the crystals would noticeably bend when force was applied to pick up the crystals. As soon as the force was removed the crystals would promptly return to their original linear morphologies.

Subsequently, video microscopy of bending crystals with tweezers was performed to further demonstrate their observed elastic response (Figure 2-7). Crystallization experiments yielded a very wide size distribution of crystals out of which crystals between 500 μm and 2 mm long and ca. 20 μm thick were chosen. The CFZ-HCl crystals typically lie with the (001) face normal to the substrate. When a slight force was applied, the crystal rotated 90° about the *a*-axis. When a force was applied to the (001) face, the crystal bent and assumed its original shape upon removal of the force. The crystal arched again when a second force was applied. As such, the crystals can be bent many times without noticeable deformation to the crystal. In one experiment, a crystal was bent 8 times without noticeable deformation. However, upon applying a larger force, the crystal snapped, and the crystalline fragments adopted the original straight configuration. Further, no differences in vibrational spectra (Raman) were evident before and after bending at the point of maximum curvature in these crystals (Figure 2-8). Naturally curved crystals also showed no differences in molecular vibrations compared to the reference CFZ-HCl crystals.

2.5.4 Characterization of Biomimetic CFZ-HCl Microcrystalline Formulation

To formulate micronized CFZ-HCl salt crystals and characterize the extent to which they mimicked CLDIs, ^{1}H-NMR, single crystal Raman micro-spectroscopy, and pXRD were used for comparative analysis. Following micronization and sterilization of bulk CFZ-HCl, chemical and structural characteristics of CFZ-HCl salt crystals remained relatively unchanged (Figure 2-9). ^{1}H-NMR spectral (Figure 2-9A) and single crystal Raman micro-spectroscopy peaks (Figure 2-9B) were preserved with almost identical match, indicating that the chemical structure of CFZ-HCl crystals was not altered by micronization or sterilization. Furthermore, pXRD spectra revealed that most diffraction peaks were preserved as well, including the CFZ-HCl signature peak at $2\theta = 7.2°$ that is absent in CFZ free base, indicating the preservation of the crystal structure (Figure 2-9C).

Following dispersion of individual drug crystals in IV diluent buffer, the micronized, sterilized microparticles were completely dispersed. Ultimately, the size and the dispersion of the particles can be adjusted by varying the concentration of the detergent present in the diluent (e.g., polysorbate 80); the higher the concentration, the smaller and more dispersed the particles are (data not shown). In this case, the IV injection, the maximum concentration of polysorbate 80 was used (0.5%) to make the particles as small and as dispersed as possible. As a result, the microcrystals exhibited the expected Cy5 and FITC fluorescence of CFZ-HCl and were homogeneous in size distribution (Figure 2-9D). By utilizing dynamic light scattering analysis (Figure 2-9E), there was one narrow particle distribution of 547 ± 160 nm, an ideal size for parenteral formulations. In contrast, prior to micronization, the starting material exhibited 2 major wide particle size distributions of 621 ± 300 nm and 5035 ± 592 nm, respectively (Figure 2-9E). Thus, air jet milling produced a stable micronized product that could be readily sterilized, preserving a desirable size distribution.

2.6 Conclusions

As a weakly basic, poorly soluble small-molecule chemical that is FDA-approved, orally bioavailable, slowly cleared, and administered at high doses for prolonged periods of time, CFZ affords us the opportunity to reverse engineer the construction of a mechanopharmaceutical device that was found to form naturally inside cells. We report that, because of its physicochemical properties, CFZ is highly prone to precipitation in acidic endolysosomal compartments in macrophages, where it self-assembles into a highly ordered CFZ-HCl biocrystal, possessing many interesting optical and biomechanical features. Furthermore, single-cell Raman imaging revealed that CFZ was present both as a free base and hydrochloride salt form within intracellular vesicles (Figure 2-4). Although quantitation of intracellular CFZ content was not reasonably feasible, qualitative analysis of the solid-state forms – free base and HCl salt crystals – facilitated manufacture of a biomimetic microcrystalline formulation to be used for parenteral administration of the compound. Furthermore, micro-Raman analysis

complimented other solid-state analyses in the context of CFZ-HCl crystal bending experiments.

Macrophage-mediated crystallization is an important example of how these cells self-assemble a crystal with features that allow for easier adaptability to the mechanical environment of the cell, thereby allowing a massive drug loading within the cell. Importantly, the additional Cl (in HCl) is most likely reinforced within CFZ biocrystals through the presence of multiple chloride channels in macrophages and their highly regulated role in cellular physiology. Here, we show that the salt chloride also plays an integral role in the structural stability and intracellular mechanical adaptation via elasticity. Furthermore, mechanical flexibility of exogenous elements within cells could be a critical design parameter toward engineering organic intracellular constructs to endow cells with unnatural yet stable and beneficial features for therapeutic applications. Finally, viscoelasticity, pressures and connected mechano-transductive elements are innately connected to inflammatory cell phenotypes. As such, the mechanochemical characterization of intracellular properties could be important for cell-based mechano-biological applications leading to a new class of pharmaceutics: mechano-pharmaceutics.

2.7 Resulting Publications

1. Horstman EM, Keswani RK, Frey BA, Rzeczycki PM, **LaLone V**, Bertke JA, Kenis, PJA, Rosania GR. Elasticity in Macrophage-Synthesized Biocrystals. 2017. *Angewandte Chemie*. Vol 129, Issue 7, p. 1841-1845.

2. Woldemichael T, Keswani RK, Rzeczycki PM, Murashov MD, **LaLone V**, Gregorka B, Swanson JA, Stringer KA, Rosania, GR. Reverse Engineering the Intracellular Self-Assembly of a Functional Mechanopharmaceutical Device. 2018. *Scientific Reports*. Vol 8, Article number: 2934.

3. Murashov M, Diaz-Espinosa J, **LaLone V**, Tan J, Laza R, Wang X, Stringer KA, Rosania GR. Synthesis and Characterization of a Biomimetic Formulation of Clofazimine Hydrochloride Microcrystals for Parenteral Administration. 2018. *Pharmaceutics*. Vol 10, Issue 4.

2.8 Acknowledgements

2.8.1 For aspects of work published in *Angewandte Chemie*, 2017

We thank the National Science Foundation (NSF) for a Graduate Research Fellowship to E.M.H. (DGE-1144245), National Institute of General Medical Sciences (NIGMS) for funding support to G.R.R. (R01GM078200), University of Michigan of Office of Research MCubed Program funding to G.R.R., Michigan Institute for Clinical & Health Research Pilot Seed funding to G.R.R. and R.K.K. (NIH: UL1TR000433) and the Interdisciplinary REU (Research Experiences for Undergraduates) Program housed in the College of Pharmacy, University of Michigan for funding B.A.F. through the NSF-Division of Biological Infrastructure (NSF-DBI) (DBI-1263079). We acknowledge the support of Dr. Gislaine Kuminek, Dr. Nair Rodriguez-Hornedo, Dr. Gi Sang Yoon and Sudha Sud (Department of Pharmaceutical Sciences, College of Pharmacy, University of Michigan) for help with DSC and animal experiments, Dr. Danielle Gray, George L. Clark (X-ray Facility and 3M Materials Laboratory, University of Illinois) for discussion about crystallographic data, and Lucas C. Gonzalez (Department of Chemical and Biomolecular Engineering, University of Illinois) for help with crystallization experiments.

2.8.2 For aspects of work published in *Scientific Reports*, 2018

The authors acknowledge funding from M-Cubed and NIH grant R01GM078200 to GRR. We thank Dr. Nair Rodriguez-Hornedo (Department of Pharmaceutical Sciences, University of Michigan) for allowing the use of HPLC instrumentation in her lab.

2.8.3 For aspects of work published in *Pharmaceutics*, 2018

This research was funded by the University of Michigan (MCubed, College of Pharmacy Upjohn Award, and MEDC Mi-TRAC (Kickstart) Award) and grants from the National Institutes of Health (NIH) (R01 GM078200; R01 GM111400; and P50 CA186786).

2.9 Figures

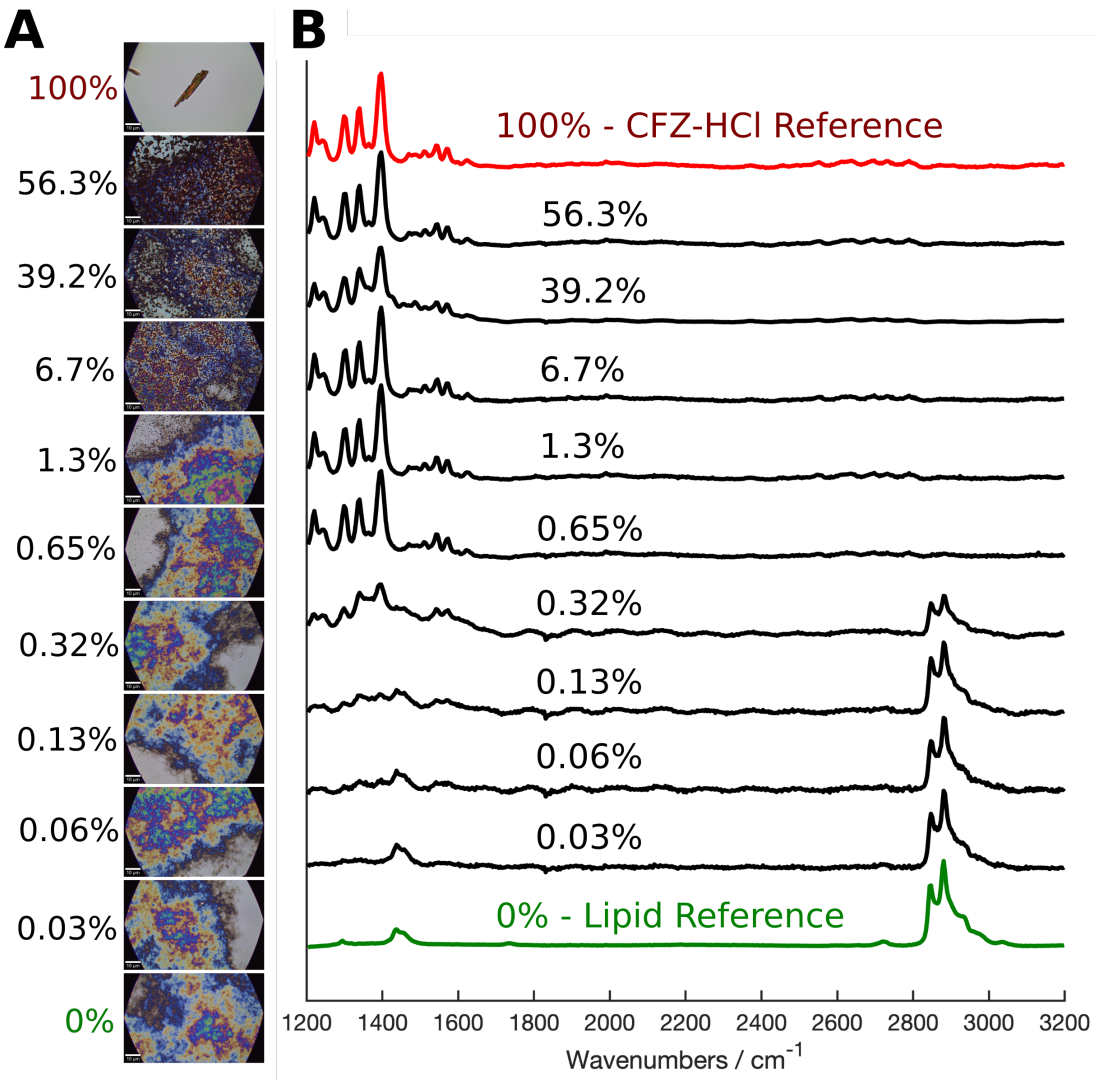

Figure 2-1. Stoichiometric CFZ-HCl:lipid mixtures for quantitative interpretation of Raman spectra.

(A) Brightfield reflected light images of pure CFZ-HCl crystal (for reference) and dry-dispersions of CFZ-HCl and phospholipid on silicon chips. **(B)** Corresponding Raman spectra acquired from samples.

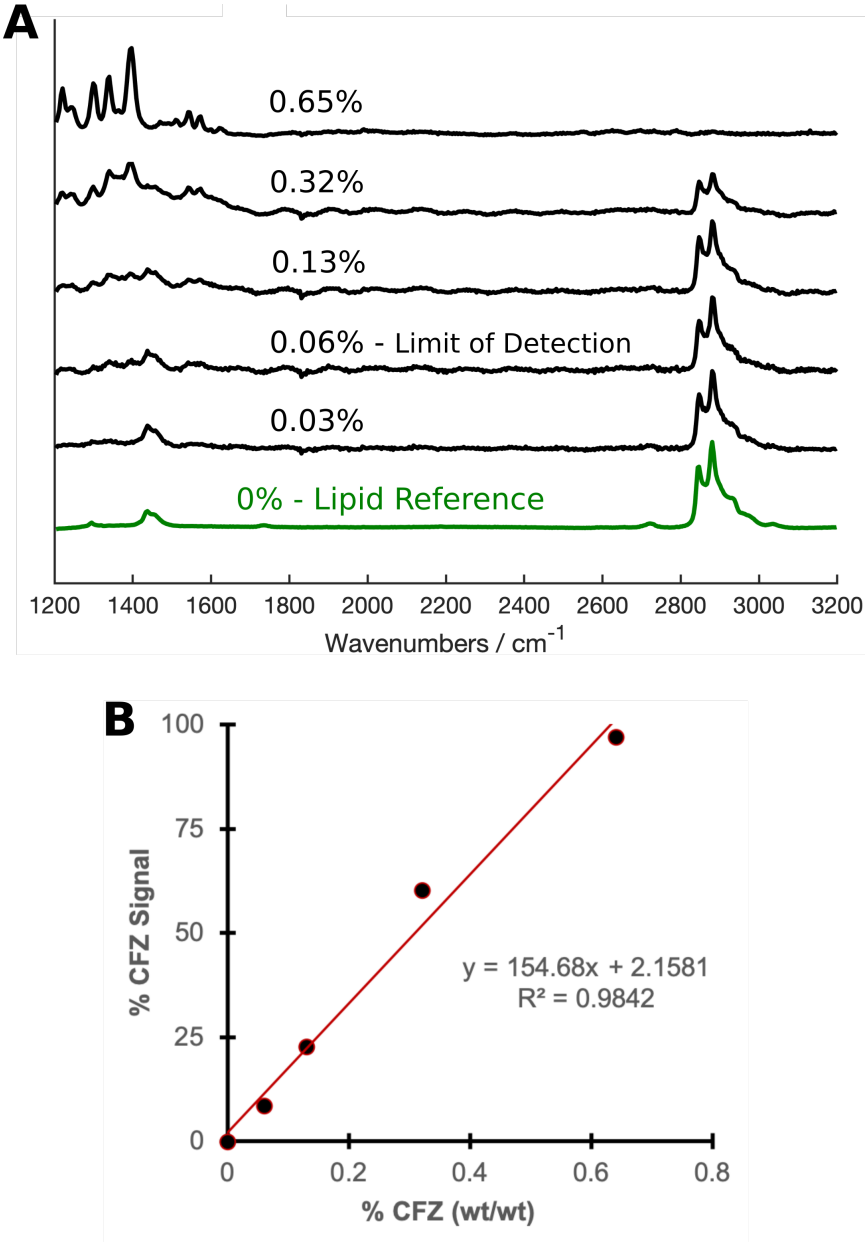

Figure 2-2. Linear quantitative range for CFZ-HCl in phospholipid.

(A) Corresponding Raman spectra acquired from calibration samples across the linear range. **(B)** Linear correlation of % CFZ signal (acquired from linear combination modelling with reference spectra) and % CFZ w/w; quantitative range was from 0.06% to 0.65% relative mass.

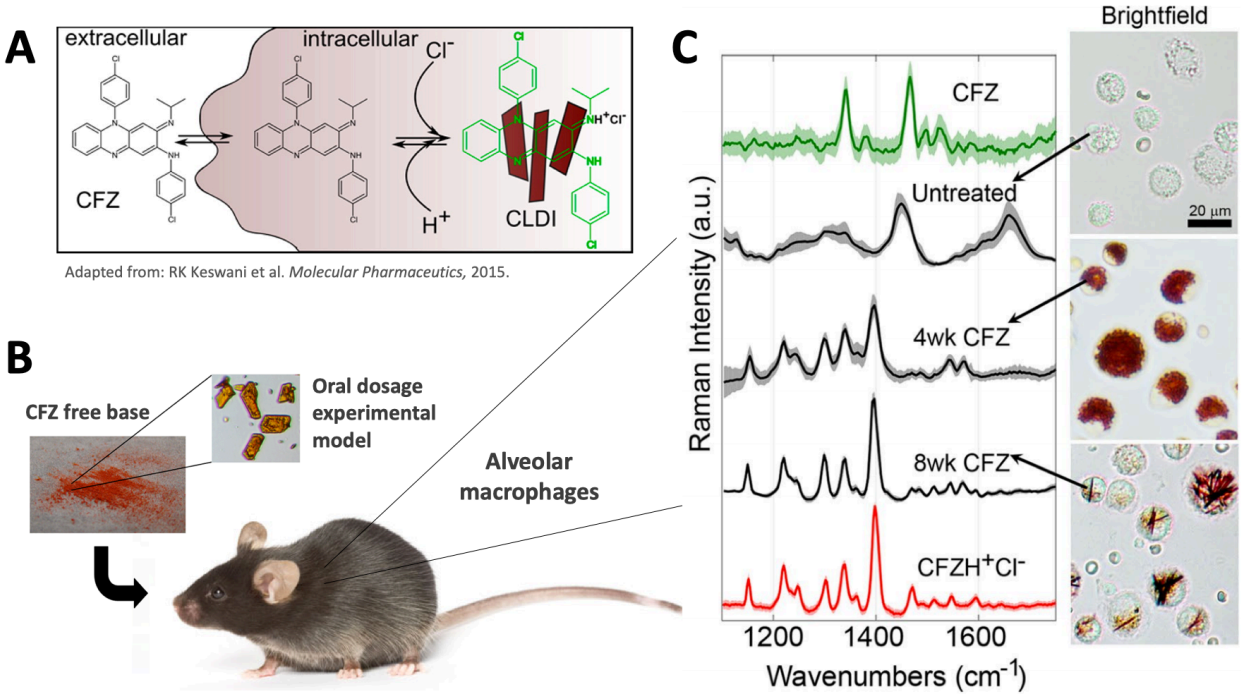

Figure 2-3. Intracellular self-assembled CFZ-HCl biocrystals in macrophages.

(A) Illustration depicting the chemical structures of soluble CFZ (free base) and intracellularly-accumulating CFZ-HCl (solid precipitates); adapted from R.K. Keswani et al. 2015. **(B)** Graphic of *in vivo* experimental setup depicting the oral dosage of CFZ. **(C)** Raman spectra of free base CFZ, CFZ-HCl, untreated and treated alveolar macrophages (4 and 8wks CFZ-fed mice) show distinct Raman peaks distinguishing between the different forms of the drug (red in the brightfield images): free base CFZ (1341 and 1465 cm^{-1}), CFZ-HCl (1399 cm^{-1}).

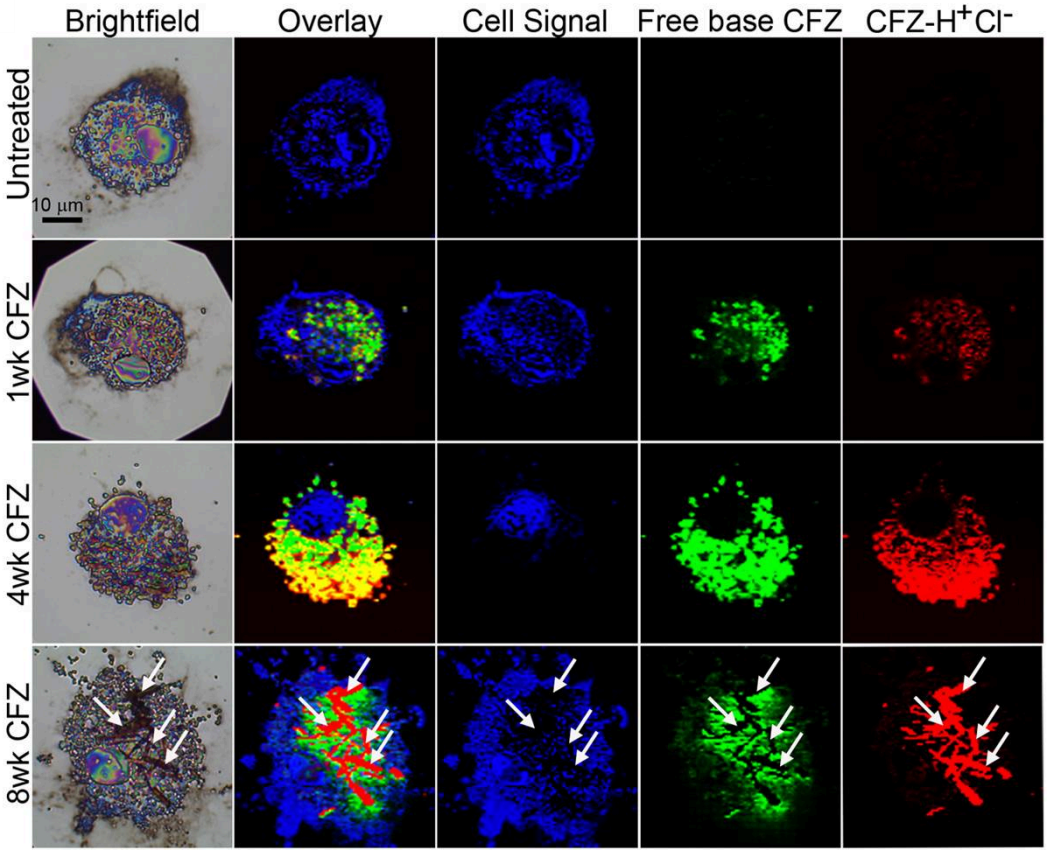

Figure 2-4. Subcellular distribution images of CFZ in alveolar macrophages.

Reflected brightfield and Raman images of alveolar macrophages from CFZ-fed mice prepared on silicon chip substrates; basis spectral fitting was used to show the temporal accumulation and cytoplasmic packaging of CFZ into highly ordered CLDIs.

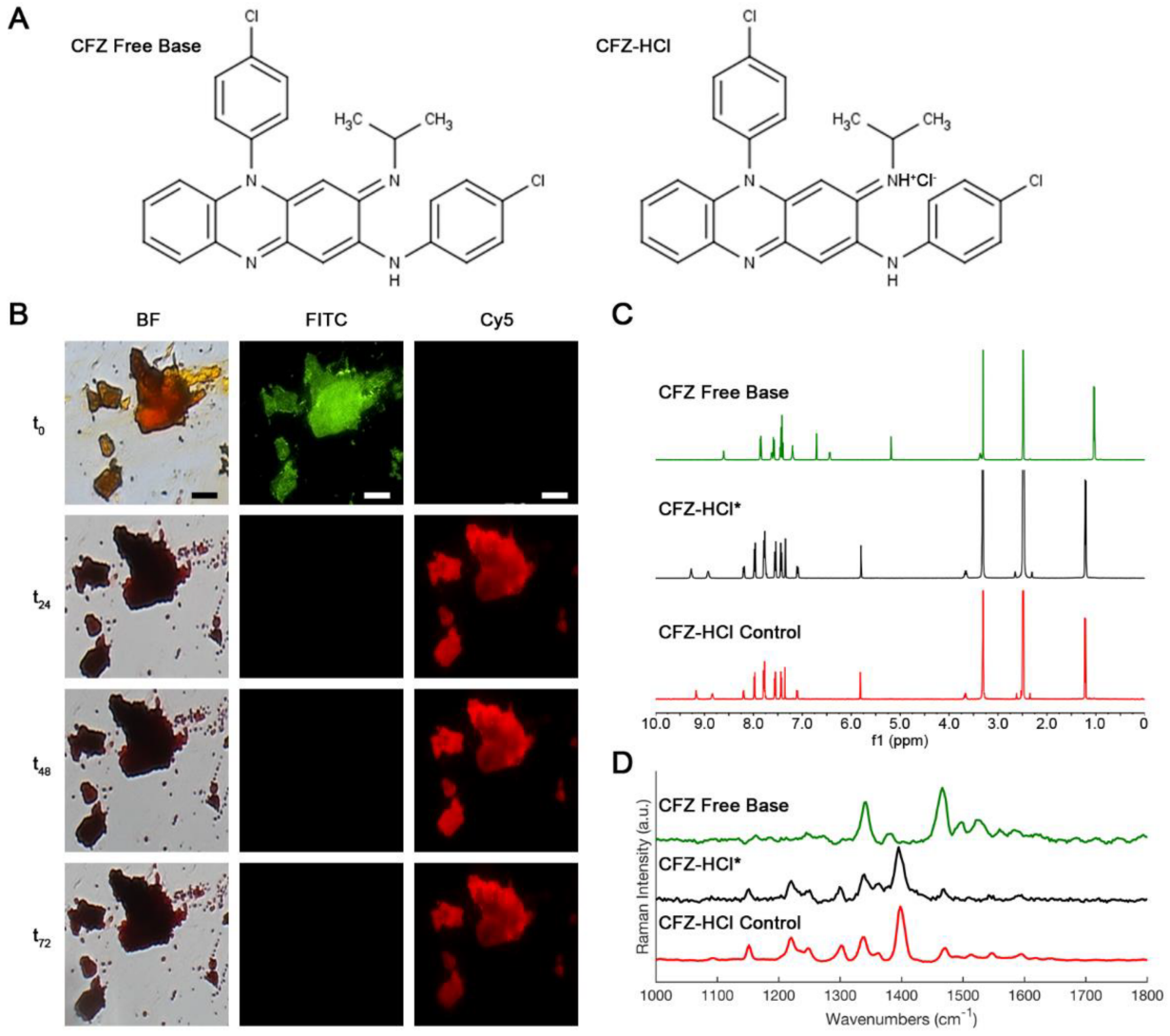

Figure 2-5. Monitoring conversion of CFZ free base to CFZ-HCl.

(A) Chemical structures of CFZ free base and CFZ-HCl. **(B)** Brightfield (BF)/fluorescent (FITC, Cy5) microscopy images; **(C)** 1H-NMR, and **(D)** Raman micro-spectroscopy spectra of synthesized CFZ-HCl salt crystals via new synthesis scheme (*) compared to the established CFZ-HCl salt crystals and CFZ free base. Scale bar = 50 µm.

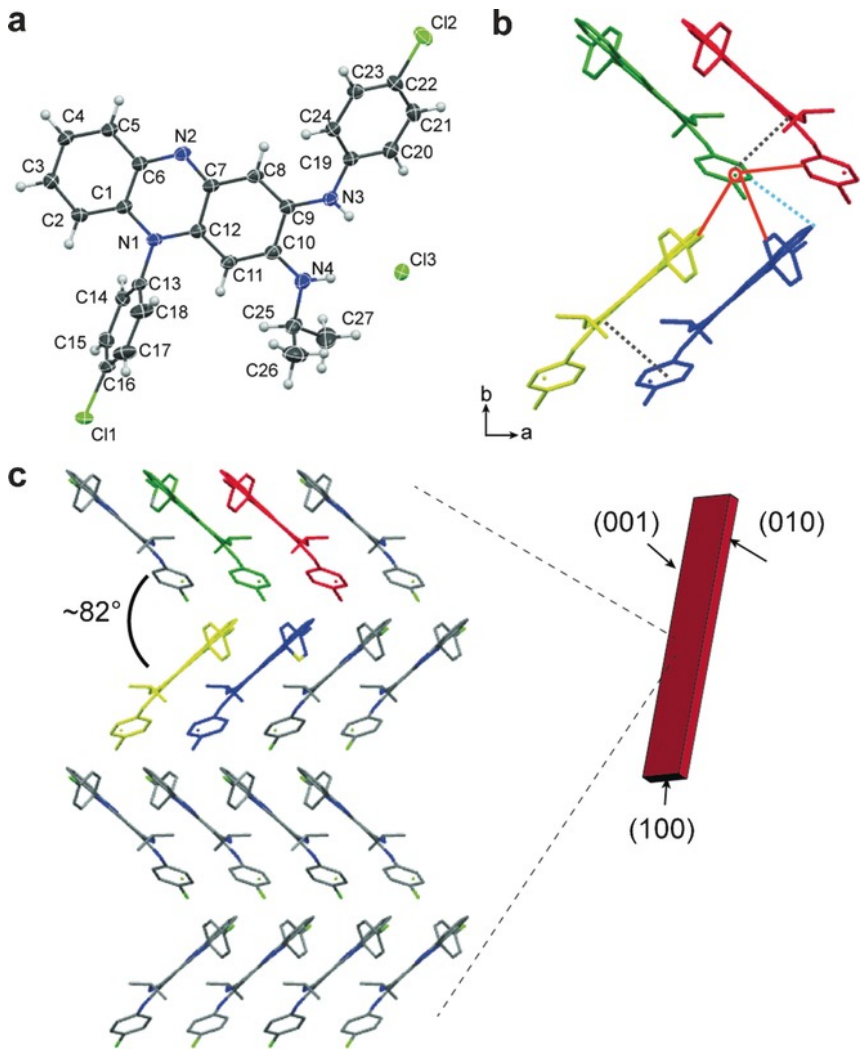

Figure 2-6. Supramolecular organization of CFZ-HCl crystals.

(a) Asymmetric unit of CFZ-HCl displayed as an ellipsoid plot with 50% probability. The atomic positions for all non-hydrogen atoms are labeled. **(b)** One section of the corrugated packing with solid orange lines indicating CH…Cl interactions, C-H…π indicated with a light blue dotted line and π…π interactions indicated by light grey dotted lines (unit cell looking along the c-axis). The molecules are displayed as capped sticks with the hydrogen atoms removed for better visualization of the crystal packing. **(c)** Crystallographic projections of packing along the (001) face showing the corrugated packing. The projection is made up of 2 × 2 × 0.5 (a × b × c) unit cells.

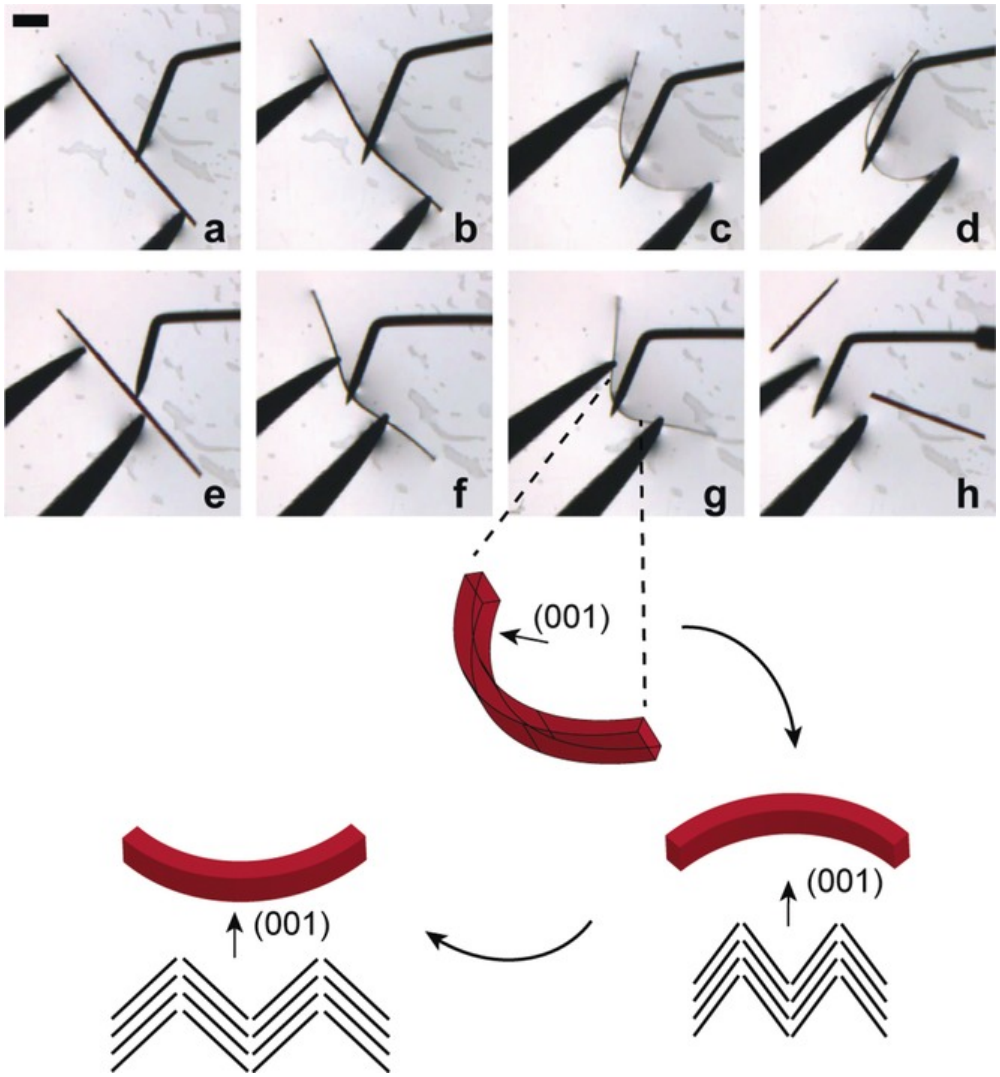

Figure 2-7. CFZ-HCl crystal bending images extracted from video.

(a–d) A CFZ-HCl crystal was bent by applying a force with a crystallization probe while the crystal was held stationary against a pair of tweezers. **(e)** The force was removed, and the crystal quickly regained the original position before **(f)** another force was applied to the crystal. Scale bar is 100 μm. The bottom schematic shows how the angle of corrugation would look like on the convex and concave edges of the crystal during bending.

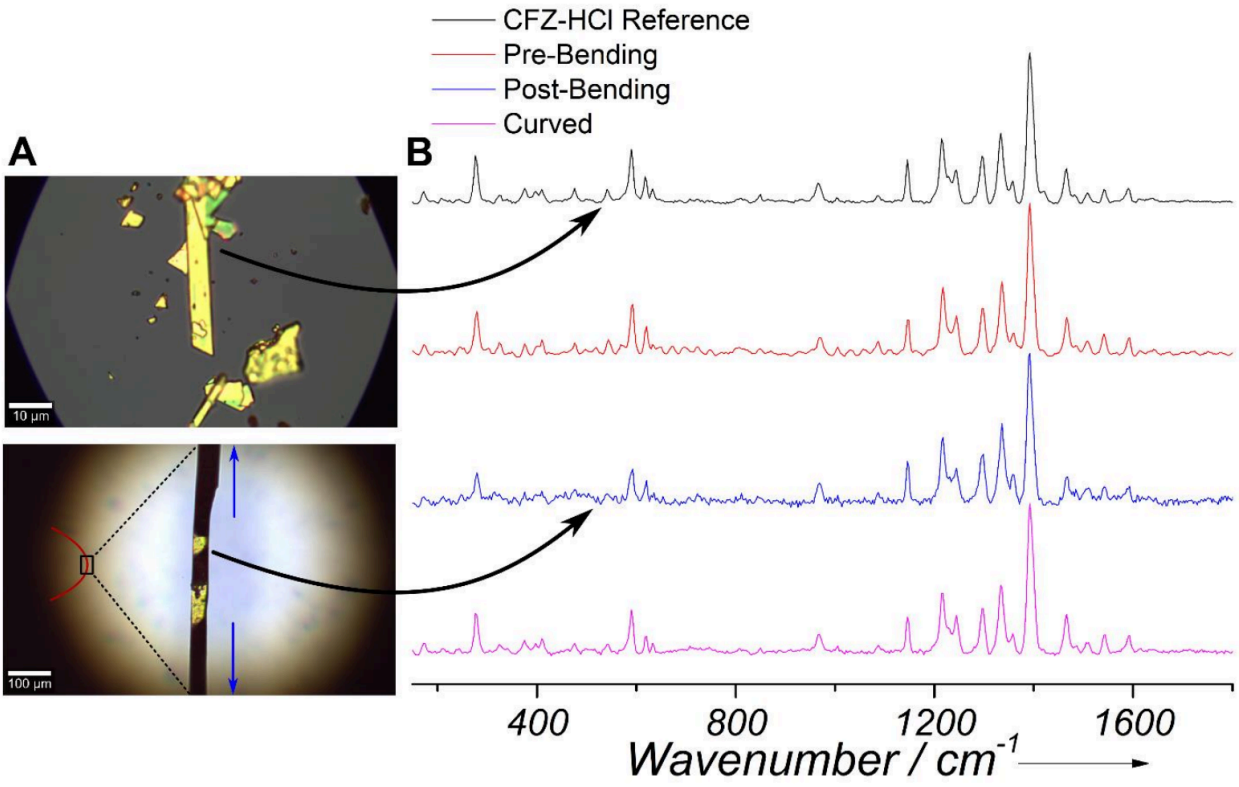

Figure 2-8. Raman analysis of CFZ-HCl crystal bending.

(A) Raman Reflectance Brightfield images of (top) short CFZ-HCl crystals and (bottom) at the bent point of a long CFZ-HCl elastic crystal. Blue arrows indicate moving away from the confocal plane used to obtain the point spectra of CFZ-HCl; **(B)** Raman Spectra of CFZ-HCl reference crystals (top) with crystals that were subjected to mechanical bending (before and after) (second and third from top) and crystals that had an inherent curvature (bottom).

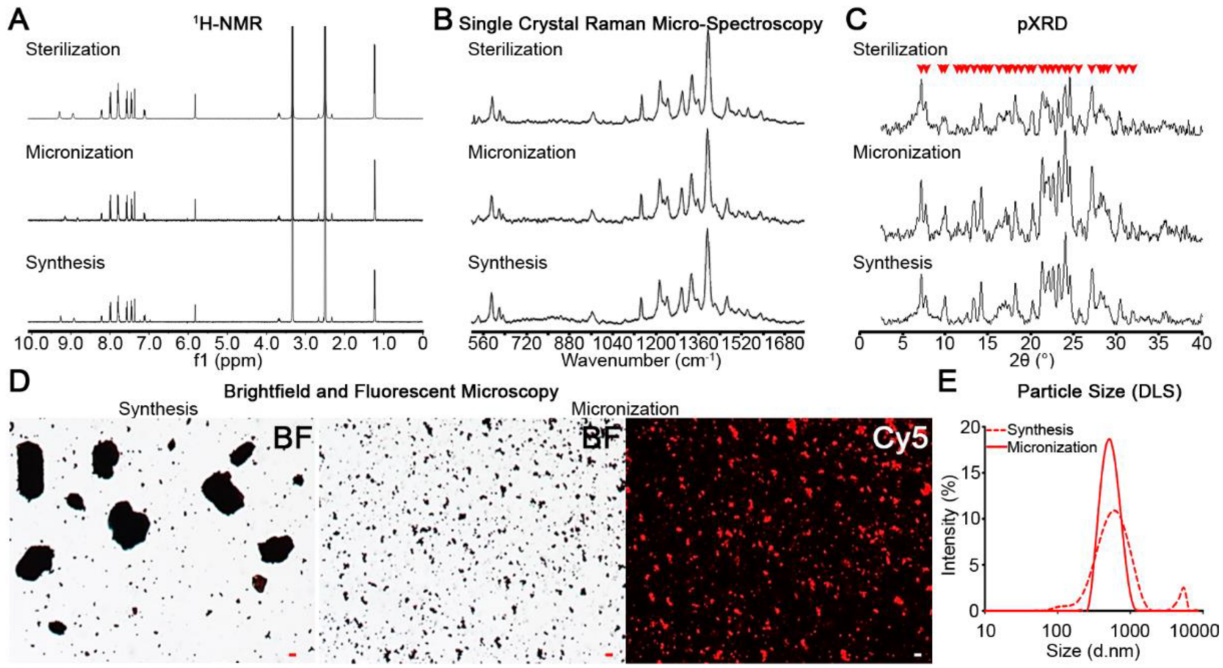

Figure 2-9. Integrity of CFZ-HCl salt crystals throughout the manufacturing process of biomimetic micronized formulation.

Analytical evidence supporting crystal integrity by **(A)** 1H-NMR, **(B)** single crystal Raman micro-spectroscopy, and **(C)** powder X-ray diffraction (pXRD). The red arrows in pXRD spectrum **(C)** indicate the peaks that are preserved after micronization and sterilization. The efficacy of micronization is depicted in brightfield and fluorescent images **(D)** and particle size distribution **(E)**. Scale bar = 5 μm.

2.10 References

1. Steel HC, Anderson R, Germishuizen WA, Cholo MC, Fourie PB. Clofazimine: current status and future prospects. Journal of Antimicrobial Chemotherapy. 2011;67(2):290-8. doi: 10.1093/jac/dkr444.

2. Barry VC, Belton JG, Conalty ML, Denneny JM, Edward DW, O'Sullivan JF, et al. A New Series of Phenazines (Rimino-Compounds) With High Antituberculosis Activity. Nature. 1957;179(4568):1013-5. doi: 10.1038/1791013a0.

3. Yoon GS, Keswani RK, Sud S, Rzeczycki PM, Murashov MD, Koehn TA, et al. Clofazimine biocrystal accumulation in macrophages upregulates interleukin 1 receptor antagonist production to induce a systemic anti-inflammatory state. Antimicrobial agents and chemotherapy. 2016;60(6):3470-9.

4. Arbiser JL, Moschella SL. Clofazimine: A review of its medical uses and mechanisms of action. Journal of the American Academy of Dermatology. 1995;32(2, Part 1):241-7. doi: https://doi.org/10.1016/0190-9622(95)90134-5.

5. Tyagi S, Ammerman NC, Li S-Y, Adamson J, Converse PJ, Swanson RV, et al. Clofazimine shortens the duration of the first-line treatment regimen for experimental chemotherapy of tuberculosis. Proceedings of the National Academy of Sciences. 2015;112(3):869. doi: 10.1073/pnas.1416951112.

6. Lechartier B, Cole ST. Mode of Action of Clofazimine and Combination Therapy with Benzothiazinones against <span class="named-content genus-species" id="named-content-1">Mycobacterium tuberculosis</span&gt. Antimicrobial Agents and Chemotherapy. 2015;59(8):4457. doi: 10.1128/AAC.00395-15.

7. Williams K, Minkowski A, Amoabeng O, Peloquin CA, Taylor D, Andries K, et al. Sterilizing Activities of Novel Combinations Lacking First- and Second-Line Drugs in a Murine Model of Tuberculosis. Antimicrobial Agents and Chemotherapy. 2012;56(6):3114. doi: 10.1128/AAC.00384-12.

8. on behalf of the Efficacy Subgroup R-T, Nuermberger EL, Dooley KE, Obuku EA, Durakovic N, Belitsky V, et al. World Health Organization Group 5 Drugs for the Treatment of Drug-Resistant Tuberculosis: Unclear Efficacy or Untapped Potential? The Journal of Infectious Diseases. 2012;207(9):1352-8. doi: 10.1093/infdis/jis460.

9. Baik J, Stringer KA, Mane G, Rosania GR. Multiscale distribution and bioaccumulation analysis of clofazimine reveals a massive immune system-mediated xenobiotic sequestration response. Antimicrobial Agents and Chemotherapy. 2013;57(3):1218-30.

10. Baik J, Rosania GR. Molecular imaging of intracellular drug–membrane aggregate formation. Molecular Pharmaceutics. 2011;8(5):1742-9.

11. Baik J, Rosania GR. Macrophages Sequester Clofazimine in an Intracellular Liquid Crystal-Like Supramolecular Organization. PLOS ONE. 2012;7(10):e47494. doi: 10.1371/journal.pone.0047494.

12. Sukpanichnant S, Hargrove NS, Kachintorn U, Manatsathit S, Chanchairujira T, Siritanaratkul N, et al. Clofazimine-Induced Crystal-Storing Histiocytosis Producing Chronic Abdominal Pain in a Leprosy Patient. The American Journal of Surgical Pathology. 2000;24(1):129.

13. Keswani RK, Baik J, Yeomans L, Hitzman C, Johnson AM, Pawate AS, et al. Chemical analysis of drug biocrystals: a role for counterion transport pathways in intracellular drug disposition. Molecular Pharmaceutics. 2015;12(7):2528-36.

14. O'Connor R, O'Sullivan JF, O'Kennedy R. The Pharmacology, Metabolism, and Chemistry of Clofazimine. Drug Metabolism Reviews. 1995;27(4):591-614. doi: 10.3109/03602539508994208.

15. Yoon GS, Sud S, Keswani RK, Baik J, Standiford TJ, Stringer KA, et al. Phagocytosed Clofazimine Biocrystals Can Modulate Innate Immune Signaling by Inhibiting TNFα and Boosting IL-1RA Secretion. Molecular Pharmaceutics. 2015;12(7):2517-27. doi: 10.1021/acs.molpharmaceut.5b00035.

16. Keswani RK, Yoon GS, Sud S, Stringer KA, Rosania GR. A far-red fluorescent probe for flow cytometry and image-based functional studies of xenobiotic sequestering macrophages. Cytometry Part A. 2015;87(9):855-67. doi: 10.1002/cyto.a.22706.

17. Spencer LJ. Curvature in Crystals. Mineralogical Magazine and Journal of the Mineralogical Society. 1921;19(95):263-74. doi: 10.1180/minmag.1921.019.95.05.

18. Panda MK, Ghosh S, Yasuda N, Moriwaki T, Mukherjee GD, Reddy CM, et al. Spatially resolved analysis of short-range structure perturbations in a plastically bent molecular crystal. Nature Chemistry. 2014;7:65. doi: 10.1038/nchem.2123

19. Reddy CM, Gundakaram RC, Basavoju S, Kirchner MT, Padmanabhan KA, Desiraju GR. Structural basis for bending of organic crystals. Chemical Communications. 2005;(31):3945-7. doi: 10.1039/B505103G.

20. Koshima H, Matsuo R, Matsudomi M, Uemura Y, Shiro M. Light-Driven Bending Crystals of Salicylidenephenylethylamines in Enantiomeric and Racemate Forms. Crystal Growth & Design. 2013;13(10):4330-7. doi: 10.1021/cg400675r.

21. Godwod K, Nagy AT, Rek Z. The application of the X-ray triple-crystal spectrometer for measuring the radius of curvature of bent single crystals. physica status solidi (a). 1976;34(2):705-10. doi: 10.1002/pssa.2210340235.

22. Terao F, Morimoto M, Irie M. Light-Driven Molecular-Crystal Actuators: Rapid and Reversible Bending of Rodlike Mixed Crystals of Diarylethene Derivatives. Angewandte Chemie International Edition. 2012;51(4):901-4. doi: 10.1002/anie.201105585.

23. Baumgartner J, Morin G, Menguy N, Perez Gonzalez T, Widdrat M, Cosmidis J, et al. Magnetotactic bacteria form magnetite from a phosphate-rich ferric hydroxide via nanometric ferric (oxyhydr)oxide intermediates. Proceedings of the National Academy of Sciences. 2013;110(37):14883-8. doi: 10.1073/pnas.1307119110.

24. Siponen MI, Legrand P, Widdrat M, Jones SR, Zhang W-J, Chang MCY, et al. Structural insight into magnetochrome-mediated magnetite biomineralization. Nature. 2013;502:681. doi: 10.1038/nature12573.

25. Wang Y, Lomakin A, Hideshima T, Laubach JP, Ogun O, Richardson PG, et al. Pathological crystallization of human immunoglobulins. Proceedings of the National Academy of Sciences. 2012;109(33):13359-61. doi: 10.1073/pnas.1211723109.

26. Weller PF, Goetzl EJ, Austen KF. Identification of human eosinophil lysophospholipase as the constituent of Charcot-Leyden crystals. Proceedings of the National Academy of Sciences. 1980;77(12):7440-3. doi: 10.1073/pnas.77.12.7440.

27. Mulay SR, Anders H-J. Crystallopathies. New England Journal of Medicine. 2016;374(25):2465-76. doi: 10.1056/NEJMra1601611.

28. Sullivan DJ, Gluzman IY, Goldberg DE. Plasmodium Hemozoin Formation Mediated by Histidine-Rich Proteins. Science. 1996;271(5246):219-22. doi: 10.1126/science.271.5246.219.

29. Aplin RT, McDougall AC. Identification of crystals of the rimino-phenazine compound B663 (lamprene: Clofazimine) in mouse spleen macrophages by thin layer chromatography and mass spectrum analysis. Experientia. 1975;31(4):468-9. doi: 10.1007/bf02026384.

30. Vicari P, Sthel VM. Cystine Crystals in Bone Marrow. New England Journal of Medicine. 2015;373(23):e27. doi: 10.1056/NEJMicm1415736.

31. Martinon F, Pétrilli V, Mayor A, Tardivel A, Tschopp J. Gout-associated uric acid crystals activate the NALP3 inflammasome. Nature. 2006;440(7081):237-41. doi: 10.1038/nature04516.

32. Bocklitz TW, Guo S, Ryabchykov O, Vogler N, Popp J. Raman Based Molecular Imaging and Analytics: A Magic Bullet for Biomedical Applications!? Analytical Chemistry. 2016;88(1):133-51. doi: 10.1021/acs.analchem.5b04665.

33. Fu D, Zhou J, Zhu WS, Manley PW, Wang YK, Hood T, et al. Imaging the intracellular distribution of tyrosine kinase inhibitors in living cells with quantitative hyperspectral stimulated Raman scattering. Nature Chemistry. 2014;6(7):614-22.

34. LaLone V, Mourão MA, Standiford TJ, Raghavendran K, Shedden K, Stringer KA, et al. An Expandable Mechanopharmaceutical Device (3): a Versatile Raman Spectral Cytometry Approach to Study the Drug Cargo Capacity of Individual Macrophages. Pharmaceutical Research. 2018;36(1):2. doi: 10.1007/s11095-018-2540-0.

CHAPTER 3

A Versatile Raman Spectral Cytometry Approach to Study the Drug Cargo Capacity of Individual Macrophages

3.1 Relevance to Thesis

To address specific aim 1 of my thesis and create the foundation for ultraquantitative Raman spectral cytometry, a versatile Raman methodology was developed to study the drug cargo capacity of individual macrophages, specifically to measure the intracellular accumulation and distribution of small molecule xenobiotics. In the studies presented herein, I utilized the cell sample preparation for alveolar macrophages – first discussed in Chapter 2 of my thesis – that involved adherence of cells to silicon chips before washing and air-drying; in this way, water evaporated from the cells, depositing all non-volatile molecular components of interest as thin dry dispersions on the surface of silicon chips. Furthermore, the novel drug:lipid stoichiometric calibration methodology was first published from the work presented in this chapter where a multitude of FDA-approved colorless small molecule drugs were screened for accumulation inside alveolar macrophages in an effort to show proof-of-concept for our Raman analytical approach.

The preliminary statistical foundation for the methodology was also first reported and published in this study; using a non-negative least squares regression (aka linear combination modelling), I herein showed the validity of this approach for Raman spectral deconvolution with the ultimate purpose of quantitative intracellular imaging of drug accumulation inside macrophages. When harmonized effectively with the stoichiometric calibration mixtures of drug and phospholipid, this statistical model enabled Raman-

based screening of drug accumulation throughout cell populations and quantitative measurement of intracellular drug inclusions. Using this method, I was able to generate results which suggested the intracellular phase separation and self-aggregation of a small molecule tyrosine kinase inhibitor, nilotinib. In contrast, investigation of chloroquine and etravirine revealed that these compounds accumulated primarily via lipid partitioning rather than intracellular precipitation. Furthermore, the integrated area scan acquisition methodology in which the excitation laser scans across the specimen of interest and sums together the total Raman signal (crucial to ultraqauntitative theory) was first developed and reported on in this work. In this chapter the area scan approach was used to estimate the % weight of drug inside a single cell as a fraction of the total cell's dry mass. Although these Raman measurements are relative weight %, they represent the first report of quantitative analysis of intracellular drug distribution and accumulation in relation to endogenous biomolecules on a per-pixel basis.

In its entirety, this chapter serves as robust proof-of-concept and feasibility testing for Raman microanalytical measurement of intracellular drug accumulation and distribution using a least squares regression statistical model with stoichiometric mixtures of drug and phospholipid for quantitative model calibration. Despite its scientific validity, all the work presented in this chapter was performed *in vitro*; although it is valid in terms of proof-of-concept, the research presented in this chapter alone lacks clinical feasibility, specifically the evidence that shows it can be used to generate meaningful measurements in the context of disease progression *in vivo*. Though relevant, this aspect of the project more appropriately falls under the scope of specific aim 3 and is discussed thoroughly in Chapter 5 of my thesis. In summary, the work presented in this chapter addresses the major goals of specific aim 1 of my thesis and serves as the published foundation for other aspects of single-cell Raman analysis work.

3.2 Abstract

To improve cytometric phenotyping abilities and better understand cell populations with high interindividual variability, a novel Raman-based microanalysis was developed to characterize macrophages based on chemical composition, specifically to measure and characterize intracellular drug distribution and phase separation in relation to endogenous cellular biomolecules. The microanalysis was developed for the commercially-available WiTec alpha300R confocal Raman microscope. Alveolar macrophages were isolated and incubated in the presence of pharmaceutical compounds nilotinib, chloroquine, or etravirine. A Raman data processing algorithm was specifically developed to acquire the Raman signals emitted from single-cells and calculate the signal contributions from each of the major molecular components present in cell samples. Our methodology enabled analysis of the most abundant biochemicals present in typical eukaryotic cells and clearly identified “foamy” lipid-laden macrophages throughout cell populations, indicating feasibility for cellular lipid content analysis in the context of different diseases. Single-cell imaging revealed differences in intracellular distribution behavior for each drug; nilotinib underwent phase separation and self-aggregation while chloroquine and etravirine accumulated primarily via lipid partitioning. This methodology establishes a versatile cytometric analysis of drug cargo loading in macrophages requiring small numbers of cells with foreseeable applications in toxicology, disease pathology, and drug discovery.

3.3 Introduction

Serving as the frontline of the mammalian inflammatory immune response, macrophages play a pivotal role in the defense and maintenance of all organ systems. At the gas-air interface of the lungs reside alveolar macrophages. Within the alveoli, these cells sequester inhaled particulate matter while pulmonary blood flow through the lung also exposes them to systemically circulating drug compounds.(1-3) Small molecules with high lipophilicity and weakly basic amines groups may passively diffuse through cellular

membranes, becoming protonated and positively charged within the acidic lysosomal compartments.(4-7) The electrostatically-charged form of the molecule has a much lower membrane permeability which prevents its exit by passive diffusion, causing intracellular accumulation of the compound. Bioaccumulation of small molecules has been reported for a multitude of drug compounds and in many cases has been linked with the concurrent accumulation of lipids within various organs and cell types.(8-10) In many cases, these foreign chemical compounds have been reported to accumulate within alveolar macrophages.(11, 12) To date, there is no direct association with toxicity but in terms of drugs, regulatory agencies (FDA and corresponding administrations in Europe and Japan) generally consider it a potentially adverse reaction and as such, are hesitant to grant such compounds market-approval.(13) Despite an abundance of research endeavors over the past 30 years, the relationship between drug exposure, lipid accumulation, and observed organ toxicity has yet to be firmly established.(14-16) The presence of “foamy” lipid-laden macrophages has historically served as the histopathological hallmark with transmission electron microscopy providing the gold standard for diagnosis.(17, 18) Though robust and adaptable, perhaps macrophages have a quantifiable limit to how much foreign material they can stably carry. As such, we believe quantitative characterization of this system and its limits would surely serve to improve our understanding of the risk-benefit properties for a multitude of clinically-effective drugs.

Confocal Raman micro-spectroscopy offers a novel approach for the quantitative study of bioaccumulation phenomena at the microscopic level, allowing direct chemical analysis of single cells without the need for radiolabels or fluorescent tags.(19-23) In short, an excitation laser is coupled to a confocal microscope via fiber optic cable and focused into a 3D voxel which then scans the sample. A portion of the laser light is absorbed by the sample, inducing molecular vibrations, while the remaining energy is scattered as light of different wavelengths. Scattered light is separated by a diffraction grating and the number of emitted photons at each wavelength is detected across a CCD detector array. The change in wavelength relative to the laser is referred to as the Raman

shift and is measured in wavenumbers (cm^{-1}); the number of photons detected at each wavenumber form the basis of Raman spectra which serve as molecular “fingerprints” and can be interpreted to characterize the chemical composition of the analyzed sample. Advantages of Raman-based techniques include minimal sample preparation, non-destructive analysis, and potential identification of unknown chemical species present within a sample of interest. While conventional methods such as flow cytometry, immunostaining, and fluorescent dyes provide only relative measurements, Raman enables the direct measurement of unadulterated cellular samples. Wielding submicron spatial resolution capabilities, confocal Raman micro-spectroscopy enables chemical composition analysis at the subcellular and cell population levels.(24-26)

In an effort to improve cytometric phenotyping abilities and better understand a cell population that is highly variable between individuals, a novel Raman-based microanalysis was developed and employed to characterize pulmonary alveolar macrophages on the basis of chemical composition, specifically to measure and characterize intracellular drug distribution and phase separation in relation to proteins, lipids, and nucleic acids. Although Raman-based measurements of intracellular drug accumulation have been reported previously, to the best of our knowledge this study represents the first report of drug distribution mapped at the subcellular level in relation to the most abundant endogenous molecular species comprising typical eukaryotic cells.(4, 27, 28) Additionally, we introduce a novel analytical approach for the screening of bioaccumulation phenomena throughout cell populations, thereby establishing the analytical foundations for a robust quantitative high-content cytometric methodology that only requires a small number of cells. This makes the approach feasible for use in the clinical setting which will permit a more accurate cellular phenotypic analysis than ever before possible. Overall, this study demonstrates the feasibility of our novel sample preparation and Raman-based chemical characterization methodology for the purposes of alveolar macrophage compositional phenotyping and intracellular drug accumulation measurements.

3.4 Materials and Methods

3.4.1 BAL Cell Isolation, Culture, and Preparation

C57BL/6 mice (4-week old males; Jackson Laboratory, Bar Harbor, ME) were acclimatized for 1 week in a pathogen-free animal facility prior to euthanasia via CO_2 asphyxiation. The tracheae were surgically isolated, cannulated, and alveolar cells were procured via bronchoalveolar lavage (BAL) with sterile phosphate-buffered saline (DPBS; Gibco Life Technologies, Carlsbad, CA) containing 0.5mM EDTA (Sigma).(29) BAL cell suspensions were centrifuged and cell pellets were resuspended in RPMI 1640 medium (Gibco Life Technologies, Carlsbad, CA) at ~300 cells/μL and 15μL of suspension was transferred to surface of sterilized silicon chips (5x5mm; Ted Pella, Inc., Redding, CA) within a 24-well plate (1 chip per well); cells were incubated (37°C, 5% CO_2) for 1 hour to allow for adherence of macrophages. RPMI 1640 medium (750μL), blank or containing drug at the indicated concentration, was added to each well and cells were incubated for specified amounts of time (37°C, 5% CO_2). Following drug incubation, culture medium was removed via vacuum and silicon chips were rinsed via brief submersion in isotonic saline (0.9% NaCl wt/wt) then deionized water to remove salt; the residual water was wicked away immediately with a Kimwipe to prevent cell lysis. Samples were air-dried, depositing the non-volatile cellular components as dry dispersions on the surface of silicon chips.

3.4.2 Reagents and Reference Components

To generate representative reference sample spectra, the chemical components of interest were dissolved in an appropriate solvent and an aliquot was transferred to the surface of a silicon chip. The solvent evaporated at room temperature leading to deposition of reference material in the form of thin dispersions on the surface of the chip. Protein, lipid, and nucleic acid reference spectra were acquired from dispersions of bovine albumin (MP Biomedicals, Solon, OH), 1,2-dipalmitoyl-*sn*-glycero-3-phosphocholine

(DPPC; Avanti Polar Lipids, Inc., Alabaster, AL), and DNA (from salmon sperm; AmResco Inc., Solon, OH), respectively. The following drug compounds were procured from various sources: nilotinib (free base; LC laboratories, Woburn, MA), chloroquine (diphosphate salt; Sigma-Aldrich Inc., St. Louis, MO), and etravirine (Advanced ChemBlocks Inc., Burlingame, CA). Drugs were dissolved in methanol, spotted on silicon chips and allowed to dry; reference spectra were obtained from each dry dispersion.

3.4.3 Stoichiometric Calibration Methodology

Formulated as stoichiometric mixtures of drug and DPPC dissolved in a solution of methanol and water (5:1 respective volumetric ratio), a known volume was transferred to the surface of a silicon chip and the solvent was allowed to air-dry. Calibration samples were intelligently designed to result in thin dispersions of drug and phospholipid (in known mass ratios) that most closely represented the dimensions and conditions of the drug-treated cell samples under investigation. Additionally, stoichiometric mixtures of protein and DNA were dissolved in water, deposited onto silicon chips, and allowed to air-dry. Reference and calibration samples were analyzed using large area scan methodology and average spectra with standard deviations from each scan are reported herein. Least squares regression modelling was used to quantitatively interpret the acquired calibration spectra and extract the % signal for each component (i.e., phospholipid and drug). Linear correlation of % drug signal with the actual mass ratio of drug in phospholipid enabled inferring the extent of drug accumulation in discrete lipid inclusions.

3.4.4 Raman Measurements

All Raman spectra and images were acquired by the WiTec alpha300R confocal Raman microscope equipped with the 532nm solid-state sapphire excitation laser (0-55 mW, tunable intensity range) and a 100x air objective (Zeiss Epiplan-NEOFLUAR, N.A. = 0.9) coupled to CCD detector via a multi-mode fiber of 100μm diameter, serving as the

confocal pinhole. Single-cell Raman imaging was performed via continuous area scan across entire sample region. Each Raman image consisted of 90 × 90 spectra with exposure time of 0.3 seconds each, resulting in 8100 spectra with a total acquisition time of approximately 45 minutes per cell. Point spectra were acquired by focusing laser on nuclei or cytoplasmic inclusions and averaging Raman signal for 25 seconds. Integrated Raman spectra were acquired via continuous scan of a 20 × 20μm area using a 50x air objective lens (Zeiss Epiplan-NEOFLUAR, N.A. = 0.75) with pixel dimensions of 1μm^2; the integration time was set to 0.1 seconds per spectrum, yielding 400 spectra with an acquisition time of ~1 minute per cell.

3.4.5 Algorithmic Data Processing

Unless noted otherwise, all Raman spectral data were preprocessed using equivalent algorithm parameters. Initial data preprocessing was performed in WiTec Project FOUR software to remove cosmic ray interference and perform spectral smoothing. The data were then exported to Matlab® (Natick, MA USA) and the remainder of preprocessing and analysis were performed using algorithms developed in-house. The spectral regions of interest were excised from the dataset between the wavenumbers 1200-3200 (cm^{-1}) and used for all subsequent preprocessing. Background subtraction was performed via baseline estimation within multiple shifted windows across the spectra followed by regression of the varying baseline to window points via spline approximation. The spectra were then normalized by the standard deviation (yielding a standard deviation of 1 for all spectra). Spectral regions of interest, 1200-1800 cm^{-1} and 2700-3200 cm^{-1} (including 2100-2300 cm^{-1} for etravirine-treated samples), were then interpreted via statistical analysis. Each pixel of integrated area scans was preprocessed individually and the spectral signals were summed across the entire scanned area, yielding a single Raman spectrum for each cell analyzed.

3.4.6 Statistical Interpretation of Raman Hyperspectral Datasets

To extract relevant chemical information from the acquired hyperspectral datasets, non-negative least squares regression modelling was employed; using pure component reference spectra, measured Raman spectra were deconvoluted to determine the relative signal contributions from each component of interest according to the following model:

$$I_{\tilde{\nu}} = N_1 k_{\tilde{\nu}_1} + N_2 k_{\tilde{\nu}_2} + N_3 k_{\tilde{\nu}_3} + \varepsilon_{\tilde{\nu}}$$

Where:

$\tilde{\nu}$ = relative wavenumber or Raman shift (cm^{-1})

$I_{\tilde{\nu}}$ = measured sample spectrum

$k_{\tilde{\nu}_n}$ = component "n" reference spectrum

N_n = component "n" regression estimate

$\varepsilon_{\tilde{\nu}}$ = residual spectrum

The relative signal contribution for each component was calculated using the regression estimators; the following example calculation was provided for clarity:

$$\% \text{ Component 1 Signal} = \frac{N_1}{N_1 + N_2 + N_3} * 100$$

To assess model accuracy, the coefficient of determination (R^2) was calculated by comparing the variance initially present in the measured sample spectrum with the remaining variance (calculated across the residual spectrum) after regression analysis and subsequently used to determine the fraction of information contained within the measured Raman spectrum that is unexplained by the reference component library as follows:

$$R^2 = 1 - \left(\frac{variance(\varepsilon_{\tilde{\nu}})}{variance(I_{\tilde{\nu}})}\right)$$

$$\% \text{ Unexplained Signal} = (1 - R^2) * 100$$

For single cell imaging, the algorithm was applied on a per-pixel basis to every spectrum of cell image and pseudo-color Raman maps were generated using the relative signal contributions from each of the reference components. The coefficient of determination (R^2) was calculated for each pixel and used to determine the relative percent of Raman signal unexplained by the reference library spectra; 3D surface plots were generated to indicate specific subcellular regions that deviated from the reference library components. For drug-treated cell samples, a four-component regression model was applied and the relative drug signal contribution was translated into relative drug mass according to the stoichiometric calibration curve. To assess subcellular drug distribution, single-cell Raman images were acquired and 3D surface plots were generated with the relative drug mass plotted on the z-axis.

3.5 Results and Discussion

3.5.1 Experimental Setup and Raman Microanalysis

Herein a silicon chip served as robust and reliable sample substrate; despite being exceptionally economical, they are often overlooked as a candidate-substrate for Raman microanalysis of single cells.(19) Sample preparation on silicon enabled isolation of adherent BAL cells from healthy mice, presumably alveolar macrophages, as thin dry dispersions on the surface of the chip. Upon reflected brightfield inspection, the cells exhibited a rainbow-colored appearance which was attributed to the thin-film interference of light passing through the sample and reflection from the silicon surface; indicating the vertical thickness of each cell was in the submicron range. Assuming the sample thickness to be less than 1.5 microns (equal to the theoretical height of the confocal voxel) Raman images acquired across a single z-plane were representative of the total cellular contents. Single-cell Raman imaging methodology was employed to acquire Raman hyperspectral datasets for 36 individual cells, which were then used to develop a robust computational algorithm (Figure 3-1B). The automated spectral pre-processing parameters, which included cosmic ray removal, a moving average smoothing matrix,

baseline correction, and normalization, were optimized to extract the pure sample Raman spectra on a per-pixel-basis.

3.5.2 Statistical Modelling and Single-Cell Imaging

To translate the acquired Raman signals into chemically relevant information, a least squares regression model was employed.(30, 31) Although more sophisticated statistical approaches are commonly utilized (i.e., principal component analysis (32, 33)), least squares regression is most appropriate because it allows for direct quantitative measurement of specific phenotypic/compositional changes in macrophages that occur in response to drug exposure or lung injury, thereby providing direct extraction of biologically-relevant information from the acquired spectra. Utilizing the most abundant biochemical components present within a typical eukaryotic cell (i.e., protein, lipid, and nucleic acid) as reference spectra (Figure 3-1A), the measured sample spectra were deconvoluted into the relative signal contribution from each component, yielding R^2 values of >0.9 for most pixels of each Raman image – image pixels with R^2 <0.75 were used to identify cell edges and assign silicon substrate to black. In terms of spectral modeling, extracted biomolecular components from eukaryotic cells are reported to yield Raman signals which can be accurately modelled using pure component reagent reference spectra (i.e., bovine albumin, bovine heart lipids, salmon sperm DNA, etc.) from commercially-available sources(23, 34-38); this is possible because all cellular proteins are composed of polypeptide chains with 20 different amino acids, lipids are primarily composed of long hydrocarbon chains, and nucleic acids are long sugar-phosphate chains of only 5 different nucleotides (DNA and RNA). A pseudo-color ternary scale (Figure 3-1C) was used to visualize the relative signal contributions from each component across the entirety of each measured cell, thereby generating Raman chemical images of individual cells (Figure 3-1D). Furthermore, regression analysis residuals were utilized to calculate the percent of unexplained spectral variance at each pixel of the Raman images (Figure 3-1E).

Punctate patterns were detected throughout the cytoplasm which gave rise to Raman signals unaccounted for by the reference spectra library; the most notable spectral deviations, revealed by the residual spectra, occurred around 1593 cm^{-1} (Figure S-2). The Raman band consistently observed at 1585 cm^{-1} likely represents mitochondrial cytochrome c; further studies are required to understand the relationship between this Raman signal and metabolic activity in eukaryotic cells.(39, 40) The presence of the cytochrome c peak in a punctate pattern associated with the cytoplasm of cells suggests cells remained viable during the course of drug treatment and confirms that cytochrome c did not leak out of mitochondria into the cytosol, before or during Raman image data acquisition. Within single cells, the cytoplasm could be clearly distinguished from the protein-rich nuclei; cytoplasmic inclusions gave rise to heterogeneous Raman signals which we attributed to the presence of lipid-rich inclusions (e.g., lamellar bodies, lysosomes, other membranous organelles, etc.) and nucleic acid-rich regions (e.g., mitochondria, stress granules, P bodies, etc.). Our Raman imaging methodology successfully revealed compositional heterogeneity on a per-cell basis and identified "foamy" lipid-laden macrophages throughout, indicating the feasibility of cell population phenotyping on a compositional basis (Figure 3-2A). Cell morphology as measured by our Raman methodology, namely subcellular distribution of biomolecular components and compartmentation of components in specific organelles (i.e., nucleus, cytoplasm, lipid-rich inclusions, etc.) was consistent with that reported by alternative staining techniques (i.e., phalloidin for protein, Oil Red O or Nile red for lipid, and DAPI for DNA)(41, 42) as well as Raman imaging studies reported by other groups (25, 33).

To more thoroughly explore the intracellular structure of cells and confirm the validity of our statistical model, 1.5 × 1.5μm area average spectra corresponding with specific subcellular compartments were extracted from single-cell Raman images; the three regions of interest were nuclei, cytoplasm, and lipid-rich cytoplasmic regions which were respectively assigned visually as the large red circular spots (~10% cell volume), yellow-orange cytoplasmic regions, and bright-green cytoplasmic regions (Figure 3-2B). 25 spectra were extracted from each of the specified regions of interest and deconvoluted

via regression modelling to estimate the relative signal contribution from each major component of interest (Figure 3-2C). The lipid-rich regions emitted Raman spectra which closely matched that of the phospholipid reference spectra DPPC, the primary chemical component of pulmonary surfactant.(43) Additionally, point spectra were acquired from the nuclei and corresponding cytoplasmic inclusion regions for 120 individual cells (Figure S-3, S-4). As evidenced by the averaged point spectra from 120 cytoplasmic inclusions, the unexplained band at 1585 cm^{-1} was absent from the most spectra, presumably because the entirety of each cell was not scanned. The calculated difference spectra revealed wavenumbers at which the most pronounced spectral differences occurred, which closely corresponded with the tentative vibrational assignments for the major Raman peaks of the most abundant biochemical species present in a typical eukaryotic cell (Table S-2)(23, 44). Cytoplasmic regions and the nuclei of untreated cells primarily yielded Raman signals most closely matching that of protein with less apparent contributions from lipid and nucleic acid. This was consistent with the following theoretical relative masses reported for a typical eukaryotic cell (dry weight): 65% protein, 15% lipid, 5% nucleic acid (15% heterogeneous mixture of small molecular metabolites and ions).(45) Regression modelling estimated relative Raman signal contributions within the nuclei were 78.7 $\pm$ 5.64% protein signal and 14.8 $\pm$ 5.26% nucleic acid signal with a negligible lipid signal of 6.46 $\pm$ 4.03% (average $\pm$ S.D., n=120 cells). Quantitation via stoichiometric calibration with protein-to-DNA mixtures measured nucleic acid content at 20.6 $\pm$ 5.14% of total dry mass within nuclei (Figure S-5) which was consistent with expected theoretical nucleic acid content for a typical eukaryotic cell nucleus.

3.5.3 Screening Cell Populations for Intracellular Drug Accumulation

For characterization of drug sequestration and accumulation within alveolar macrophages, three test compounds were chosen based on physicochemical properties and previous reports of intracellular accumulation (Table S-3).(4, 10, 46) Reference spectra were acquired for each and characteristic peaks were identified to confirm each

compound emitted a spectrally-unique Raman signal (Figure S-6). The tyrosine kinase inhibitor nilotinib was chosen as the model compound for initial algorithm and quantitative method development purposes because it yields a relatively strong Raman signal and its intracellular accumulation has been reported by previous studies.(4) Stoichiometric calibration mixtures were generated, diluting the drug into lipid at known ratios, and the acquired Raman spectra were deconvoluted via regression modelling to extract the % nilotinib signal for each (Figure 3-3A). This methodology defined the linear range by correlating % drug signal with the actual relative mass (% wt/wt) in each calibration sample (Figure 3-3B); the linear range was experimentally determined to be 3.5% - 100% nilotinib (wt/wt).

We then tested our methodology's ability to detect temporal accumulation of sequestered drug compounds by isolating and incubating alveolar macrophages in the presence of 8 μM nilotinib for 24 and 48 hours. Samples were collected at appropriate time points, washed, dried, and analyzed via integrated Raman area scans (Figure 3-4A). The resulting "integrated" spectra represented the entirety of a cell's chemical components because Raman signals were acquired across each entire cell and were summed into the total Raman signal, yielding a single "integrated" spectrum for each cell analyzed.(47) 20 individual cells were analyzed from each of the populations and their integrated spectra were algorithmically processed and interpreted via regression modelling (Figure 3-4B). Difference spectra were calculated by subtracting the average integrated spectrum of untreated control cells from each treated cell's integrated spectrum; the calculated difference spectra matched closely with the pure nilotinib reference spectrum and the observed spectral differences were attributed to temporal accumulation of nilotinib within the alveolar macrophages.

By deconvoluting the integrated spectra via regression modelling and employing the calibration curve, the mass % of drug accumulation relative to each cell's total dry weight was determined for cell populations (Figure 3-4C). Our results indicated that after 48 hours nilotinib represented 20% of an exposed cell's total chemical composition on average. This suggests nilotinib becomes one of the most abundant chemical species

present within alveolar macrophages after 48-hour exposure, exceeding theoretical estimates for typical lipid content of 15%.(45) It should be noted that differential accumulation was observed throughout the population with some cells sequestering noticeably more drug than others. It is quite likely that differences in drug sequestering ability and/or phenotype exist on a cell-by-cell basis throughout each macrophage population, as this has been reported for other compounds.(12) Since integrated area scans summed the Raman signals from across the entirety of each cell, the unknown band at 1585 cm^{-1}, attributed to mitochondrial cytochrome c, was clearly present in untreated cell spectra. Spectral overlap of this Raman signal with nilotinib's characteristic Raman peak resulted in minimal spectral interference: an average of 1.29% nilotinib (wt/wt) was reported in untreated cells (which was below nilotinib's limit of quantitation) and false-positives for drug detection occurred in <50% of the population. To verify method feasibility for the study of small molecules other than nilotinib, the test compounds chloroquine and etravirine were utilized. Stoichiometric calibration mixtures were utilized to experimentally determine the quantitative range of regression modelling for both compounds (Figure S-7).

We then incubated isolated alveolar macrophages in the presence of 50 μM chloroquine or etravirine for 4 hours, before preparation and analysis via integrated Raman scans. The average untreated cell spectrum was subtracted from each of the processed spectra acquired from treated cells and difference spectra were generated for each treatment group (Figure S-8). Spectral overlay revealed clear matches between each drug's reference spectrum and the calculated difference spectra, indicative of chemical bioaccumulation within exposed cells. Quantitative modelling estimated total cellular chloroquine content at 19.8 ± 13.9% (wt/wt) for the 20 cells analyzed; no false-positives were detected among the untreated population. Etravirine accumulation was measured at 6.40 ± 3.47% (wt/wt) of the total cellular contents for 20 cells analyzed, suggesting method feasibility for detection and screening of differential drug bioaccumulation in cell populations. The accumulation of drug molecules inside cells can be attributed to ion trapping of weakly basic molecules within the acidic lysosomes of

cells, which is an important phenomenon with significant pharmacokinetic implications that is typically underrecognized but has been reported for many compounds.(4, 12, 48)

3.5.4 Quantitative Single-Cell Imaging for Intracellular Drug Distribution Analysis

Our Raman imaging algorithm was coupled with the stoichiometric calibration curve to quantitatively characterize intracellular accumulation and distribution of drug compounds in relation to subcellular compartments and endogenous biomolecules of interest. Drug incubation concentrations and exposure time were selected based on similar experimental studies that have also explored drug distribution inside cells, so our observations can be compared with the previous reports.[4,10] First, the single-cell Raman imaging methodology was utilized to acquire datasets for individual macrophages incubated in the presence of 20 μM nilotinib for 8 hours. Four-component regression modelling extracted % component signals on the per-pixel basis with the pseudo-color ternary scale indicating the relative signal contribution from endogenous biomolecules; the % drug signal was plotted on the z-axis so that the biological color intensity was contingent on signal contribution: accordingly fading to black as the drug's signal contribution increased (Figure 3-5A). On the x-y plane, Raman imaging enabled clear distinction between nucleus and cytoplasm and revealed the presence of lipid-rich regions, presumably lamellar bodies, throughout the cytoplasm (Figure 3-5B). Translation of nilotinib signals to relative mass (wt/wt) and subsequent generation of 3D surface plots revealed distinct cytoplasmic inclusions, each approximately 2-3 microns in diameter and consisting of 30-65% nilotinib (wt/wt) in each of the specified regions (Figure 3-5C). Nilotinib was below its limit of quantitation (3.5% wt/wt) for most pixels of the cell image. Extraction of average spectra from indicated regions of interest allowed for clear visual matching of the major signal-contributing components throughout different regions of the cell (Figure 3-5D). Considering the physical dimensions of the confocal voxel and the resolution of these images, our results strongly suggest that nilotinib is phase separating and potentially precipitating intracellularly, presumably from within the acidic lysosomal

compartments also known to accumulate lipids. Perhaps this explains why nilotinib self-aggregates were observed in close proximity to lipid-rich cytoplasmic regions.(49)

We then characterized the intracellular distribution patterns of chloroquine and etravirine accumulation in alveolar macrophages to show feasibility for quantitative chemical imaging of other compounds. Single-cell Raman images were acquired for cells from each treatment group and the datasets were algorithmically processed and interpreted using four-component regression modelling with respective drug reference spectra; the 3D pseudo-color scale was applied to each pixel of the processed datasets with the compound of interest plotted on the z-axis (Figure 3-6, 3-7) to visualize signal contributors. Utilizing stoichiometric calibration curves for chloroquine and etravirine (Figure S-7), the % drug signal was translated to relative mass (% wt/wt) for each pixel of the Raman images and 3D surface plots were generated to reveal the intracellular distribution of each compound. We detected chloroquine throughout the entire cell: nucleus and cytoplasm measured 10-15% (wt/wt), periphery regions of the cell were 15-20%, while the central lipid-rich region measured only 1-3% (Figure 3-6C). Representative spectra were extracted from regions of interest and overlaid to match the Raman signals throughout the cell with those of the reference components and verify spectral contributions from chloroquine (Figure 3-6D). In contrast to chloroquine behavior, etravirine was practically absent from the cellular nucleus (Figure 3-7C). The compound's signal varied throughout the cytoplasm, with many regions showing clear spectral contribution while others, specifically near the cell periphery, yielded drug-free Raman spectra (Figure 3-7D). Note the characteristic etravirine Raman peak at 2224 cm^{-1}, attributed to the compound's dual nitrile groups, was clearly detectable within treated cells.

To the best of our knowledge, this study represents the first report of Raman-based measurements for quantitation of intracellular distribution of small molecule drugs in relation to the endogenous biomolecules of typical eukaryotic cells. Differential distribution behavior is attributable to the physicochemical properties of each drug compound. High logP (>3) of enabled drug partitioning into lipid membranes while the

weakly basic amines of nilotinib and chloroquine also enabled lysosomal ion-trapping accumulation. The low solubility of nilotinib facilitated phase separation and self-aggregation from within the lysosomes, creating a solubility-equilibrium which greatly enhances intracellular accumulation. Our methodology offers a novel approach to quantitatively study intracellular drug accumulation and the corresponding phenotypic changes (i.e., phospholipid accumulation, “foam” cell formation, etc.) that are often associated with drug exposure and accumulation. Our results directly demonstrate the ability to monitor changes in the biochemical composition of alveolar macrophages that occur in response to drug exposure; more importantly, changes in the lipid and/or drug content of these cells have been heavily implicated in the pathogenesis of a multitude of lung injuries (i.e., drug exposure, idiopathic pulmonary fibrosis, etc.) for this cell population which can feasibly be obtained in the clinical setting.

3.6 Conclusions

This study presents the foundation for a robust sample preparation and microanalysis methodology for Raman-based characterization of alveolar macrophages, specifically in the context of intracellular drug accumulation. Herein, we have demonstrated the ability to distinguish subcellular compartments based on chemical composition and identify “foamy” lipid-laden macrophages throughout cell populations; regression modelling coupled with our novel quantitative calibration enabled direct Raman measurements of cellular drug accumulation and intracellular distribution. Although future technological advances will enable faster, more reliable measurements, our proposed methodology will remain relevant. The broader implications and future directions of this work surround the mysterious and poorly understood role of “foamy” lipid-laden macrophages in the pathogenesis of a multitude of diseases such as drug-induced phopsholipidosis and associated organ toxicity, idiopathic pulmonary fibrosis, and aspiration-induced lung injury including acute respiratory distress syndrome.(11, 41, 50) Direct quantitation of total lipid content per cell is the next logical step in method development and will facilitate elucidation of the mysterious interplay between the lipid-

laden macrophage phenotype and health status of the individual, specifically in the context of drug exposure and accumulation. We will analyze many cells throughout many populations; these datasets may then be statistically characterized using straightforward component-component linear correlations, principal component analysis, machine learning methods (such as mixed effects random forests), and predictive linear mixed models. This novel Raman-based cytometric approach will provide compositional profiles on the single-cell basis, thereby enabling the quantitative study of lung injury pathogeneses in a way which has not previously been possible. Since airway and alveolar macrophages are readily accessible in humans, we believe this cell population and our proposed methodology could provide a unique opportunity for the direct study of drug accumulation in patients, thereby enabling personalized therapies in the clinical setting. As humanity moves toward a future fraught with widespread drug use and greater overall exposure to xenobiotic small molecules, there exists an increasing need for the analysis of our absolute (bio)chemical composition in an effort to establish a reliable cytometric baseline profile for the idealized healthy individual.

3.7 Resulting Publications

1. **LaLone V**, Mourao MA, Standiford TJ, Raghavendran K, Shedden K, Stringer KA, Rosania GR. An Expandable Mechanopharmaceutical Device (3): a Versatile Raman Spectral Cytometry Approach to Study the Drug Cargo Capacity of Individual Macrophages. 2019. *Pharmaceutical Research*. Vol 36, Issue 2.

3.8 Acknowledgements

Financial support of NIH R01GM078200 to Gus R. Rosania and University of Michigan M-Cubed to Kathleen A. Stringer, Theodore J. Standiford, and Krishnan Raghavendran. Financial support was also provided by an Upjohn-Valteich award to

GRR. We also thank Ashirvad Varma and Jason M. Albert for insight regarding Matlab data processing scripts.

3.9 Figures

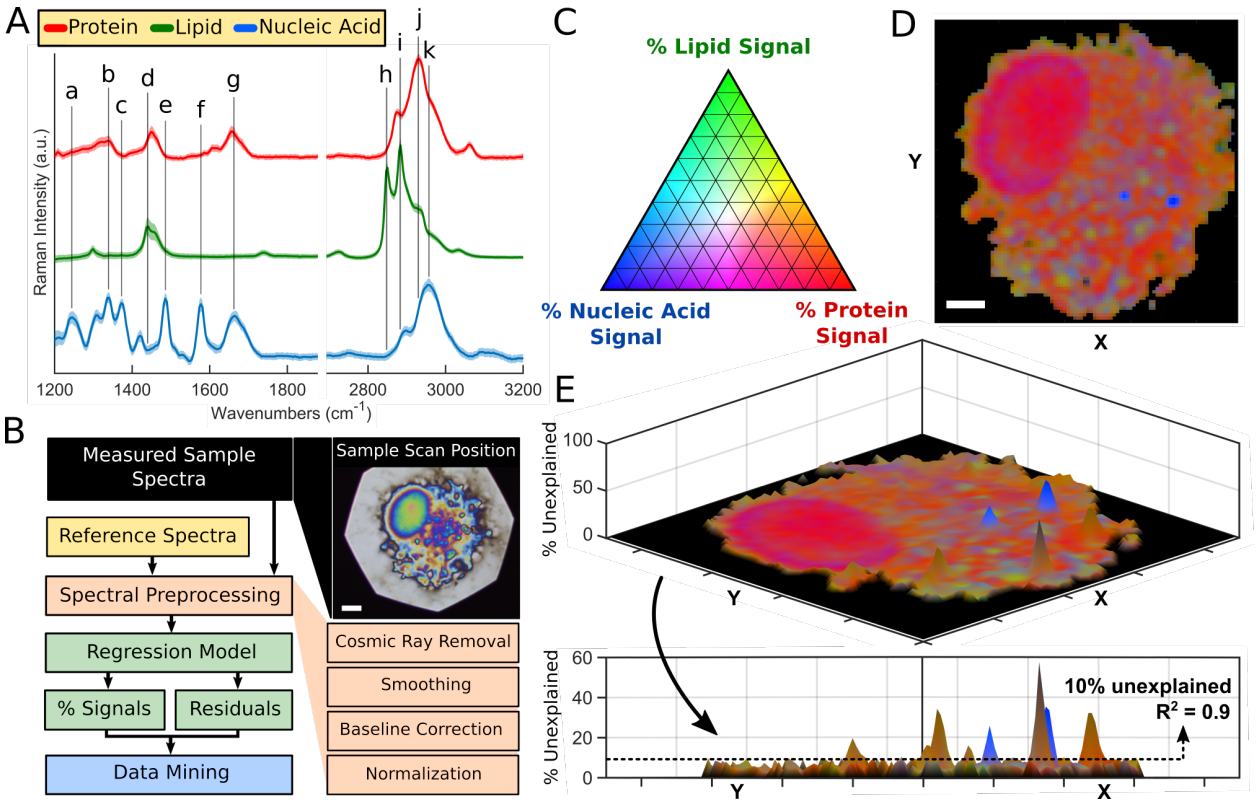

Figure 3-1. Raman imaging reveals spatial distribution and relative abundance of major biochemical components throughout single cells.

(A) Regression model reference spectra with tentative vibrational assignments as indicated (a-k). **(B)** Computational algorithm outline for Raman data processing and interpretation methodology; reflected brightfield image of scan position. Scale bar: 5 µm. **(C)** Pseudo-color ternary scale for visualization of component signals (%) throughout Raman images. **(D)** Compiled Raman image results for a single cell; spectra were processed and interpreted on a per-pixel basis as described in the methods. Scale bar: 5 µm. **(E)** 3D surface plot with unexplained signals (%) on the z-axis; calculated R^2>0.9 for most pixels of cell image (R^2 = 0.9 is equivalent to 10% unexplained).

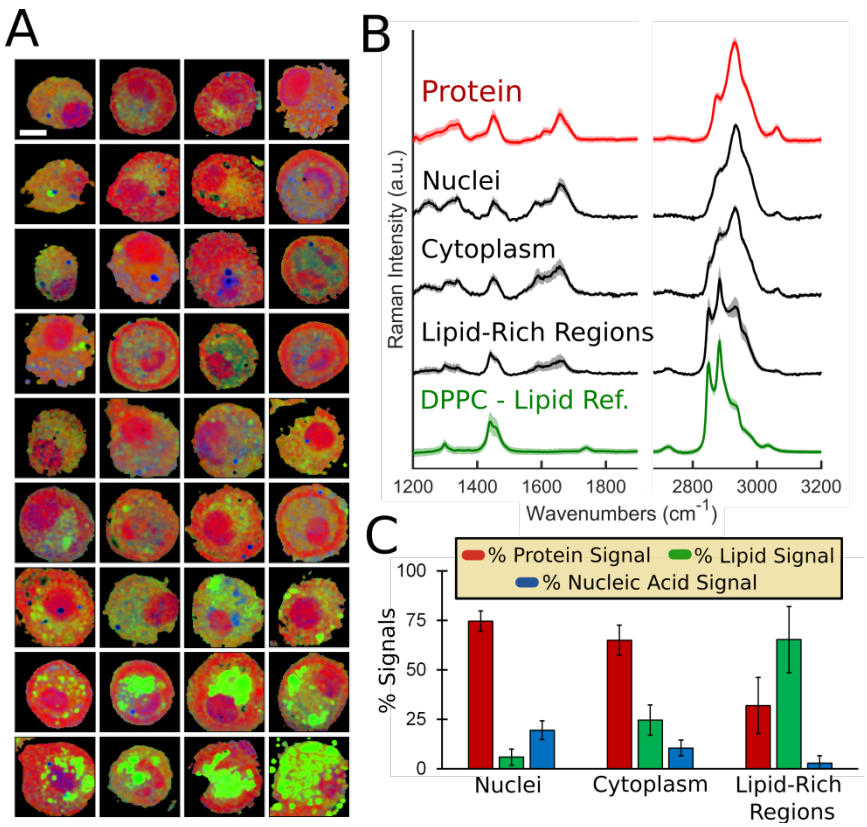

Figure 3-2. Alveolar macrophages exhibit heterogeneous composition on a per-cell basis.

(A) Gallery of 36 cells analyzed with Raman imaging methodology. Scale bar: 10 μm. **(B)** Extracted average spectra (S.D. shown by shadow) from nuclei, cytoplasmic regions, and lipid-rich regions overlaid with protein and lipid (DPPC) reference spectra (n=25 spectra each group). **(C)** Regression modelling results for shown extracted spectra (average ± S.D.).

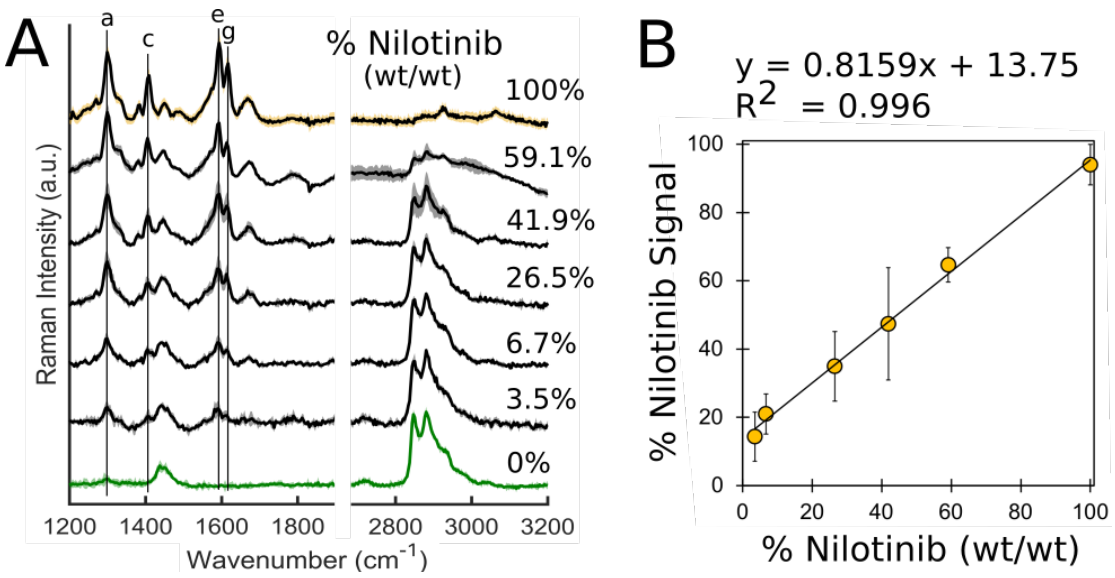

Figure 3-3. Stoichiometric calibration dataset for nilotinib in phospholipid.

(A) Average Raman spectra (S.D. shown by shadow) acquired from area scans of each calibration standard. **(B)** Calibration curve showing strong correlation between % nilotinib signal acquired from regression modelling and actual % nilotinib (wt/wt) present in standard.

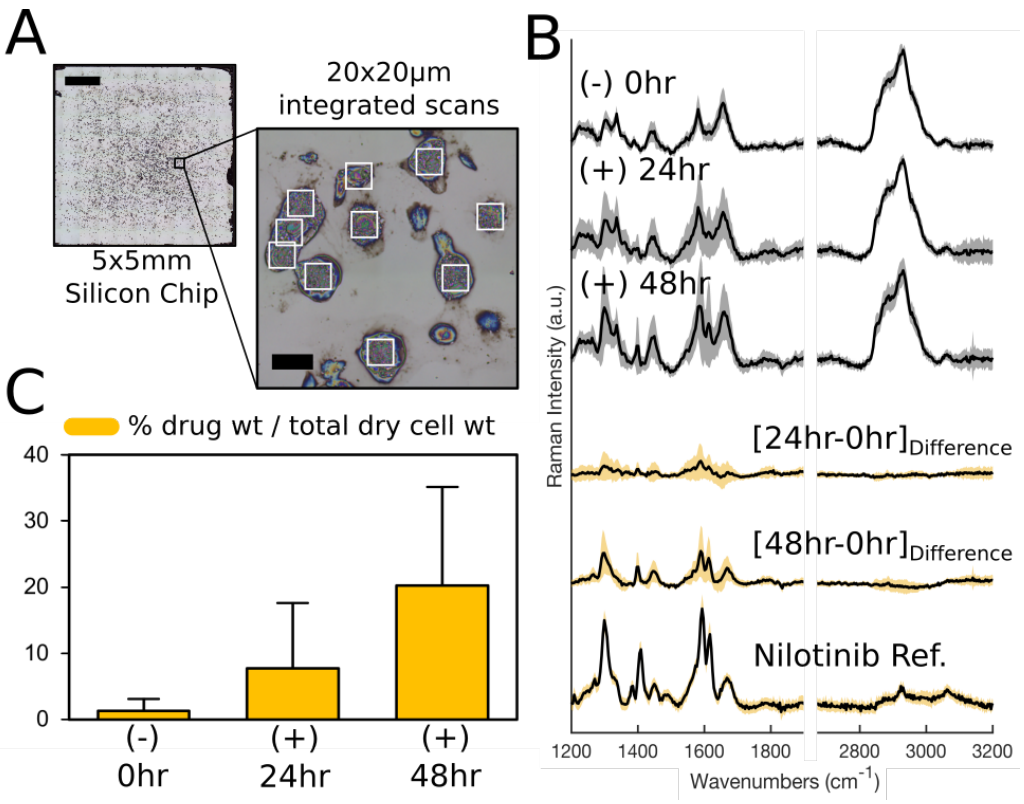

Figure 3-4. Screening cell populations for intracellular nilotinib accumulation.

(A) Representative reflected brightfield image of alveolar macrophages prepared on silicon chip, illustrating the integrated scan areas for a group of cells. Scale bars: 1000 μm and 30 μm. **(B)** The average integrated Raman spectra (S.D. shown by shadow) for each cell population (n=20 cells each group); difference spectra reveal spectral contributions which closely match characteristic peaks of nilotinib reference spectra. **(C)** Quantitative measurements of nilotinib accumulation for each cell population (average ± S.D.).

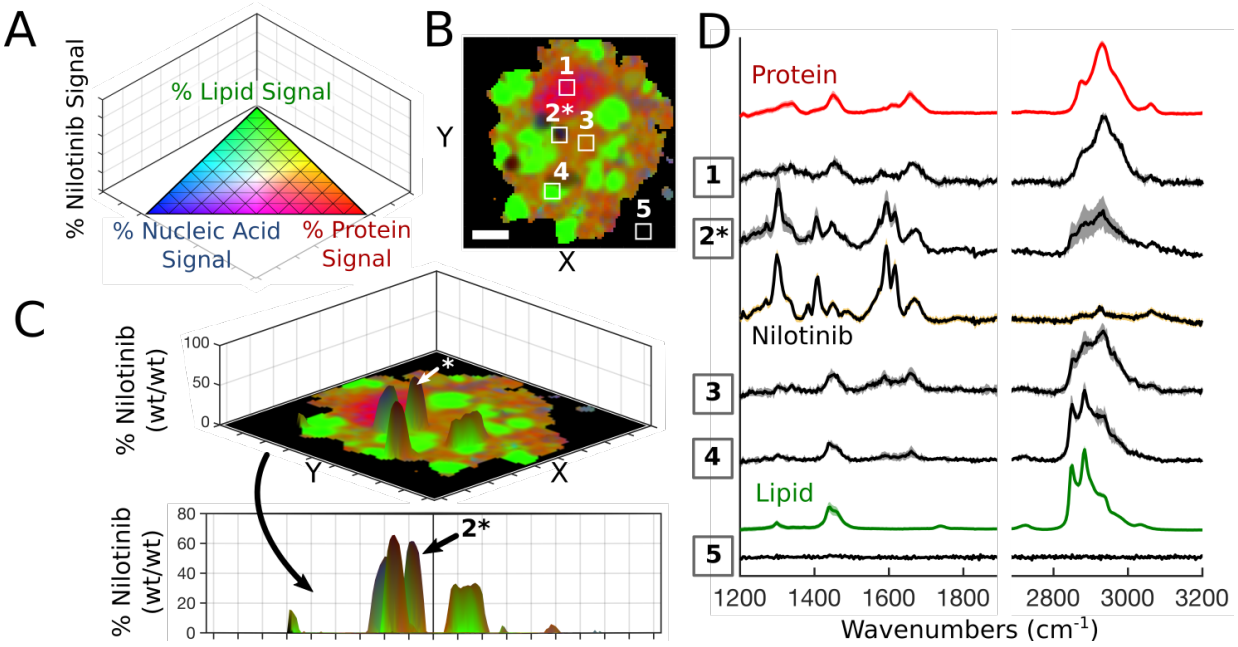

Figure 3-5. Single-cell imaging for intracellular nilotinib distribution analysis.

(A) 3D pseudo-color ternary scale with % nilotinib on z-axis; colors fade to black as % nilotinib approaches 100. **(B)** Compiled Raman image results for a single treated cell. **(C)** The relative nilotinib mass plotted on the z-axis of 3D surface plot. Scale bar: 5 μm. **(D)** Extracted average spectra (S.D. shown by shadow) from indicated regions of interest (panel B) overlaid with relevant reference spectra.

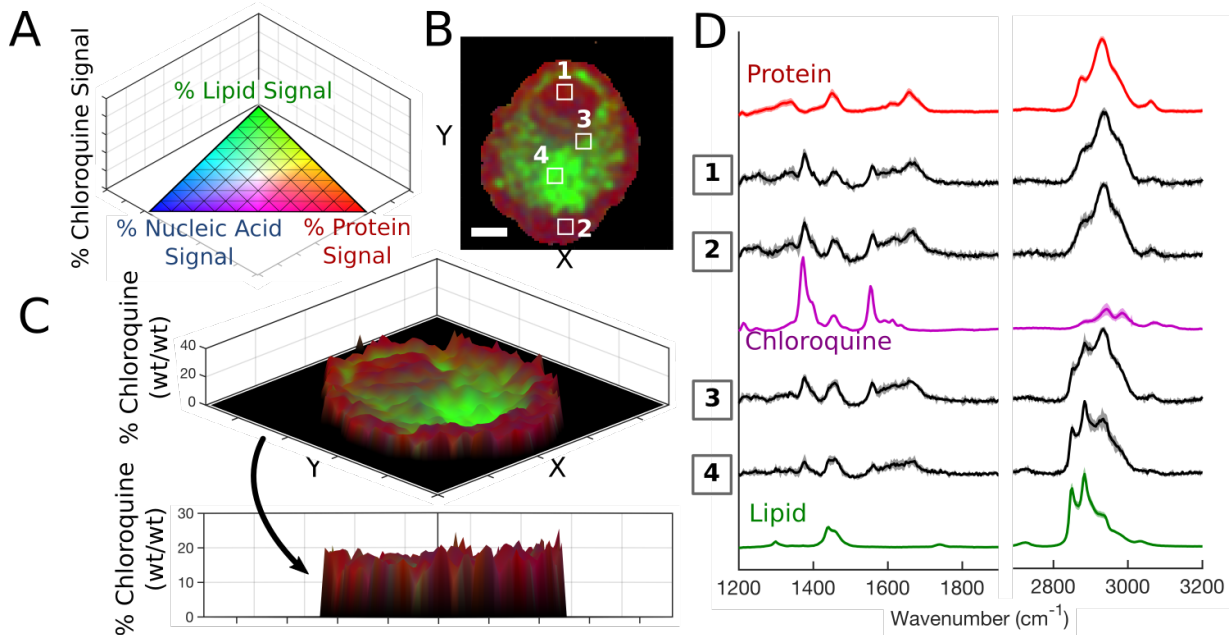

Figure 3-6. Single-cell imaging for intracellular chloroquine distribution analysis.

(A) 3D pseudo-color ternary scale with % chloroquine on z-axis; colors fade to black as % chloroquine approaches 100. **(B)** Compiled Raman image results for a single treated cell. **(C)** The relative chloroquine mass plotted on the z-axis of 3D surface plot. Scale bar: 5 μm. **(D)** Extracted average spectra (S.D. shown by shadow) from indicated regions of interest (panel B) overlaid with relevant reference spectra.

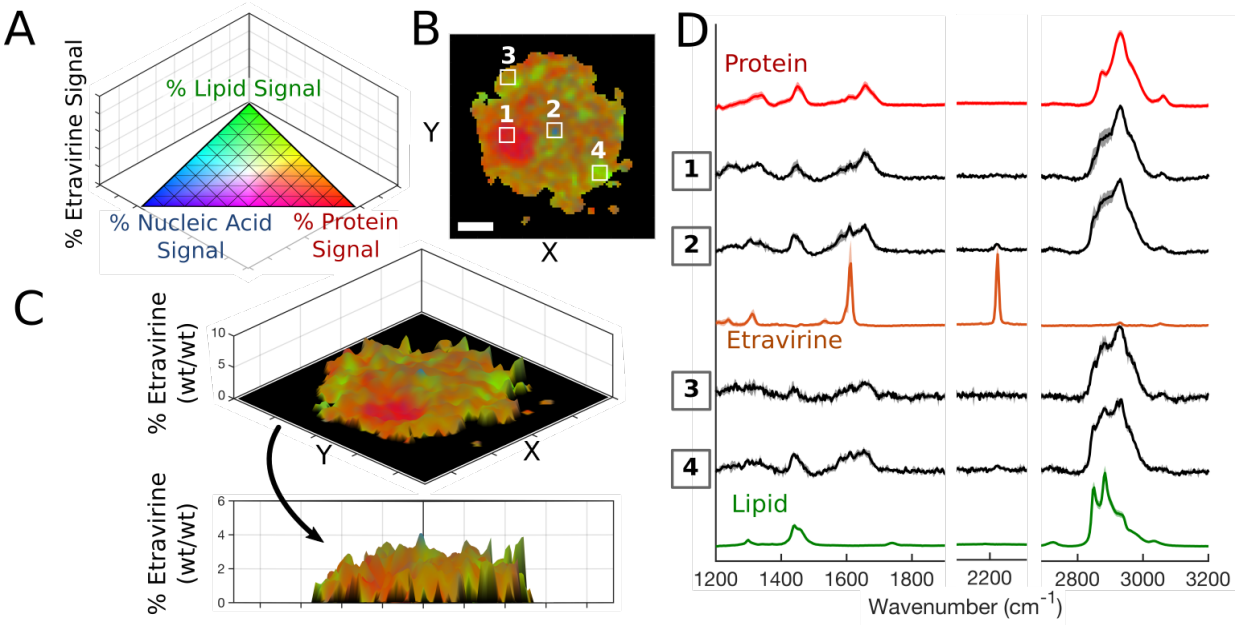

Figure 3-7. Single-cell imaging for intracellular etravirine distribution analysis.

(A) 3D pseudo-color ternary scale with % etravirine on z-axis; colors fade to black as % etravirine approaches 100. **(B)** Compiled Raman image results for a single treated cell. **(C)** The relative etravirine mass was plotted on the z-axis of 3D surface plot. Scale bar: 5 µm. **(D)** Extracted average spectra (S.D. shown by shadow) from indicated regions of interest (panel B) overlaid with relevant reference spectra.

3.10 References

1. Fels AO, Cohn ZA. The alveolar macrophage. Journal of Applied Physiology. 1986;60(2):353-69.

2. Hocking WG, Golde DW. The pulmonary-alveolar macrophage. New England Journal of Medicine. 1979;301(11):580-7.

3. Hussell T, Bell TJ. Alveolar macrophages: plasticity in a tissue-specific context. Nature Reviews Immunology. 2014;14(2):81-93. doi: 10.1038/nri3600.

4. Fu D, Zhou J, Zhu WS, Manley PW, Wang YK, Hood T, et al. Imaging the intracellular distribution of tyrosine kinase inhibitors in living cells with quantitative hyperspectral stimulated Raman scattering. Nature Chemistry. 2014;6(7):614-22.

5. Antonini JM, Reasor MJ. Accumulation of amiodarone and desethylamiodarone by rat alveolar macrophages in cell culture. Biochemical Pharmacology. 1991;42:S151-S6. doi: http://dx.doi.org/10.1016/0006-2952(91)90405-T.

6. Logan R, Kong AC, Krise JP. Time-Dependent Effects of Hydrophobic Amine-Containing Drugs on Lysosome Structure and Biogenesis in Cultured Human Fibroblasts. Journal of Pharmaceutical Sciences. 2014;103(10):3287-96. doi: 10.1002/jps.24087.

7. Kaufmann AM, Krise JP. Lysosomal sequestration of amine-containing drugs: Analysis and therapeutic implications. Journal of Pharmaceutical Sciences. 2007;96(4):729-46. doi: 10.1002/jps.20792.

8. Anderson N, Borlak J. Drug-induced phospholipidosis. FEBS Letters. 2006;580(23):5533-40. doi: 10.1016/j.febslet.2006.08.061.

9. Halliwell WH. Cationic Amphiphilic Drug-Induced Phospholipidosis. Toxicologic Pathology. 1997;25(1):53-60. doi: 10.1177/019262339702500111.

10. Zheng N, Zhang X, Rosania GR. Effect of phospholipidosis on the cellular pharmacokinetics of chloroquine. Journal of Pharmacology and Experimental Therapeutics. 2011;336(3):661-71.

11. Martin WJ, Standing JE. Amiodarone pulmonary toxicity: biochemical evidence for a cellular phospholipidosis in the bronchoalveolar lavage of human subjects. Journal of Pharmacology and Experimental Therapeutics. 1988;244(2):774-9.

12. Rzeczycki P, Yoon GS, Keswani RK, Sud S, Stringer KA, Rosania GR. Detecting ordered small molecule drug aggregates in live macrophages: a multi-parameter microscope image data acquisition and analysis strategy. Biomedical Optics Express. 2017;8(2):860-72. doi: 10.1364/BOE.8.000860.

13. Sadrieh N. The Regulatory Challenges of Drug-Induced Phospholipidosis - Presented in part at the FDA Advisory Committee for Pharmaceutical Science and Clinical Pharmacology meeting. 2010.

14. Garg J, Agrawal N, Marballi A, Agrawal S, Rawat N, Sule S, et al. Amiodarone induced pulmonary toxicity: An unusual response to steroids. The American Journal of Case Reports. 2012;13:62.

15. Yoneda KY, Hardin KA, Gandara DR, Shelton DK. Interstitial Lung Disease Associated with Epidermal Growth Factor Receptor Tyrosine Kinase Inhibitor Therapy in Non–Small-Cell Lung Carcinoma. Clinical Lung Cancer. 2006;8:S31-S5. doi: https://doi.org/10.3816/CLC.2006.s.011.

16. Chatman LA, Morton D, Johnson TO, Anway SD. A Strategy for Risk Management of Drug-Induced Phospholipidosis. Toxicologic Pathology. 2009;37(7):997-1005. doi: doi:10.1177/0192623309352496.

17. Reasor MJ, Hastings KL, Ulrich RG. Drug-induced phospholipidosis: issues and future directions. Expert Opinion on Drug Safety. 2006;5(4):567-83.

18. Reasor MJ, Kacew S. Drug-induced phospholipidosis: are there functional consequences? Experimental Biology and Medicine. 2001;226(9):825-30.

19. Bocklitz TW, Guo S, Ryabchykov O, Vogler N, Popp J. Raman Based Molecular Imaging and Analytics: A Magic Bullet for Biomedical Applications!? Analytical Chemistry. 2016;88(1):133-51. doi: 10.1021/acs.analchem.5b04665.

20. Fu D, Lu F-K, Zhang X, Freudiger C, Pernik DR, Holtom G, et al. Quantitative chemical imaging with multiplex stimulated Raman scattering microscopy. Journal of the American Chemical Society. 2012;134(8):3623-6.

21. Hosokawa M, Ando M, Mukai S, Osada K, Yoshino T, Hamaguchi H-o, et al. In vivo live cell imaging for the quantitative monitoring of lipids by using Raman microspectroscopy. Analytical Chemistry. 2014;86(16):8224-30.

22. Ho S-H, Shimada R, Ren N-Q, Ozawa T. Rapid in vivo lipid/carbohydrate quantification of single microalgal cell by Raman spectral imaging to reveal salinity-induced starch-to-lipid shift. Biotechnology for Biofuels. 2017;10(1):9.

23. Lu F-K, Basu S, Igras V, Hoang MP, Ji M, Fu D, et al. Label-free DNA imaging in vivo with stimulated Raman scattering microscopy. Proceedings of the National Academy of Sciences. 2015;112(37):11624-9.

24. Konorov SO, Schulze HG, Atkins CG, Piret JM, Aparicio SA, Turner RF, et al. Absolute quantification of intracellular glycogen content in human embryonic stem cells with Raman microspectroscopy. Analytical Chemistry. 2011;83(16):6254-8.

25. Stiebing C, Matthäus C, Krafft C, Keller A-A, Weber K, Lorkowski S, et al. Complexity of fatty acid distribution inside human macrophages on single cell level using Raman micro-spectroscopy. Analytical and Bioanalytical Chemistry. 2014;406(27):7037-46.

26. Galler K, Requardt RP, Glaser U, Markwart R, Bocklitz T, Bauer M, et al. Single cell analysis in native tissue: Quantification of the retinoid content of hepatic stellate cells. Scientific Reports. 2016;6.

27. El-Mashtoly SF, Petersen D, Yosef HK, Mosig A, Reinacher-Schick A, Kötting C, et al. Label-free imaging of drug distribution and metabolism in colon cancer cells by Raman microscopy. The Analyst. 2014;139(5):1155-61. doi: 10.1039/c3an01993d.

28. Konrad M, Johanna N, Ulrich S, Nils MN, A. SD, Martina H. Label-Free Imaging of Metal–Carbonyl Complexes in Live Cells by Raman Microspectroscopy. Angewandte Chemie International Edition. 2010;49(19):3310-2. doi: doi:10.1002/anie.201000097.

29. Gonçalves R, Mosser DM. The Isolation and Characterization of Murine Macrophages. Current Protocols in Immunology. 2015;111(1):14.1.1-.1.6. doi: doi:10.1002/0471142735.im1401s111.

30. Ong YH, Lim M, Liu Q. Comparison of principal component analysis and biochemical component analysis in Raman spectroscopy for the discrimination of apoptosis and necrosis in K562 leukemia cells. Optics Express. 2012;20(20):22158-71.

31. Bergholt MS, Zheng W, Lin K, Ho KY, Teh M, Yeoh KG, et al. Characterizing variability in in vivo Raman spectra of different anatomical locations in the upper gastrointestinal tract toward cancer detection. Journal of Biomedical Optics. 2011;16(3):037003--10.

32. Morita S-i, Takanezawa S, Hiroshima M, Mitsui T, Ozaki Y, Sako Y. Raman and Autofluorescence Spectrum Dynamics along the HRG-Induced Differentiation Pathway of MCF-7 Cells. Biophysical Journal. 2014;107(10):2221-9. doi: https://doi.org/10.1016/j.bpj.2014.10.002.

33. Ichimura T, Chiu L-d, Fujita K, Machiyama H, Kawata S, Watanabe TM, et al. Visualizing the appearance and disappearance of the attractor of differentiation using Raman spectral imaging. Scientific Reports. 2015;5:11358. doi: 10.1038/srep11358

34. Kuzmin AN, Pliss A, Prasad PN. Changes in Biomolecular Profile in a Single Nucleolus during Cell Fixation. Analytical Chemistry. 2014;86(21):10909-16. doi: 10.1021/ac503172b.

35. O'Malley J, Kumar R, Kuzmin AN, Pliss A, Yadav N, Balachandar S, et al. Lipid quantification by Raman microspectroscopy as a potential biomarker in prostate cancer. Cancer Letters. 2017;397:52-60. doi: https://doi.org/10.1016/j.canlet.2017.03.025.

36. Kuzmin AN, Pliss A, Kachynski AV. Biomolecular component analysis of cultured cell nucleoli by Raman microspectrometry. Journal of Raman Spectroscopy. 2013;44(2):198-204. doi: doi:10.1002/jrs.4173.

37. Kuzmin AN, Levchenko SM, Pliss A, Qu J, Prasad PN. Molecular profiling of single organelles for quantitative analysis of cellular heterogeneity. Scientific Reports. 2017;7(1):6512. doi: 10.1038/s41598-017-06936-z.

38. Kuzmin A, Pliss A, Prasad P. Ramanomics: New Omics Disciplines Using Micro Raman Spectrometry with Biomolecular Component Analysis for Molecular Profiling of Biological Structures. Biosensors. 2017;7(4):52.

39. Hamada K, Fujita K, Smith NI, Kobayashi M, Inouye Y, Kawata S, editors. Raman microscopy for dynamic molecular imaging of living cells. SPIE. 2008.

40. Okada M, Smith NI, Palonpon AF, Endo H, Kawata S, Sodeoka M, et al. Label-free Raman observation of cytochrome c dynamics during apoptosis. Proceedings of the National Academy of Sciences. 2012;109(1):28-32. doi: 10.1073/pnas.1107524108.

41. Romero F, Shah D, Duong M, Penn RB, Fessler MB, Madenspacher J, et al. A Pneumocyte–Macrophage Paracrine Lipid Axis Drives the Lung toward Fibrosis. American Journal of Respiratory Cell and Molecular Biology. 2015;53(1):74-86. doi: 10.1165/rcmb.2014-0343OC.

42. Farrera C, Fadeel B. Macrophage Clearance of Neutrophil Extracellular Traps Is a Silent Process. The Journal of Immunology. 2013. doi: 10.4049/jimmunol.1300436.

43. Goerke J. Pulmonary surfactant: functions and molecular composition. Biochimica et Biophysica Acta (BBA) - Molecular Basis of Disease. 1998;1408(2):79-89. doi: https://doi.org/10.1016/S0925-4439(98)00060-X.

44. Movasaghi Z, Rehman S, Rehman IU. Raman Spectroscopy of Biological Tissues. Applied Spectroscopy Reviews. 2007;42(5):493-541. doi: 10.1080/05704920701551530.

45. Lodish H, Berk A, Zipursky SL, Matsudaira P, Baltimore D, Darnell J. Molecular cell biology 4th edition. National Center for Biotechnology Information Bookshelf. 2000.

46. Ter Heine R, Mulder JW, Van Gorp ECM, Wagenaar JFP, Beijnen JH, Huitema ADR. Intracellular and plasma steady-state pharmacokinetics of raltegravir, darunavir, etravirine and ritonavir in heavily pre-treated HIV-infected patients. British Journal of Clinical Pharmacology. 2010;69(5):475-83. doi: 10.1111/j.1365-2125.2010.03634.x.

47. Schie IW, Kiselev R, Krafft C, Popp J. Rapid acquisition of mean Raman spectra of eukaryotic cells for a robust single cell classification. Analyst. 2016;141(23):6387-95.

48. Baik J, Stringer KA, Mane G, Rosania GR. Multiscale distribution and bioaccumulation analysis of clofazimine reveals a massive immune system-mediated xenobiotic sequestration response. Antimicrobial Agents and Chemotherapy. 2013;57(3):1218-30.

49. van Manen H-J, Kraan YM, Roos D, Otto C. Single-cell Raman and fluorescence microscopy reveal the association of lipid bodies with phagosomes in leukocytes. Proceedings of the National Academy of Sciences of the United States of America. 2005;102(29):10159-64.

CHAPTER 4

Inkjet-Printed Micro-Calibration Standards for Ultraquantitative Raman Spectral Cytometry

4.1 Relevance to Thesis

To address specific aim 2 of my thesis research and develop a micro-Raman-based analytical methodology to simultaneously measure the absolute, or total amount, of each major biomolecular component (or sequestered xenobiotic) present inside a single eukaryotic cell, I invented and developed cell-sized micro-calibration standards. Using an inkjet materials printer, I was able to successfully deposit 10pL droplets of aqueous ink formulations into microarrays across the surface of silicon chips: conveniently the same sample substrate used for cell sample preparation. The major innovative aspect of this work stemmed from collaborations with a multitude of interdisciplinary scientists and engineers. Formulation of protein inks were relatively facile, as my model protein (albumin) dissolved readily into water. Since lipids are the second most abundant biomolecular species present in typical eukaryotic cells, there was a need to formulate lipids and protein together in known ratios before inkjet printing these substances into micro-calibration standards. To overcome the low solubility barrier of lipids in water, I utilized synthetic high-density lipoprotein nanodiscs (HDLs), which were synthesized in collaboration with pharmaceutical formulation scientists.

These HDL nanoparticles exhibited a particle size of approximately 10nm, conveniently similar in size to a single albumin molecule, and therefore were essentially “dissolved”, for all practical purposes. Furthermore, HDLs allowed lipids to be mixed homogeneously with albumin in water, ultimately enabling the inkjet printing of micro-

calibration standards that have the same relative and absolute mass as actual biological cells (e.g., 500pg of protein and 150pg of lipid together in a single cell). When the water evaporates from each droplet, the non-volatile components are deposited as thin dry dispersions on the surface of the silicon chip (for clarity, a10pL droplet of a 100pg/pL albumin solution contains 1000pg of total protein once water evaporates), thereby mimicking the sample preparation of actual eukaryotic cells that we are ultimately seeking to measure. Collaboration with materials science engineers allowed us to characterize the actual dimensions of the cell sample preparation and the micro-calibration standards, and ultimately show that they are on the same size scale.

Since I was able to fabricate cell-sized calibration standards of known mass and composition, these standards could then be utilized to quantitatively-calibrate the Raman microscope for single-cell analysis. As previously introduced in Chapter 3 of my thesis, the integrated area scan acquisition methodology was utilized and herein shown to be a valid approach for the ultraquantitative measurements proposed; this approach involves the excitation laser scanning across an area of interest (i.e., a single cell or a single calibration standard) and collecting the total, or integrated, Raman signal. Since this signal was collected over the entirety of the sample, it was assumed to be representative, both qualitatively and quantitatively, of that sample's molecular composition. By fabricating and analyzing a range of micro-calibration standards with various relative compositions, I was able to verify the linearity of acquired Raman signals in relation to absolute, or total, mass present within a given area scan (i.e., as the total mass within a scanned area increases, the acquired Raman signals increase linearly). In this way, the signal-to-mass ratio (i.e., CCD counts / picogram material) for a multitude of molecular components of interest could be experimentally determined for a given set of acquisition parameters on a given instrument. Conveniently, this theory harmonized perfectly with the current working statistical model, non-negative linear least squares regression, allowing to simultaneously solve for the picograms of each major biomolecular component of interest present within a single cell by deconvoluting the integrated spectrum acquired across the entirety of said cell using quantitatively-calibrated reference spectra.

The invention of the inkjet-printed micro-calibration standards and application presented herein for ultraquantitative Raman spectral cytometry directly addresses specific aim 2 of my thesis and simultaneously enables quantitative cytometric phenotyping based on chemical composition the likes of which has never been reported before. In this chapter we show proof-of-concept for cell analysis using human skin fibroblasts (in the context of Niemann-Pick type C cholesterol/lipid storage disorder) and pig alveolar macrophages (in the context of amiodarone-induced phospholipidosis). The application of our mimic cell microarrays for quantitative calibration of single-cell measurements is not limited to Raman microscopy, as demonstrated herein; this technology could prove useful for quantitation in other single-cell techniques such as laser desorption and/or ionization mass spectrometry. The findings from this study represent a significant advancement in the cytometry field and open the doors of quantitative scientific perception to the entirety of the intracellular biomolecular matrix without artificial chemical tags, providing an approach by which scientists and clinicians may holistically explore the unadulterated biochemical realm within single cells: the building blocks of life.

4.2 Abstract

Herein we report the development of a cytometric analysis platform for measuring the contents of individual cells in absolute (picogram) scales; this study represents the first report of Raman-based quantitation of the absolute mass – or the total amount – of multiple endogenous biomolecules within single-cells. To enable ultraquantitative calibration, we engineered single-cell-sized micro-calibration standards of known composition by inkjet-printer deposition of biomolecular components in microarrays across the surface of silicon chips. We demonstrate clinical feasibility by characterizing the compositional phenotype of human skin fibroblast and porcine alveolar macrophage cell populations in the respective contexts of Niemann-Pick disease and drug-induced phospholipidosis: two types of lipid storage disorders. We envision this microanalytical platform as the foundation for many future biomedical applications, ranging from

diagnostic assays to pathological analysis to advanced pharmaco/toxicokinetic research studies.

4.3 Introduction

Single-cell analytical technologies have transformed modern biomedical sciences by providing researchers an avenue through which to explore subcellular phenomena and characterize cell population heterogeneity. Over the past decade these techniques have seen rapid development due to rising awareness of the significance of cell population diversity and the pathophysiological consequences of cell subpopulations that play crucial roles in different disease states.(1) Lipid storage diseases, either inherited (e.g., Niemann-Pick disease) or acquired (e.g., drug-induced phospholipidosis, atherosclerosis), manifest as the inappropriate accumulation of lipids and other small molecules within various cells of the body; many of these disorders are poorly understood and notoriously challenging to diagnose.(2-6) As such, a cytometric approach to quantitatively measure the absolute amount of cellular material and bioaccumulating contents – herein referred to as “ultraquantitation” – would provide valuable insight into the mechanisms of storage disorder pathogenesis at the single-cell level where it occurs, with foreseeable application as a diagnostic tool in the clinical setting.

Since the first reported Raman microanalysis of eukaryotic cells in 1990, technological innovation has facilitated the evolution of Raman microscopes into powerful analytical tools with incredible potential in the biomedical sciences.(7-13) Raman microscopy enables the chemical analysis of single cells with submicron resolution.(14-18) In short, an excitation laser induces molecular vibrations in the sample which scatter light across a multitude of wavelengths; the scattered lights are collected and directed across a Charge-Coupled Device (CCD) and the number of photons at each wavelength are converted to electrical signals (i.e., CCD counts), generating Raman spectra which serve as molecular fingerprints that can be interpreted to determine the chemical composition of the sample. Although there are a multitude of reliable reports on Raman-

based “absolute” quantitation at the single-cell level, these studies utilize approaches which are limited to estimates of single-cell content from population measurements (e.g., 0.1mg protein/10^6 cells equates to 100pg protein/cell)(19, 20) or to absolute concentration measurements of multiple biomolecules within specific subcellular compartments (e.g., mg/mL protein, lipid, RNA, and DNA within mitochondria, nucleus, etc.).(18, 21) While these studies report on “absolute” measurements in single-cells, the population average and intracellular concentration measurements are inadequate to answer our long-term research question: how much total material is present in each individual cell? Is there a single cell population or multiple, distinct cell populations in the sample? While population average and subcellular concentration measurements certainly provide valuable insight, there are a number of cytometric phenomena that could go unnoticed because of the significant heterogeneity of cell populations. As it specifically relates to the phenotypic analysis of cellular lipid content, the major advantages of our ultraquantitative absolute measurements of total cellular composition are the ability to quantitatively identify “foamy” lipid-laden outlier cells within a population (whereas the influence of lipid-laden outlier cells is diminished through population average measurements of lipid content) and to quantitatively characterize the distribution of compositional phenotypes throughout a cell population (i.e., two cells might have equivalent intracellular concentrations of lipid but one is much bigger and therefore carries a greater total quantity of cargo). We are herein expanding upon the quantitative aspects of previous approaches such as these to make absolute measurements of the total amount of biomolecular material present inside individual eukaryotic cells.

Although the Raman bioanalytical field has blossomed over the past three decades, with substantial advancements in overall instrument performance and a multitude of commercial instruments now available on the market, a standardized quantitative calibration technology for the absolute simultaneous measurement of biomolecular contents in single cells has yet to be firmly established; as such, we herein propose a Raman analytical methodology for the simultaneous measurement of the major biomolecular components present within single cells using a novel quantitative calibration

technology.(22) Our methodology's theoretical foundation was inspired by two separate Raman-based studies of eukaryotic cells: the first measured the absolute amount of a single analyte, glycogen, inside human embryonic stem cells using thin layers of pure glycogen as calibration standards while the second verified integrated area scans over the entirety of individual cells as the optimal Raman acquisition parameters for robust single cell classification.(23, 24) Harmonizing the theoretical concepts from these two studies elucidated the feasibility of simultaneous absolute quantitation of each major biomolecular component within typical eukaryotic cells, namely protein, lipid, carbohydrate, and nucleic acid.

Through extensive multidisciplinary collaboration, we fabricated cell-sized micro-calibration standards of known mass and composition using inkjet printing technology with custom biomolecular ink formulations. We utilized synthetic high-density lipoprotein nanodiscs (HDLs) to overcome solubility barrier and dissolve known amounts of phospholipid in aqueous ink formulations. Using an inkjet materials printer, 10pL ink droplets were deposited in microarray patterns across the surface of silicon chips; the water from the aqueous-based ink formulations quickly evaporated, depositing the non-volatile biomolecular components as thin dry dispersions across the surface of silicon chips; for example, a 10pL droplet of a 100mg/mL albumin ink solution would contain in total 1000pg of protein that would be deposited as water evaporated. Using the established method for cell sample preparation,(16) eukaryotic cells were allowed to adhere to the surface of silicon chips before brief washing and air-drying to form thin dispersions on the surface of silicon chips. The thin-film interference of light passing through the sample and reflecting off the silicon surface led to a rainbow-colored appearance of cell samples and suggested that the height of dry cell dispersions was typically less than 1μm. To confirm, we measured the topography of air-dried cell dispersions on silicon using atomic force microscopy. Similarly, we confirmed that the height and area of the inkjet-printed, micro-calibration standards was similar to the height and area of the cell samples of interest.

For the acquisition of Raman data, we employed a continuous area scan methodology where the excitation laser scans across the entirety of a given sample, collecting individual spectra at each pixel of the analyzed area; because the height of the 532nm laser confocal voxel (~1.5μm) exceeded the height of our micro-calibration and cell samples, the total mass of each sample could be analyzed in a single-plane Raman area scan. When analyzed with equivalent acquisition parameters, Raman data acquired from the biomolecular micro-calibration standards could be used to quantitatively interpret Raman data acquired from cells of interest. Because each micro-calibration standard contained a known total mass of material, the total (or "integrated") Raman signal acquired from that standard can be used to define the signal-to-mass ratio (i.e., CCD counts/picogram) for the acquisition methodology. Using linear combination modelling with quantitatively-calibrated pure component reference spectra, the integrated Raman spectrum from a single cell (CCD counts) could thereby be deconvoluted into the total mass of each component of interest present within that cell (picograms of protein, lipid, nucleic acid, etc.).

Through extensive multidisciplinary collaboration, we fabricated cell-sized micro-calibration standards of known absolute mass and biomolecular composition; using equivalent acquisition parameters, integrated Raman area scan data acquired from the micro-calibration standards was used to quantitatively interpret Raman data acquired from cells of interest. This approach enabled quantitative phenotypic characterization of cell populations – applicable to multiple cell types and species – on the basis of absolute biomolecular composition, specifically measuring the total amounts of protein, lipid, nucleic acid and carbohydrate present inside individual eukaryotic cells. It should be noted that the proposed calibration technique is currently limited to dried cells because the micro-calibration standards are fabricated as dry dispersions, though rehydration has not yet been tested. Conveniently, this apparent methodological shortcoming actually harmonizes well with our long-term goal of clinical sample analysis where cell samples are commonly prepared as dry dispersions on substrates via cytocentrifugation. Ultimately, the development of robust quantitative micro-calibration standards for Raman

instruments will facilitate interlaboratory comparisons of Raman-based cell analyses and contribute to the harmonious advancement of Ramanomics disciplines at the global level.(14) We have termed our novel approach ultraquantitative Raman spectral cytometry and believe it represents a significant advancement in the field of Raman-based biomedical applications.

4.4 Materials and Methods

4.4.1 Materials

Silicon chips (5x5mm; Ted Pella, Inc., Redding, CA) served as substrates for all Raman measurements performed herein. The following reagents were used to generate the reference spectra library: bovine albumin (MP Biomedicals; Solon, OH), 1,2-dipalmitoyl-sn-glycero-3-phosphocholine (DPPC; Avanti Polar Lipids, Inc., Alabaster, AL), 1,2-dioleoyl-sn¬-glycero-3-phsophocholine (DOPC; Avanti Polar Lipids, Inc., Alabaster, AL), DNA (from salmon sperm; AmResco Inc., Solon, OH), and cholesterol (ovine; Avanti Polar Lipid, Inc., Alabaster, AL). Polysorbate 20 (Bio-Rad Laboratories, Inc., Hercules, CA) was utilized as surfactant in diluent for albumin ink formulations. The following reagents were used to formulate HDL nanoparticle suspensions: 22A (PVLDLFRELLNELLEALKQKLK) was synthesized by Genscript (Piscataway, NJ), using solid-phase Fmoc (9-fluorenylmethyl carbamate) chemistry and purified with reverse phase chromatography (>95 % pure). 1,2-dipalmitoyl-sn-glycero-3-phosphocholine (DPPC) was purchased from NOF America Corporation (White Plains, NY) and cholesterol was obtained from Sigma-Aldrich (St. Louis, MO).

4.4.2 Preparation and Characterization of Synthetic High-Density Lipoproteins

Synthetic high-density lipoproteins (HDL) composed of 22A peptide and DPPC was prepared by a co-lyophilization procedure (Di Bartolo et al., 2011). Briefly, peptide and phospholipid were dissolved in glacial acetic acid, mixed at 1:2 wt/wt ratio, and

lyophilized overnight. The powder was rehydrated with water to make 30 mg/mL (based on peptide concentration) HDL and thermocycled between 55° C (10 min) and room temperature (10 min) thrice to facilitate HDL formation. HDL containing cholesterol was prepared using a thin film method (Tang et al., 2017). DPPC and cholesterol (10:1 wt/wt) were dissolved in chloroform and 22A was dissolved in water/methanol (3:4 v/v) solvents. Then, lipid and peptide solutions were combined at 1:2 (wt/wt) 22A-to-DPPC ratio, sonicated for 1 min at room temperature, and solvents evaporated under the stream of N2 gas to form a thin film. Lastly, the film was rehydrated in water for a final 90 mg/mL concentration (60mg/mL lipid and 30mg/mL peptide 22A) and then probe sonicated for 2 min at 4W with 10 sec pulses to form HDL-containing cholesterol. The resulting HDL complexes were diluted to 1 mg/mL (based on peptide concentration) with water and analyzed by gel permeation chromatography (GPC) for purity using 7.8 mm x 30 cm Tosoh TSK gel G3000SWxl column (Tosoh Bioscience, King of Prussia, PA) with 1 mL/min flow rate (PBS pH 7.4). Free peptide and HDL peaks were detected at 220 nm. The HDL hydrodynamic diameters were determined in water at 1 mg/mL by dynamic light scattering (DLS) using a Zetasizer Nano ZSP, Malvern Instruments (Westborough, MA). The volume intensity average values (± SD) were reported. Nanoparticle size and morphology were verified using transmission electron microscopy.

4.4.3 Aqueous Printer Ink Formulations

All fluidic printer inks were formulated as aqueous solutions and/or nanoparticulate suspensions in HPLC-grade water. To ensure accurate and precise performance of different ink solutions, each was formulated to achieve the following fluid property specifications: viscosity within the ranges of 0.010 to 0.012 Pa*s at 25^{o}C, surface tension within the range of 28-33 mN/m, a maximum suspended particle size of 200nm or less, and the absence of dissolved gas. A stock solution of 100mg/mL albumin was formulated in diluent (0.25% polysorbate 20 in HPLC-grade water) to reduce surface tension between 28 and 33 dynes/cm and achieve viscosity between 0.010 and 0.012 Pa*s; in this way, a 10pL drop would theoretically contain 1000pg of protein with negligible surfactant content

(<0.5% wt/wt). Additional albumin inks were formulated by serial dilutions of albumin stock with diluent to generate 500pg, 250pg, and 100pg protein micro-calibration standards. By formulating aqueous printer inks with (synthetic) high density lipoprotein particles (stock solution containing 90mg/mL HDL in water), we were able to use the inkjet printer to fabricate calibration dot microarrays with known amount of total phospholipid present. Multi-component calibration mixtures were created by stoichiometric mixtures of albumin stock solution with HDL or HDL+cholesterol stock solutions; by varying the concentrations of protein and HDL particles and incorporating cholesterol, we inkjet-printed mixed composition micro-calibration standards of three unique compositions: 1) 350pg protein/peptide, 200pg lipids, and 20pg cholesterol; 2) 575pg protein/peptide, 150pg lipids, and 0pg cholesterol; 3) 550pg protein/peptide, 100pg lipids, and 10pg cholesterol.

4.4.4 Piezoelectric Inkjet Printing of Microarrays

Approximately 1.5mL of each fluidic printer ink was first de-gassed via sonication and filtered through a 0.22μm filter directly into separate printer cartridges (10pL drop volumes). A Dimatix MP-2831 piezoelectric inkjet materials printer (FUJIFILM Dimatix, Inc., Santa Clara, CA) equipped with specific cartridge fluid modules and piezoelectric inkjet nozzles, was used to deposit droplets of 10pL volumes with tailor-made ink formulations in a defined array pattern across the surface of silicon chips. Printing parameters, specifically the piezoelectric jetting waveform shown in Figure 4-1b and the nozzle temperature set to 35^{o}C, were used to enable successful deposition of each fluid across the surface of the silicon chips as microarrays. We printed these droplets on to 5mm x 5mm silicon wafer chips that are well-suited for Raman spectral imaging, as they possess a low and constant background signal that can be subtracted out from the cellular signal. The droplets were air dried directly on the chip in approximately 1 minute with a substrate temperature of 40^{o}C and atmospheric pressure (1 atm), and were visible as brightly colored spots under reflected light illumination.

4.4.5 Atomic Force Microscopy

Topographical images of micro-calibration standards and fibroblast preparations on silicon chips were obtained using a Bruker Innova AFM with TESPA probes in tapping mode to measure the height across the area of each sample of interest. The data in each image was plane-fit to establish a level background of the silicon substrate and height data at each image pixel was used to generate pseudo-color topographical maps for each sample analyzed using NanoScope Analysis v1.6.

4.4.6 Raman Measurements

All Raman measurements were recorded using a WITec alpha300 R Confocal Raman Imaging Microscope (Ulm, Germany) equipped with a 50X air objective lens (Zeiss EC EPIPLAN, N.A.=0.75) and 532nm solid-state excitation laser (0-55mW, tunable intensity range with attenuator dial) coupled to a CCD detector via a 100μm diameter multi-mode fiber-optic cable. Raman area scans were performed by first locating the optimal laser focal plane for sample excitation (yielding the greatest signal intensity from 2800-3100cm-1 for biological materials) then continuously acquiring data across that area of interest by scanning in raster pattern, presumably exciting the entirety of the sample material present. The excitation laser intensity was kept constant between sample scans. Fibroblast cell datasets and corresponding calibration standard datasets were acquired via 60x60μm area scans and step-size of 1μm (3600 spectra/pixels) with an integration time of 0.05 sec per pixel, for an acquisition time of 3 min per cell (or micro-calibration standard). Alveolar macrophage cell datasets and corresponding calibration datasets were acquired via 25x25μm area scans with a step-size of 1μm (625 spectra/pixels) with an integration time of 0.1 sec per pixel, for an acquisition time of 1 min per cell (or micro-calibration standard). By continuously acquiring Raman signal data in a raster pattern across the scan area at the optimal focal plane, hyperspectral Raman datasets were generated which were presumably representative of the entirety of each sample that was

analyzed. 40 fibroblast cells from each group (WT and NPC) and 35 macrophages from each group (control and drug-treated) were analyzed herein; each cell was scanned once.

4.4.7 Spectral Preprocessing and Hyperspectral Image Processing

All acquired Raman spectra underwent equivalent preprocessing procedures; cosmic ray removal (filter size: 4; dynamic factor: 4.6) is performed on a per-pixel basis in WITec Project FOUR software before data is exported to Matlab® (Mathworks, Inc., Natick, MA) where remainder of preprocessing is executed via an algorithm developed in-house. Spectral background subtraction was performed by regression fitting of baseline estimation throughout multiple shifted windows across the integrated spectrum via spline approximation. Throughout this work, two different types of pseudo-colored images were generated from Raman area scan datasets: “single-band” images and “multi-band” images. Single-band images were generated by selecting a single Raman band (the Raman intensity at a single wavenumber), specifically 2930cm^{-1}, and converting the intensity (CCD counts) at each pixel across the image into a color. Multi-band images were generated by separately calculating the “lipid signal” (sum of spectral intensities from 2800-2900cm^{-1}, assigned to green channel; pixel intensity range displayed from 0-500 CCD counts) and the “protein signal” (sum of spectral intensities from 2905-2935cm^{-1}, assigned to red channel; pixel intensity range displayed from 0-500 CCD counts), and then overlaying the two images. To calculate the “integrated Raman intensity” for each area scan (of a single cell or micro-calibration standard), all pixel spectra are added together to generate a single “integrated” spectrum which is representative of the composition and total amount of material present within the given area scan. The spectral region of interest (2700-3200cm-1) was excised from the integrated spectrum and interpreted via statistical models discussed in the following sections.

4.4.8 Statistical Model for Ultraquantitative Spectral Deconvolution

To generate reference spectra, biomolecular components of interest were dissolved in appropriate solvent at ~1mg/mL (DI water for protein and nucleic acid; methanol for lipids and cholesterol) and spotted onto the surface of silicon chips; the solvent evaporated at room temperature, depositing all non-volatile solutes across the surface of silicon chips. Reference spectra were acquired via continuous large area scans of each dried dispersion and the average spectrum across each scan was extracted, thereby generating "molecular fingerprints" for each biochemical component of interest. Using Raman datasets acquired from protein and HDL calibration microarrays, the pure component reference spectra were scaled accordingly to directly relate the total mass of each component present within an analyzed microarray dot to the integrated Raman signal acquired from across that region (i.e., CCD counts / picogram). Measured Raman spectra were deconvoluted via linear combination modelling (aka: non-negative least squares regression modelling) with the ultraquantitative reference spectra as per the following equation:

$$I_{\tilde{\nu}} = N_1 k_{\tilde{\nu}_1} + N_2 k_{\tilde{\nu}_2} + N_3 k_{\tilde{\nu}_3} + N_4 k_{\tilde{\nu}_4} + \varepsilon_{\tilde{\nu}}$$

Where:

$I_{\tilde{\nu}}$ = integrated sample spectrum (CCD counts)

$k_{\tilde{\nu}_n}$ = "n" reference spectrum (CCD counts / picogram)

N_n = "n" measurement (picograms)

$\varepsilon_{\tilde{\nu}}$ = residual spectrum (CCD counts)

$\tilde{\nu}$ = relative wavenumber or Raman shift (cm^{-1})

n = biomolecular component (e.g., protein, lipid, etc.)

The linear combination spectral model accuracy of fit was assessed by calculating coefficient of determination (R^2) for each micro-calibration standard spectrum fit according to the following equation:

$$Spectral\ model\ fit\ (R^2) = 1 - \left(\frac{variance(\varepsilon_{\tilde{\nu}})}{variance(I_{\tilde{\nu}})}\right)$$

We refer to this approach as “ultraquantitative” spectral deconvolution; it conveniently yields regression estimate coefficients with units of picograms because it harmonizes effectively with the fundamental theory of linear spectroscopy.

4.4.9 Additional Statistical Models for Interpretation of Cytometric Data

Principal component analysis (PCA) was also performed on integrated Raman spectra; standard normal variate scaling was performed on each integrated spectrum prior to PCA execution in Matlab®. Logistic regression analysis of ultraquantitative results (picogram measurements) from cell datasets and K-means cluster analysis of PCA results (PC scores) were both performed in R Studio using scripts written in-house; logistic regression model was performed as per the following equations (for fibroblast and macrophage datasets respectively):

$$Population \sim Protein + Lipid + Cholesterol + Carbohydrate\ \&\ Nucleic\ Acid$$

and

$$Population \sim Protein + Lipid + Carbohydrate\ \&\ Nucleic\ Acid$$

4.4.10 Instrument Calibration Check Procedure and Error Analysis

A novel Raman instrument calibration and daily check was developed to assess instrument performance and drift and quantitatively correct for any errors that may be inadvertently introduced as a result of extraneous factors. Conveniently, the silicon chip substrates served as calibration standards for detector alignment (using major silicon peak at 521cm-1). The optimal focal plane can be located (z-plane of greatest Raman signal at a given laser intensity) and by varying the intensity of excitation laser across a

range of 0-55mW, acquiring Raman spectra at given intervals, enabled generation of instrument performance curves which were indicative of the instrument's performance.

4.4.11 Sample Preparation of Primary Human Skin Fibroblasts

Primary human fibroblast cell lines were obtained from the NIGMS Human Cell Repository at the Coriell Institute for Medical Research. A control (WT) cell line GM08399 and NPC cell line with mutations in the NPC1 gene GM18453 (I1061T/I1061T) were cultured in DMEM, 1% penicillin/streptomycin, and 10% FBS. Cells were suspended in culture medium containing 10% FBS at a concentration of 10,000 cells/mL. 5x5mm silicon chips were pre-sterilized and transferred to wells of 24-well plate before addition of 1 mL of each cell suspension to separate wells. The plates were incubated overnight (37^{o}C, 5% CO_2) to allow cells to adhere to surface of substrate. Following incubation, culture medium was removed by vacuum and silicon chips were rinsed via brief submersion in isotonic saline (0.9% NaCl wt/wt) then deionized water to remove excess salt; residual water was wicked away immediately with a KimWipe to prevent cell lysis. This methodology prepared cell samples as thin dry dispersions of non-volatile biomolecular components deposited onto the surface of silicon chip substrates.

4.4.12 Isolation, Incubation, and Preparation of Porcine Alveolar Macrophages

Porcine alveolar macrophages were isolated via bronchoalveolar lavage with 40mL instillation of isotonic saline (0.9% NaCl wt/wt) into the lung of a fully-anesthetized male pig (Michigan State Swine Research; *Sus scrofa domesticus*; Yorkshire/Yorkshire mix; ~13-15 weeks old) according to IACUC-approved protocol (PRO00008551). The acquired cell suspension was diluted to 500,000 cells/mL in RPMI medium 1640, 5% FBS, and 1% penicillin/streptomycin. 15µL aliquots were seeded onto 5x5mm silicon chip substrates in a 24-well plate, allowed to adhere to substrate surface (60 minutes, 37^{o}C, 5% CO_2), before wells were filled to 750µL with blank control medium or treatment

medium containing 8μM amiodarone, a widely used antiarrhythmic known to accumulate in alveolar macrophages and induce intracellular accumulation of phospholipids. Treatment populations were incubated for 3 days (37°C, 5% CO_2), replacing medium every 24 hours, to allow cells to sequester drug and induce intracellular accumulation of phospholipids. Following incubation, culture medium was removed by vacuum and silicon chips were rinsed via brief submersion in isotonic saline (0.9% NaCl wt/wt) then deionized water to remove excess salt; residual water was wicked away immediately with a KimWipe to prevent cell lysis. This methodology prepared cell samples as thin dry dispersions of non-volatile biomolecular components deposited onto the surface of silicon chip substrates.

4.5 Results and Discussion

4.5.1 Engineering Solutions to Biophysical Barriers of Cell-Sized Biomolecular Calibration Standard Fabrication

The first step was engineering and fabrication of cell-sized calibration standards. Microarrays have previously been generated with DNA, RNA, protein, and pharmacological agents for use in biosensors, immunoassays, and high throughput screening procedures for identification of drug candidates.(25-28) Using a piezoelectric inkjet materials printer to deposit 10pL ink droplets in microarrays across the surface of silicon chips, we successfully fabricated cell-sized micro-calibration standards of known composition; printer inks were formulated as aqueous solutions of analytes at biologically-relevant concentrations (Figure 4-1a). As residual water evaporated from the droplets, a known mass of dry material was deposited onto surface of the chip (Figure 4-1b). Ink solutions were formulated with analytes of interest in concentrations ranging from 0-100mg/mL (equivalent to 0-100pg/pL), yielding micro-calibration standards across an absolute mass range of 0-1000pg when using a deposited ink volume of 10pL. The fabrication of water-soluble analyte microarrays, namely protein, was achieved with ink concentrations of albumin up to 100mg/mL. Synthetic high-density lipoprotein (HDL)

nanodiscs were utilized to overcome the barrier of low lipid solubility in aqueous solution and to achieve proper fluid properties.(29-31) HDL nanodiscs were synthesized as stoichiometric mixtures of phospholipid (1,2-dipalmitoyl-sn-glycero-3-phosphocholine, DPPC) and biomimetic peptide 22A (2:1 mass ratio) via thermocycling method to achieve up to 90mg/mL HDL in water.(32) Characterization of HDLs revealed an average particle diameter of 10nm (Figure S-9).(33-35) We demonstrated the ability to print micro-calibration standards across a total lipid range of 0-600pg; at 90mg/mL HDL, a 10pL ink droplet contained 600pg of lipid and 300pg of peptide for a total mass of 900pg. HDLs allowed for incorporation of known amounts of lipophilic analytes (i.e., cholesterol) and proved miscible with albumin in lipid-to-protein ratios expected to occur in living cells, enabling fabrication of biologically-relevant micro-calibration standards of mixed composition.(36)

4.5.2 Comparative Analysis of Cell-Sized Calibration Standards and Actual Eukaryotic Cells

Cell samples of interest were prepared, according to a method previously developed by our group, on silicon chips as thin dry dispersions to mimic the state of the micro-calibration standards and analyzed by atomic force microscopy (AFM) and Raman microscopy, exploiting the non-destructive nature of both techniques (Figure 4-1c, d).(16) Reflected brightfield imaging revealed similar appearance for micro-calibration standards and cell samples of interest (Figure 4-2a-c). AFM analysis enabled comparison of topographical morphology between micro-calibration standards and cell samples (Figure 4-2d-f, S-10 – S-12). Micro-calibration standards were found to have diameters and height ranges of the same order as cells and yielded comparable Raman signals (Figure S-13). All maximum sample heights, actual cells and micro-calibration standards, were in the submicron range and found to be shorter than the height of the Raman excitation laser's confocal voxel (Figure 4-1e), suggesting the entirety of each sample may be analyzed in a single x-y plane area scan.(23, 37) Raman area scans revealed the density and distribution of molecular components throughout each analysis region, illustrating how

thicker sample regions with presumably greater amounts of material yield stronger Raman signals compared to thinner regions with less total material (Figure 4-2g-i, S-14 – S-23). Integrated Raman spectra were calculated from the total Raman signal across each analysis area, yielding a single spectrum for each sample that is representative of the total molecular content present within the area scan (Figure 4-2j); a greater integrated Raman intensity was acquired from 900pg of HDL than from 1000pg of protein, suggesting different analytes of interest emit different Raman signal strengths under the same excitation parameters.

4.5.3 Instrument Performance and Error Analysis

Although 633nm and 785nm lasers are generally used for Raman analysis of biological cells, in this study we utilized a 532nm excitation laser because the visible green light enabled facile characterization of the confocal voxel dimensions and yielded the strongest Raman signals from our samples, and thus allowed measuring the smallest amounts of material. During preliminary feasibility testing, we also fabricated microarrays on glass slides and prepared macrophages via cytocentrifugation on glass slides (Figure S-24). Alternative sample substrates (e.g., CaF2) could be compatible with inkjet-printed micro-calibration standards, to the extent that the samples yield strong Raman signals, and that the background Raman signals from the substratum can be subtracted. Instrument performance curves suggested instrument-introduced errors were present but negligible; further work is needed in advancement of Raman instruments to ensure measurement accuracy, which our calibration standards will help facilitate (Figure S-25). From preliminary experiments, we verified that the performance of each individual inkjet cartridge nozzle exhibits excellent drop-to-drop consistency, generating droplet rows which show minimal measurement variability, ~5%, while different nozzles within the same cartridge show a greater variation in drop size, leading to columns measuring somewhat greater variability, ~10-15% (Figure S-26).

4.5.4 Micro-Calibration Standards and the Linearity of Scattered Raman Signals

Micro-calibration standards were composed of proteins and lipids in ratios and total mass ranges consistent with theoretical estimates for typical eukaryotic cells, thereby demonstrating the feasibility of commercially-available piezoelectric inkjet printing technology for creation of cell-sized biomolecular micro-calibration standards; using constant experimental parameters, the integrated Raman signals were acquired from areas of interest for a multitude of micro-calibration standards from each group (Figure 4-3a-g). Using linear combination modelling, pure component reference spectra were scaled to optimize fit of entire calibration standard dataset, thereby building a quantitative spectral library which directly related the acquired CCD counts to picograms for each component (Figure 4-3h). Linear combination spectral modelling yielded reliably accurate fits which were assessed by coefficient of determination (R^2) for each micro-calibration standard spectrum fit; R^2 values were greater than 0.975 for all samples with the exception of the 100pg protein micro-calibration standards (attributable to lower signal-to-noise ratio of the integrated spectra acquired from lesser sample mass), verifying the accuracy of integrated sample spectral fit using pure component reference spectra (Figure 4-3i). Protein, lipid, and protein-to-lipid ratio measurements for all micro-calibration standards showed strong correlation with the expected values, revealing the linearity of integrated Raman signals in relation to the absolute mass of each material present within the scanned area of interest and suggesting supramolecular interactions between biological analytes do not interfere with the linearity of the scattered Raman signals (Figure 4-3j-l, 4-4, 4-5, and 4-6).(38)

4.5.5 High-Content Phenotypic Analysis of Cell Populations

To show proof-of-concept for our methodology and establish validity for cytometric applications, human skin fibroblast populations - wild type (WT) and Niemann-Pick Type C (NPC) – and porcine alveolar macrophages – untreated and drug-treated groups - were prepared as dry dispersions on the surface of silicon chips, closely resembling the micro-

calibration standards; a small number of cells from each population were analyzed (Figure 4-7a). It is worth noting that this sample preparation technique may be applied to non-adherent cell types through conventional cytocentrifugation to deposit and dry suspended cells onto silicon chip substrates; in this way alternative substrates could be utilized (i.e., CaF_2, glass slides, etc.) for cell preparation, depending on substrate chosen for micro-calibration standard printing or other experimental needs (Figure S-24). Raman images of single cells revealed the subcellular distribution of protein (red channel) and lipid (green channel), enabling clear distinction between nuclei and cytoplasm (Figure 4-7b). Furthermore, Raman imaging revealed lipid-rich inclusions (presumably lamellar bodies) in alveolar macrophages treated with 8μM amiodarone, a lipophilic weakly basic drug that induces phospholipidosis, an adverse drug reaction characterized by a lipid-laden macrophage phenotype (Figure 4-7c and 4-8).(5, 6, 39, 40) Stoichiometric mixtures of protein and DNA were used to estimate relative Raman signal strength of carbohydrates and nucleic acids (Figure S-27); in future validation work, additional biomolecular components (e.g., DNA, RNA, polysaccharides, cytochrome c, etc.) will be incorporated into the mixed composition micro-calibration standards. Using our quantitatively-calibrated reference spectra library to perform linear combination modelling (Figure 4-7d), integrated cell spectra were deconvoluted, thereby yielding measurements for total picograms of each biomolecular component present within each cell analyzed. The high variability of our cytometric composition measurements highlights the necessity of single-cell analyses, because cell population diversity and cell subpopulations are currently believed to play crucial roles in different disease states and have significant pathophysiological consequences. Although different cell types are expected to have different total mass contents, our reported picogram measurements are on the same order of magnitude as other reports of single-cell measurements in the literature.(41)

On average, there was a significant increase in total lipid content observed in the NPC cells relative to the WT group; 261.4±112pg compared to 195.6±140pg (mean±SD; p-value<0.05; t-test). The WT cell population exhibited a strong lipid-protein correlation (Pearson's coefficient, 0.782); NPC cells exhibited moderate correlation (Pearson's

coefficient, 0.542), which was indicative of greater compositional heterogeneity on the single-cell basis (qualitatively verified by Raman images) and an uncoupling of the typical lipid-to-protein ratio. This presumably resulted from the compromised cholesterol transport and metabolism at the cellular level that is the hallmark of NPC disease (Figure 4-7e). Although cellular cholesterol measurements were not statistically-significant between WT and NPC, with respective values of 9.5±7.4 and 11.5±8.0 (mean ± SD; p-value>0.05; t-test), measurements were near our experimentally-determined limit of cholesterol quantitation (10pg in a 1000pg cell; or 1% wt/wt) and consistent with conventional methods of analysis, involving homogenization of cell populations and subsequent bulk measurements (normalizing the measured cholesterol content to the protein content of the entire population), yielding values in range of 5-20pg/cell.(4) For untreated and drug-treated macrophage populations, average lipid contents were 22.4±13.0pg/cell and 32.5±16.2pg/cell respectively, suggesting significant cellular lipid accumulation in response to amiodarone exposure (mean ± SD; p-value<0.05; t-test); these values are consistent with literature reports for amiodarone-induced phospholipidosis.(5) Lipid and protein were strongly correlated in untreated and drug-treated alveolar macrophages, with respective correlation coefficients of 0.880 and 0.908 (Figure 4-7g). Exposure to amiodarone induced a 1.5-fold increase in lipid-to-protein ratio per cell, evidenced by the increased slope of the drug-treated group's trend line. Logistic regression analysis revealed significant increases in lipid content and significant decreases in carbohydrate and nucleic acid content for the drug-treated cells compared to the untreated control cells (Figure S-28, Table S-5) but was unable to show significance for lipid increases in NPC group compared to WT with p-value=0.066 (Figure S-29, Table S-6). Principal component analysis (PCA) was performed on the same spectral datasets in parallel with ultraquantitation (Figure 4-7f, h); the first principal components (accounting for 57.6% of spectral variance in fibroblasts and 63.3% in macrophages) exhibited major peaks at 2850cm^{-1} and 2884cm^{-1} (the characteristic Raman bands for C-H vibrations of lipids) and, as verified by our ultraquantitative results, were attributed to differences in cellular lipid content. K-means clustering of PCA results (Figure S-30) could not differentiate WT and NPC fibroblasts, but discrimination of untreated and drug-treated

alveolar macrophages yielded significant accuracy of 0.9143, sensitivity of 0.9714, and specificity of 0.8571 (p-value<0.05).

Using the stoichiometric drug:lipid mixtures (Figure 4-9A) described previously in Chapters 2 and 3 of this thesis, calibration mixtures of amiodarone were generated and Raman spectra were acquired from each (Figure 4-9B). Based on the known relative mass (% wt/wt) of drug, the ultraquantitative reference spectra for amiodarone (CCD counts/picogram) could be estimated by scaling the drug's reference spectra accordingly with the lipid reference acquired from the micro-calibration standards (Figure 4-9C). To show temporal drug-induced changes throughout cell populations, aliquots of alveolar macrophages from a single untreated pig, were incubated *in vitro* with 8μM amiodarone for 0 to 5 days. Following treatment, 25 cells from each population were analyzed and the average integrated spectra were reported for each population, showing a clear temporal increase in lipid signals accompanied by a weaker amiodarone signal, as revealed by the difference spectra (Figure 4-10). Amiodarone drug content estimates were reported in picograms, suggesting a steady temporal increase in amiodarone drug content from 5.3 ±3.3 to to 13.5±7.4 between days 1 and 5 *in vitro*; these values represent estimates and should be taken with a grain of salt; they were reported herein merely to show illustrate the feasibility and approach of ultraquantitative Raman spectral cytometry in the context of drug bioaccumulation.

4.6 Conclusion

In conclusion, ultraquantitative single-cell Raman analysis enables more in-depth phenotypic characterization of cell populations than ever before possible with foreseeable application in basic research for the study of cellular accumulation phenomena, such as lysosomal storage disorders. The application of our mimic cell microarrays for quantitative calibration of single-cell measurements is not limited to Raman microscopy, as demonstrated herein; this technology could prove useful for quantitation in other single-cell techniques such as laser desorption and/or ionization mass spectrometry. The

findings from this study represent a significant advancement in the cytometry field and opens the doors of quantitative scientific perception to the entirety of the intracellular biomolecular matrix without artificial chemical tags, providing an approach by which scientists and clinicians may holistically explore the unadulterated biochemical realm within single cells: the building blocks of life.

4.7 Resulting Publications

1. **LaLone V**, Fawaz MV, Morales-Mercado J, Mourao MA, Snyder CS, Kim SY, Lieberman AP, Tuteja A, Mehta G, Standiford TJ, Ragahvendran K, Shedden K, Schwendeman A, Stinger KA, Rosania GR. Inkjet-Printed Micro-Calibration Standards for Ultraquantitative Raman Spectral Cytometry. 2019. *Analyst*. Accepted for Publication: 9 May 2019.

4.8 Acknowledgements

Financial support of U.S. National Institutes of Health (R01GM078200 to GRR, R01NS063967 to APL, T32 GM007767 and T32 HL125242 to MVF, R01GM111400 to KAS), University of Michigan M-Cubed (to KAS, TJS, KR), Upjohn-Valteich award (to GRR), Ara Parseghian Medical Research Foundation (to APL and AS), University of Michigan Protein Folding Diseases Initiative (to APL and AS), American Foundation for Pharmaceutical Education (to MVF), DOD OCRP Early Career Investigator Award W81XWH-13-1-0134 (to GM), DOD Pilot award W81XWH-16-1-0426 (to GM). We thank Dr. Ki-Han Kim and the Office of Naval Research (ONR) for financial support under grant N00014-12-1-0874, Dr. Kenneth Caster and the Air Force Office of Scientific Research (AFOSR) for financial support under grant FA9550-10-1-0523, the National Science Foundation and Nanomanufacturing program for support through grant #1351412. We thank Dr. Pilar Herrero-Fierro and the Lurie Nanofabrication Facility for help with inkjet printing of calibration microarrays. We also thank Michigan Center for Integrative

Research in Critical Care (MCIRCC), Dr. Kevin Ward, Dr. Hakam Tiba, Brendan McCracken, and Dr. Robert Dickson for help with the porcine experiments.

4.9 Figures

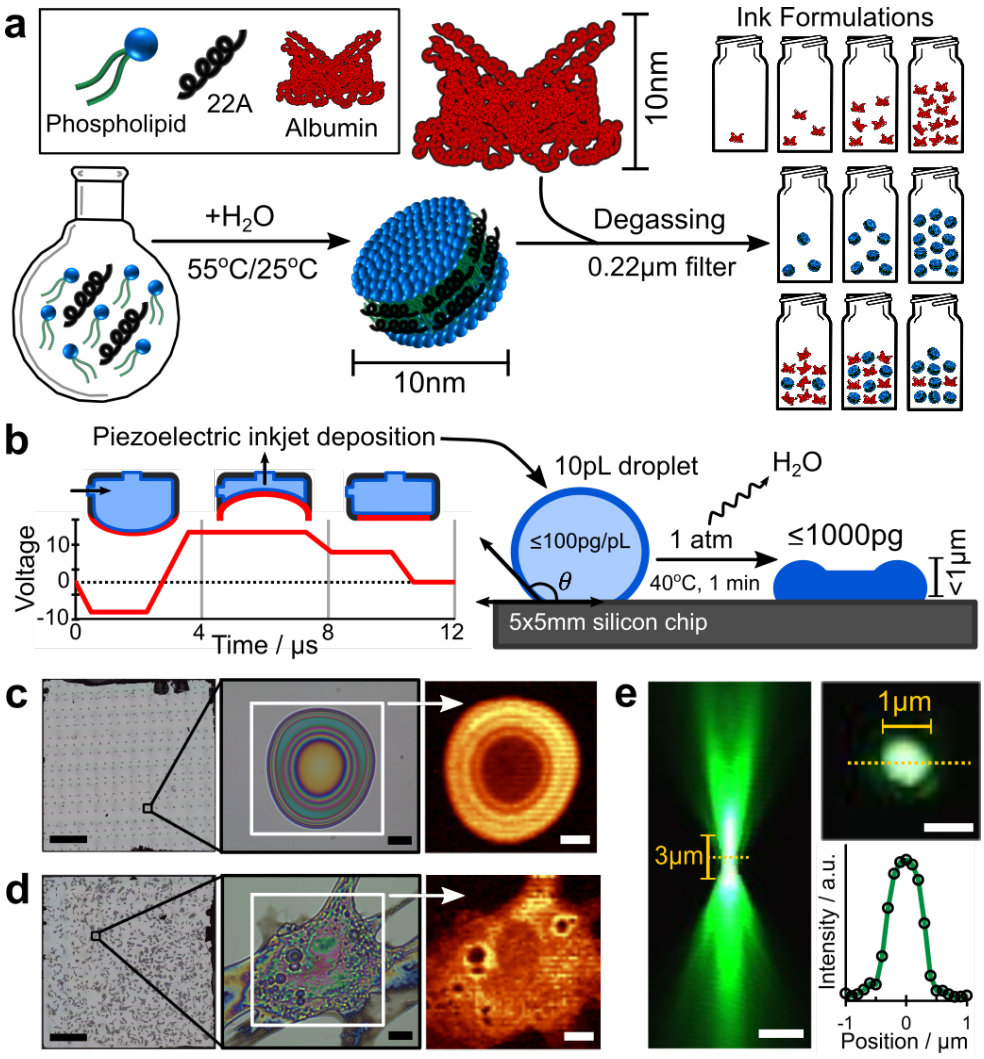

Figure 4-1. Schematic illustrating the synthesis, inkjet printing, and analysis of micro-calibration standards for quantitative measurements in actual biological cells.

(a) Procedure for HDL synthesis and biomolecular ink formulations. **(b)** Piezoelectric jetting waveform for controlled-deposition of 10pL ink droplets onto silicon substrate. Reflected brightfield images of 5x5mm silicon chips (scale bars: 1000μm) and sample areas of interest with corresponding Raman area scan (white box; scale bars: 10μm) data for **(c)** fabricated micro-calibration standards and **(d)** fibroblasts. Raman images reconstructed from C-H vibration intensity at 2930cm^{-1}. **(e)** Vertical cross-section of confocal voxel; reflected light image stack was used to reconstruct in 3D. Scale bars: 3μm (left) and 1μm (right).

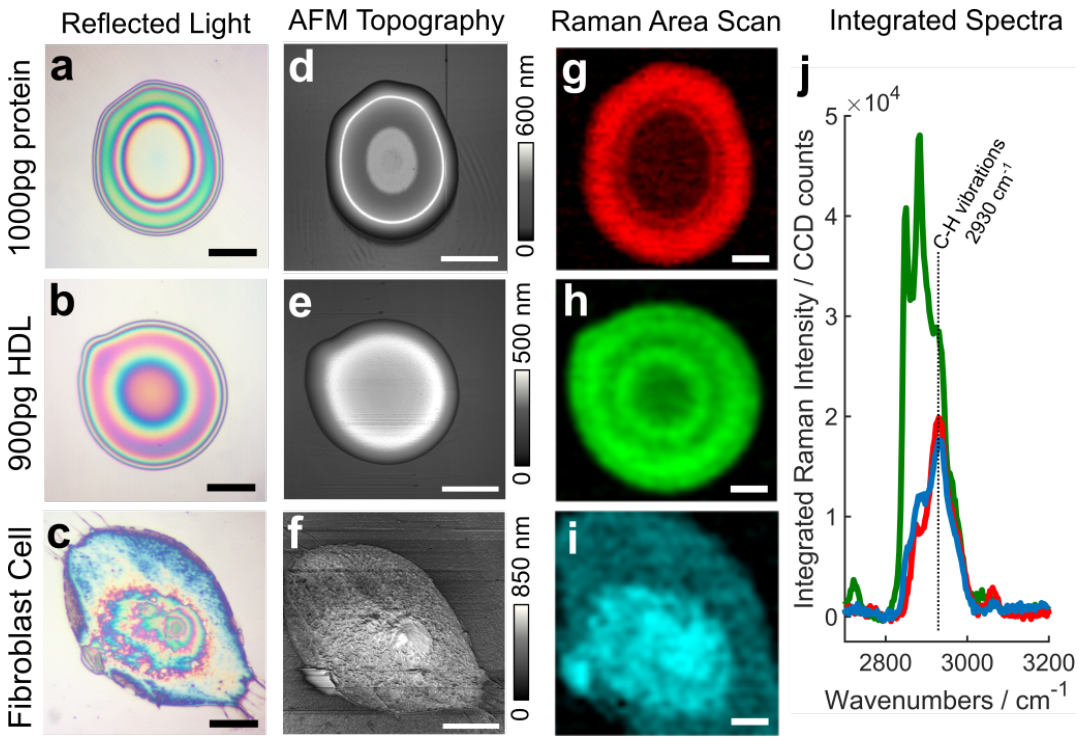

Figure 4-2. AFM and Raman images of calibration standards and a single cell.

Reflected light images of 1000pg protein **(a)**, 900pg HDL **(b)**, and fibroblast **(c)** samples; scale bars: 20μm. Respective AFM surface profiles **(d-f)**; scale bars: 20μm. Respective single-band Raman images reconstructed from C-H vibrations at 2930cm^{-1} **(g-i)** and calculated integrated Raman spectra for each overlaid on same y-axis **(j)**; scale bars: 10μm.

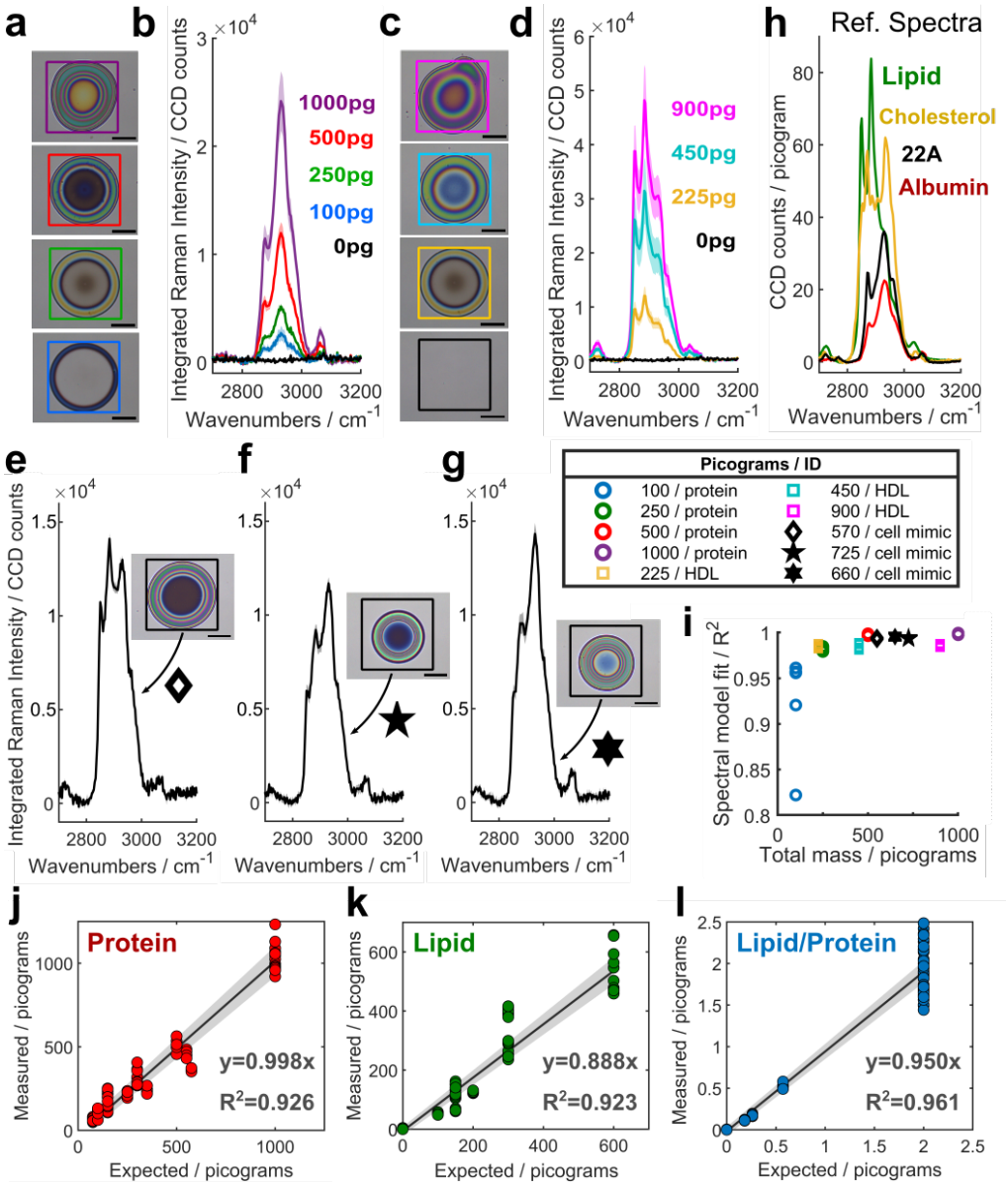

Figure 4-3. Verifying linearity of micro-calibration standard Raman signals.

Reflected brightfield images, analysis areas and corresponding integrated spectra for **(a-b)** protein, **(c-d)** HDL, and **(e-g)** mixed composition micro-calibration standards; scale bars: 20μm. **(h)** Reference spectra library for linear combination modelling. **(i)** Accuracy of spectral fits. Linear regression of measured component content in relation to expected amount for protein **(j)**, lipid **(k)**, and lipid-to-protein ratio **(l)**; shaded regions: 95% confidence interval.

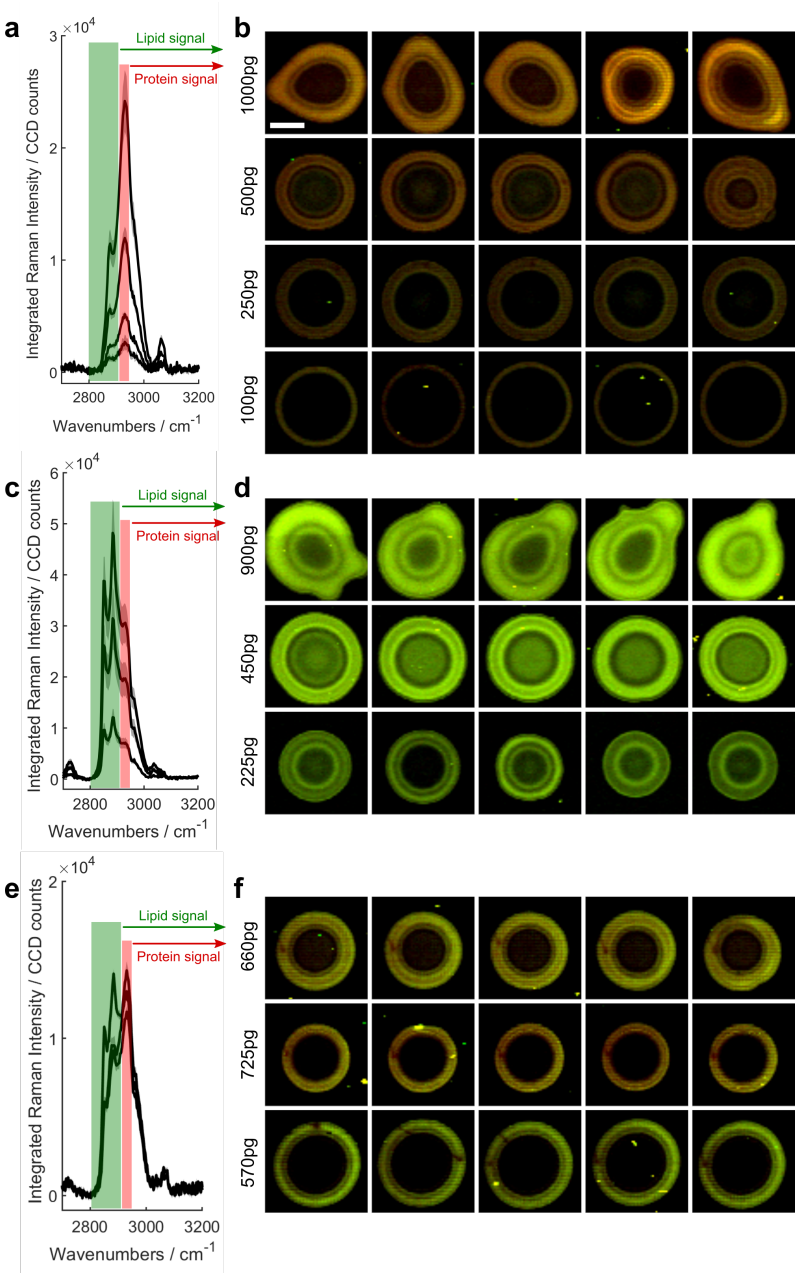

Figure 4-4. Raman images revealing biomolecular distribution in micro-calibration standards.

Multi-band Raman images of **(a,b)** protein, **(c,d)** HDL, and **(e,f)** mixed composition micro-calibration standards generated from Raman calibration datasets used for fibroblast quantitation. Scale bar: 20μm.

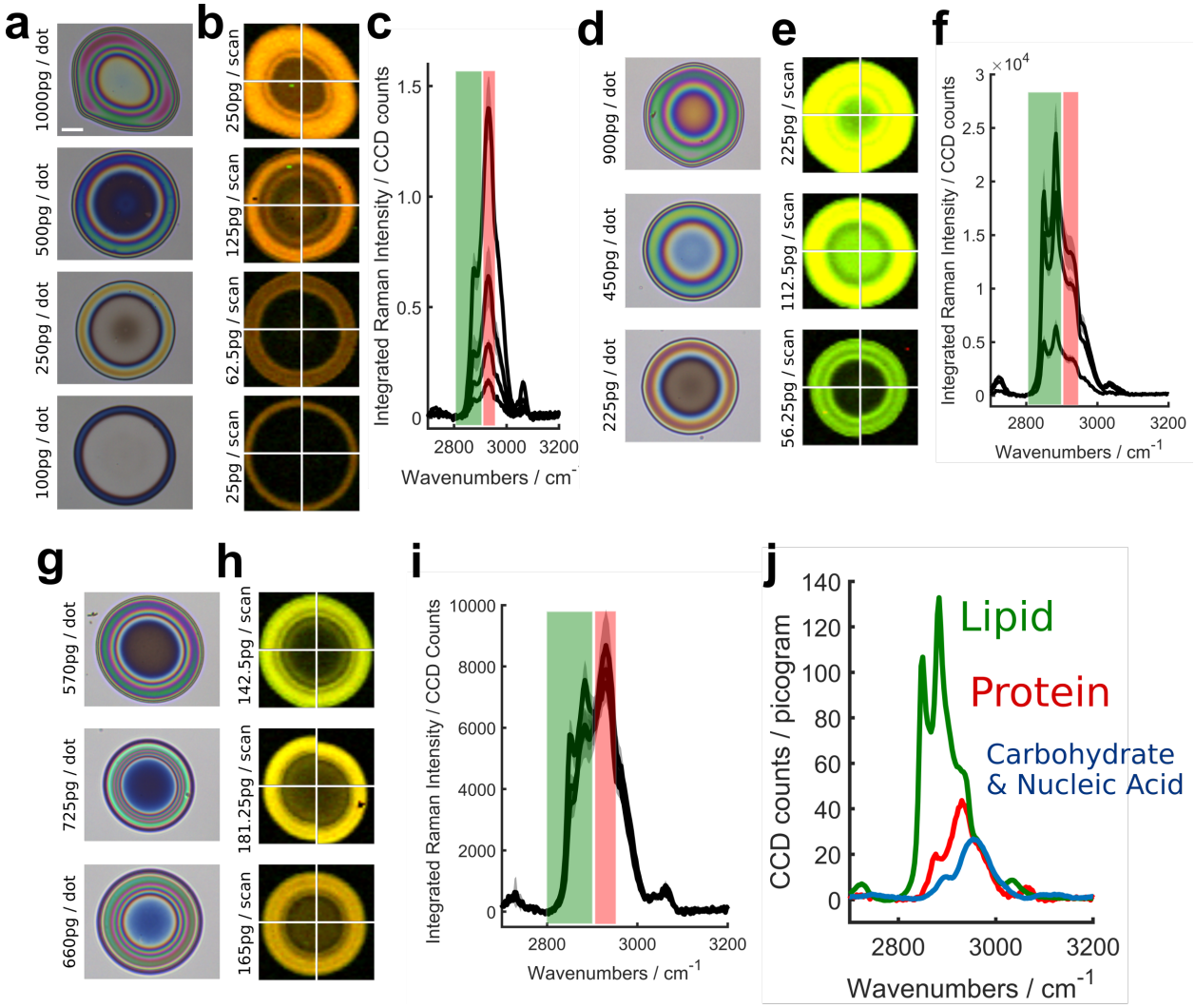

Figure 4-5. Quartered micro-calibration standard Raman area scans.

(a-c) protein micro-calibration standard brightfield images (scale bar:20μm), multi-band Raman images generated from 25x25μm area scans, and integrated Raman spectra. **(d-f)** HDL micro-calibration standard brightfield images (scale bar:20μm), multi-band Raman images generated from 25x25μm area scans, and integrated Raman spectra. **(g-i)** mixed composition micro-calibration standard brightfield images (scale bar:20μm), multi-band Raman images generated from 25x25μm area scans, and integrated Raman spectra. **(j)** Ultraquantitative pure component reference spectra used for linear combination modelling of alveolar macrophage dataset.

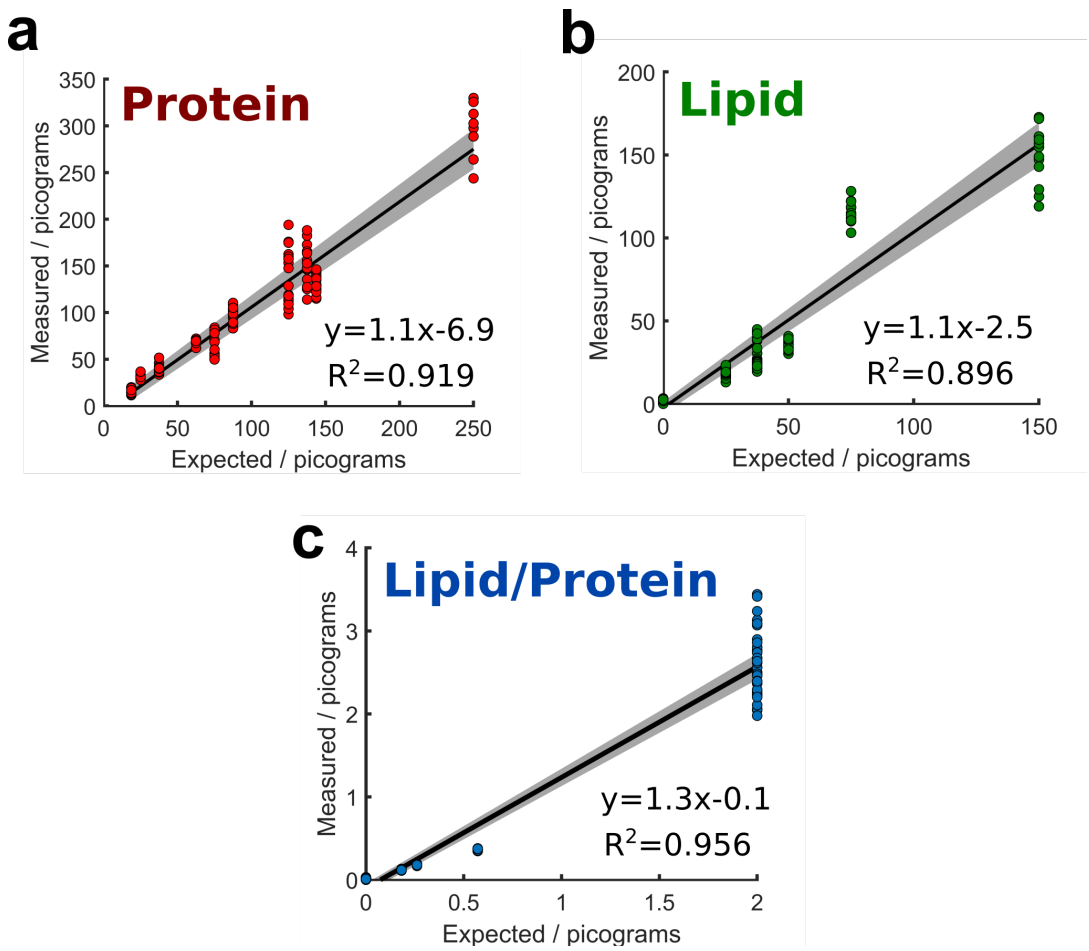

Figure 4-6. Quartered calibration micro-calibration standard measurements for quantitative calibration of alveolar macrophage datasets.

Linear regression of measured component content in relation to expected amount for protein **(a)**, lipid **(b)**, and lipid-to-protein ratio **(c)** including measured values from entire calibration dataset; shaded regions represent 95% confidence interval for measurement accuracy.

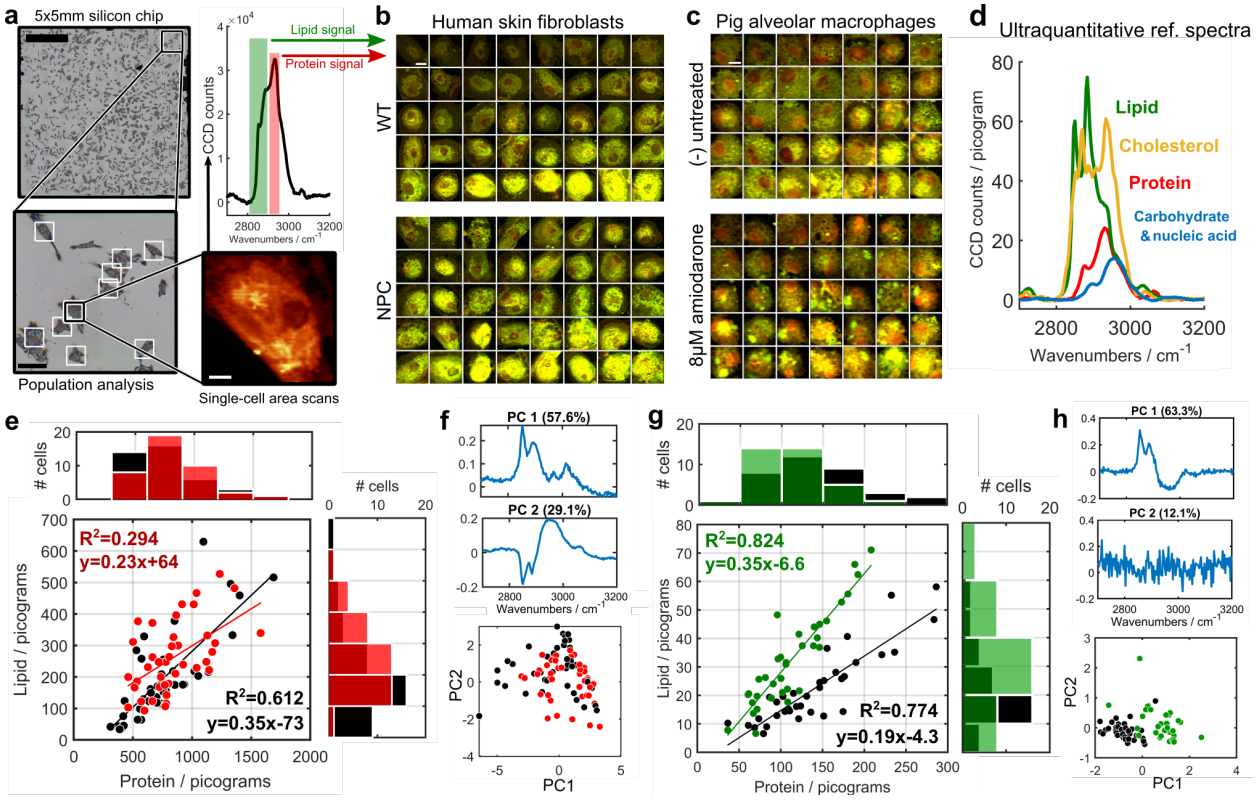

Figure 4-7. Ultraquantitative cytometric analysis of fibroblasts and macrophages.

(a) Data acquisition and processing procedure; scale bars (from top-left to bottom-right): 1000μm, 100μm, and 10μm. Multi-band Raman images for **(b)** human skin fibroblasts (scale bar: 20μm) and **(c)** pig alveolar macrophages (scale bar: 10μm). **(d)** Reference spectra for linear combination modelling. **(e)** Single-cell compositional correlation plot and histograms showing fibroblast population distributions; each data point represents a single cell. WT in black, NPC in red. **(f)** First two PCA loading spectra and PCA score distribution plots (WT in black, NPC in red). **(g)** Single-cell compositional correlation plot and histograms showing alveolar macrophage population distributions; each data point represents a single cell. Untreated control group in black, drug-treated group in green. **(h)** First two PCA loading spectra and PCA score distribution plots (untreated in black, drug-treated in green).

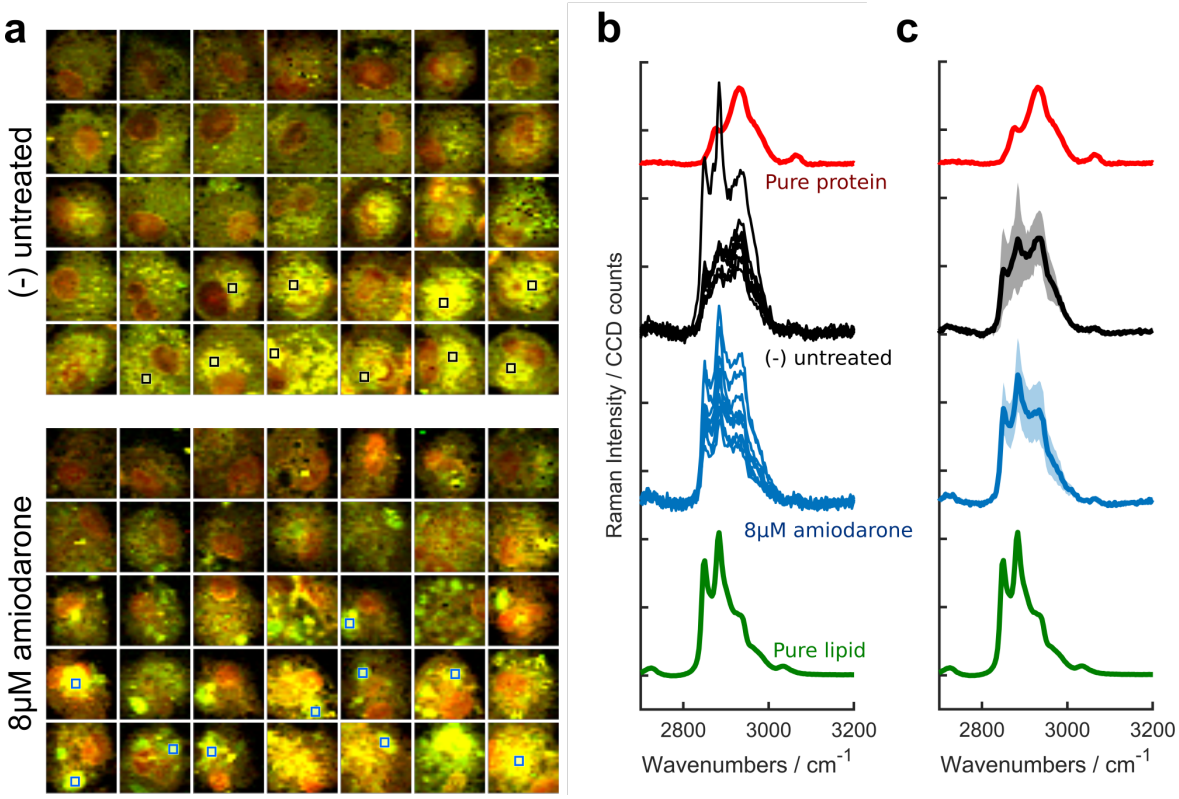

Figure 4-8. Subcellular distribution analysis of drug-treated macrophages.

(a) Multi-band Raman images of alveolar macrophage Raman datasets; each scan is 25x25μm. **(b)** 3x3μm average spectra extracted from lipid-rich inclusions of 10 most lipid-laden cells from each population; pure protein and lipid (DPPC) reference spectra overlay. **(c)** Average+/-SD (shown in shadow) of each group of extracted spectra.

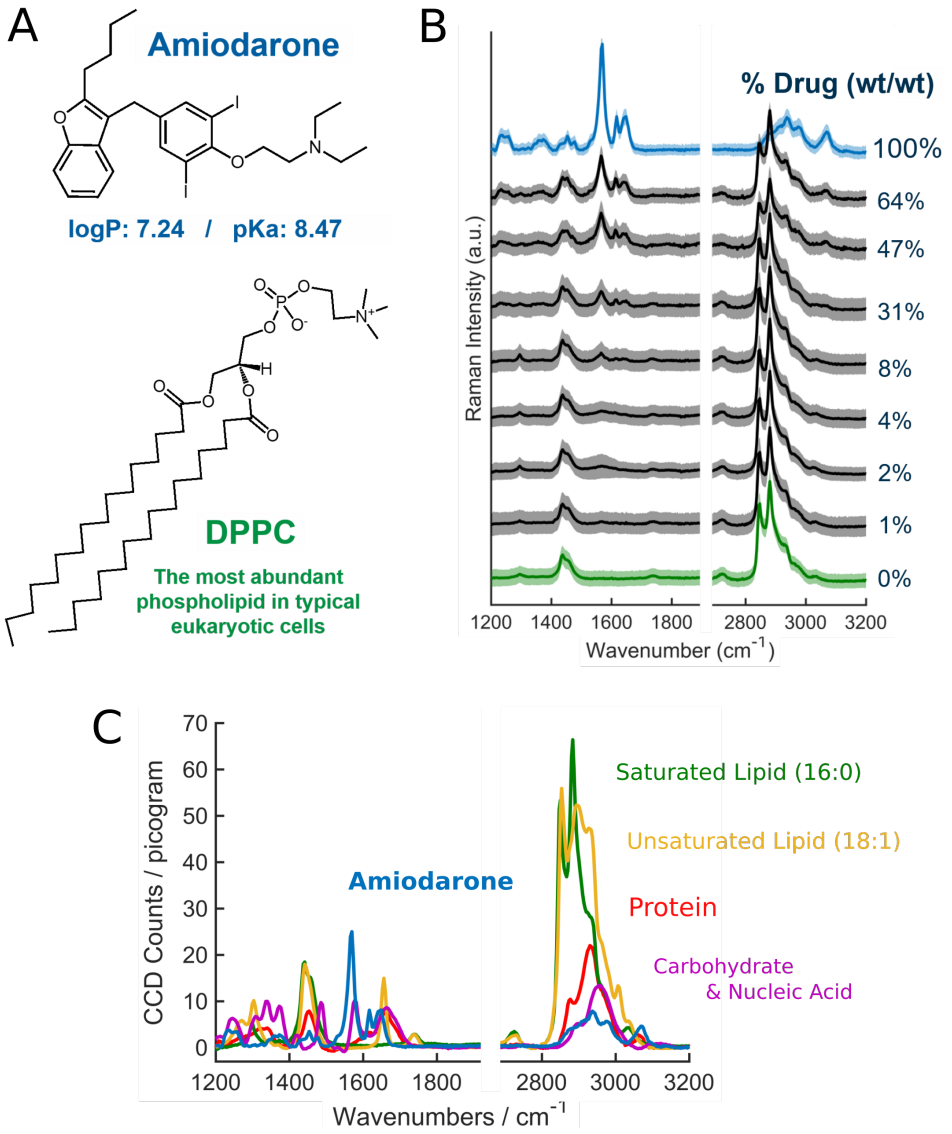

Figure 4-9. Estimating the signal-to-mass ratio for amiodarone.

(A) Chemical structures for amiodarone and dipalmitoylphosphatidylcholine (DPPC), the two components used to generate stoichiometric mixtures. **(B)** Raman analysis of calibration mixtures and **(C)** estimated ultraquantitative reference spectral library; protein and lipid signal-to-mass ratios (CCD counts/picogram) were calculated from micro-calibration standard dataset while others were estimated.

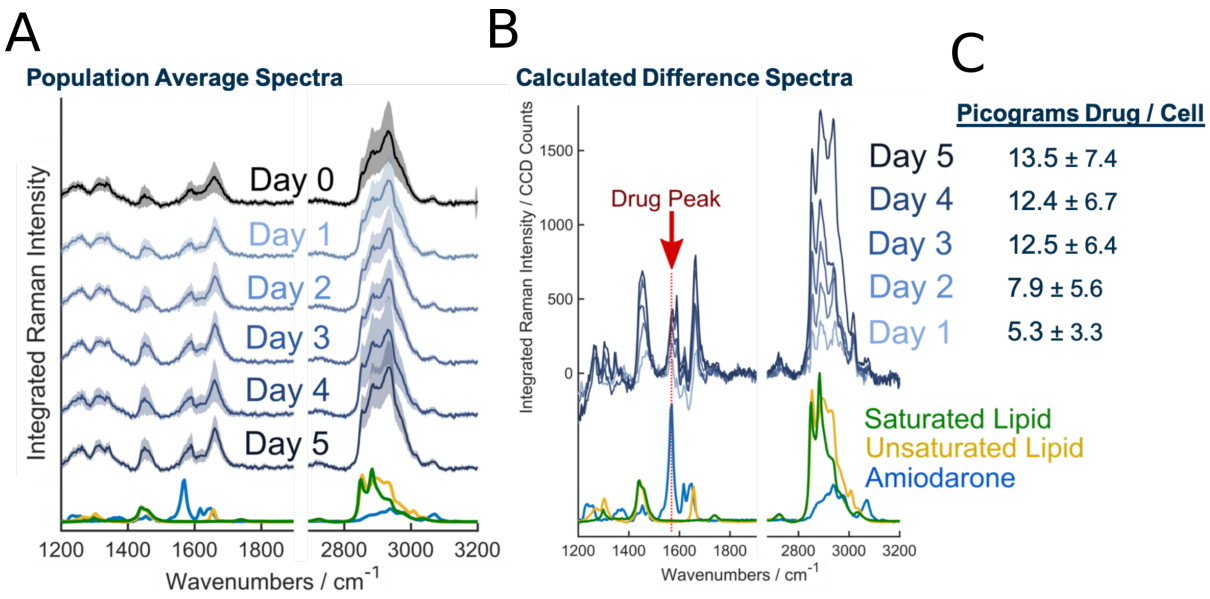

Figure 4-10. Measuring temporal accumulation of amiodarone in macrophages.

(A) Pig alveolar macrophages were incubated *in vitro* for 0-5 days with 8μM amiodarone and the integrated Raman spectra were acquired for populations of cells from each group (n=25 cells per group). **(B)** Calculated difference spectra reveal temporal increase in Raman signals that match those of amiodarone and lipids. **(C)** Single-cell measurements for amiodarone accumulation (average ± SD).

4.10 References

1. Yang Y, Huang Y, Wu J, Liu N, Deng J, Luan T. Single-cell analysis by ambient mass spectrometry. TrAC Trends in Analytical Chemistry. 2017;90:14-26. doi: https://doi.org/10.1016/j.trac.2017.02.009.

2. Wassif CA, Cross JL, Iben J, Sanchez-Pulido L, Cougnoux A, Platt FM, et al. High incidence of unrecognized visceral/neurological late-onset Niemann-Pick disease, type C1, predicted by analysis of massively parallel sequencing data sets. Genetics In Medicine. 2015;18:41. doi: 10.1038/gim.2015.25

3. Liscum L, Ruggiero RM, Faust JR. The intracellular transport of low density lipoprotein-derived cholesterol is defective in Niemann-Pick type C fibroblasts. The Journal of Cell Biology. 1989;108(5):1625-36. doi: 10.1083/jcb.108.5.1625.

4. Tängemo C, Weber D, Theiss S, Mengel E, Runz H. Niemann-Pick Type C disease: characterizing lipid levels in patients with variant lysosomal cholesterol storage. Journal of Lipid Research. 2011;52(4):813-25. doi: 10.1194/jlr.P013524.

5. Martin WJ, Standing JE. Amiodarone pulmonary toxicity: biochemical evidence for a cellular phospholipidosis in the bronchoalveolar lavage of human subjects. Journal of Pharmacology and Experimental Therapeutics. 1988;244(2):774-9.

6. Reasor MJ, Ogle CL, Walker ER, Kacew S. Amiodarone-induced Phospholipidosis in Rat Alveolar Macrophages1-3. Am Rev Respir Dis. 1988;137:510-8.

7. Puppels GJ, de Mul FFM, Otto C, Greve J, Robert-Nicoud M, Arndt-Jovin DJ, et al. Studying single living cells and chromosomes by confocal Raman microspectroscopy. Nature. 1990;347:301. doi: 10.1038/347301a0.

8. Bocklitz TW, Guo S, Ryabchykov O, Vogler N, Popp J. Raman Based Molecular Imaging and Analytics: A Magic Bullet for Biomedical Applications!? Analytical Chemistry. 2016;88(1):133-51. doi: 10.1021/acs.analchem.5b04665.

9. Bergholt MS, Zheng W, Huang Z. Characterizing variability in in vivo Raman spectroscopic properties of different anatomical sites of normal tissue in the oral cavity. Journal of Raman Spectroscopy. 2012;43(2):255-62. doi: 10.1002/jrs.3026.

10. Bergholt MS, Zheng W, Lin K, Ho KY, Teh M, Yeoh KG, et al. Characterizing variability in in vivo Raman spectra of different anatomical locations in the upper gastrointestinal tract toward cancer detection. BIOMEDO. 2011;16(3):037003--10.

11. Albro MB, Bergholt MS, St-Pierre JP, Vinals Guitart A, Zlotnick HM, Evita EG, et al. Raman spectroscopic imaging for quantification of depth-dependent and local heterogeneities in native and engineered cartilage. npj Regenerative Medicine. 2018;3(1):3. doi: 10.1038/s41536-018-0042-7.

12. You AYF, Bergholt MS, St-Pierre J-P, Kit-Anan W, Pence IJ, Chester AH, et al. Raman spectroscopy imaging reveals interplay between atherosclerosis and medial calcification in the human aorta. Science Advances. 2017;3(12):e1701156. doi: 10.1126/sciadv.1701156.

13. Zhou X, Dai J, Chen Y, Duan G, Liu Y, Zhang H, et al. Evaluation of the diagnostic potential of ex vivo Raman spectroscopy in gastric cancers: fingerprint versus high wavenumber. BIOMEDO. 2016;21(10):105002-.

14. Kuzmin A, Pliss A, Prasad P. Ramanomics: New Omics Disciplines Using Micro Raman Spectrometry with Biomolecular Component Analysis for Molecular Profiling of Biological Structures. Biosensors. 2017;7(4):52.

15. Wu H, Volponi JV, Oliver AE, Parikh AN, Simmons BA, Singh S. In vivo lipidomics using single-cell Raman spectroscopy. Proceedings of the National Academy of Sciences. 2011;108(9):3809-14. doi: 10.1073/pnas.1009043108.

16. LaLone V, Mourão MA, Standiford TJ, Raghavendran K, Shedden K, Stringer KA, et al. An Expandable Mechanopharmaceutical Device (3): a Versatile Raman Spectral Cytometry Approach to Study the Drug Cargo Capacity of Individual Macrophages. Pharmaceutical Research. 2018;36(1):2. doi: 10.1007/s11095-018-2540-0.

17. Hammoud MK, Yosef HK, Lechtonen T, Aljakouch K, Schuler M, Alsaidi W, et al. Raman micro-spectroscopy monitors acquired resistance to targeted cancer therapy at the cellular level. Scientific Reports. 2018;8(1):15278. doi: 10.1038/s41598-018-33682-7.

18. Kuzmin AN, Levchenko SM, Pliss A, Qu J, Prasad PN. Molecular profiling of single organelles for quantitative analysis of cellular heterogeneity. Scientific Reports. 2017;7(1):6512. doi: 10.1038/s41598-017-06936-z.

19. Mourant JR, Short KW, Carpenter S, Kunapareddy N, Coburn L, Powers TM, et al. Biochemical differences in tumorigenic and nontumorigenic cells measured by Raman and infrared spectroscopy. BIOMEDO. 2005;10(3):031106-03110615. doi: 10.1117/1.1928050.

20. Mourant JR, Dominguez J, Carpenter S, Powers TM, Guerra A, Short KW, et al., editors. Determining the gross biochemical composition of cells and tissue with Raman spectroscopy. Biomedical Optics 2006; 2006: International Society for Optics and Photonics.

21. Pliss A, Kuzmin AN, Kachynski AV, Prasad PN. Nonlinear Optical Imaging and Raman Microspectrometry of the Cell Nucleus throughout the Cell Cycle. Biophysical Journal. 2010;99(10):3483-91. doi: https://doi.org/10.1016/j.bpj.2010.06.069.

22. Salehi-Reyhani A, Ces O, Elani Y. Artificial cell mimics as simplified models for the study of cell biology. Experimental Biology and Medicine. 2017;242(13):1309-17. doi: 10.1177/1535370217711441.

23. Konorov SO, Schulze HG, Atkins CG, Piret JM, Aparicio SA, Turner RF, et al. Absolute quantification of intracellular glycogen content in human embryonic stem cells with Raman microspectroscopy. Analytical chemistry. 2011;83(16):6254-8.

24. Schie IW, Kiselev R, Krafft C, Popp J. Rapid acquisition of mean Raman spectra of eukaryotic cells for a robust single cell classification. Analyst. 2016;141(23):6387-95.

25. Barbulovic-Nad I, Lucente M, Sun Y, Zhang M, Wheeler AR, Bussmann M. Bio-Microarray Fabrication Techniques—A Review. Critical Reviews in Biotechnology. 2006;26(4):237-59. doi: 10.1080/07388550600978358.

26. Ihalainen P, Määttänen A, Sandler N. Printing technologies for biomolecule and cell-based applications. International Journal of Pharmaceutics. 2015;494(2):585-92. doi: https://doi.org/10.1016/j.ijpharm.2015.02.033.

27. Daly R, Harrington TS, Martin GD, Hutchings IM. Inkjet printing for pharmaceutics – A review of research and manufacturing. International Journal of Pharmaceutics. 2015;494(2):554-67. doi: https://doi.org/10.1016/j.ijpharm.2015.03.017.

28. Sumerel J, Lewis J, Doraiswamy A, Deravi LF, Sewell SL, Gerdon AE, et al. Piezoelectric ink jet processing of materials for medicaland biological applications. Biotechnology Journal. 2006;1(9):976-87. doi: doi:10.1002/biot.200600123.

29. Segrest JP, Jackson RL, Morrisett JD, Gotto AM. A molecular theory of lipid—protein interactions in the plasma lipoproteins. FEBS Letters. 1974;38(3):247-53. doi: doi:10.1016/0014-5793(74)80064-5.

30. Tang J, Li D, Drake L, Yuan W, Deschaine S, Morin EE, et al. Influence of route of administration and lipidation of apolipoprotein A-I peptide on pharmacokinetics and cholesterol mobilization. Journal of Lipid Research. 2017;58(1):124-36. doi: 10.1194/jlr.M071043.

31. Schwendeman A, Sviridov DO, Yuan W, Guo Y, Morin EE, Yuan Y, et al. The effect of phospholipid composition of reconstituted HDL on its cholesterol efflux and anti-inflammatory properties. Journal of Lipid Research. 2015;56(9):1727-37. doi: 10.1194/jlr.M060285.

32. Jean-Louis Dasseux RS, Klaus Büttner, Isabelle Cornut, Günther Metz, Jean Dufourcq. Multimeric Apoa-I agonist compounds. 1997.

33. Blanche PJ, Gong EL, Forte TM, Nichols AV. Characterization of human high-density lipoproteins by gradient gel electrophoresis. Biochimica et Biophysica Acta (BBA) - Lipids and Lipid Metabolism. 1981;665(3):408-19. doi: https://doi.org/10.1016/0005-2760(81)90253-8.

34. Di Bartolo BA, Nicholls SJ, Bao S, Rye K-A, Heather AK, Barter PJ, et al. The apolipoprotein A-I mimetic peptide ETC-642 exhibits anti-inflammatory properties that are comparable to high density lipoproteins. Atherosclerosis. 2011;217(2):395-400. doi: https://doi.org/10.1016/j.atherosclerosis.2011.04.001.

35. Guo Y, Yuan W, Yu B, Kuai R, Hu W, Morin EE, et al. Synthetic High-Density Lipoprotein-Mediated Targeted Delivery of Liver X Receptors Agonist Promotes Atherosclerosis Regression. EBioMedicine. 2018;28:225-33. doi: https://doi.org/10.1016/j.ebiom.2017.12.021.

36. Li D, Fawaz MV, Morin EE, Ming R, Sviridov D, Tang J, et al. Effect of Synthetic High Density Lipoproteins Modification with Polyethylene Glycol on Pharmacokinetics and Pharmacodynamics. Molecular Pharmaceutics. 2018;15(1):83-96. doi: 10.1021/acs.molpharmaceut.7b00734.

37. Besseling TH, Jose J, Blaaderen AV. Methods to calibrate and scale axial distances in confocal microscopy as a function of refractive index. Journal of Microscopy. 2015;257(2):142-50. doi: doi:10.1111/jmi.12194.

38. Galler K, Requardt RP, Glaser U, Markwart R, Bocklitz T, Bauer M, et al. Single cell analysis in native tissue: Quantification of the retinoid content of hepatic stellate cells. Scientific Reports. 2016;6.

39. Jiang H, Passarelli MK, Munro PM, Kilburn MR, West A, Dollery CT, et al. High-resolution sub-cellular imaging by correlative NanoSIMS and electron microscopy of amiodarone internalisation by lung macrophages as evidence for drug-induced phospholipidosis. Chemical Communications. 2017;53(9):1506-9.

40. Reasor MJ, Ogle CL, Kacew S. Amiodarone-induced pulmonary toxicity in rats: Biochemical and pharmacological characteristics. Toxicology and Applied Pharmacology. 1989;97(1):124-33. doi: http://dx.doi.org/10.1016/0041-008X(89)90061-6.

41. Mourant JR, Dominguez JR, Carpenter SR, Short KR, Powers TR, Michalczyk R, et al. Comparison of vibrational spectroscopy to biochemical and flow cytometry methods for analysis of the basic biochemical composition of mammalian cells: SPIE; 2006.

CHAPTER 5

Bioanalytical Spectropathology: Translational Feasibility of Ultraquantitative Micro-Raman Cytometry for *In Vivo* Disease Profiling

5.1 Relevance to Thesis

As described in Chapter 1 of my thesis, the accumulation of amiodarone inside alveolar macrophages induces a “foamy” lipid-laden cell phenotype and may ultimately result in pulmonary toxicity; amiodarone-induced lung toxicity may manifest as chronic or acute lung injury and the role of the “foamy” lipid-laden macrophage is poorly understood. To address specific aim 3 of my thesis and facilitate the translation of micro-Raman spectroscopy to the clinical setting, I utilized the ultraquantitative methodology that was previously described in Chapter 4 of my thesis to perform phenotypic analysis of alveolar macrophage populations. The inkjet-printed micro-calibration standards were used for quantitative cytometric compositional phenotyping for *in vivo* contexts of chronic and acute lung injuries in animal subjects. More specifically, alveolar macrophage populations were acquired from mice and pigs and analyzed via ultraquantitative Raman spectral cytometry to measure changes in biomolecular component content on a single cell basis as a result of different lung injuries.

Although the role of “foamy” lipid-laden macrophages in lung disease pathogenesis is poorly understood, they are commonly found in the lung patients experiencing amiodarone-induced pulmonary toxicity and pulmonary fibrosis that could be idiopathic in nature. As such, the analytical methodology and data handling approaches presented herein represent an avenue by which clinicians and scientists may begin to quantitatively characterize the role of these cells and their cargo loading capacity. Although the studies

presented herein are currently of limited in relevance to clinicians, they represent a robust proof-of-concept for the clinical feasibility and translational aspects of micro-Raman spectroscopy for cytometric analyses in the real-world patient population. The data handling and interpretation approaches presented here could be easily translated to human BAL cell samples for non-specific screening analyses with the potential to detect and qualitatively identify unknown chemical components present within alveolar macrophages of real-world humans. This chapter shows that ultraquantitative Raman spectral cytometry can be reliably utilized in the clinical setting to yield quantitative cytometric information that could foreseeably be used to facilitate clinical decision making.

It is well known that alveolar macrophages are responsible for clearing out biological debris, inhaled particulates, pathogens, and other xenobiotics from the alveolar spaces of the lung. As the cells sequester foreign material, they grow in overall mass due to phagocytosed contents; as each cell matures, they ascend towards the upper respiratory tract via the mucociliary escalator before being expectorated or swallowed. As the alveolar macrophages are depleted, interstitial and peripheral precursor cells are recruited to alveolar space to maintain steady-state of cell population. Herein, this system was referred to as the macrophage-mucociliary clearance complex and was postulated to play a critical role in the maintenance of healthy pulmonary function and potentially serve as a biomarker for overall pulmonary health based on the degree of macrophage cargo loading. Since humans live for approximately 75 years in developed countries, the lung macrophage populations of certain patients may be carrying substantial cargo loads, which could foreseeably contribute to the progression of lung disease and decline of function, as observed in cases of idiopathic pulmonary fibrosis. Although the ultraquantitative cytometric Raman measurements made here represent a new perspective by which to assess cellular storage disorders in the context of pulmonary diseases, there remains a great deal of future validation work in order to confidently employ this technology for diagnostic purposes in the clinical setting. Regardless, this work establishes the validity of the technical analytical parameters and therefore serves to facilitate the translation of micro-Raman spectroscopy to the clinical setting.

5.2 Abstract

Macrophage lipidosis contributes to atherosclerosis and liver fibrosis; we hypothesize that it also plays a role in lung fibrosis, including idiopathic pulmonary fibrosis (IPF) and potentially acute respiratory distress syndrome (ARDS); the roles of macrophage cargo loading in IPF pathogenesis and ARDS prognosis have yet to be elucidated. To improve cytometric phenotyping for bronchoalveolar lavage (BAL) cell populations with high interindividual variability, a Raman-based microanalytical platform was developed to characterize alveolar macrophages (AMs) on the basis of their chemical composition, specifically to measure the absolute amount (i.e., picograms) of protein, lipid, and other biomolecular components present within single cells, thereby enabling the quantitative study of the role of macrophage cargo loading in the context of lung injuries (e.g., “foamy” lipid-laden macrophages in IPF). Ultraquantitative micro-Raman cytometry revealed changes in the total protein, lipid, nucleic acid, and cholesterol content of individual alveolar macrophages acquired via BAL from untreated and fibrotic mice subjects; it also enabled quantitative compositional phenotyping of porcine alveolar macrophages from multiple animals – to understand interindividual variability – and temporal measurements of how a single animal’s BAL profile changes during ARDS. Furthermore, this Raman technique enabled detection of two different unknown chemical entities present inside BAL cells acquired from mice and pigs, suggesting feasibility for Raman-based identification of patient-specific causes of chronic and acute lung injuries (e.g., exposure to pollutants, toxins, or drugs). The long-term goal of this project is the translation of Raman cytoanalytical technologies to the clinical setting to be used to study lung injuries and diseases in human patients.

5.3 Introduction

5.3.1 The Physiological Role of Alveolar Macrophages in the Lung

As the foundation of the innate immune system, resident macrophages are mediators of inflammatory signaling and serve as the frontline of phagocytic defense throughout most organs and tissues of the body. Alveolar macrophages reside on the epithelial surfaces of the alveoli, providing defense against inhaled pathogens and xenobiotic particles.(1, 2) Although the whole human lung is composed of over 40 types of cells (including epithelial, interstitial, connective tissue, vascular, hematopoietic, and lymphocytes), under normal conditions the main cell types present in the alveolar space – where gas exchange occurs between inhaled air and the blood – consist of type I pneumocytes, type II pneumocytes, and alveolar macrophages (AMs).(3) Within the alveoli, AMs sequester inhaled particulate matter while pulmonary blood flow through the lung also exposes them to systemically circulating drug compounds.(1, 4, 5) Conveniently, AMs are relatively easy to harvest from human or animal subjects via bronchoalveolar lavage (BAL), involving the instillation of saline into the lower respiratory tract; once recovered, the BAL fluid contains a cell suspension that is typically rich in AMs (>90% of cells by number).(6) AMs have historically been the most widely studied of all macrophage subpopulations of the lung due to relatively facile acquisition via BAL; many studies have demonstrated profound heterogeneity within the same and throughout different AM populations, specifically in terms of their biochemical, biophysical, morphological, and functional characteristics.

It has been reported that AMs exhibit a wide range of sizes, even within a single population; these studies have been conducted via gradient centrifugation to fractionate the lavaged AMs into subpopulations based on overall size and density.(7-10) Numerous investigators have hypothesized that the differences in cell size can be attributed to the age of each specific cell, where the largest macrophages are presumably the oldest. This hypothesis implies that a population of AMs consists of a diverse mix of cells at multiple stages of maturation. AMs are commonly believed to differentiate from the interstitial

macrophages of the lung and/or from peripheral blood monocytes recruited into the alveoli space; local proliferation, or self-renewal, of AMs already within the alveoli space may also serve to maintain AM numbers within the alveolar spaces.(11-13) AMs must be regenerated within the alveolar spaces for the population to maintain a steady-state number because these immune cells, with their phagocytosed cargo, are continuously migrating up the respiratory tract via the mucociliary escalatory before they are either swallowed or expectorated; in this way, AMs serve as the major mediators of clearance of foreign particles and materials from the lung, an often overlooked physiological system which we herein refer to as the macrophage-mucociliary clearance complex. It is believed that as pathogenic, particulate, or xenobiotic burden on the lung increases, more AMs are recruited to alveolar spaces via chemotactic signaling to help clear the material and maintain a healthy clean environment within the alveoli of the lung.

5.3.2 Chronic Lung Injuries and Idiopathic Pulmonary Fibrosis

Pulmonary fibrosis, or lung scarring, is defined as the formation of excess fibrous connective tissue within the distal airspaces of the lung, and when progressive, can cause respiratory failure and is commonly found to be a disease of aging.(14, 15) Fibrotic lung diseases have been reported to occur in response to drug bioaccumulation (as in the case of amiodarone, bleomycin, and methotrexate), inhaled dusts of silica or other hard metals, and bacteria.(16-19) Despite a widely-accepted appreciation for the pathological and inflammatory features of lung fibrosis, the disease often arises from idiopathic origins. The diagnosis of idiopathic pulmonary fibrosis (IPF) therefore presents a current challenge to the scientific and medical community.(20) Because of the chronic nature of IPF, median survival of patients is only 2 to 3 years but some patients may live much longer.(21) Furthermore, there is limited information regarding predictors of mortality for IPF patients. Computed tomography (CT) scans (more common) and surgical lung biopsies (less common) are utilized in the diagnosis of fibrotic diseases but these approaches are plagued by interobserver and interlobar variabilities in the interpretation of results.(22-25) For this reason, investigators have suggested that BAL provides

additional information that could aid in the accurate diagnosis of IPF.(26) Current evidence suggests that pathogenesis of IPF is driven by abnormal activation of the alveolar epithelial cells releasing mediators which ultimately result in the secretion of excessive amounts of extracellular matrix, namely collagens, that are responsible for progressive destruction of healthy lung architecture and decline of lung function.(15) In addition to abnormally-functioning alveolar epithelial cells, “foamy” lipid-laden macrophages are believed to play a causal role in disease pathogenesis because they are present in the lungs of fibrotic patients.(27) In line with our previous hypothesis regarding macrophage cargo loading and aberrant inflammatory responses in the lung, we herein quantitatively explore the *in vivo* lipid cargo-carrying capacity of alveolar macrophages in the context of oxidized phospholipid-induced pulmonary fibrosis in mice using ultraquantitative Raman cytometry. This experimental model will serve to show proof-of-concept for Raman cytometric analyses in the context of chronic lung injuries, ultimately facilitating translation of the technology to the clinical setting.

5.3.3 Acute Respiratory Distress Syndrome

Acute respiratory distress syndrome (ARDS) is a rapidly-progressing life-threatening condition that occurs in critically ill patients (e.g., ~40% of cases are sepsis-related). ARDS is characterized by diffuse lung inflammation, pulmonary edema from leaky capillaries, and hypoxemia and occurs on a time-scale of days to weeks.(28) Furthermore, there are multiple disorders that predispose patients to increased risk such as chronic alcohol use, chronic lung disease, low serum pH, and amiodarone exposure.(29-33) In ARDS the microvascular endothelium and the alveolar epithelium are injured, resulting in increased vascular permeability and flooding of alveolar space with edema fluid. In addition to fluid and blood infiltrate into alveolar spaces, the course of ARDS often results in the accumulation of neutrophils in alveoli, leading some investigators to believe ARDS is a neutrophil-dependent inflammatory injury.(34, 35) Acting as sentinels of the immune system, neutrophils are rapidly recruited to sites of injury (i.e., the alveoli of lung in ARDS) where they phagocytose pathogens or utilize their

so-called neutrophil extracellular traps (NETs), formed via expulsion of the cell's DNA decorated with granule proteins, to incapacitate pathogens.(36, 37) Excessive formation of NETs has been implicated in inflammatory disorders such as sepsis and atherosclerosis(38) and NETs that are not removed from tissues may cause inflammatory immune responses. Clearance of neutrophils, NETs, damaged alveolar epithelial cells, and extracellular matrix breakdown products plays a role in the progression of inflammation and survival during ARDS and other acute lung injuries.(39) As discussed previously, alveolar macrophages are responsible for clearing debris from the air spaces, dampening inflammation, and facilitating tissue repair(40) and as such, the cargo-carrying capacity of these cells could feasibly play an important role in pathogenesis and outcome of acute lung injuries such as ARDS. The pathologic hallmark of ARDS is diffuse alveolar damage but can only be detected via surgical biopsy of the lung(41) so a quantitative phenotypic analysis of alveolar macrophages could foreseeably serve to further elucidate the physiological role these immune cells play in ARDS pathogenesis. Because of their phylogenetic distance and biological divergence from humans, rodents serve as poor test subjects for *in vivo* experimental models of ARDS; to address this, a large animal multi-insult injury model – in pigs – was used to more closely recapitulate the pathophysiology of ARDS in humans.

5.3.4 Bioanalytical Raman Spectropathology for the Study of Macrophages

Whether the injury is chronic or acute, the role of alveolar macrophages – specifically regarding their cargo carrying capacity and its implications with inflammation – in the pathogenesis of lung diseases such as IPF and ARDS has yet to be fully elucidated. As previously discussed, AM populations are inherently heterogeneous because of cell turnover (continuous mucociliary clearance, peripheral monocyte recruitment, and macrophage maturation in alveoli) that is necessary to clear the lung of foreign particles and pathogenic material. With rising awareness of the significance of cell population diversity and the pathophysiological consequences of cell subpopulations that play crucial roles in different disease states, there exists a niche for a microanalytical

methodology that enables quantitative characterization of the AM-mediated clearance pathway at the single-cell level. Improved phenotypic characterization of AM populations (on the single-cell basis) will provide insight into the role these cells play in lung injuries and pathologic conditions. As such, we herein propose the use of ultraquantitative confocal micro-Raman spectroscopy for the quantitative measurement of alveolar macrophage cargo loading in the contexts of two experimental animal models: oxidized phospholipid-induced pulmonary fibrosis in mice and multi-insult ARDS in pigs. The Raman-based cytometric approach provides compositional profiles on a single-cell basis, thereby enabling the quantitative study of lung injury pathogeneses in a way which has not previously been possible. Micro-Raman spectroscopy involves an excitation laser that scans a cell of interest, inducing molecular vibrations that emit a multitude of scattered lights from the sample which can be quantitatively interpreted to determine the composition of the sample; the analysis is inherently non-specific (all material – endogenous or foreign – yields a signal without molecular tags). Because of its non-specific nature, Raman analysis also opens the doors of scientific perception to the presence of unknown molecular entities that may only be present within specific subpopulations of cells and have thereby previously gone undetected. Since airway and alveolar macrophages are readily accessible in humans, we believe this cell population and our proposed methodology could provide a unique opportunity for the direct study of AM populations in patients, thereby enabling personalized therapies in the clinical setting. Furthermore, the study of human AMs would provide direct insight into the cargo that accumulates over an individual's lifespan and enable the study of environmental and lifestyle factors in the context of lung health and diseases such as IPF and ARDS.

5.4 Materials and Methods

5.4.1 Materials

Silicon chips (5x5mm; Ted Pella, Inc., Redding, CA) served as substrates for all Raman measurements performed herein. The following reagents were used to generate

the reference spectra library: bovine albumin (MP Biomedicals; Solon, OH), 1,2-dipalmitoyl-sn-glycero-3-phosphocholine (DPPC; Avanti Polar Lipids, Inc., Alabaster, AL), 1,2-dioleoyl-sn¬-glycero-3-phsophocholine (DOPC; Avanti Polar Lipids, Inc., Alabaster, AL), DNA (from salmon sperm; AmResco Inc., Solon, OH), and cholesterol (ovine; Avanti Polar Lipid, Inc., Alabaster, AL). Polysorbate 20 (Bio-Rad Laboratories, Inc., Hercules, CA) was utilized as surfactant in diluent for albumin ink formulations. The following reagents were used to formulate HDL nanoparticle suspensions: 22A (PVLDLFRELLNELLEALKQKLK) was synthesized by Genscript (Piscataway, NJ), using solid-phase Fmoc (9-fluorenylmethyl carbamate) chemistry and purified with reverse phase chromatography (>95 % pure). 1,2-dipalmitoyl-sn-glycero-3-phosphocholine (DPPC) was purchased from NOF America Corporation and cholesterol was obtained from Sigma-Aldrich (St. Louis, MO). Inkjet-printed micro-calibration standards of known mass and composition (as previously described in Thesis Chapter 4) were used to generate quantitatively-calibrated reference spectra to be used for linear combination modelling.

5.4.2 *In Vivo* Pulmonary Fibrosis Mouse Model

Mice (4-week-old, male C57BL/6) were purchased from the Jackson Laboratory (Bar Harbor, ME) and acclimatized for 1 week in a specific-pathogen-free animal facility. Mice were subjected to oropharyngeally-delivered oxidized phosphocholine (10μg/g) to induce pulmonary fibrosis. At 1, 4, and 14 days following injury, mice were euthanized via CO_2 asphyxiation and exsanguination, and alveolar macrophages were obtained by bronchoalveolar lavage from control and treatment groups (three mice per group at each timepoint); Raman spectra were acquired from individual cells (n=150; 50 cells per animal) throughout each population. Animal care was provided by the University of Michigan's Unit for Laboratory Animal Medicine (ULAM), and the experimental protocol was approved by the Committee on Use and Care of Animals. All animal experiments were done according to the protocol guidelines.

5.4.3 *In Vivo* Acute Respiratory Distress Syndrome Pig Model

This study utilized male Yorkshire mix swine that (approximately 35-50kg in weight) were acquired from an approved vendor via the University of Michigan Unit for Laboratory Animal Medicine. All experiments were conducted in the Pre-Clinical Operative and Intensive Care Unit facility at the Michigan Center for Integrative Research in Critical Care (MCIRCC) by an experienced investigative team. At baseline, all animals were healthy, and free of disease and antibiotic exposure. Animals were sedated, mechanically ventilated (tidal volume: 15ml/kg; FiO2: 100%) and monitored by an experienced team using established and approved protocols. Animals were monitored continuously using a pulmonary artery catheter, and numerous noninvasive monitors (e.g., electrocardiogram, pulse oximetry, end-tidal capnography, SvO2, cardiac output, etc.), serial arterial blood gases, venous blood chemistry measurements and chest x-rays. Once animals are fully instrumented and hemodynamically stable, a bronchoscopy was performed using disposable bronchoscopes (Ambu aScope) to preclude procedural contamination from animal to animal, collecting baseline bronchoalveolar lavage (BAL) fluid and alveolar macrophages. Following baseline measurements, animals received an injection of an E. coli inoculum (strain CFT073; 4×10^{11} CFU) into the kidney parenchyma under direct visualization. In advance of experiments, a collection of gastric juice from healthy control animals under other approved protocols was pooled and centrifuged. The supernatant was decanted and the gastric juice particles were resuspended in saline titrated to pH ~ 1 with HCl. Following the administration of the E. coli inoculum, the gastric solution was instilled evenly and diffusely to both lungs bronchoscopically. Intravenous crystalloid fluids were given (maximum 10ml/kg/h) but no additional resuscitation was administered. Each experiment was terminated based on pre-determined humane end points.

5.4.4 Bronchoalveolar Lavage Cell Preparation

Alveolar cells were procured via BAL with sterile isotonic saline (0.9% NaCl wt/wt). BAL cell suspensions were centrifuged and cell pellets were resuspended in RPMI 1640 medium (Gibco Life Technologies, Carlsbad, CA) at ~300 cells/μL and 15μL of suspension was transferred to surface of sterilized silicon chips (5x5mm; Ted Pella, Inc., Redding, CA) within a 24-well plate (1 chip per well). Cells were incubated (37°C, 5% CO_2) for 1 hour to allow for adherence of macrophages. Following brief incubation, silicon chips were removed from plate wells and rinsed via brief submersion in isotonic saline (0.9% NaCl wt/wt) then deionized water to remove salt. The residual water was wicked away immediately with a Kimwipe to prevent cell lysis. Samples were air-dried, depositing the non-volatile cellular components as dry dispersions on the surface of silicon chips.

5.4.5 Cytological Staining of Porcine BAL Samples for Cell Differential Count

Following acquisition of BAL cells from porcine ARDS model, the cells were counted and diluted to a concentration of 0.5×10^6 cells/mL in RPMI 1640 medium (5% fetal bovine serum) before transferring 200μL of suspension to sample chamber cuvette (with prepared glass microscope slides mounted with paper pad) and centrifuging at 500 rpm for 5 minutes in a Thermo Cytospin 4 Cytocentrifuge (Thermo Fisher Scientific, Waltham, MA). Following centrifugation, the slide was removed and allowed to air-dry for 10 minutes then dipped 7 times into fixative solution (fast green in methanol), 7 times into stain solution 1 (Eosin G in phosphate buffer), 7 times into stain solution 2 (thiazine dye in phosphate buffer), and 7 times each into two different water rinse solutions. The final preparation was then allowed to air-dry before microscopy images were taken and cell differentials were counted.

5.4.6 Raman Measurements

All Raman measurements were recorded using a WITec alpha300 R Confocal Raman Imaging Microscope (Ulm, Germany) equipped with a 50X air objective lens (Zeiss EC EPIPLAN, N.A.=0.75) and 532nm solid-state excitation laser (0-55mW, tunable intensity range with attenuator dial) coupled to a CCD detector via a 100μm diameter multi-mode fiber-optic cable. Raman area scans were performed by first locating the optimal laser focal plane for sample excitation (yielding the greatest signal intensity from 2800-3100cm-1 for biological materials) then continuously acquiring data across that area of interest by scanning in raster pattern, presumably exciting the entirety of the sample material present. The excitation laser intensity was kept constant between sample scans. Alveolar macrophage cell datasets and corresponding calibration standard datasets were acquired via 25x25μm area scans with a step-size of 1μm (625 spectra/pixels) with an integration time of 0.1 sec per pixel, for an acquisition time of 1 min per cell (or micro-calibration standard). By continuously acquiring Raman signal data in a raster pattern across the scan area at the optimal focal plane, hyperspectral Raman datasets were generated which were presumably representative of the entirety of each sample that was analyzed.

5.4.7 Statistical Analysis of Raman Datasets

All acquired Raman spectra underwent equivalent preprocessing procedures; cosmic ray removal (filter size: 4; dynamic factor: 4.6) is performed on a per-pixel basis in WITec Project FOUR software before data is exported to Matlab® (Mathworks, Inc., Natick, MA) where remainder of preprocessing is executed via an algorithm developed in-house. Spectral background subtraction was performed by regression fitting of baseline estimation throughout multiple shifted windows across the integrated spectrum via spline approximation. To calculate the “integrated Raman intensity” for each area scan (of a single cell or micro-calibration standard), all pixel spectra are added together to generate a single “integrated” spectrum which is representative of the composition and total amount

of material present within the given area scan. The spectral region of interest (2700-3200cm-1) was excised from the integrated spectrum and interpreted via statistical models.

To generate reference spectra, biomolecular components of interest were dissolved in appropriate solvent at ~1mg/mL (DI water for protein and nucleic acid; methanol for lipids and cholesterol) and spotted onto the surface of silicon chips; the solvent evaporated at room temperature, depositing all non-volatile solutes across the surface of silicon chips. Reference spectra were acquired via continuous large area scans of each dried dispersion and the average spectrum across each scan was extracted, thereby generating "molecular fingerprints" for each biochemical component of interest. Using Raman datasets acquired from protein and HDL calibration microarrays, the pure component reference spectra were scaled accordingly to directly relate the total mass of each component present within an analyzed microarray calibration standard to the integrated Raman signal acquired from across that region (i.e., CCD counts / picogram). Measured Raman spectra were deconvoluted via linear combination modelling (aka: non-negative least squares regression modelling) with the ultraquantitative reference spectra as per the following equation:

$$I_{\tilde{\nu}} = N_1 k_{\tilde{\nu}_1} + N_2 k_{\tilde{\nu}_2} + N_3 k_{\tilde{\nu}_3} + N_4 k_{\tilde{\nu}_4} + \varepsilon_{\tilde{\nu}}$$

Where:

$I_{\tilde{\nu}}$ = integrated sample spectrum (CCD counts)

$k_{\tilde{\nu}_n}$ = "n" reference spectrum (CCD counts / picogram)

N_n = "n" measurement (picograms)

$\varepsilon_{\tilde{\nu}}$ = residual spectrum (CCD counts)

$\tilde{\nu}$ = relative wavenumber or Raman shift (cm^{-1})

n = biomolecular component (e.g., protein, lipid, etc.)

The linear combination spectral model accuracy of fit was assessed by calculating coefficient of determination (R^2) for each micro-calibration standard spectrum fit according to the following equation:

$$Spectral\ model\ fit\ (R^2) = 1 - \left(\frac{variance(\varepsilon_{\tilde{\nu}})}{variance(I_{\tilde{\nu}})}\right)$$

Principal component analysis (PCA) was also performed on integrated Raman spectra; standard normal variate scaling was performed on each integrated spectrum prior to PCA execution in Matlab®. Logistic regression analysis of ultraquantitative results (picogram measurements) from cell datasets was performed in R Studio using scripts written in-house.

5.5 Results and Discussion

5.5.1 Quantitative Calibration of Raman Spectral Deconvolution

Quantitative calibration for Raman cytometry was achieved using inkjet-printed micro-calibration standards of known composition using the methodology described for alveolar macrophages in Chapter 4; the linear range was verified across 0-250 picograms of total material (within a given area scan), yielding an R^2 of at least 0.9 for protein, lipid, and protein/lipid measurements. Raman signal-to-mass relationships were established for each biomolecular component of interest (i.e., protein, lipids, cholesterol, and nucleic acids/carbohydrates), yielding quantitatively-calibrated pure component reference spectra (units of CCD count per picogram material). For more in-depth discussion on quantitative calibration and methodology, see calibration dataset used for alveolar macrophage analysis in Chapter 4 of this thesis.

5.5.2 Cytometric Profiling of BAL Cells from Healthy and Fibrotic Mice

Ultraquantitative micro-Raman cytometry revealed the total protein, lipid, nucleic acid, carbohydrate, and cholesterol content of individual alveolar macrophages (AMs) acquired via BAL from the lungs of untreated mice subjects. It is worth noting that the BAL methodology utilized herein flushes the entirety of each subjects' lungs, from the trachea and upper respiratory down, and all cells are mixed together before analysis. The "control" AMs acquired from untreated presumably healthy mice, measured 128±47pg protein/cell, 27±16pg lipid/cell, 3±4pg nucleic acid & carbohydrate/cell, and 3±5pg cholesterol/cell (population average ± S.D.) and established the baseline cytometric profile of "health" for the purposes of this study (Figure 5-1, "Control" group). It should be noted that these values are consistent with average ratios of biomolecular components measured in typical eukaryotic cells.(42-44) Less than 3% of the cells were outliers containing elevated amounts of specific biomolecular components; most cells appeared to contain correlated amounts of protein and lipid (Pearson's coefficient 0.356), while a minority subpopulation of cells deviated from the typical lipid-to-protein ratio, showing disproportionately elevated levels of lipid compared to protein (Figure 5-2, "Control" group). There were also protein-rich outliers (measuring >300pg protein/cell) which exhibited proportionately normal lipid content. Carbohydrate & nucleic acid content showed no apparent correlation with total protein content throughout the control cells, perhaps due to a diverse range of transcriptional activity levels observed throughout single cells. Furthermore, lipid and cholesterol showed somewhat strong correlation (Pearson's coefficient 0.45), suggesting there is a balance between the ratio of these two components in healthy macrophage populations.

Consistent with reports of lipid-laden "foamy" macrophages observed in the lungs of fibrotic patients and of oxidized phospholipid-induced fibrosis in the experimental mouse model herein used, our Raman methodology quantitatively-identified "foamy" lipid-laden macrophages (outlier cells in correlation plots) increased in number and total lipid content, as shown by protein-lipid correlation coefficients shifting from positive (0.356 for control mice) to increasingly negative (-0.158, -0.217, and -0.275 for 1, 4, and 14 days

post-injury groups). It is interesting to note that the protein content only increased slightly following oxidized phospholipid-induced fibrotic lung injury. We also measured significant increases in nucleic acid and carbohydrate content 4 days following injury, with a partial recovery by 14 days post-injury. Furthermore, correlation between protein and carbohydrate/nucleic acid content increased significantly immediately following injury (Pearson's coefficient -0.1 in control group, 0.49 after 1 day, 0.37 after 4 days, and 0.07 after 14 days), presumably due to a temporal response in cell activation status following induction of fibrotic lung injury that eventually returned back to baseline after 14 days. In contrast to cellular nucleic acid and carbohydrate content, lipid and cholesterol cargo loading appears to accumulate and remain elevated 14 days after initial injury induction (Figure 5-1). Additionally, note the strong correlation observed between lipid and cholesterol observed in the post-injury AM populations; based on the data it appears as though elevated cholesterol content inside single-cells is typically associated with corresponding increases in lipid content, although in some cases – as observed in 4 days post-injury group – there may be individual cells carrying increased amounts of phospholipid cargo unaccompanied by a corresponding increase in cholesterol content.

Ultraquantitative cytometry results were corroborated by an alternative statistical approach, principal component analysis (PCA) which was run in parallel on the integrated Raman spectral dataset. PCA is an implicit statistical approach commonly utilized for Raman spectral analysis which generates a set of basis spectra, each accounting for a percent of the variance observed throughout the dataset; the first principal component accounts for the greatest variance and last accounts for mostly noise. When the major peaks of the PCA basis spectra (Figure 5-3A) correspond to wavenumbers (cm^{-1}) of major peaks in molecular species of interest, the PCA score plots can be interpreted in a quasi-meaningful way. For all mouse AM Raman data, the first principal component ("PC 1") accounted for 44.4% of the variance throughout. In the positive space, the major peaks occurred at 1437cm^{-1}, 2850cm^{-1}, and 2884cm^{-1} which correspond with the major vibrational peaks of lipid molecules while the peaks in the negative space closely corresponded to those of proteins and nucleic acids. By corroborating this PCA data with

ultraquantitation results, we can infer with statistical confidence that the major source of compositional variance throughout all cells analyzed was most likely due to changes in the ratio of lipid to protein and/or nucleic acids. The PC scatter plots reveal that a subpopulation of cells from all groups – presumably the lipid-laden outlier cells – reside in the positive realm of PC 1 which suggests disproportionately elevated lipid-to-protein content and corroborates ultraquantitative measurements of lipid-laden macrophages (Figure 5-3B). PC 3 was able to effectively discriminate the 4 days post-injury cells from the rest which could be attributed to differences in lipid but most likely primarily due to disproportionate increases in nucleic acid and carbohydrate content.

Beyond the scope of the intended biomolecular measurements, an unknown chemical entity was detected in punctate cytoplasmic patterns throughout a subpopulation of single cells acquired from untreated mice; the unknown compound emitted relatively strong Raman signals at 1156cm^{-1} and 1559cm^{-1} which did not correspond to any characteristic Raman peaks from the major biomolecular components in typical eukaryotic cells (Figure 5-4). The relatively strong Raman shift at 1559cm^{-1} was indicative of vibrational modes of C=C conjugated double bonds so a multitude of feasible reference compounds were analyzed via micro-Raman in an attempt to match the spectral signals; cytochrome c, heme-containing blood cells, vitamin a, and leukotriene B4 were all analyzed under equivalent acquisition parameters but none matched the unknown signal observed in the subpopulation of cells (Figure 5-10).

5.5.3 Cytometric Phenotyping of Pig BAL Cells Before and During ARDS

Ultraquantitative Raman spectral cytometric analysis of 5 different pigs' physiological baseline BAL cell populations enabled quantitative compositional phenotyping of porcine alveolar macrophages; every animal was an independent experiment, and all were performed on different days (Figure 5-5). The BAL methodology utilized for the anaesthetized pig employs a bronchoscope that was manually directed into a specific lobe of interest in the lower airway of the lung. The pig AMs analyzed herein

were consistently from an anatomically-specific region of the porcine lung (in contrast to the mice AMs). Consistent with literature reports, baseline BAL cell differentials were >90% alveolar macrophages as determined via cytological staining(45). Interindividual differences in compositional phenotypes of baseline AMs were observed between the five animals cytometrically profiled and the most pronounced difference was seen in pigs #2 and #3 where the carbohydrate & nucleic acid contents were slightly elevated compared to other subjects at baseline. Additionally, the frequency of lipid-laden outlier cells in pig #2 was greater than all other animals at baseline (although pig #2 had less lipid-laden outlier cells compared to any of the fibrotic mice). BAL cell populations from pigs #1, #4, and #5 measure at most (within a single cell) 30pg of carbohydrate & nucleic acid whereas pigs #2 and #3 had at least 10% of cells measuring >40pg carbohydrate & nucleic acid. There are a multitude of feasible explanations for elevated nucleic acid & carbohydrate content in alveolar macrophages acquired from untreated pigs; one possible explanation is the presence of an intracellular microbial pathogen known as *Mycoplasma hyopneumoniae.* Known to be endemic throughout pig herds worldwide, this pathogen can be a significant economic burden for the pig farming industry because it is estimated to infect nearly ~10% of animals(46). Alternatively, increased carbohydrate & nucleic acid content could be explained by metabolic changes or increased transcriptional activation state due to other unknown causes. Compositional correlation plots reveal that increases in carbohydrate & nucleic acid content are correlated with increases in protein content within individual cells to a near-equivalent degree throughout each animal's baseline AM population, regardless of the frequency of carbohydrate & nucleic acid-rich outlier cells (Figure 5-6). Carbohydrate & nucleic acid exhibited consistently weakly negative correlation with lipid content, suggesting cellular content of these two components are independently regulated. Furthermore, though not observed in all pigs' AM populations, lipid and cholesterol content were strongly correlated. Although elevated cholesterol content typically corresponded to increased lipid content, increased lipid content was also detected independently without proportionate increase in cholesterol in a subpopulation of cells.

As previously described for the mice AM analysis, the ultraquantitative results for the baseline pig spectral dataset were corroborated by PCA which generated a unique set of basis spectra to implicitly account for the spectral variance observed throughout the Raman dataset (Figure 5-7). Though biochemically-informed interpretation of PC1 was initially difficult, many of the peaks corresponded with those of pure DNA, thereby indirectly verifying the ultraquantitative results. Additionally, outlier cells were accounted for by PC2 and PC3, as can be clearly seen in the PC3 vs. PC2 scatter plots. In the positive space, PC2 closely represents protein spectral signature, while the negative space of PC2 corresponds with lipid; PC3 corresponds with lipid in the positive space and carbohydrate & nucleic acid in the negative space. Although difficult to interpret with biomolecular-relevance, the heterogeneity detected by PCA serves to verify the ultraquantitative results; using ultraquantitation, phenotypically-diverse AM populations (as observed in pigs #2 and #3) were quantitively characterized while the results were simultaneously verified in an unbiased manner by PCA. Where PCA provides a qualitative measure of cell population heterogeneity, the major advantage of ultraquantitation lies in its ability to provide actual picogram measurements of the biomolecular changes occurring inside single cells and throughout each population.

To show proof-of-concept for temporal profiling of AMs during ARDS, we performed a sequential BAL at time=8hr following the multi-insult injury of anesthetized pig #2. Cytocentrifugation and staining of baseline and ARDS BAL cells revealed a significant shift in cell differential from primarily AMs (91%) to primarily neutrophils (94%) 8hr after the injury; it should be noted that there was a significant increase in the concentration of BAL cells during ARDS ($1.2 \bullet 10^6$ cells/mL at baseline vs $20.8 \bullet 10^6$ cells/mL at 8hr) such that the total number of macrophages was actually relatively similar between lavages, suggesting there was a massive influx of neutrophils into the alveolar space by the 8hr timepoint (Figure 5-8, A & B). The BAL cell preparation for Raman analysis involves adherence of cells to silicon chip which tends to separate out some neutrophils, but further developments are necessary to confidently separate the two cell types in mixed-differential BAL suspensions; for the purposes of this analysis we exploited

the apparent size differences of neutrophils and AMs to manually select and analyze cells that appeared to be AMs. Integrated Raman spectra from 100 cells from each population (Figure 5-8C) were deconvoluted via linear combination modelling with pure component reference spectra (Figure 5-8D) to yield picogram measurements for each major biomolecular component of interest on the single-cell basis. Compositional correlation plots revealed significant increases in protein, carbohydrate & nucleic acid content in the ARDS population (Figure 5-8E). Despite increases in cellular protein content, the lipid-to-protein ratio remained similar as evidenced by the unchanged correlation coefficient (Figure 5-8F). This observation could be explained by phagocytosis of neutrophils, NETs, other cellular debris, or perhaps an increased transcriptional activation state of the AMs during ARDS; further studies are necessary to confirm and test these hypotheses. PCA was used to corroborate ultraquantitative results; integrated Raman spectra from 100 baseline cells and 100 ARDS cells yielded similar basis spectra as the interindividual analysis of multiple pig subjects at baseline (Figure 5-9A). Specifically, PC1 was nearly identical between the analyses. This was particularly interesting because ultraquantitative results attributed the major biomolecular differences to increased carbohydrate & nucleic acid content, which was observed in pig#2 baseline (compared to other pig subjects) as well as in pig #2 ARDS timepoint (where carbohydrates & nucleic acids increased to an even greater extent). Many cells overlap between groups (baseline vs ARDS) in the PC and compositional scatterplots, which was expected because they are heterogeneous populations (Figure 5-9B). Furthermore, an unknown signal contributor, emitting strong Raman signals at ~1467cm^{-1}, was detected in punctate cytoplasmic patterns in ~10% of cells during ARDS (time=8hr post-injury); this unknown signal was unique from that observed in the untreated mouse AMs and we were unable to match it with reference spectra during preliminary experiments (Figure 5-10). Regardless, there were subpopulations of cells that could be clearly distinguished between these groups and thereby showing proof-of-concept for the application of Raman cytometric phenotyping in the context of acute lung injuries such as ARDS.

5.6 Conclusions

Absolute measurements of individual engorged outlier macrophages – for both increased absolute mass and disproportionate increases in specific biomolecular component content (i.e., lipids and nucleic acids) – highlight the advantages of the ultraquantitative micro-Raman methodology presented herein for analysis of complex populations at the single-cell level where conventional biomolecular assays lose resolution due to measuring only population average values. By traditional techniques, cell suspensions are commonly homogenized before assaying homogenate solution for specific biomolecular components separately; in contrast to traditionally-limited approaches, our methodology enabled the simultaneous measurement of multiple biomolecular components inside single cells, thereby providing a more representative picture of individual cells' compositional phenotypes and cell-to-cell variability throughout different populations and during disease pathogenesis. Furthermore, the ability to non-specifically detect unknown chemical entities inside individual cells opens the doors of scientific perception to a previously-unexplored realm, specifically in terms of diagnostic potential for human patients with IPF, with potential to take the "idiopathic" out of idiopathic pulmonary fibrosis by identifying unknown macrophage cargo that may be contributing to IPF pathogenesis.

Although the ultraquantitative Raman measurements presented herein represent an advancement in the field of quantitative Raman cytometry, we have only shown proof-of-concept for the translational feasibility of the methodology in the context of *in vivo* experimental disease pathogenesis. We hypothesize that the clinical setting and human populations are where the major untapped advantages of this technique will emerge, specifically in terms of quantitative Raman-based characterization of patient-specific AM cargo (e.g., lipids, cholesterol, exposure to pollutants, toxins, drugs, pathogens, etc.) and how cargo loading of the macrophage-mucociliary clearance complex relates to idealized health. As humanity further engineers a future fraught with chemicals and xenobiotic material, there will foreseeably arise a biomedical niche for quantitative assessment of the degree of cargo loading within an individual's alveolar macrophage population. It will

be important to profile a multitude of healthy “control” individuals to obtain a quantitative baseline cytometric profile of idealized health. Further advances in quantitative analysis approaches and micro-calibration technology will enable faster, more accurate and reliable measurements, but the methodology proposed herein will remain relevant.

5.7 Acknowledgements

I thank Dr. Tom Sisson and Dr. Patrick Bradley for collaborating and performing the fibrotic mouse experiments. I thank Michigan Center for Integrative Research in Critical Care (MCIRCC), Dr. Kevin Ward, Dr. Hakam Tiba, Brendan McCracken, and Dr. Robert Dickson for help with the porcine experiments.

5.8 Figures

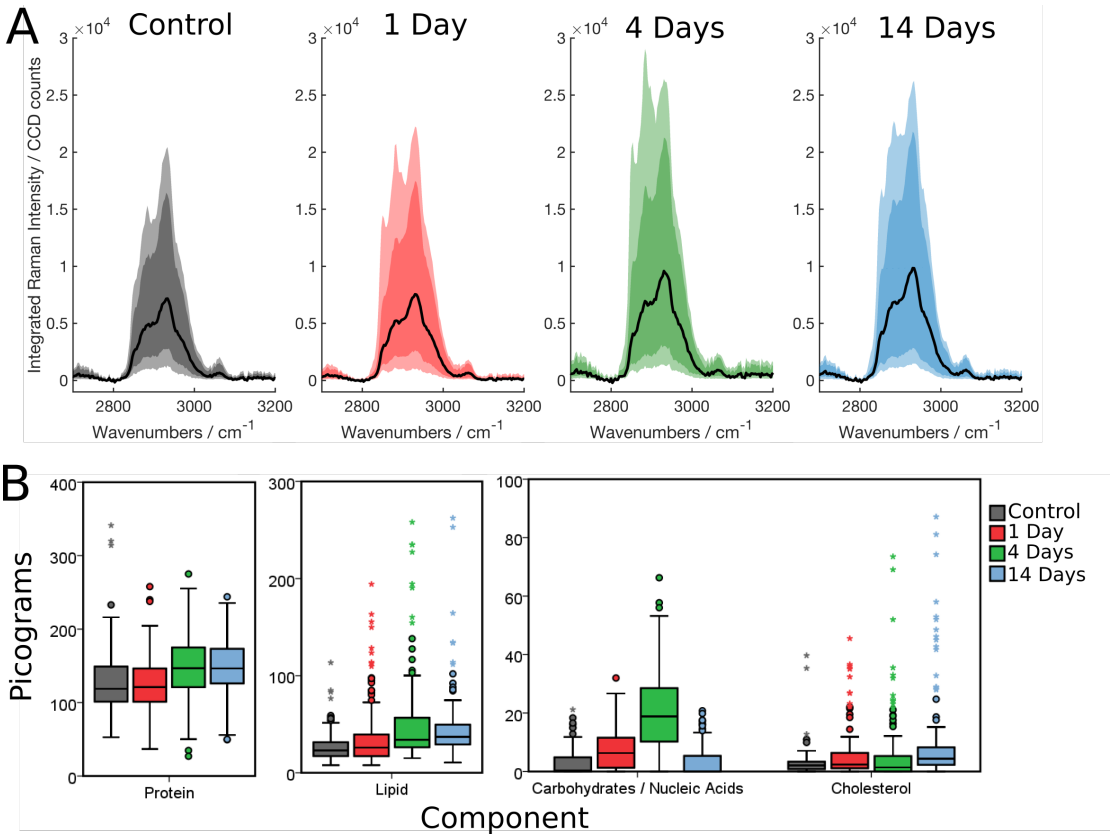

Figure 5-1. Raman spectral quantitation results for BAL cells of untreated and fibrotic mice.

(A) Integrated Raman spectral datasets from BAL cell populations; median spectra shown as solid black lines with 0.05, 0.25, 0.75. and 0.95 quantiles shown by shadows. n=150 cells each group (3 mice per group, 50 cells per mouse). **(B)** Population distribution boxplots to visualize the quantitative results from linear combination modelling of integrated Raman spectra using pure component reference spectra.

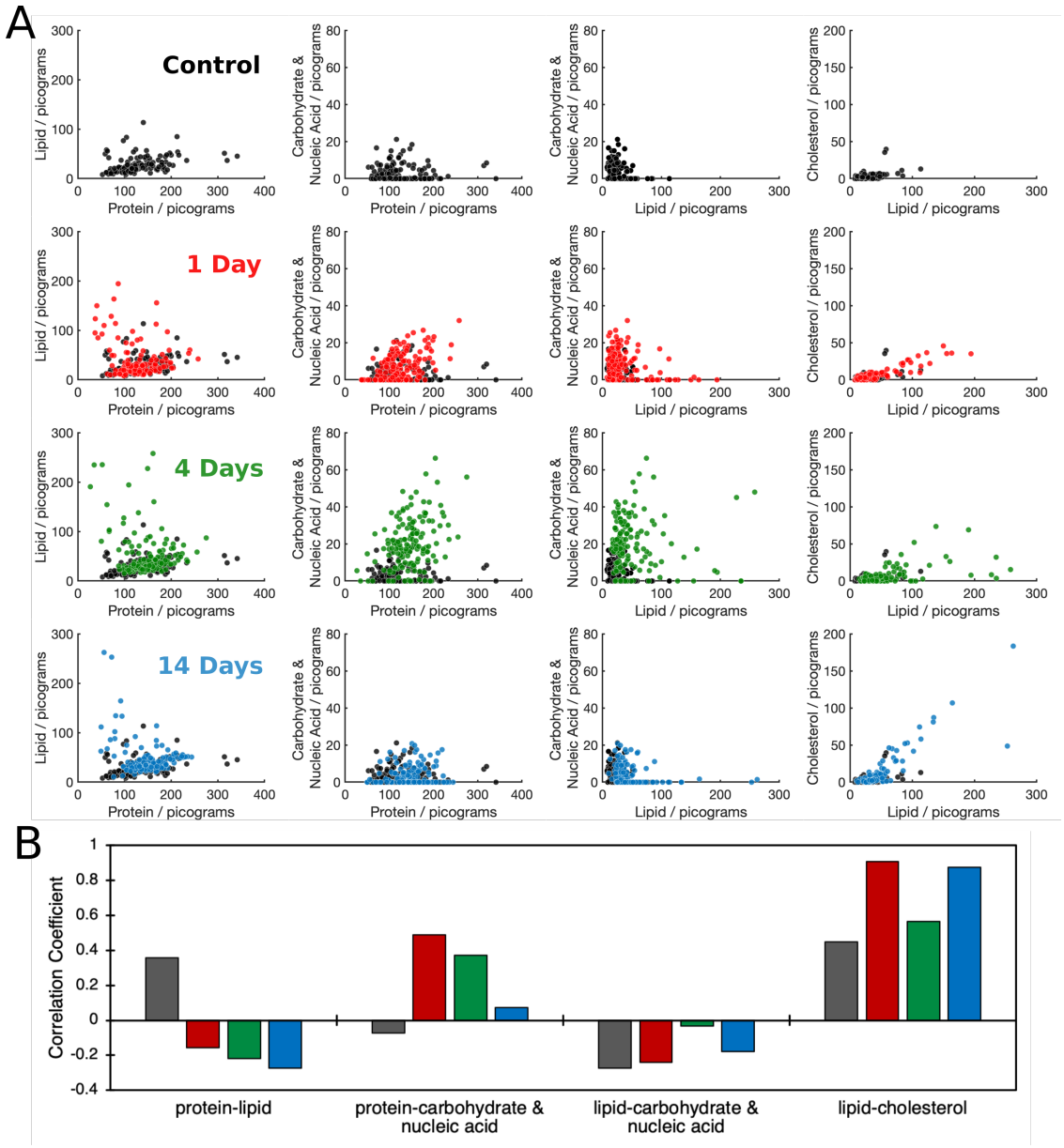

Figure 5-2. Compositional cytometry results for *in vivo* pulmonary fibrosis mouse model.

(A) Component-component correlation plots illustrating the relationship and balance between biomolecular content on single-cell basis throughout BAL cell populations from healthy (control) and fibrotic mice subjects; each point represents a single cell. **(B)** Pearson's correlation coefficients calculated from the compositional correlation plots.

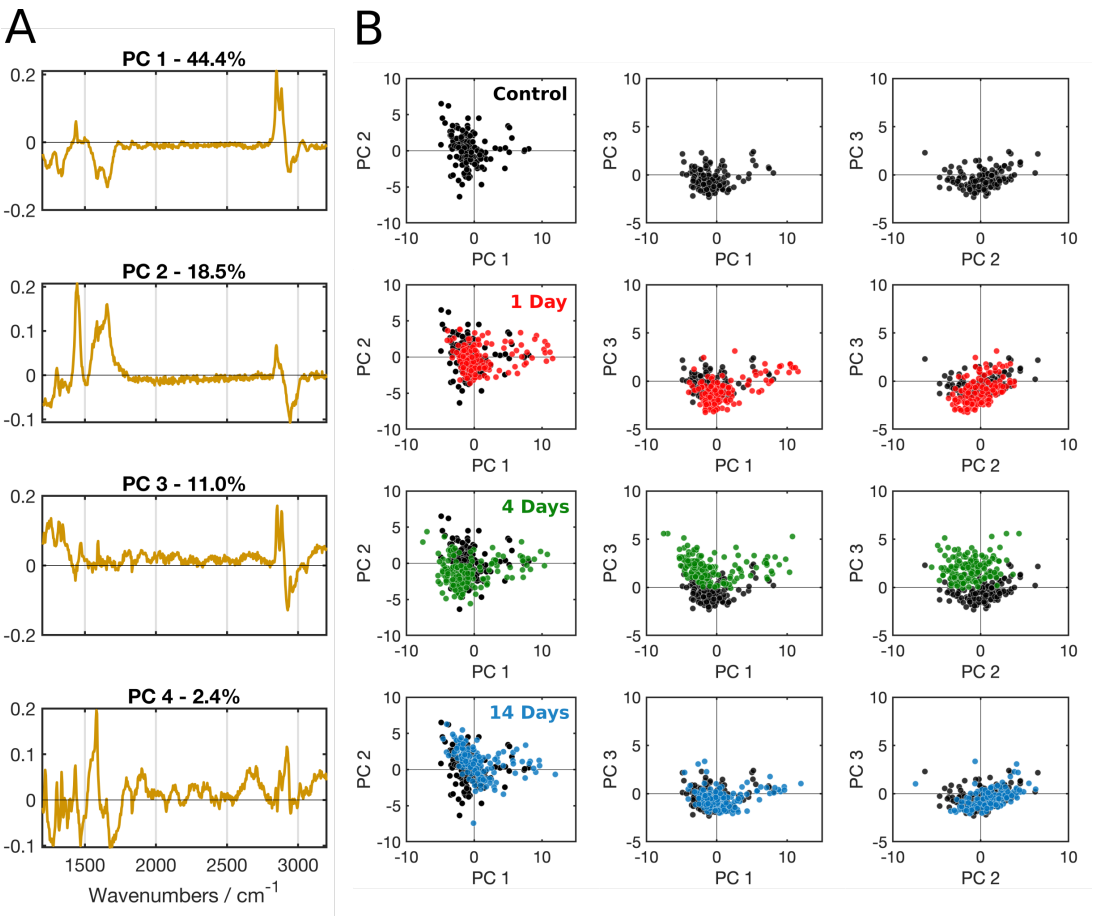

Figure 5-3. Principal component analysis for *in vivo* pulmonary fibrosis mouse model.

(A) Basis spectra with corresponding percent of spectral variance accounted for throughout entire Raman dataset. **(B)** PC scatter plots comparing the PCA results from fibrotic subjects' cell populations (colored points) to the control groups (black points).

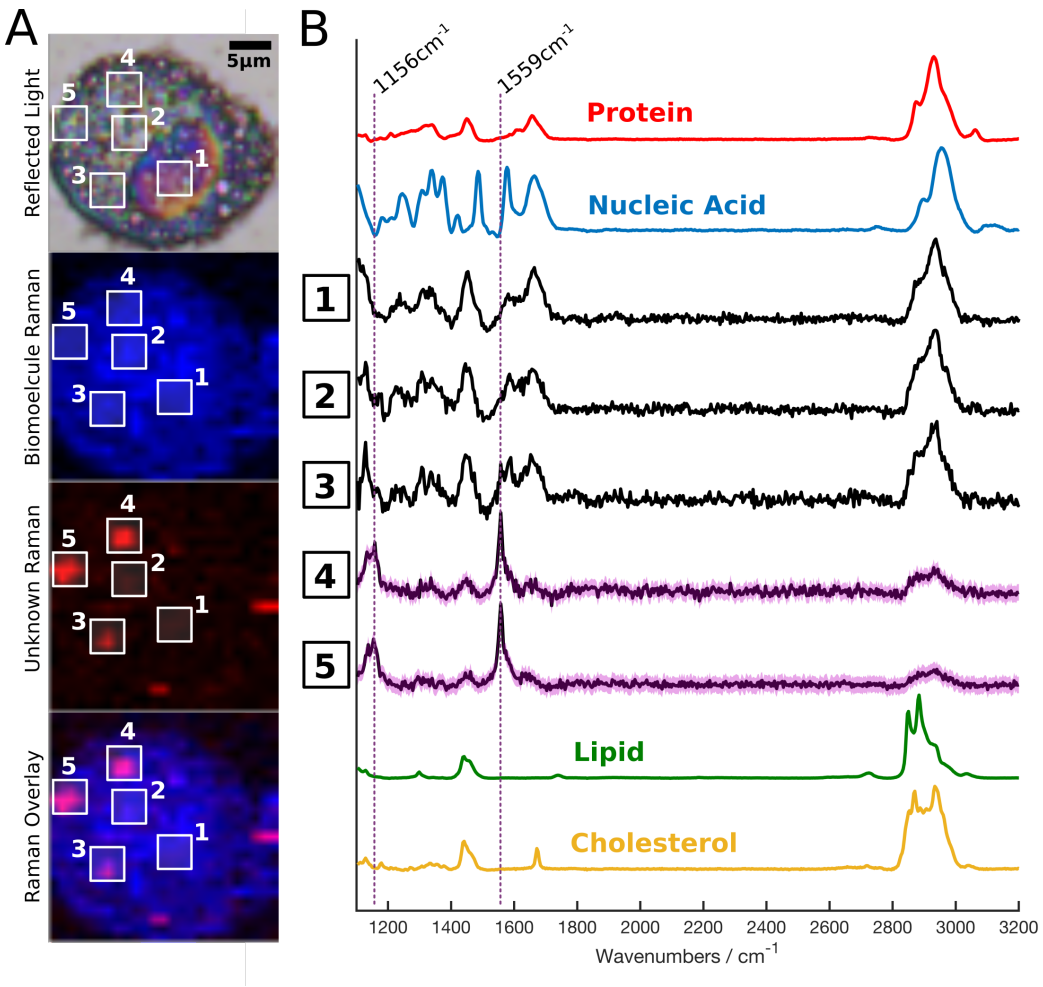

Figure 5-4. Single-cell Raman data reveals unknown signal contributor present in punctate pattern throughout cytoplasm of individual cells.

(A) Reflected brightfield image and corresponding Raman images of a single alveolar macrophage acquired from an untreated mouse subject via BAL; Biomolecule and Unknown Raman images were generated by plotting signal intensities at 2930cm^{-1} and 1559cm^{-1} respectively. **(B)** Raman spectral overlay showing biomolecular component reference spectra (in color with labels) and extracted spectra from indicated subcellular regions of the cell.

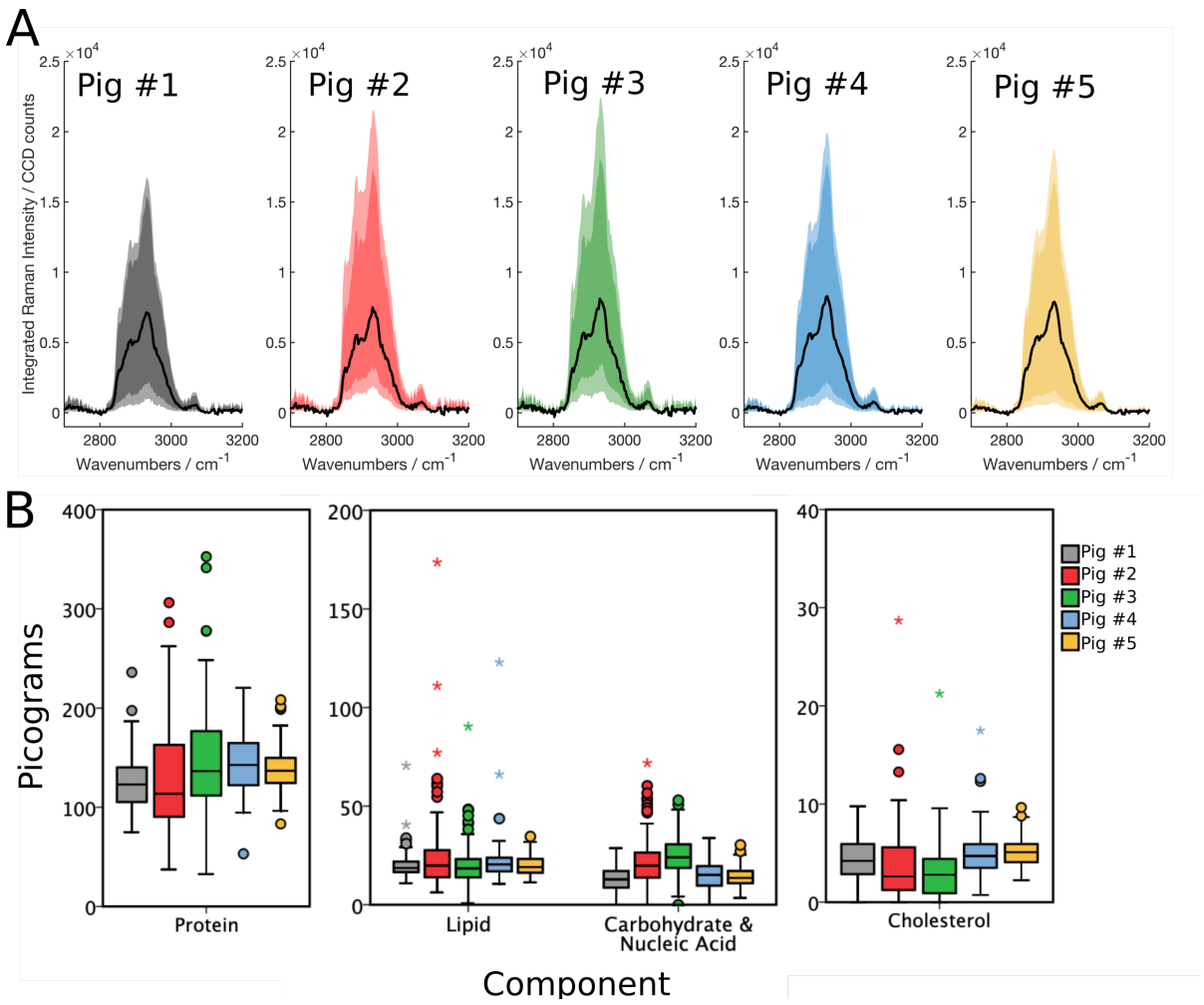

Figure 5-5. Raman spectral quantitation results for BAL cell populations acquired at baseline profile for 5 different pig subjects.

(A) Integrated Raman spectral datasets from BAL cell populations (at least 100 cells each group); median spectra shown as solid black lines with 0.05, 0.25, 0.75. and 0.95 quantiles shown by shadows. **(B)** Population distribution boxplots to visualize the quantitative results from linear combination modelling of integrated Raman spectra using pure component reference spectra.

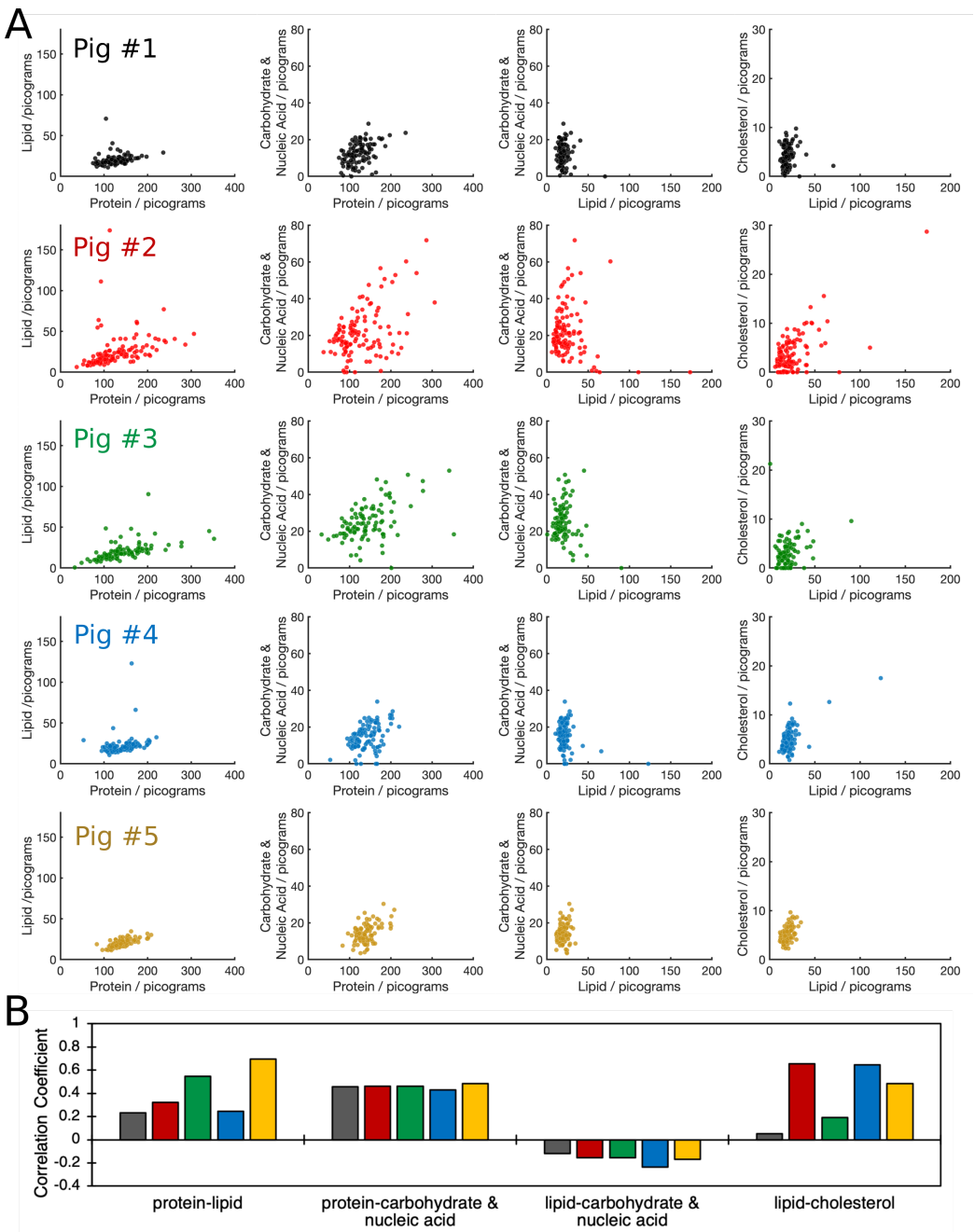

Figure 5-6. Compositional cytometry results for baseline BAL cell profiles from 5 different pig subjects.

(A) Component-component correlation plots illustrating the relationship and balance between biomolecular content on single-cell basis throughout BAL cell populations from baseline profile of different animal subjects; each point represents a single cell. **(B)** Pearson's correlation coefficients calculated from the compositional correlation plots.

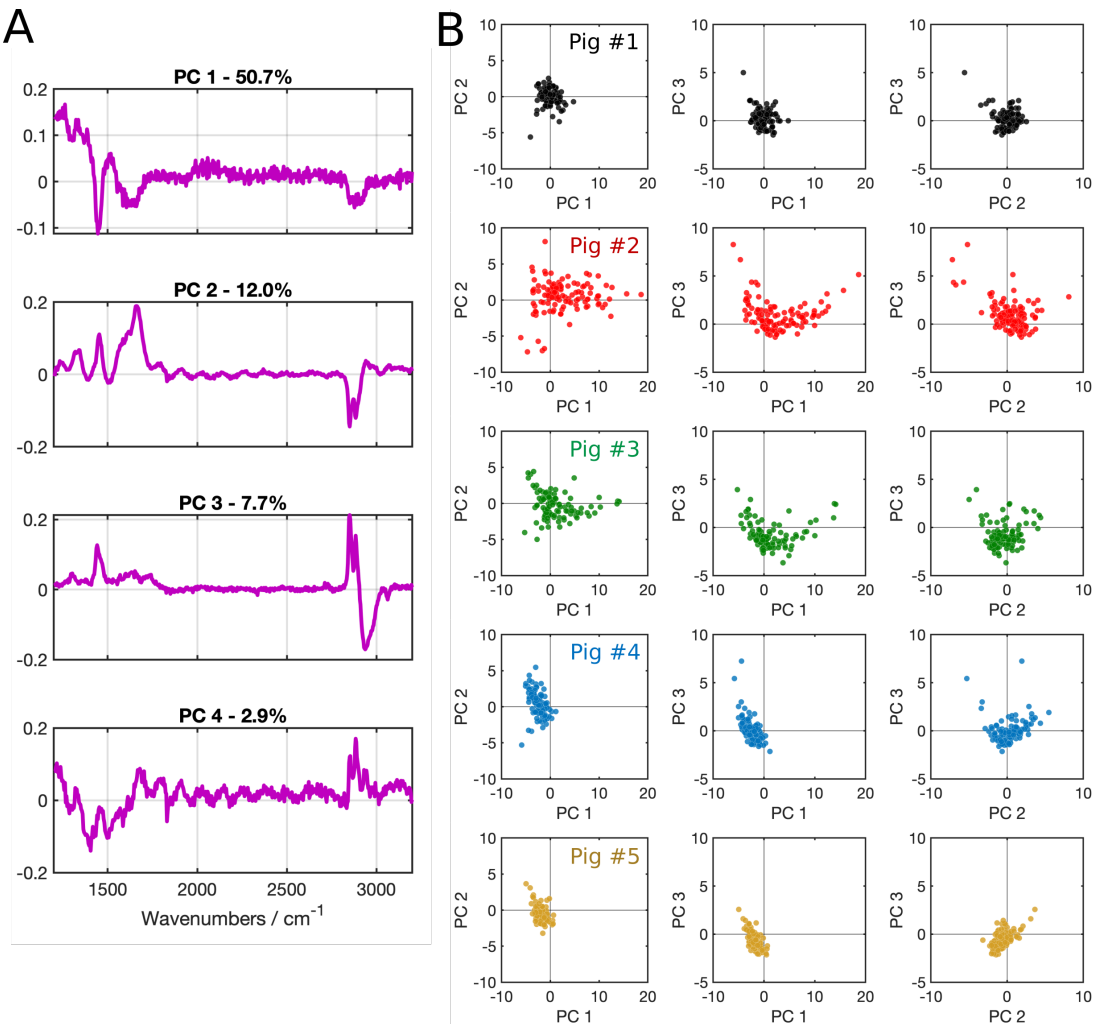

Figure 5-7. Principal component analysis comparing interindividual variability of baseline BAL cell populations.

(A) Basis spectra with corresponding percent of spectral variance accounted for throughout entire Raman dataset. **(B)** PC scatter plots comparing the distribution of PCA results from each subject's cell population.

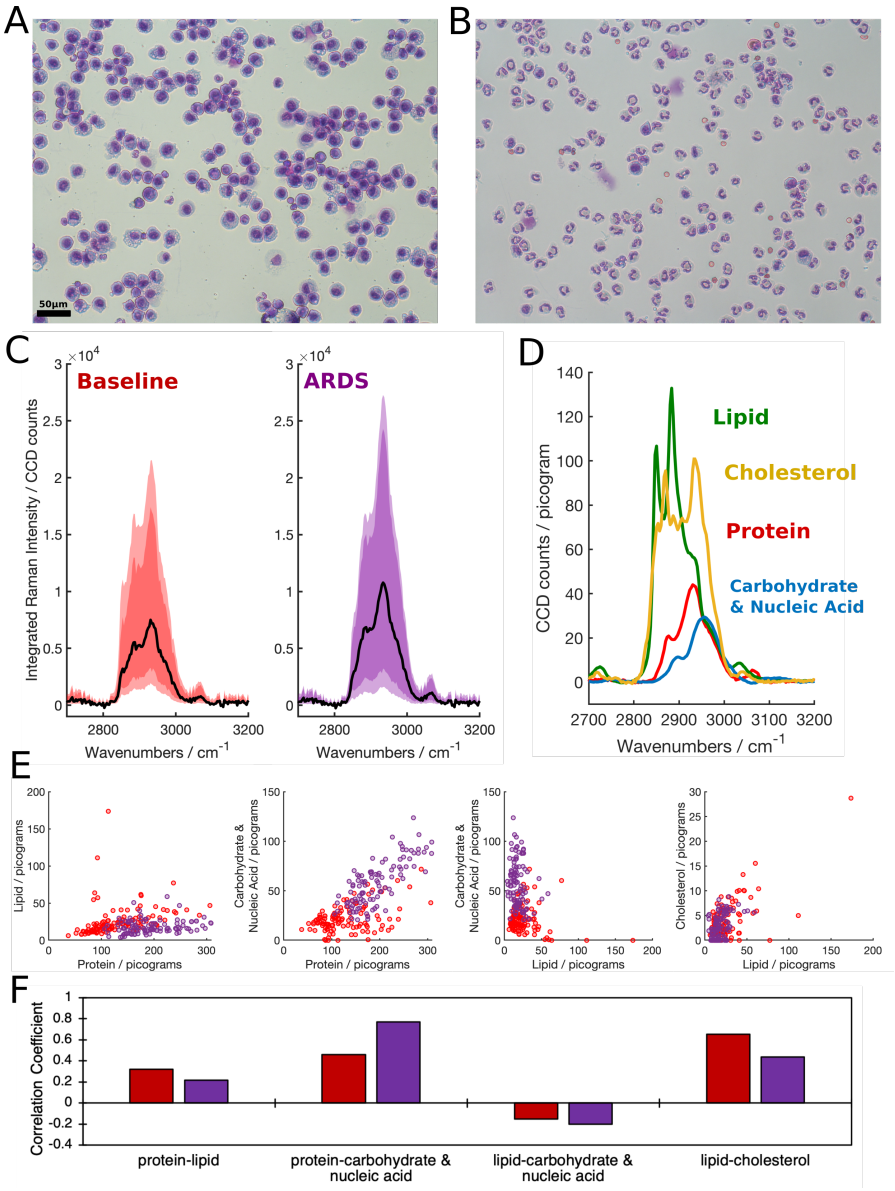

Figure 5-8. Sequential BAL analysis at baseline and during ARDS for *in vivo* multi-insult model in a single pig subject.

(A) Cytological stain of BAL samples at baseline (time=0hr) and **(B)** ARDS (time=8hr). **(C)** Integrated Raman spectral datasets from BAL cell populations (100 cells each group); median spectra shown as solid black lines with 0.05, 0.25, 0.75. and 0.95 quantiles shown by shadows. **(D)** Ultraquantitative reference spectra used for linear combination modelling. **(E)** Compositional correlation plots and **(F)** Pearson's correlation coefficients for ultraquantitative cytometry results.

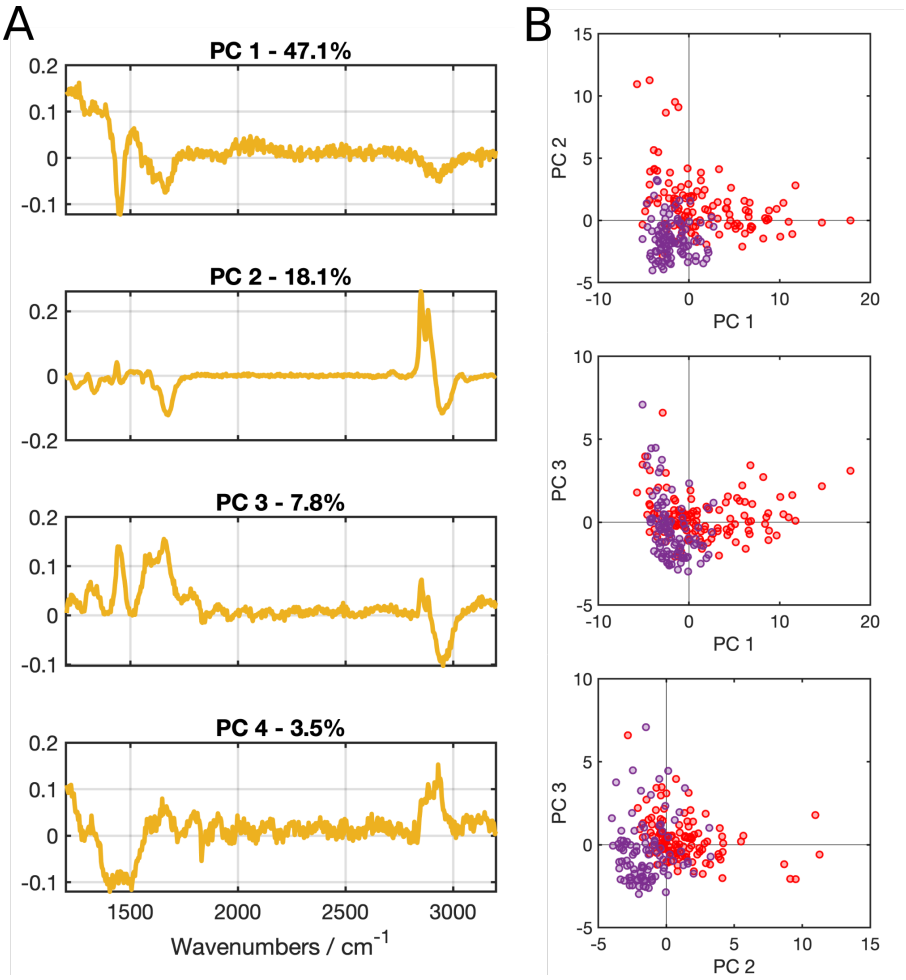

Figure 5-9. Principal component analysis at baseline and during ARDS for *in vivo* multi-insult model in a single pig subject.

(A) Basis spectra with corresponding percent of spectral variance accounted for throughout entire Raman dataset. **(B)** PC scatter plots comparing the distribution of PCA results for AM cell population between baseline and during ARDS timepoint of experiment.

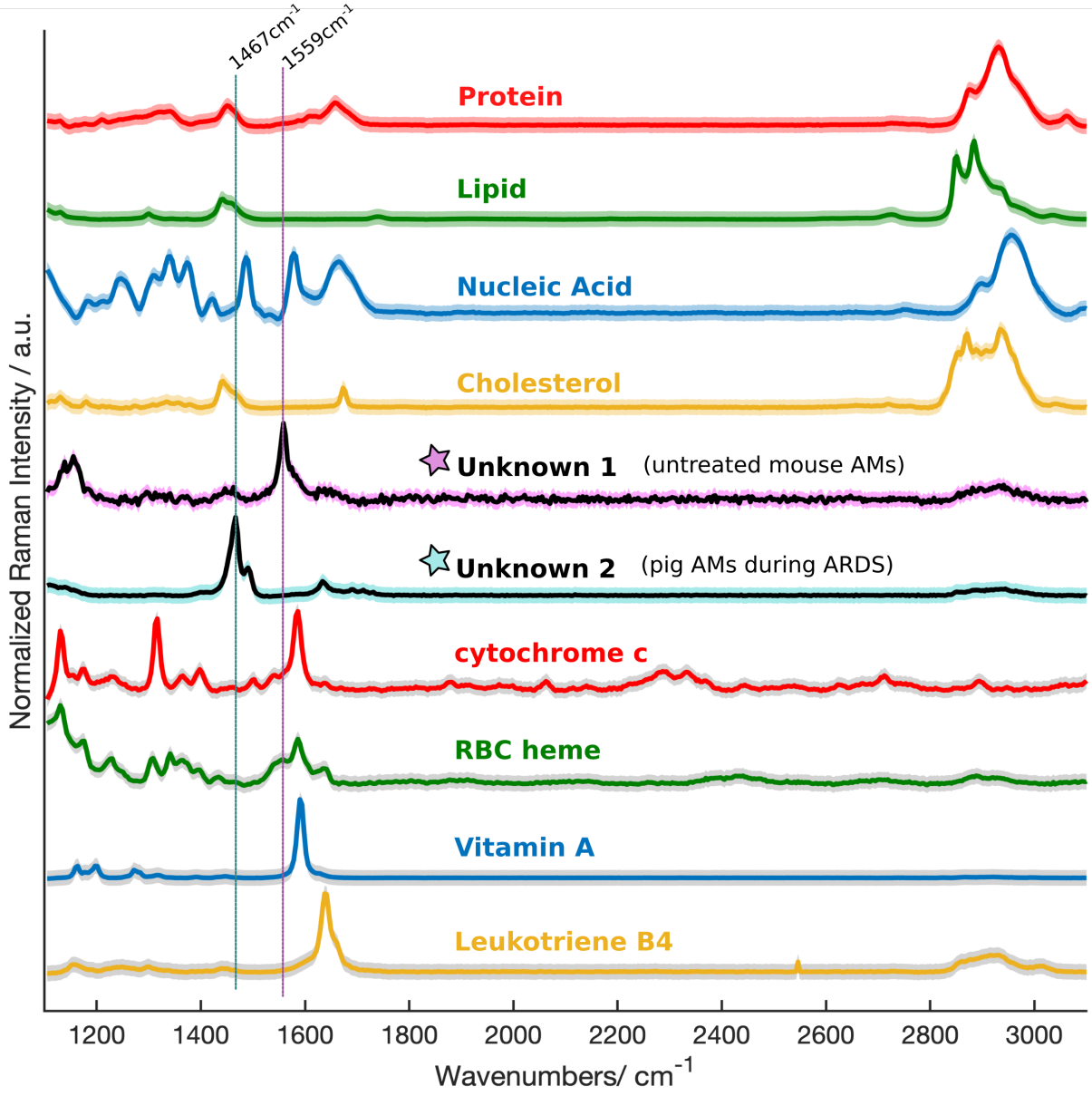

Figure 5-10. Spectral overlay of major biomolecular components, unknown signal contributors, and other test compounds.

Raman spectral overlay showing the characteristic signal peaks emitted from unknown 1 (observed in untreated mouse AMs) and unknown 2 (observed in pig AMs during progression of ARDS. The unknown signal contributors did not match any of the reference compounds tested; the signals appear in region of the spectrum where conjugated double bonds typically produce signals (1450-1650cm^{-1}).

5.9 References

1. Hocking WG, Golde DW. The pulmonary-alveolar macrophage. New England Journal of Medicine. 1979;301(11):580-7.

2. Lehnert BE. Pulmonary and thoracic macrophage subpopulations and clearance of particles from the lung. Environmental Health Perspectives. 1992;97:17-46. doi: 10.1289/ehp.929717.

3. Franks TJ, Colby TV, Travis WD, Tuder RM, Reynolds HY, Brody AR, et al. Resident Cellular Components of the Human Lung. Proceedings of the American Thoracic Society. 2008;5(7):763-6. doi: 10.1513/pats.200803-025HR.

4. Fels AO, Cohn ZA. The alveolar macrophage. Journal of Applied Physiology. 1986;60(2):353-69.

5. Hussell T, Bell TJ. Alveolar macrophages: plasticity in a tissue-specific context. Nature Reviews Immunology. 2014;14(2):81-93. doi: 10.1038/nri3600.

6. Hunninghake GW, Gadek JE, Kawanami O, Ferrans VJ, Crystal RG. Inflammatory and immune processes in the human lung in health and disease: evaluation by bronchoalveolar lavage. The American Journal of Pathology. 1979;97(1):149-206.

7. Laskin DL, Weinberger B, Laskin JD. Functional heterogeneity in liver and lung macrophages. Journal of Leukocyte Biology. 2001;70(2):163-70. doi: 10.1189/jlb.70.2.163.

8. Harbison ML, Godleski JJ, Mortara M, Brain JD. Correlation of lung macrophage age and surface antigen in the hamster. Laboratory Investigation. 1984;50(6):653-8.

9. Bursuker I, Goldman R. On the origin of macrophage heterogeneity: a hypothesis. Journal of the Reticuloendothelial Society. 1983;33(3):207-20.

10. Zwilling BS, Campolito LB, Reiches NA. Alveolar Macrophage Subpopulations Identified by Differential Centrifugation on a Discontinuous Albumin Density Gradient. American Review of Respiratory Disease. 1982;125(4):448-52. doi: 10.1164/arrd.1982.125.4.448.

11. Landsman L, Jung S. Lung Macrophages Serve as Obligatory Intermediate between Blood Monocytes and Alveolar Macrophages. The Journal of Immunology. 2007;179(6):3488. doi: 10.4049/jimmunol.179.6.3488.

12. Tarling JD, Coggle JE. Evidence for the pulmonary origin of alveolar macrophages. Cell Proliferation. 1982;15(6):577-84. doi: 10.1111/j.1365-2184.1982.tb01064.x.

13. Tarling JD, Lin H-s, Hsu S. Self-Renewal of Pulmonary Alveolar Macrophages: Evidence From Radiation Chimera Studies. Journal of Leukocyte Biology. 1987;42(5):443-6. doi: 10.1002/jlb.42.5.443.

14. Gross TJ, Hunninghake GW. Idiopathic Pulmonary Fibrosis. New England Journal of Medicine. 2001;345(7):517-25. doi: 10.1056/NEJMra003200.

15. King TE, Pardo A, Selman M. Idiopathic pulmonary fibrosis. The Lancet. 2011;378(9807):1949-61. doi: https://doi.org/10.1016/S0140-6736(11)60052-4.

16. Garg J, Agrawal N, Marballi A, Agrawal S, Rawat N, Sule S, et al. Amiodarone induced pulmonary toxicity: An unusual response to steroids. The American Journal of Case Reports. 2012;13:62.

17. Ott MC, Khoor A, Leventhal JP, Paterick TE, Burger CD. Pulmonary toxicity in patients receiving low-dose amiodarone. Chest. 2003;123(2):646-51.

18. Adamson IY, Bowden DH. The pathogenesis of bleomycin-induced pulmonary fibrosis in mice. The American Journal of Pathology. 1974;77(2):185-97.

19. Bedrossian CW, Miller WC, Luna MA. Methotrexate-induced diffuse interstitial pulmonary fibrosis. Southern Medical Journal. 1979;72(3):313-8.

20. KATZENSTEIN A-LA, MYERS JL. Idiopathic Pulmonary Fibrosis. American Journal of Respiratory and Critical Care Medicine. 1998;157(4):1301-15. doi: 10.1164/ajrccm.157.4.9707039.

21. Ley B, Collard HR, Talmadge E. King J. Clinical Course and Prediction of Survival in Idiopathic Pulmonary Fibrosis. American Journal of Respiratory and Critical Care Medicine. 2011;183(4):431-40. doi: 10.1164/rccm.201006-0894CI.

22. HUNNINGHAKE GW, ZIMMERMAN MB, SCHWARTZ DA, TALMADGE E. KING J, LYNCH J, HEGELE R, et al. Utility of a Lung Biopsy for the Diagnosis of Idiopathic Pulmonary Fibrosis. American Journal of Respiratory and Critical Care Medicine. 2001;164(2):193-6. doi: 10.1164/ajrccm.164.2.2101090.

23. Collins CD, Wells AU, Hansell DM, Morgan RA, MacSweeney JE, Du Bois RM, et al. Observer variation in pattern type and extent of disease in fibrosing alveolitis on thin section computed tomography and chest radiography. Clinical Radiology. 1994;49(4):236-40. doi: https://doi.org/10.1016/S0009-9260(05)81847-1.

24. MacDonald SLS, Rubens MB, Hansell DM, Copley SJ, Desai SR, Bois RMd, et al. Nonspecific Interstitial Pneumonia and Usual Interstitial Pneumonia: Comparative

Appearances at and Diagnostic Accuracy of Thin-Section CT. Radiology. 2001;221(3):600-5. doi: 10.1148/radiol.2213010158.

25. Aziz ZA, Wells AU, Hansell DM, Bain GA, Copley SJ, Desai SR, et al. HRCT diagnosis of diffuse parenchymal lung disease: inter-observer variation. Thorax. 2004;59(6):506. doi: 10.1136/thx.2003.020396.

26. Ohshimo S, Bonella F, Cui A, Beume M, Kohno N, Guzman J, et al. Significance of Bronchoalveolar Lavage for the Diagnosis of Idiopathic Pulmonary Fibrosis. American Journal of Respiratory and Critical Care Medicine. 2009;179(11):1043-7. doi: 10.1164/rccm.200808-1313OC.

27. Romero F, Shah D, Duong M, Penn RB, Fessler MB, Madenspacher J, et al. A Pneumocyte–Macrophage Paracrine Lipid Axis Drives the Lung toward Fibrosis. American Journal of Respiratory Cell and Molecular Biology. 2015;53(1):74-86. doi: 10.1165/rcmb.2014-0343OC.

28. Ware LB, Matthay MA. The Acute Respiratory Distress Syndrome. New England Journal of Medicine. 2000;342(18):1334-49. doi: 10.1056/nejm200005043421806.

29. Pepe PE, Potkin RT, Reus DH, Hudson LD, Carrico CJ. Clinical predictors of the adult respiratory distress syndrome. The American Journal of Surgery. 1982;144(1):124-30. doi: https://doi.org/10.1016/0002-9610(82)90612-2.

30. Hudson LD, Milberg JA, Anardi D, Maunder RJ. Clinical risks for development of the acute respiratory distress syndrome. American Journal of Respiratory and Critical Care Medicine. 1995;151(2):293-301. doi: 10.1164/ajrccm.151.2.7842182.

31. Moss M, Bucher B, Moore FA, Moore EE, Parsons PE. The Role of Chronic Alcohol Abuse in the Development of Acute Respiratory Distress Syndrome in Adults. JAMA. 1996;275(1):50-4. doi: 10.1001/jama.1996.03530250054027.

32. Teerakanok J, Tantrachoti P, Chariyawong P, Nugent K. Acute Amiodarone Pulmonary Toxicity After Surgical Procedures. The American Journal of the Medical Sciences. 352(6):646-51. doi: 10.1016/j.amjms.2016.08.013.

33. Ashrafian H, Davey P. Is amiodarone an underrecognized cause of acute respiratory failure in the ICU? CHEST Journal. 2001;120(1):275-82.

34. Prescott SM, McIntyre TM, Zimmerman G. Two of the usual suspects, platelet-activating factor and its receptor, implicated in acute lung injury. The Journal of Clinical Investigation. 1999;104(8):1019-20. doi: 10.1172/JCI8506.

35. Matthay MA. Conference Summary: Acute Lung Injury. Chest. 1999;116:119S-26S. doi: https://doi.org/10.1378/chest.116.suppl_1.119S.

36. Brinkmann V, Reichard U, Goosmann C, Fauler B, Uhlemann Y, Weiss DS, et al. Neutrophil Extracellular Traps Kill Bacteria. Science. 2004;303(5663):1532. doi: 10.1126/science.1092385.

37. Fuchs TA, Abed U, Goosmann C, Hurwitz R, Schulze I, Wahn V, et al. Novel cell death program leads to neutrophil extracellular traps. The Journal of Cell Biology. 2007;176(2):231. doi: 10.1083/jcb.200606027.

38. Saffarzadeh M, Preissner KT. Fighting against the dark side of neutrophil extracellular traps in disease: manoeuvres for host protection. Current Opinion in Hematology. 2013;20(1):3-9. doi: 10.1097/MOH.0b013e32835a0025.

39. Teder P, Vandivier RW, Jiang D, Liang J, Cohn L, Puré E, et al. Resolution of Lung Inflammation by CD44. Science. 2002;296(5565):155. doi: 10.1126/science.1069659.

40. Farrera C, Fadeel B. Macrophage Clearance of Neutrophil Extracellular Traps Is a Silent Process. The Journal of Immunology. 2013. doi: 10.4049/jimmunol.1300436.

41. Thille AW, Esteban A, Fernández-Segoviano P, Rodriguez J-M, Aramburu J-A, Peñuelas O, et al. Comparison of the Berlin Definition for Acute Respiratory Distress Syndrome with Autopsy. American Journal of Respiratory and Critical Care Medicine. 2013;187(7):761-7. doi: 10.1164/rccm.201211-1981OC.

42. Mourant JR, Short KW, Carpenter S, Kunapareddy N, Coburn L, Powers TM, et al. Biochemical differences in tumorigenic and nontumorigenic cells measured by Raman and infrared spectroscopy. Journal of Biomedical Optics. 2005;10(3):031106-03110615. doi: 10.1117/1.1928050.

43. Mourant JR, Dominguez J, Carpenter S, Powers TM, Guerra A, Short KW, et al., editors. Determining the gross biochemical composition of cells and tissue with Raman spectroscopy. Biomedical Optics 2006; 2006: International Society for Optics and Photonics.

44. Kuzmin AN, Levchenko SM, Pliss A, Qu J, Prasad PN. Molecular profiling of single organelles for quantitative analysis of cellular heterogeneity. Scientific Reports. 2017;7(1):6512. doi: 10.1038/s41598-017-06936-z.

45. Judge EP, Hughes JML, Egan JJ, Maguire M, Molloy EL, O'Dea S. Anatomy and Bronchoscopy of the Porcine Lung. A Model for Translational Respiratory Medicine.

American Journal of Respiratory Cell and Molecular Biology. 2014;51(3):334-43. doi: 10.1165/rcmb.2013-0453TR.

46. Moorkamp L, Hewicker-Trautwein M, Grosse Beilage E. Occurrence of Mycoplasma hyopneumoniae in Coughing Piglets (3–6 weeks of age) from 50 Herds with a History of Endemic Respiratory Disease. Transboundary and Emerging Diseases. 2009;56(1-2):54-6. doi: 10.1111/j.1865-1682.2008.01057.x.

CHAPTER 6

Measuring Fenretinide Tissue-Penetration and Spatial Drug Distribution after Local Delivery in Buccal Epithelial with Quantitative Raman Spectroscopy

6.1 Relevance to Thesis

To expand the application of micro-Raman spectroscopy beyond the scope of single-cell analyses thus far explored, I performed quantitative Raman image analysis to characterize the controlled-release and distribution of a lipophilic small molecule drug, fenretinide, throughout oral buccal mucosa tissue in an *in vivo* rabbit model. In contrast to the cellular analyses previously discussed, Raman analysis of tissue sections requires much larger scan areas and acquisition times. Furthermore, there were additional unknown signal contributors (in this case: residual blood in tissue) that added complexity to the analytical method development not previously encountered in single cells. The main goal of this project was to quantify tissue concentrations of the drug around the periphery of controlled-release PLGA implants at various timepoints following implantation of the polymer-drug complexes in rabbit subjects.

In this study, the appropriate preparation of tissue sections on glass slides was explored and optimized to generate samples which could be reliably imaged via micro-Raman spectroscopy. A novel calibration methodology was also developed in which control tissue sections were prepared on glass slides and incubated in solutions of drug; tissue uptake and partitioning of fenretinide was measured via HPLC and the measured values were correlated with Raman measurements to generate linear quantitative calibration curves. Following this development, polymeric implants (PLGA, PVP, or PVA) were formulated and implanted in the buccal mucosa of rabbit subjects to study the *in*

vivo release profiles of different formulations. This study represents the first report of tissue diffusion behavior analysis of fenretinide after local delivery via long-acting release implants. The results presented herein illustrate the ability of micro-Raman spectroscopy for assessing local delivery of small molecule drugs in the context of controlled release implants.

Since biological specimens are typically comprised primarily of proteins and lipids, whether it be single cells or tissues, the signals acquired from the prepared tissue sections were comparable to those reported previously in cell samples (i.e., alveolar macrophages). Beyond the drug concentration measurements reported here, harmonization of ultraquantitative calibration methodology with large-scale Raman-based tissue section analysis could foreseeably provide insight into other phenomena of biomedical interest, such as Raman imaging of clinical biopsy samples (e.g., liver, intestine, etc.) in the contexts of any disease or disorder where drugs and/or lipids are reported to accumulate and result in unfavorable responses like organ toxicity. In this way, the Raman-based analysis of drug distribution in tissue sections reported here provide additional support towards specific aim 3 and the central hypothesis of my thesis.

6.2 Abstract

The work presented herein is the first time, to our knowledge that tissue penetration of locally delivered fenretinide (4HPR) has been measured. 4HPR was formulated into long-acting release polymeric implants, and the release kinetics along with the drug-tissue penetration were evaluated. Three different millicylindrical implant formulations were evaluated including: water-soluble matrix implants that provided continuous release based on the dissolution of the hydrophobic drug, porous poly(lactic-co-glycolic) acid [PLGA] implants capable of providing very long-acting continuous release (1-2 months) and PLGA implants loaded with the amorphous form of 4HPR as a solid dispersion in a polyvinylpyrrolidone (PVP) – triethyl-o-acetyl-citrate (TEAC) matrix. These implants were injected directly below the rabbit buccal mucosa in the lamina

propria and evaluated for their release kinetics and ability to enhance drug-tissue distribution. A quantitative Raman spectroscopic imaging method was developed to quantify drug-tissue concentration gradients in excised tissue sections. These studies show that drug release from implants was much faster in the mouth compared to our previous *in vivo* release studies in connective tissues, likely due to greater affinity of 4HPR to buccal epithelia and/or increased blood flow relative to the underlying connective tissue. The penetration distance for 90% depletion of 4HPR in the buccal tissues was on the order of 0.5-8 mm for all formulations. The PLGA implants loaded with PVP-TEAC-4HPR provided the greatest drug movement through tissues, likely as a result of supersaturated drug concentrations surrounding the implant. Hence, this site-specific drug delivery strategy may be useful for oral cancer chemoprevention by delivering therapeutic and widespread 4HPR levels at the target site.

6.3 Introduction

Fenretinide (4HPR), a synthetic Vitamin A derivative, has been shown to have incredible chemopreventive promise, however the inability to effectively deliver it has been its mainstay dilemma. In clinical trials with oral dosing, limited efficacy was observed due to dose limiting toxicities, while the drug's tissue disposition at the site of action was not evaluated. To overcome this limited efficacy with the oral dosing route, local drug delivery can be employed, which is capable of delivering a large amount of drug at target site while alleviating the undesirable side effects associated with oral dosing. However, the inability to achieve widespread drug-tissue distribution is the most prevalent challenge to overcome during local drug delivery (1, 2). Not surprisingly, there are many pharmacokinetic factors that govern drug distribution in tissues including: rates of diffusion, convection, elimination, protein binding, cellular uptake, capillary permeation, degradation and permeability into cell and subcellular components (which may lead to bioaccumulation), and finally intracellular metabolism and efflux (3). To maximize tissue distribution, often penetration enhancers are added to the formulation such as solubilizing agents, bile salts, chelators, and anionic or cationic polymers(4).

As part of our previous efforts in developing local long-acting chemoprevention strategies for oral cancer, we have designed millicylindrical implants loaded with 4HPR, a drug shown to have chemopreventive properties (5-9). Local delivery of hydrophobic 4HPR presents a significant challenge owing to its extreme water insolubility, with a logP of 6.31. Previous studies in our lab evaluated 4HPR plasma levels after subcutaneous (s.c.) injections from a controlled release poly(lactic-co-glycolic acid) (PLGA) vehicle, and found that after 2 weeks it was unclear whether the actual drug was exhibiting controlled release properties due to dissolution into surrounding interstitial fluid, or by slow release from tissue lipid "reservoirs" where 4HPR could have accumulated after fast dissolution.(10) We have also shown that 4HPR has a high propensity for non-specific tissue binding, and that the ability to solubilize the drug was the limiting factor in tissue uptake, likely due to affinity for phospholipids and secondarily from protein interactions.(11) We have shown that 4HPR can be released slowly over 6 weeks from water soluble matrix (poly-vinyl alcohol [PVA]/sucrose) millicylindrical implants *in vivo* in connective tissue, while the PLGA implants containing pore-forming agents provide very long release profiles of > 2 mo. We have also found an incredible 1000-fold 4HPR solubility enhancement with amorphous dispersions of PVP-4HPR (9/1 w/w), which was sustainable for more than 1 week in media. These formulations were evaluated *in vivo* for their potential to improve 4HPR tissue penetration distance. For clinical translation of oral cancer chemoprevention, rabbit buccal epithelia was chosen to evaluate these implants, due to similarity in tissue permeability, thickness and degree of keratinization of oral epithelia to humans.

Several approaches can be taken to quantitate drug-tissue distribution depending upon the molecule's properties or duration of drug exposure. A fluorescent molecule can be easily imaged, however, conjugating a fluorescent moiety onto a drug can alter its tissue diffusion properties. One could also radio-label the drug and use PET imaging, however it is not suitable for long-term studies due to stability of the radio-isotope. For molecules not fitting these criteria, the gold standard for drug-distribution studies is tissue sectioning, which could mean hundreds of tissue sections per distributive analysis,

followed by drug extraction from tissues, HPLC analysis, and data processing. Because this approach is quite laborious, and handling of large volumes of samples has the potential to introduce errors, therefore we sought a different approach to measure drug-tissue distribution.

In recent years, Raman spectroscopy has emerged as a reliable and informative technology for the execution of novel biomedical analyses. The phenomenon involves exciting a sample with monochromatic light (typically a laser), thereby inducing molecular vibrations within the sample; the vibrational modes consume a fraction of the light energy and the remainder is “scattered” as photons of shifted energy levels (or shifted wavelengths). By measuring the number of photons emitted at each wavelength, the instrument generates a Raman spectrum for the sample under investigation. Accurate interpretation of these spectra yields detailed quantitative chemical information about the molecules present in the sample. By coupling a Raman spectrometer to a confocal microscope, chemical analysis of samples can be performed with submicron spatial resolution. One major advantage of Raman Imaging is the non-destructive nature of the analyses; tissue sections undergo minimal preparation ensuring the natural distribution patterns of the compound of interest are unadulterated. We chose to investigate the utility of Raman micro-spectroscopy for quantitative assessment of 4HPR distribution in rabbit buccal tissues from millicylinder implant formulations. Raman micro-spectroscopy has been successfully employed for measurement of retinoid content in hepatic stellate cells using a similar analytical approach as we are proposing here (12). We have found that 4HPR exhibits a very strong Raman signal, due to the light scattering properties of the alkene conjugated poly-olefin chain (C=C vibrational mode), characteristic of retinoids and vitamin A derived molecules. 4HPR’s most prominent Raman band, the C=C vibrational mode at 1582 cm^{-1}, occurs in a region of the Raman spectrum which is typically free of significant spectral contributions from endogenous biomolecules. As such, the integrated intensity of this Raman peak can serve to quantitatively measure drug content in biological tissues.

Herein, we propose novel analytical methodology for quantitative Raman calibration and algorithm validation and then successfully apply these techniques to characterize 4HPR distribution in buccal tissue. This is the first time that 4HPR's tissue penetration has been evaluated. Since Raman micro-spectroscopy can be used to analyze almost any organic compound and requires no artificial chemical labels, our methodology could feasibly be utilized to characterize the natural distribution patterns for a multitude of colorless small molecules in a variety of tissue types.

6.4 Materials and Methods

6.4.1 Reagents and Materials

4HPR was generously supplied by Merck Co. Excipients and polymers used for millicylinders formulations included: PLGA (50:50, 24-38kDa, acid end-capped, Evonik), polyvinyl alcohol, (PVA, 9-10 kDa, 80% hydrolyzed, Sigma Aldrich, St. Louis, MO), D-sucrose (Sigma-Aldrich), polyvinylpyrrolidone (PVP K30, 40 kDa, BASF, Florham Park, NJ), triethyl-acetyl-citrate (TEAC), and magnesium carbonate ($MgCO_3$). Silicon tubing (0.8 mm i.d., BioRad Laboratories) was used for implant fabrication via extrusion. All other materials were reagent grade or better including ethanol (EtOH), and Tween 80. Solvents for UPLC/UV analysis were HPLC grade including acetonitrile (ACN), double distilled water (ddH_2O), and phosphoric acid (H_3PO_4). Acitretin (Sigma Aldrich, St. Louis, MO) served as an internal standard for the extractions. Tissues were sectioned using optimum cutting temperature compound (OCT, Tissue Tek), and adhered to poly-lysine coated glass slides prior to incubation. Phosphate buffer saline (PBS) was used for tissue incubation media. Oil-red-O and Harris hematoxylin stains were utilized in tissue histological examinations.

6.4.2 4HPR Millicylinder Formulations

Three 4HPR millicylinder formulations were evaluated for drug-tissue penetration enhancement:

1. PVA/Sucrose +10% 4HPR (crystalline drug)
2. PLGA+ PVP/4HPR/TEAC (controlled release of amorphous solid dispersion)
3. PLGA+ 10% 4HPR +3% $MgCO_3$ (porous, very-long acting release)

Millicylinder preparation methods have been described in detail.(11) Briefly, PVA/ D-sucrose (40%, 30% w/v respectively in ddH_2O) millicylinders were loaded with 10% 4HPR, extruded into silicon tubing, dried in vacuum oven at room temperature for 2 days, then 40 ˚C for 2 days, and cut from tubing into 1 cm lengths with an inner diameter of 0.8 mm. PLGA+ PVP-4HPR-TEAC implants were prepared as described previously(11) by first preparing the amorphous solid dispersion of PVP-4HPR-TEAC (9/1/1 mass ratio) by dissolving in MeOH, pouring into a thin film, drying 2 days in vacuum oven at 40 °C, then cryomilling the film into fine particles <90 μm (Retsch swing mill cryomill, PN 20.749.001). These particles were then loaded into PLGA (dissolved in acetone) at a ratio of 50/50 (PLGA to PVP-4HPR-TEAC particles), mixed, extruded, then dried and cut to size as described above. The third formulation was a porous matrix composed of PLGA+ 10% 4HPR+3% $MgCO_3$ and was prepared as previously described.(11) 4HPR loading levels were verified using the millicylinder extraction assay as described in following section.

6.4.3 4HPR Millicylinder Loading and Release: Digestion Assay

4HPR loading and *in vivo* release amounts were determined via an implant digestion assay. For the PLGA implants, one millicylinder was weighed, and PLGA and 4HPR were co-dissolved by addition of 0.5 mL THF, followed by precipitation of PLGA with addition of 9.5 mL EtOH. The samples were centrifuged, and supernatant was assayed by UPLC/UV. For the PVA/sucrose implants, the implant was dissolved in 10 mL of EtOH.

6.4.4 4HPR UPLV-UV Assay

4HPR levels in millicylinder digests and serum were measured by UPLC/UV. The reverse phase UPLC/UV analysis was carried out with a Waters Acquity UPLC system and Empower software under the following conditions: Acquity BEH C18 2.1x100 mm column, mobile phase 80:20 ACN: ddH_2O + 0.1% phosphoric acid (H_3PO_4), isocratic flow rate of 0.65 mL/min, UV detection at 365 nm, and total analysis time of 2 min. 4HPR LLOQ is 0.05 µg/mL.

6.4.5 Implantation of Millicyclinders in Rabbit Buccal Mucosa Lamina Propria

4HPR millicylinders were evaluated in rabbit buccal mucosa lamina propria for their ability to enhance drug-tissue distribution and also their release rate. Female New Zealand rabbits 3 months of age were purchased from Charles River Laboratories. All experiments were conducted in accordance to University of Michigan's AALAC protocols. Prior to implantation, rabbits were anesthetized with 5% isofluorane via inhalation, and pre-weighed implants were inserted into the buccal region via an 18G trocar. Each rabbit received 2 implants (1 per cheek), with 1 cheek utilized for Raman imaging analysis for drug distribution, and the other for determining the amount of drug released (n=3 animals per formulation per time point). Serum samples were collected prior to implantation and at the study endpoints via ear vein sampling. After days 1 and 14, rabbits were euthanized via intravenous injection of saturated potassium chloride solution. The buccal tissues were harvested and frozen flatly in their native conformation on dry ice and stored short-term at -80 °C until tissue sectioning occurred. For the drug-tissue distribution analysis, a ~15 mm length of buccal tissue containing a cross-section of the millicylinder was mounted onto a cutting chuck with OCT, and a 20 µm section near the middle of the implant was placed onto a glass slide, and imaged via Raman spectroscopy. For drug release from the implants, the implants were carefully freed from the surrounding tissue, and drug was extracted via the loading assay. The 4HPR release rate from the implants in rabbit buccal epithelia was compared to that in rat s.c. previously published.(11)

6.4.6 4HPR Serum Levels

4HPR sera levels in rabbits were assayed at time zero and at study endpoints. A 100 uL aliquot of serum was spiked with internal standard (5 µL of 0.5 mg/mL acitretin), extracted with 300 uL ACN by sonication on ice for 10 min, clarified by centrifuging at 12,000 rcf for 10 min, and the amount of 4HPR in supernatant was determined by UPLC assay, and extraction recovery normalized to the internal standard recovery.

6.4.7 4HPR-Incubated Tissue Sections as Calibration Standards for Raman

Rabbit buccal epithelia was cryosectioned (Leica 3050S crysotat) into 20 μm thick sections in z-plane orientation, so that each section contained a cross-section of all layers of epithelia (mucosa, lamina propia, and epithelium) along with millicylinder, and were thaw mounted onto poly-lysine coated glass slides. A representative tissue mass was recorded by averaging the weight of 3 tissue sections collected intermittently throughout the relatively homogeneous tissue block. The tissues sections were pre-treated by incubating in PBS + 0.5% Tween for 30 min, then incubated in 4HPR/PBST 0.5% calibration solutions (n=4) ranging from 1-500 µg/mL for 4 h, followed by tissue wash PBS and ddH_2O. At each concentration level, 3 tissues were extracted and assayed for 4HPR uptake by UPLC, and 1 was reserved for Raman imaging analysis, such that Raman imaging calibration curve could be constructed from UPLC 4HPR-tissue uptake results. The 4HPR tissue concentration was expressed as μg 4HPR/mg tissue, using the average mass of 1 tissue section for that bulk tissue block. Additionally, 4HPR tissue partitioning coefficient (Kp) was calculated from the concentration of free drug in incubation media (C_{free}) and the tissue uptake (C_{tissue}).

$$Kp = \frac{C_{tissue}}{C_{free}}$$

6.4.8 Raman Measurements

To acquire a Raman image, the excitation laser was raster-scanned across the sample region of interest, collecting a Raman spectrum at every pixel and generating what is termed a hyperspectral image. All Raman images were acquired by a WiTec alpha300R confocal Raman microscope equipped with the 532nm solid-state sapphire excitation laser (tuned to ~35mW intensity) and a 10x air objective (Zeiss Epiplan-NEOFLUAR, NA (numerical aperature) = 0.25) coupled to a CCD detector via a multi-mode fiber of 100μm diameter, serving as the confocal pinhole. Calibration standard spectra were acquired by raster scanning over three separate 2000 x 200 micron regions of each drug-incubated buccal tissue; relatively high spatial resolution was attained with a step-size of 20 microns and pre-bleaching of biological autofluorescence was accomplished by programming laser focus to pause for 0.5 seconds at each point before acquiring spectra over integration time of 0.5 seconds. In order to achieve reasonable acquisition times over the test sample regions of interest, large area raster scans were performed with a step-size of 50 microns, pausing for 0.4 seconds at each point before acquiring spectra over integration time of 0.2 seconds. Depending on the spatial dimensions of tissue region scanned, total acquisition times ranged from six to fourteen hours per test sample.

6.4.9 Raman Data Processing

For the purposes of drug distribution analysis throughout multiple layers of buccal tissue, the Raman images are typically comprised of at least 30,000 individual spectra. This creates a need for automated computational algorithms to process, interpret, and translate the acquired Raman signals into relevant chemical information to address the scientific question of interest. Using WiTec Project FOUR Software, all Raman spectra were first cleared of cosmic rays (filter size: 4, dynamic factor: 2) and noise was reduced via a moving average smoothing matrix; baseline subtraction was performed by fitting a 9^{th} order polynomial to spectral data points in the following wavenumber ranges: 205-515,

840-900, 1345-1405, 1495-1530, 1770-2690, and 3120-3750 (cm^{-1}). To generate Raman images, data was exported to MATLAB and an in-house algorithm was developed to ultimately identify and integrate 4HPR's characteristic Raman peak at 1582 cm^{-1} at every pixel of the scanned tissue section (See Figure S-32 algorithm protocol). The glass background was first subtracted and a decision tree was employed to distinguish and remove spectral contributions from the naturally occurring biomolecule heme (which yields a strong interfering Raman signal at ~1588 cm^{-1}) from that of 4HPR. A signal-to-noise ratio of ≥3 was installed as the detection limit for a peak. Spectra were normalized to account for variation in tissue thickness, the 4HPR Raman peak at 1582cm^{-1} was integrated, and the drug/tissue mass ratio was calculated from the calibration curve. Because spectral analysis algorithms are relatively detailed processes, it is imperative to confirm the accuracy of each step in the process in order to ensure validity of the overall algorithm. To optimize and verify algorithm parameters, test samples were generated and analyzed as per acquisition methodology, processed through the algorithm, and used to determine the rates of false positive and false negative 4HPR detection in different biochemical tissue environments. For all *in vivo* 4HPR-dosed tissue Raman images, algorithm result outputs were manually compared with unprocessed spectral images and regions where sample burning occurred were cropped out so as not to artificially influence drug distribution analysis.

6.4.10 Drug Concentration-Diffusion Distance Curves

4HPR tissue distribution in the buccal epithelia was determined by generating drug concentration-diffusion distance curves (i.e., penetration distance) based on the Raman imaging, whereby concentrations were generated from signal intensity via calibration standard tissue sections. To prepare these penetration distance plots, a 1 mm wide region containing the center of the implant was selected in both the y-plane (i.e., same tissue layer) and the z-plane (through different tissue layers). Additionally, the z-layer diffusion was expressed as drug movement towards the epithelium and also towards the mucosa. The distinction between these different tissue layer compositions is suspected to affect

the drug penetration. The diffusion distance was reported at the location where drug concentration decreased to 10% of its initial value (C_{10}), i.e., 90% drug depletion.

6.4.11 Lipid Level Estimation in Tissue Sections by Oil-Red-O Staining

Lipid levels in buccal epithelia tissue sections were quantified by image analysis using Aperio ImageScope (V12.1.0) of the tissue uptake of lipid specific oil-red-o-stain. The glass-mounted tissue sections were fixed with 10% neutral buffered formalin, rinsed with ddH_2O, then stained with oil-red-o stain (dissolved in EtOH), and counterstained with Harris Hematoxylin.

6.5 Results and Discussion

6.5.1 Raman 4HPR Tissue Calibration Standards

The first step in developing our quantitative Raman imaging method was to prepare a calibration curve with buccal tissue sections incubated in 4HPR dissolved in PBST 0.5% solutions (4 h previously determined to be the equilibrium binding time). As shown in Figure 6-2a, there was a linear increase in 4HPR tissue uptake as the concentration of 4HPR in incubation media increases, with correlation coefficient of r^2= 0.997. We calculated 4HPR partitioning from the PBST 0.5% media into buccal epithelium sections, and found consistent partitioning (Kp) ranging from 1.9-2.2 over a wide concentration range of 3-91 ug/mL free 4HPR in media (Figure 6-2b). This high affinity tissue partitioning may adversely impact 4HPR's ability to diffuse through tissue, that is, 4HPR will prefer to bind to tissue components (lipids, proteins) rather than diffuse via local blood flow.

Calibration sections were analyzed as per acquisition methodology and 30,000 Raman spectra were collected across all regions of each tissue section and individually processed using algorithm to determine the integrated intensity of the 4HPR peak at 1582 cm^{-1}. The average spectra for each calibration standard are reported in Figure 6-2c and

the average (+/- SE) integrated intensity yielded a linear relationship with the drug/tissue mass ratio as determined by HPLC (r^2=0.985). The linear range was 6.5 – 200.7 μg 4HPR/g tissue, and tissue regions exceeding this range were considered to have a saturated Raman signal, as represented by the white color in the Raman concentration images.

6.5.2 Raman Hyperspectral Image Processing Algorithm

To analyze 4HPR distribution throughout a single buccal tissue section (20 um thick), at least 30,000 Raman spectra were required. Acquired in a raster pattern across the tissue section under investigation, each spectrum required integration of the peak of interest (4HPR), thus creating a necessity for automated algorithms that perform processing functions in a time-efficient manner. Developed in-house, our MATLAB algorithm is capable of processing tens-of-thousands of spectra per minute with outstanding reliability. Accurate peak selection in the acquired Raman spectra required designing algorithms that could distinguish between the oxygen-carrying heme protein in blood at 1588cm^{-1}, that partially overlaps the characteristic peak of 4HPR, making distinction between the two difficult. Exploiting heme's unique Raman peak at 750cm^{-1}, we successfully employed a decision tree to identify spectral contributions from heme and used a scaled reference spectrum obtained from pure blood to subtract the interference, leaving only spectral contributions from 4HPR and other tissue components to be quantified. No other chemical components present in our system, including millicylinder excipients, interfered with the 4HPR Raman peak at 1582cm^{-1} (Figure S-31). To confirm the validity of algorithm functionality, Raman test datasets were acquired from dispersions of pure biochemical components or unadulterated buccal tissue on glass slides. Since the intended Raman results for the test samples were known, they were used to experimentally determine the reliability of the algorithm.

6.5.3 Evaluation of 4HPR Release from Millicylinder Implants

The three millicylinder formulations prepared with different polymer systems and drug-solubility enhancement were evaluated *in vivo* for their release rate as well as their drug-tissue distribution after 1 and 14 days. The effects of implantation sites on drug release rate was evaluated by comparing release into buccal mucosa laminar propria vs. underlying connective tissue, which was previously evaluated in our rat *in vivo* studies.(11) The immediately dissolving, water soluble matrix PVA/sucrose implant served as a benchmark for the dissolution-controlled release of a hydrophobic solid drug depot. The PLGA + 10% 4HPR + 3%$MgCO_3$ formulation was shown to have very long-acting release in connective tissues (> 2 months release). The PLGA+ PVP-4HPR-TEAC formulation provided superior solubility enhancement due to formation of amorphous solid dispersion between PVP, 4HPR and TEAC, and served to test the premise that the ability to solubilize the hydrophobic drug is the limiting factor in tissue dispersion.

The results for drug release from these implants are shown in Figure 6-3, and actual 4HPR implant loading is noted in the figure. All of the implants released faster in buccal epithelia compared to connective tissue, likely due to greater blood flow in the mouth compared to skin. In the PVA/sucrose formulation, the day 1 burst in buccal was almost double of the release in connective tissue, likely due to lack of slowly eroding polymer controlling the release. The PLGA-PVP-TEAC amorphous drug system also had a high burst release on day 1 in buccal (62%), while in connective tissue only 26% released, yet after 2 weeks, both released similar levels (69% and 77% respectively). This fast release is likely due to only 50% PLGA implant composition. The very long-acting release PLGA formulation with pore-forming agent $MgCO_3$, released 4HPR twice as fast in buccal (29% vs 15%) after 14 days, and therefore was most capable of these formulations at providing long duration of release in the mouth, due to PLGA's well characterized slow release properties based on this polymer's hydration and erosion profiles.

The drug-tissue concentration gradients were generated based on the Raman imaging methods and calibration curve shown in Figure 6-2. In Figure 6-4, a

representative Raman image is shown for 4HPR dispersion in buccal epithelia after 14 days of release from the PLGA-PVP-4HPR-TEAC implant. The preparation of the concentration – diffusion distance curves is clearly marked around the implant hot spot, and shows selected regions of z-plane diffusion, (through different tissue layers), and y-plane diffusion (along same tissue layer). For example, the y-diffusion distance (Figure 6-4b), is measured at the edge of the saturation zone (200 µg 4HPR/g tissue at 6000 µm) to the C_{10} (20 µg 4HPR/g tissue at 200 µm), and therefore equals a C_{10} penetration distance of 5.8 mm. A complete data set for all formulations, replicates, and time points including Raman images and concentration–diffusion distance curves, can be referenced in Appendix D Figures S-33 – S-38.

4HPR's tissue penetration from these implants is portrayed by distance by which 4HPR's concentration decreased to 10% of the initial level (C_{10}) surrounding the edges of the implant. These distances were extracted from Raman images in Appendix D Figures S-34 – S39, and are shown in Figure 6-5 for both the z-plane diffusion towards the mucosa and towards the epithelium (Figure 6-5a) in addition to the y-plane diffusion (Figure 6-5b). Most notably, the y-plane diffusion along same tissue plane is much greater than diffusion through different tissue layers. It is difficult to discern which tissue layer 4HPR prefers to move towards, (epithelia or mucosa), as no trends could be determined with this sample size (n=3). All formulations and time points had an average z-plane diffusion distance of 0.35 to 2.5 mm. Pre-cancerous cells will proliferate from the basal cell membrane, a region close to the where the implants were dosed, and therefore these implantation depths and drug diffusion distances in z-plane should be satisfactory for oral cancer chemoprevention.

A better indication of the formulation's drug tissue-penetration enhancing performance can be observed along the y-plane. The PVA/sucose implants had an average diffusion of 1.4 mm after day 1, while that value decreased to 0.9 mm after 14 days. This could be attributed to clearance of the drug from the active site where after 1 day they released 47% 4HPR, and 68% after 14 days. Perhaps the large burst release of unsolubilized drug was itself a barrier to diffusion. Next, we see that the very slow

releasing PLGA+ $MgCO_3$ formulation enabled greater drug diffusion than the solid depot, whereby 4HPR diffused on average 1.7 mm and 2.3 mm from implant after 1 and 14 days respectively. Finally, the PLGA + amorphous, solubilized drug (PVP-4HPR-TEAC), had far surpassed the other formulations in tissue penetration enhancement, such that 4HPR diffused on average of 2.5 mm and 5.6 mm after 1 and 14 days respectively. As hypothesized, the ability to deliver a solubilized form of the drug into the aqueous tissue environment was the limiting factor in its ability to achieve widespread tissue distribution. As the oral cavity is a curved surface with interruption of the mucosa surface by the rabbit's lip pomenture, some of the diffusion variability could be attributed to differences in implantation angles or depths, and therefore cross-sections may have captured slightly different diffusion planes. For all formulations, there was no detectable 4HPR in serum, which is a favorable aspect with local delivery systems, and therefore the undesired side-affects associated with systemic drug delivery could be alleviated with our systems.

Our results shown in Figure 6-5 show that we were capable of enhancing 4HPR tissue penetration by controlled release of 4HPR from PLGA implants by delivering the amorphous solid dispersion (PVP-4HPR-TEAC). However, likely other physiological factors are present that can aid in distribution or acting as a diffusion barrier, such as local blood flow, degree of keratinization of tissue, and local protein/lipid levels to name a few. To further investigate this, a histological examination of the tissue environment surrounding the implant was performed which included staining with oil-red-o specific for lipids, followed by Harrison hematoxylin stain. This microscopic examination of tissue biocomponents was colocalized with the molecular signals of proteins and lipids from Raman images. In Figure 6-6a, we see that the red lipid-specific stain has the greatest uptake in the lamina propria region (i.e., the implantation site). An attempt was made to correlate the amount of lipid and y-plane diffusion distance (along same tissue layer), for each of the 3 formulations (time points were combined). As shown in Figure 6-6b, the level of lipids does not appear to affect the diffusion distance for the PVA/sucrose and PLGA+$MgCO_3$ formulations, however we see a positive effect of diffusion distance increase as local lipid levels increase for the solubilized PLGA+PVP formulation. In

Figure 6-6c, we see that Raman mapping shows the highest levels of protein and lipid in the lamina propria region (i.e., implantation region), and is consistent with the oil-red-o staining (Figure 6-6a). Further tissue pathological investigations may prove insightful for enhancing drug diffusion distance for local delivery systems.

6.6 Conclusions

Here, we have published for the first time, the tissue diffusion behavior of 4HPR after local delivery in buccal epithelia from long-acting release implants. We have developed quantitative Raman imaging and spectral processing methods to obtain high resolution of drug distribution in tissue sections. We have shown that 4HPR diffusion distance can be enhanced 4-fold by delivering an amorphous form of 4HPR from PLGA implants, compared to the solid dispersion control prepared in a PVA/sucrose matrix. Therefore, the ability to solubilize this hydrophobic drug is a limiting factor in its tissue distribution. Furthermore, we have shown that the tissue type, i.e., buccal epithelia/lamina propria compared to connective tissue, has a significant impact on the rate of drug release from these implants, such that nearly 2-fold increase in amount of drug released occurred in the buccal epithelia, likely due to greater blood flow. There are other physiological factors that may contribute to the 4HPR diffusion, including lipid and protein level, or depth of implantation, and deserve further examination for future evaluation of the drug system's performance. We have shown that these implants are capable of delivering 4HPR to the basal cell membrane tissue regions to target the pre-cancerous cells that may arise, and may be a beneficial strategy for secondary oral cancer chemoprevention. Notably, millicylinder placement in the loose extremely well vascularized oral mucosal lamina propria had a major impact on 4-HPR release and dispersion relative the denser sub epidermal connective tissues.

6.7 Acknowledgements

The authors of this work would like to thank undergraduate research students Montana Mason for his help in Raman data acquisition and Ashirvad Varma for his help with Matlab processing of image data. Additional thanks to the University of Michigan's In vivo Animal Core (IVAC) for their help with pathological examinations.

This work was supported by funding from the following: National Institutes of Health R01 CA 171329, National Institutes of Health R01 GM 078200, and University of Michigan M-Cubed

6.8 Figures

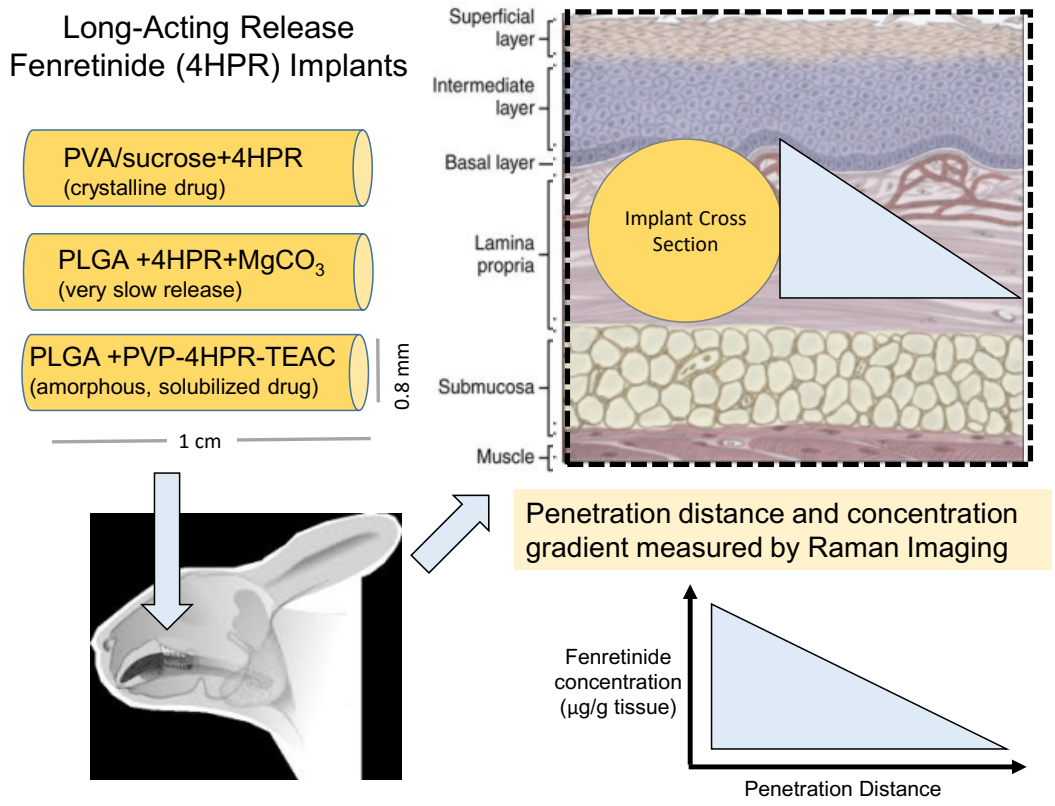

Figure 6-1. Graphical abstract for fenretinide tissue distribution analysis.

Long-acting release implants containing fenretinide (4HPR) were implanted into the buccal epithelia of rabbits. At various timepoints following implantation, the animals were sacrificed and buccal tissue sections were collected and prepared on glass slides. Raman analysis of tissue regions revealed penetration distance and concentration gradient mapping.

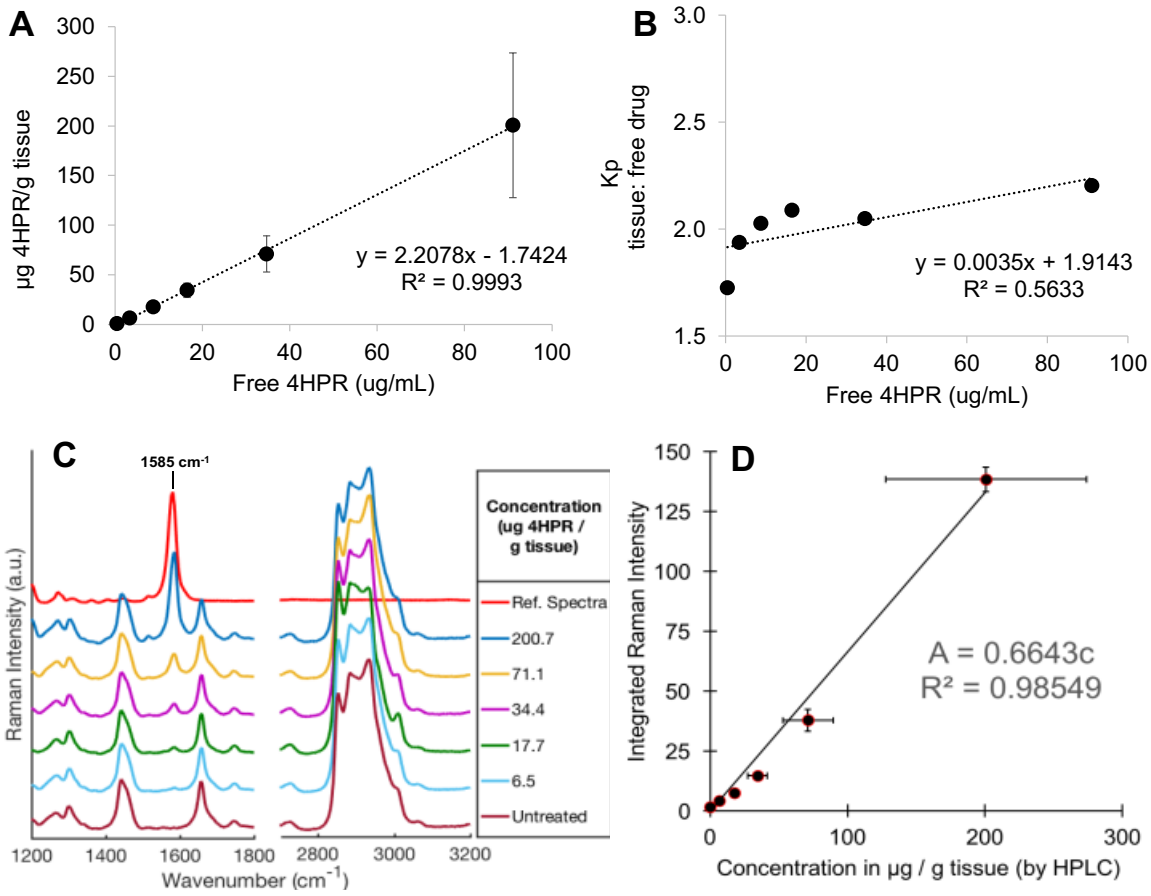

Figure 6-2. Quantitative calibration of Raman tissue imaging methodology.

Excised buccal tissues (sectioned 20 µm thick) incubated in known concentrations of 4HPR (in PBST 0.5%) were assayed via HPLC, and served as calibration standards for quantitative interpretation of Raman spectra. **(A)** 4HPR tissue uptake as a function of incubation media concentration **(B)** 4HPR partitioning (Kp) from aqueous media into tissue, **(C)** 4HPR Raman spectra showing limit of detection at 6.5 µg 4HPR/g tissue, and **(D)** Raman 4HPR-tissue calibration curve shows Raman signal intensity as a function of tissue concentration by HPLC (n=3, mean ± SE).

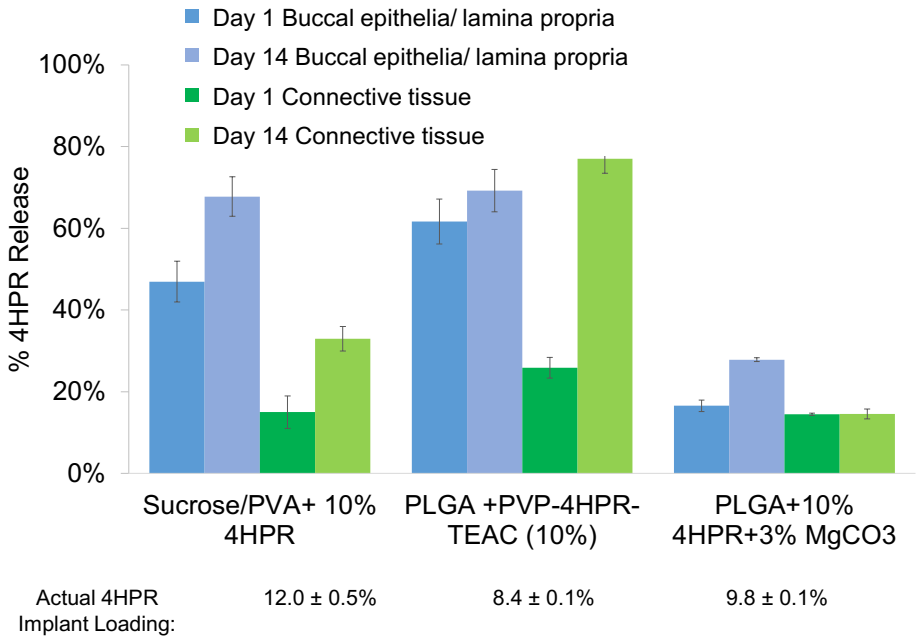

Figure 6-3. *In vivo* % release of 4HPR from millicylinder implants in rabbits.

4HPR *in vivo* release from three millicylinder formulations after 1 and 14 days in rabbit buccal epithelia/lamina propria compared to connective tissue types (mean ± SE, n=3). The PVA/sucrose implant is an immediately dissolving, water soluble matrix, the PLGA+PVP-4HPR-TEAC implant provides controlled release of a solubilized form of 4HPR, while the PLGA+ 3% $MgCO_3$ provided very long-acting drug release.

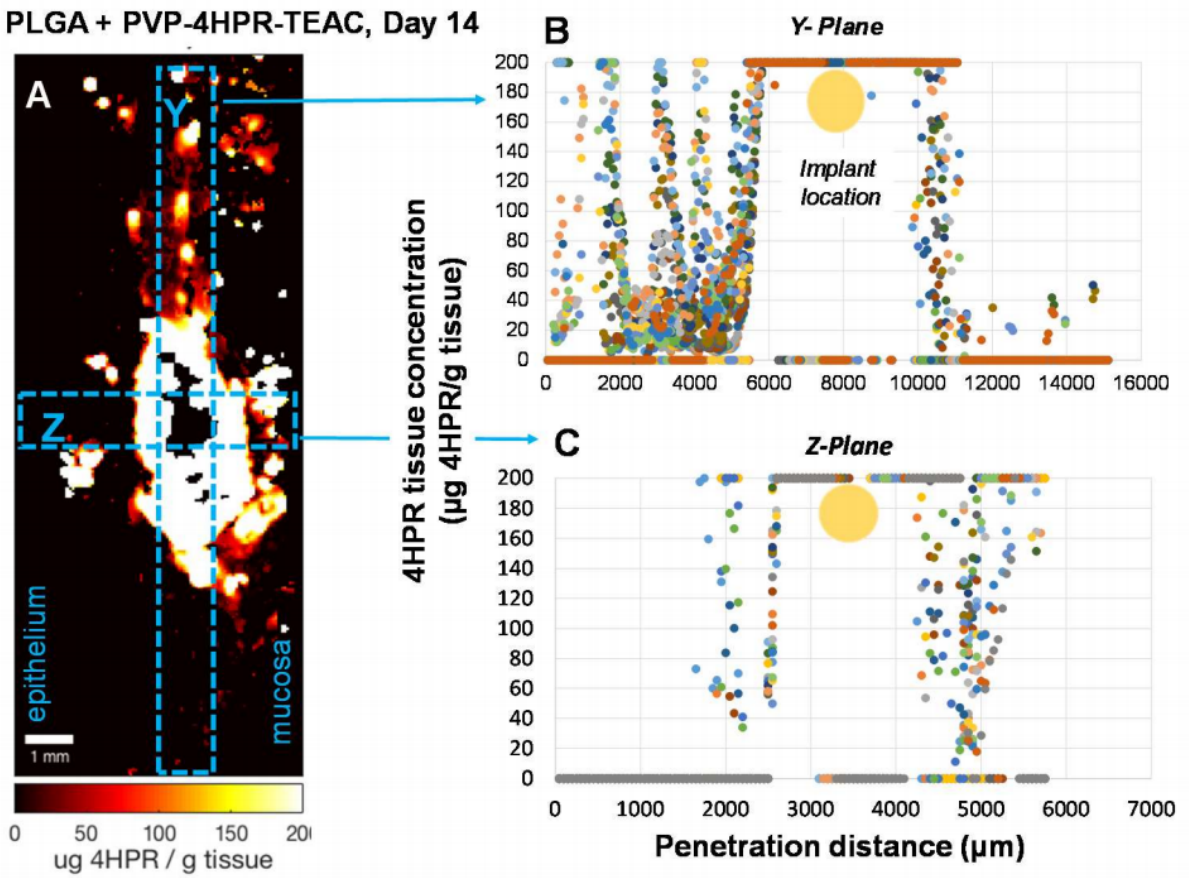

Figure 6-4. 4HPR tissue distribution after release from millicylinder implants.

(A) Representative Raman image of tissue dosed with PLGA+ PVP-4HPR-TEAC implants after 14 days detailing the process for generating drug-tissue penetration curves in both the **(B)** y-plane (same tissue layer) and **(C)** z-plane (towards epithelium or mucosa). Each data point represents a 50x50 µm pixel from the corresponding boxed region in **(A)**, and the location of millicylinder is noted on plots with a yellow circle. Full data set for each sample replicate and times points can be referenced in Appendix D.

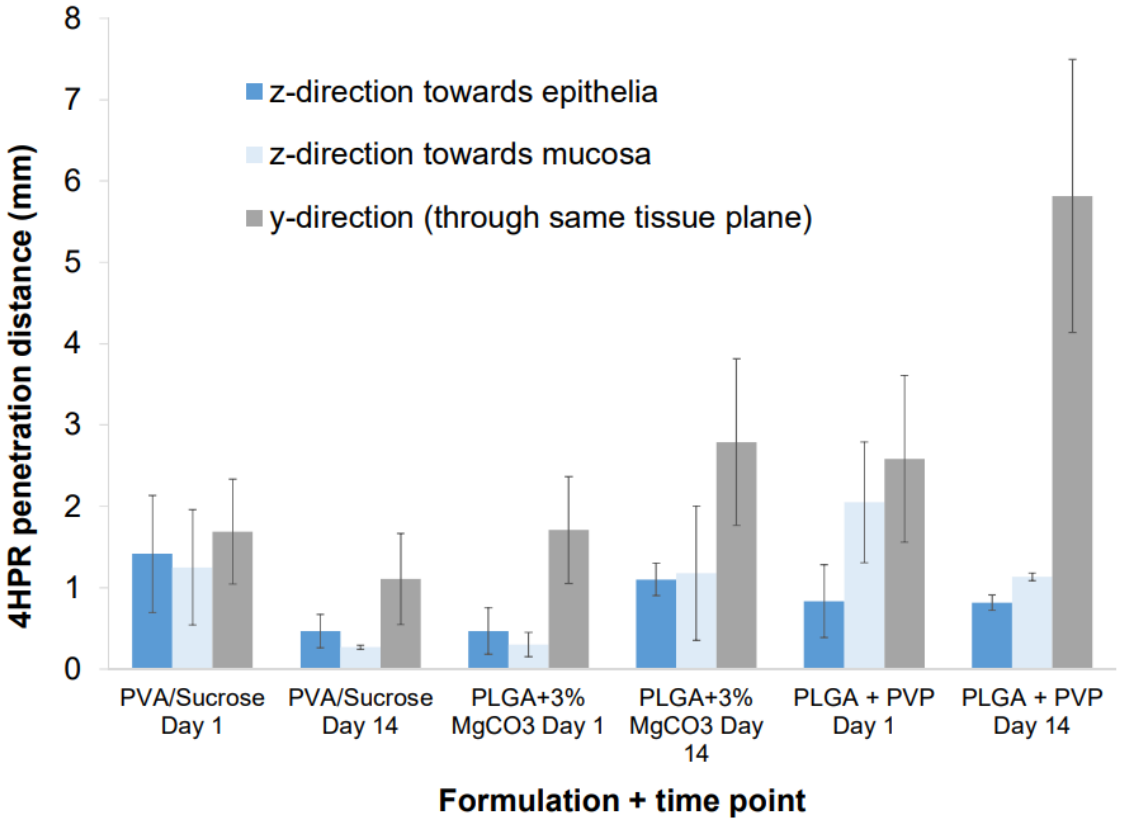

Figure 6-5. 4HPR tissue penetration distances in buccal epithelia.

4HPR penetration distances in buccal epithelia from millicylinder formulations after day 1 and 14 determined by concentration gradients in tissue sections measured by semi-quantitative Raman spectroscopy. Penetration distance represents distance by which drug concentration decreased to 10% of starting value, which was 20 µg 4HPR/g tissue, given that Raman signal intensity was saturated at perimeter of implant, giving initial concentration at edge of implant of 200 µg 4HPR/g tissue. (Mean ± SE, n=3).

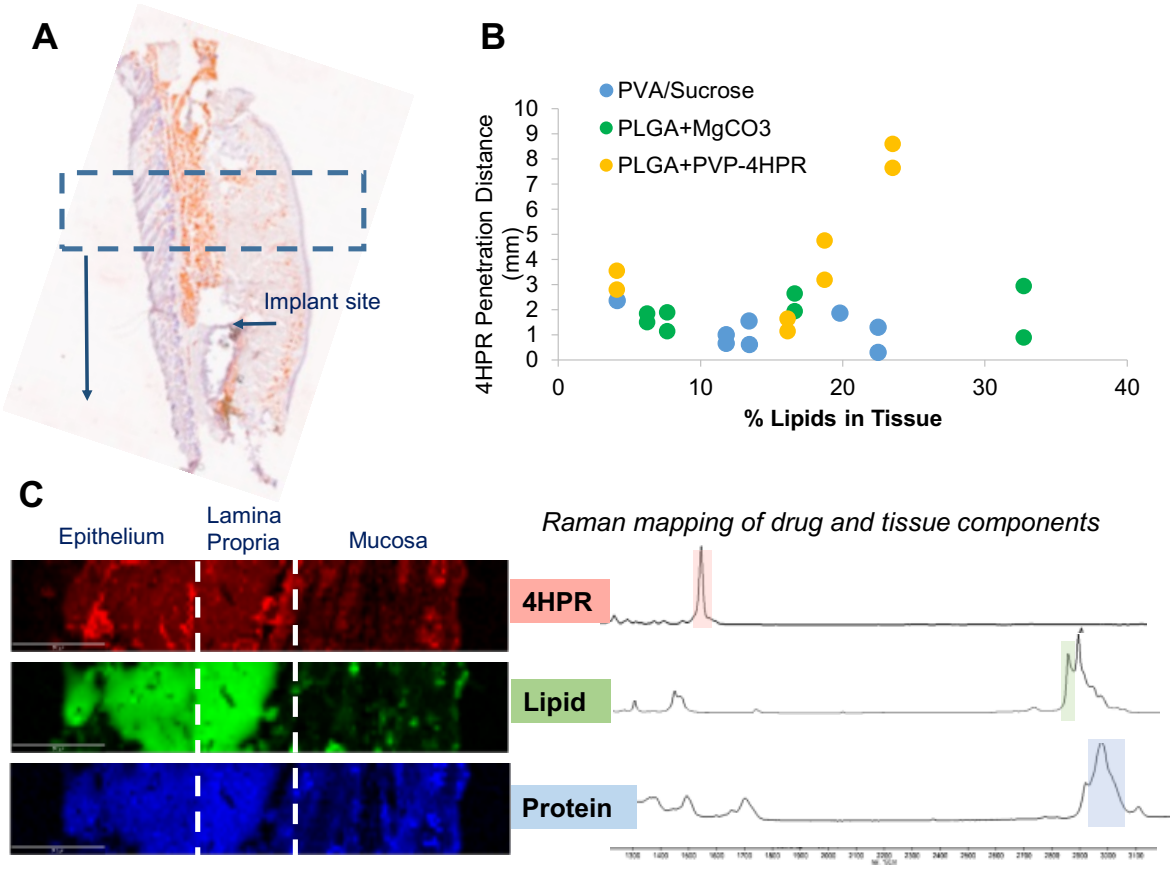

Figure 6-6. Correlation of tissue composition with 4HPR diffusion distance.

(A) Representative oil-red-o stained tissue (specific for lipids), **(B)** 4HPR penetration distance as a function of lipid level for each formulation, and **(C)** Raman mapping of 4HPR, lipid, and protein in a tissue section incubated in 4HPR/PBST solution, and co-localization of the biocomponents in the different tissue sections (epithelium, lamina propria, and mucosa).

6.9 References

1. Fleming AB, Saltzman WM. Pharmacokinetics of the carmustine implant. Clinical Pharmacokinetics. 2002;41(6):403-19. doi: 10.2165/00003088-200241060-00002.

2. Strasser JF, Fung LK, Eller S, Grossman SA, Saltzman WM. Distribution of 1,3-bis(2-chloroethyl)-1-nitrosourea and tracers in the rabbit brain after interstitial delivery by biodegradable polymer implants. The Journal of Pharmacology and Experimental Therapeutics. 1995;275(3):1647-55.

3. Haller M, Saltzman WM. Localized Delivery of Proteins in the Brain: Can Transport Be Customized? Pharmaceutical Research. 1998;15(3):377-85. doi: 10.1023/a:1011911912174.

4. Strickley R. Solubilizing Excipients in Oral and Injectable Formulations. Pharmaceutical Research. 2004;21(2):201-30. doi: 10.1023/b:pham.0000016235.32639.23.

5. Han BB, Li S, Tong M, Holpuch AS, Spinney R, Wang D, et al. Fenretinide Perturbs Focal Adhesion Kinase in Premalignant and Malignant Human Oral Keratinocytes. Fenretinide's Chemopreventive Mechanisms Include ECM Interactions. Cancer Prevention Research. 2015;8(5):419-30. doi: 10.1158/1940-6207.capr-14-0418.

6. Mallery SR, Wang D, Santiago B, Pei P, Schwendeman S, Nieto K, et al. Benefits of Multifaceted Chemopreventives in the Suppression of the Oral Squamous Cell Carcinoma (OSCC) Tumorigenic Phenotype. Cancer Prevention Research. 2016. doi: 10.1158/1940-6207.capr-16-0180.

7. Formelli F, Clerici M, Campa T, Di Mauro MG, Magni A, Mascotti G, et al. Five-year administration of fenretinide: pharmacokinetics and effects on plasma retinol concentrations. Journal of Clinical Oncology : official journal of the American Society of Clinical Oncology. 1993;11(10):2036-42.

8. Moglia D, Formelli F, Baliva G, Bono A, Accetturi M, Nava M, et al. Effects of topical treatment with fenretinide (4-HPR) and plasma vitamin A levels in patients with actinic keratoses. Cancer Letters. 1996;110(1–2):87-91. doi: http://dx.doi.org/10.1016/S0304-3835(96)04475-8.

9. Tradati N, Chiesa F, Rossi N, Grigolato R, Formelli F, Costa A, et al. Successful topical treatment of oral lichen planus and leukoplakias with fenretinide (4-HPR). Cancer Letters. 1994;76(2-3):109-11.

10. Ying Zhang CW, Sachin Mittal, Amitava Mitra, Steven P. Schwendeman. Design of controlled release PLGA microspheres for hydrophobic fenretinide. Molecular Pharmaceutics. in press.

11. Nieto K, Pei P, Wang D, Mallery SR, Schwendeman SP. In vivo controlled release of fenretinide from long-acting release depots for chemoprevention of oral squamous cell carcinoma recurrence. International Journal of Pharmaceutics. 2017;538(1-2):48-56. doi: 10.1016/j.ijpharm.2017.11.037.

12. Galler K, Requardt RP, Glaser U, Markwart R, Bocklitz T, Bauer M, et al. Single cell analysis in native tissue: Quantification of the retinoid content of hepatic stellate cells. Scientific Reports. 2016;6:24155. doi: 10.1038/srep24155.

CHAPTER 7

Conclusions, Future Outlook, and Broader Implications

7.1 General Conclusions

7.1.1 Raman Spectroscopic Microanalysis of Intracellular Drug Accumulation

Clofazimine served as a preliminary model compound for Raman-based analytical development because it is known to accumulate to a greater extent than most other compounds, at least to the best of our current understanding, and its red color provides clear evidence of bioaccumulation inside cells. Micro-Raman spectroscopy was utilized to study supramolecular biocrystalline assemblies of clofazimine (that form *in vivo* within macrophages) and a synthetic-biomimetic microcrystalline formulation.(1-3) Under excitation with visible light (i.e., 532nm laser) the Raman signal of clofazimine was amplified, presumably due to resonance effect, making the linear range of quantitation for the drug extremely narrow. Although quantitation was difficult, this study did serve as Raman-based verification of the massive degree of intracellular accumulation that is consistently observed in the macrophages of human and animal subjects treated with the compound for extended periods of time.(4-7) Despite difficulties with quantitation inside single cells, micro-Raman spectroscopy proved useful in the analytical characterization of artificially-synthesized biomimetic clofazimine microcrystals, specifically to study the flexibility and elasticity properties and evaluate changes in the crystal structure as a result of manufacturing processes such as jet milling and heat-sterilization.

Although clofazimine was a convenient compound to illustrate proof-of-accumulation, most FDA-approved drugs on the market are colorless, and therefore more difficult to observe. This is the analytical niche which micro-Raman can foreseeably

occupy due to its inherently non-specific nature of detection: to screen for and measure the intracellular accumulation, distribution, and phase transitions of colorless small molecule drugs with the propensity for bioaccumulation. Herein, I showed feasibility for Raman-based intracellular distribution analysis of a multitude of FDA-approved accumulating small molecules inside individual macrophages; the novel cell sample preparation technique presented allowed for quantitative Raman imaging of the intracellular distribution of accumulating compounds in relation to endogenous biomolecules of interest, specifically identifying subcellular compartments such as nuclei and lipid droplets.(8) The methodology also enabled clear distinction between the nucleus and cytoplasm and identified distinct cytoplasmic inclusions, exhibiting strong lipid or nucleic acid signals. Furthermore, the novel calibration methodology (involving stoichiometric mixtures of drug and phospholipid on silicon chips) provided quantitative estimation of the amount of drug content, relative to amounts of other biomolecules, present inside single cells.

These experiments also served as the foundation for statistical interpretation of Raman spectra via non-negative least squares regression (aka linear combination modelling and Biomolecular Component Analysis); the least squares regression model with protein, lipid, and nucleic acid reference spectra, accounted for the majority of spectral variance in typical alveolar macrophages from untreated animals in our experiments and also served as a reliably-robust model for other groups based on reports in the literature.(9-12) In addition, the occurrence of Raman spectral signals that were unaccounted for by the pure component reference spectra (unknown signal contributors, i.e., unknown molecular species) could be automatically picked out and analyzed more thoroughly to potentially identify the unknown compound. Overall, confocal Raman microscopy offers tremendous potential for quantitative analysis of the intracellular distribution and sequestration of small molecules in macrophages; expanding the current breadth of this technology to the clinical setting by characterizing subcellular distribution phenomena for a multitude of drugs used during treatment of various disease states would provide valuable insight into drug bioaccumulation and the role of macrophages.

7.1.2 Inkjet-Printed Micro-Calibration Standards

The development of cell-sized micro-calibration standards of known total (absolute) mass and composition represents a significant innovative advancement in the field of cytometry in that it enables quantitation of the total molecular contents of individual cells in absolute (picogram) scales. This technology opens the doors of scientific perception to the unadulterated biomolecular realm inside individual cells and can be applied to quantitively study cellular accumulation phenomena in the context of a multitude of storage disorders. With rising awareness of the significance of cell population diversity and the pathophysiological consequences of cell subpopulations that play crucial roles in different disease states, there comes a scientific niche for single-cell quantitative analysis which could foreseeably be addressed using this micro-calibration technology with Raman microscopy or alternative techniques such as mass spectrometry.(13)

From a technical perspective, fabrication of protein and nucleic acid microarrays has been previously established, but inkjet-printing of lipids has remained elusive.(14, 15) Synthetic high-density lipoprotein nanodiscs enabled the apparent dissolution (overcoming solubility barrier of lipid in water) of known amounts of phospholipid into aqueous printer ink formulations reported herein. The nanoscale particle size of synthetic high-density lipoprotein nanodiscs (~10nm diameter) allowed for repeatable and consistent inkjet-printing of lipid micro-calibration standards and also enabled homogenous mixing of lipids and proteins in aqueous inks at ratios present in actual eukaryotic cells. Furthermore, I herein showed that the linearity of integrated Raman signals (total signal acquired across a given area) is directly correlated with the total (or absolute) mass of material present within a given scan; because of this linearly-correlative relationship, non-negative least squares regression spectral deconvolution (aka linear combination modelling with pure component reference spectra) harmonizes well and enables quantitative deconvolution of integrated Raman spectra into picogram measurements for each major molecular component of interest.(16-18)

7.1.3 Ultraquantitative Raman Spectral Cytometry

With the development of cell-sized micro-calibration standards, verification of emitted Raman signal linearity, and theoretical harmonization with least squares regression statistical model, ultraquantitative micro-Raman spectral cytometry – a cytometric approach to quantitatively measure the absolute amount of cellular material and bioaccumulating contents – became a reality. While there is still further development work to be done beyond what has been presented herein, the theoretical foundation for this technique has been established. In this work the ultraquantitative approach was utilized to study drug and lipid accumulation phenomena in a multitude of cell types from different animal species and humans, suggesting this technique is broadly applicable for cytometric analysis of most eukaryotic cell specimens of interest. By measuring changes in the absolute (or total) amount of biomolecular contents on a single-cell basis, ultraquantitative Raman spectral cytometry provides a unique and novel perspective into the compositional phenotype of cells, specifically of interest in the context of storage disorders where total cellular contents are changing or increasing.

Lipid accumulation was of specific interest for the scope of this project, as drug-induced phospholipidosis is a relatively common and poorly understood side effect of bioaccumulating drug compounds. As evidenced by *in vitro* incubation experiments of alveolar macrophages with amiodarone, ultraquantitative Raman spectral cytometry could successfully and reliably differentiate between drug-treated and untreated cells whilst simultaneously providing quantitative measurements of lipid accumulation (i.e., picograms/cell). Furthermore, the Raman hyperspectral datasets could be used to generate images which revealed punctate lipid inclusions inside drug-treated cells: the histopathological hallmark of drug-induced phospholipidosis. Ultraquantitative Raman spectral cytometry also proved useful in evaluating changes in compositional phenotypes of alveolar macrophages in the contexts of chronic and acute lung injuries *in vivo*, namely in mouse pulmonary fibrosis and porcine acute respiratory distress syndrome animal models. The porcine model, involving significant multidisciplinary collaboration with critical care clinicians, served to elucidate obstacles that may be encountered in the actual

clinical setting, thereby facilitating translation of the technology for biomedical application in human patients. Ultraquantitative Raman spectral cytometry was also able to quantify biomolecular content inside human skin fibroblasts, verifying its application for the study of human cell samples.

7.1.4 Raman Analysis of Biological Tissue Sections

The Raman microanalysis of entire rabbit buccal epithelial tissue sections prepared on glass slides successfully demonstrated the ability for quantitative analysis of drug distribution and tissue penetration in the context of controlled release polymeric implants *in vivo*. This study established an appropriate methodology for tissue section preparation and quantitative calibration of micro-Raman instruments for quantitative chemical imaging of biological tissue samples. Although there has been a previous report of Raman-based quantitation of retinol compounds in tissue, this is the first report of what may be termed “large-scale” chemical imaging for distribution and tissue penetration analysis of a synthetic drug compound (i.e., retinoid derivative fenretinide) on the size-scale of millimeters.(16) Furthermore, this study showed how micro-Raman chemical imaging can be effectively used for comparative evaluation of drug delivery from different controlled release formulations in an effort to optimize drug distribution and efficacy *in vivo*.

7.2 Future Outlook

7.2.1 Increased Complexity of Inkjet-Printed Micro-Calibration Standards

The inkjet-printed micro-calibration standards presented herein represent a significant technological advancement for absolute cytometric measurements and reliably established signal-to-mass ratios (CCD counts / picogram) for protein, lipids, and cholesterol but there is still further room for improvement. Although stoichiometric mixtures – such as protein:DNA (both hydrophilic) or drug:lipid (both hydrophobic) – can

be used to determine signal-to-mass ratios for additional components as presented in this dissertation, incorporation of additional compounds into the inkjet-printed micro-calibration standards (i.e., drugs, DNA, RNA, carbohydrates, etc.) would enable more reliable quantitative calibration for the analysis of actual biological cells; the closer the micro-calibration standards mimic actual biological cells, the more reliable the measurements will become. In this way, an investigator could experimentally determine the limits of detection and quantitation for different molecular components within single cells and confidently verify the linearity of emitted Raman signals in more complex mixtures.

In addition to increasing the number of components, the micro-calibration standards could foreseeably be utilized to measure picogram quantities of different biomolecular components on a per-pixel basis throughout the entirety of a single cell. Where this work has been limited to quantitation of total (absolute) molecular contents within a single cell, it has not explored the potential for subcellular compartment measurements. More specifically, by relating the signal intensities (CCD counts) on a per-pixel basis to the distribution of mass (picograms) throughout a given micro-calibration standard, an investigator could measure the total mass (picograms) and relative composition (e.g., % protein, lipid, etc.) at every pixel of a single-cell Raman image. This is currently achievable with the micro-calibration standards as they are. In theory, an investigator could simply harmonize the single-cell Raman imaging methodology presented in Chapter 3 with the quantitatively-calibrated pure component reference spectra (determined using micro-calibration standards) presented in Chapter 4 of this thesis. In this way, one could make absolute measurements of intracellular drug inclusions and foreseeably explore cellular bioaccumulation as never before.

7.2.2 Ultraquantitative Raman Microanalysis of Intracellular Lipid Trafficking

To expand further upon the ultraquantitative foundation established in this dissertation, micro-Raman imaging could foreseeably be utilized to quantitatively study

the intracellular transport of high-density lipoproteins and their ability to clear cholesterol from within individual cells. While HDLs have exhibited the ability to clear cholesterol from within cells, the intracellular mechanisms by which this occurs are not completely understood. While fluorophore-tagged synthetic HDLs can be monitored inside single cells, the fluorophore may alter the physicochemical properties of the nanoparticle and may be confounded by potential separation of the two constituents within cell lysosomes. Multiple fluorophores could be used, correlating spatial distribution of the two to ensure particles remain intact, but this approach would still lack the ability to assess lipid transfer between the particles and cell. Utilization of deuterated phospholipids offers a unique Raman-based approach to measuring intracellular lipid distribution and preliminary studies have been reported previously by others.(21) Carbon-deuterium bonds vibrate at unique frequencies which do not occur naturally in biological cells, giving rise to a C-D signal in a background-free region of acquired Raman spectra. From an ultraquantitative perspective, the first step in designing these experiments would be to generate stoichiometric mixtures of deuterated lipid (which is commercially-available) with non-deuterated lipid (i.e., the kind used for all experiments presented herein) to experimentally determine the relative Raman signal intensities of the two lipid species. From there, the investigator could synthesize HDLs, with established ratios of deuterated to non-deuterated lipid, and incubate cells to facilitate their uptake. Using ultraquantitative Raman imaging, subcellular measurements could foreseeably be made which estimate the number and state of each HDL particle within a single cell and potentially monitor the fate of HDL-delivered lipids (i.e., by following the deuterium).

7.2.3 Potential Applications for Ultraquantitative Raman Spectral Cytometry

Ultraquantitative Raman spectral cytometry has herein been utilized in a diverse multitude of scenarios and promising feasibility for application in the clinical setting has been demonstrated but its true potential remains untapped. Amiodarone-induced phospholipidosis served as the scientific catalyst for this research endeavor so measurement of intracellular drug and phospholipid accumulation has been the

underlying goal, from a technical perspective. With the invention of inkjet-printed micro-calibration standards, a slew of biomedical research avenues has been opened through which ultraquantitative Raman spectral cytometry may serve to elucidate pathogenic phenomena involving lipid and/or drug accumulation at the cellular level.

The use of ultraquantitative Raman spectral cytometry for single-cell quantitative analysis of drug-induced phospholipidosis – specifically measuring intracellular amiodarone and phospholipid accumulation – was demonstrated in Chapter 4. The promising results suggest that quantitative Raman spectral analysis of BAL macrophages from patients taking amiodarone could provide extremely insightful single-cell pharmacokinetic information, relating macrophage drug loading to the health status of each patient, with the goal being side effect risk assessment and elucidation of a critical toxicity threshold. Although we were unable to reliably distinguish between wildtype human skin fibroblast cell lines or those with Niemann-Pick type C (NPC1 genetic variant) lipid storage disorder, the extent of lipid accumulation *in vitro* may not be representative to the real-world patient population; perhaps the degree of lipid accumulation was simply not significant enough to detect. As observed in animal subjects given *ad libitum* drug regimens for extended periods of time, bioaccumulation occurs on a much more massive scale *in vivo* than is possible *in vitro*; this may be due to a complex adaptive immuno-protective response mustered by the host's macrophages, as observed in the case of clofazimine bioaccumulation.(22, 23)

When considering using this technology for analysis of cell specimens acquired from *in vivo* injury models or humans in the clinical setting, it may be necessary to confirm the identity of specific cell types of interest; we performed some preliminary developmental work in this area but it was not reported in this dissertation and further work is still needed to validate the methods. Using our proposed sample preparation (air-dried cells as thin dispersions on the surface of silicon chips), we were able to selectively tag pig BAL cells that expressed surface marker SWC9 (presumably pig alveolar macrophage marker) with a fluorophore-conjugated antibody (DyLight 549) that could be excited with the Raman's 532nm laser. Conveniently, we found the Raman analysis could

be non-destructively performed on the cells before they were incubated with antibody. In this way, alveolar macrophages acquired from pig BAL could be positively identified following Raman analysis. Furthermore, the use of gravity-assisted cell sorting techniques using antibody-conjugated glass microbubbles would provide an exceptionally straightforward and facile separation that could be confidently performed in the clinical setting (e.g., neutrophils could be selectively removed from BAL suspensions collected during ARDS so as to analyze only macrophages). These techniques would be especially useful when studying specific cell types in the context of acute and chronic lung injuries where BAL cell populations are typically a mixture of different immune cells (e.g., macrophages, neutrophils, eosinophils, etc.)

Some additional examples of where this technology may prove especially useful are in the study of atherosclerosis (involving cholesterol crystal-laden macrophages in atherosclerotic plaques) and idiopathic pulmonary fibrosis (involving “foamy” lipid-laden macrophages in the lung). In the case of idiopathic pulmonary fibrosis, the underlying cause of the chronic inflammatory lung injury is unknown but lipid-laden macrophages are almost always observed(24, 25). Based on what is known regarding amiodarone-induced phospholipidosis, it is reasonable to hypothesize the presence of unknown xenobiotic material that has been sequestered within alveolar macrophages and is contributing to progression of the disease. As demonstrated in Chapter 5, ultraquantitative Raman spectral cytometry can detect – and therefore potentially screen for – unknown chemical compounds that accumulate in these cells. This illustrates one example of this technology’s biomedical potential in the pulmonary critical care setting. Beyond this, quantitative characterization of the macrophage-mucociliary clearance complex and its physiological limitations may be a viable long-term goal. Automation of micro-Raman instruments is being explored by certain groups already (19, 20). Harmonizing an automated high-throughput screening platform with the ultraquantitative micro-calibration approach would enable analytical validation of quantitative approaches and large-scale screening of human cell populations to generate massive Ramanomic datasets and extract the wealth of valuable information contained within.

7.3 Broader Implications

The true fathomable potential of this technique lies in the analysis of clinical biospecimens acquired from humans. When it comes to studying the effects of cellular bioaccumulation on human health, it is most relevant to directly (and non-destructively) measure what and how much is present in the samples of interest. By probing into the single-cell realm and analyzing the absolute composition of human cells, we may quantitatively elucidate an absolute baseline cytometric profile of idealized health, relating cellular cargo loading to the health status of each individual patient. Using quantitative micro-calibration standards, Raman measurements could be harmonized, effectively enabling quantitative characterization of interindividual variability, potentially on a global scale. Environmental and lifestyle factors, hypothesized to play important roles in overall health, could thereby be related to the absolute baseline cytometric profile of idealized health. As modern humans in advanced technological societies, we are exposed to a plethora of xenobiotic material; from pharmaceuticals to food additives, exhaust fumes to dust particles, microcrystals to microplastics: these ingested materials are foreign and must therefore be cleared from the body before levels accumulate beyond a toxicity threshold. We are the conscious caretakers of this world, but before we can take care of the world, we must learn to take care of ourselves. As we move toward a future fraught with widespread drug use and greater overall exposure to xenobiotic materials, there exists an increasing need for the analysis of our absolute (bio)chemical composition to establish a reliable baseline profile for the idealized healthy individual.

7.4 References

1. Horstman EM, Keswani RK, Frey BA, Rzeczycki PM, LaLone V, Bertke JA, et al. Elasticity in Macrophage-Synthesized Biocrystals. Angewandte Chemie International Edition. 2017;56(7):1815-9. doi: 10.1002/anie.201611195.

2. Woldemichael T, Keswani RK, Rzeczycki PM, Murashov MD, LaLone V, Gregorka B, et al. Reverse Engineering the Intracellular Self-Assembly of a Functional Mechanopharmaceutical Device. Scientific Reports. 2018;8(1):2934. doi: 10.1038/s41598-018-21271-7.

3. Murashov DM, Diaz-Espinosa J, LaLone V, Tan WJ, Laza R, Wang X, et al. Synthesis and Characterization of a Biomimetic Formulation of Clofazimine Hydrochloride Microcrystals for Parenteral Administration. Pharmaceutics. 2018;10(4). doi: 10.3390/pharmaceutics10040238.

4. Rzeczycki P, Yoon GS, Keswani RK, Sud S, Stringer KA, Rosania GR. Detecting ordered small molecule drug aggregates in live macrophages: a multi-parameter microscope image data acquisition and analysis strategy. Biomedical Optics Express. 2017;8(2):860-72. doi: 10.1364/BOE.8.000860.

5. Sukpanichnant S, Hargrove NS, Kachintorn U, Manatsathit S, Chanchairujira T, Siritanaratkul N, et al. Clofazimine-Induced Crystal-Storing Histiocytosis Producing Chronic Abdominal Pain in a Leprosy Patient. The American Journal of Surgical Pathology. 2000;24(1):129.

6. Yoon GS, Keswani RK, Sud S, Rzeczycki PM, Murashov MD, Koehn TA, et al. Clofazimine biocrystal accumulation in macrophages upregulates interleukin 1 receptor antagonist production to induce a systemic anti-inflammatory state. Antimicrobial Agents and Chemotherapy. 2016;60(6):3470-9.

7. Baik J, Stringer KA, Mane G, Rosania GR. Multiscale distribution and bioaccumulation analysis of clofazimine reveals a massive immune system-mediated xenobiotic sequestration response. Antimicrobial Agents and Chemotherapy. 2013;57(3):1218-30.

8. LaLone V, Mourão MA, Standiford TJ, Raghavendran K, Shedden K, Stringer KA, et al. An Expandable Mechanopharmaceutical Device (3): a Versatile Raman Spectral Cytometry Approach to Study the Drug Cargo Capacity of Individual

Macrophages. Pharmaceutical Research. 2018;36(1):2. doi: 10.1007/s11095-018-2540-0.

9. Bergholt MS, Zheng W, Lin K, Ho KY, Teh M, Yeoh KG, et al. Characterizing variability in in vivo Raman spectra of different anatomical locations in the upper gastrointestinal tract toward cancer detection. Journal of Biomedical Optics. 2011;16(3):037003--10.

10. Bergholt MS, Zheng W, Huang Z. Characterizing variability in in vivo Raman spectroscopic properties of different anatomical sites of normal tissue in the oral cavity. Journal of Raman Spectroscopy. 2012;43(2):255-62. doi: 10.1002/jrs.3026.

11. Kuzmin AN, Levchenko SM, Pliss A, Qu J, Prasad PN. Molecular profiling of single organelles for quantitative analysis of cellular heterogeneity. Scientific Reports. 2017;7(1):6512. doi: 10.1038/s41598-017-06936-z.

12. Kuzmin A, Pliss A, Prasad P. Ramanomics: New Omics Disciplines Using Micro Raman Spectrometry with Biomolecular Component Analysis for Molecular Profiling of Biological Structures. Biosensors. 2017;7(4):52.

13. Yang Y, Huang Y, Wu J, Liu N, Deng J, Luan T. Single-cell analysis by ambient mass spectrometry. TrAC Trends in Analytical Chemistry. 2017;90:14-26. doi: https://doi.org/10.1016/j.trac.2017.02.009.

14. Ihalainen P, Määttänen A, Sandler N. Printing technologies for biomolecule and cell-based applications. International Journal of Pharmaceutics. 2015;494(2):585-92. doi: https://doi.org/10.1016/j.ijpharm.2015.02.033.

15. Daly R, Harrington TS, Martin GD, Hutchings IM. Inkjet printing for pharmaceutics – A review of research and manufacturing. International Journal of Pharmaceutics. 2015;494(2):554-67. doi: https://doi.org/10.1016/j.ijpharm.2015.03.017.

16. Galler K, Requardt RP, Glaser U, Markwart R, Bocklitz T, Bauer M, et al. Single cell analysis in native tissue: Quantification of the retinoid content of hepatic stellate cells. Scientific Reports. 2016;6.

17. Schie IW, Kiselev R, Krafft C, Popp J. Rapid acquisition of mean Raman spectra of eukaryotic cells for a robust single cell classification. Analyst. 2016;141(23):6387-95.

18. Konorov SO, Schulze HG, Atkins CG, Piret JM, Aparicio SA, Turner RF, et al. Absolute quantification of intracellular glycogen content in human embryonic stem cells with Raman microspectroscopy. Analytical Chemistry. 2011;83(16):6254-8.

19. Schie IW, Rüger J, Mondol S, Ramoji A, Neugebauer U, Krafft C, et al., editors. High-throughput screening Raman spectroscopy (HTS-RS) platform for label-free single cell analysis. Biophotonics Congress: Optics in the Life Sciences Congress 2019 (BODA,BRAIN,NTM,OMA,OMP); 2019 2019/04/14; Tucson, Arizona: Optical Society of America.

20. Schie IW, Rüger J, Mondol AS, Ramoji A, Neugebauer U, Krafft C, et al. High-Throughput Screening Raman Spectroscopy Platform for Label-Free Cellomics. Analytical Chemistry. 2018;90(3):2023-30. doi: 10.1021/acs.analchem.7b04127.

21. Stiebing C, Matthäus C, Krafft C, Keller A-A, Weber K, Lorkowski S, et al. Complexity of fatty acid distribution inside human macrophages on single cell level using Raman micro-spectroscopy. Analytical and Bioanalytical Chemistry. 2014;406(27):7037-46.

22. Rzeczycki P, Woldemichael T, Willmer A, Murashov MD, Baik J, Keswani R, et al. An Expandable Mechanopharmaceutical Device (1): Measuring the Cargo Capacity of Macrophages in a Living Organism. Pharmaceutical Research. 2018;36(1):12. doi: 10.1007/s11095-018-2539-6.

23. Rzeczycki P, Yoon GS, Keswani RK, Sud S, Baik J, Murashov MD, et al. An Expandable Mechanopharmaceutical Device (2): Drug Induced Granulomas Maximize the Cargo Sequestering Capacity of Macrophages in the Liver. Pharmaceutical Research. 2018;36(1):3. doi: 10.1007/s11095-018-2541-z.

24. Romero F, Shah D, Duong M, Penn RB, Fessler MB, Madenspacher J, et al. A Pneumocyte–Macrophage Paracrine Lipid Axis Drives the Lung toward Fibrosis. American Journal of Respiratory Cell and Molecular Biology. 2015;53(1):74-86. doi: 10.1165/rcmb.2014-0343OC.

25. Moore KJ, Sheedy FJ, Fisher EA. Macrophages in atherosclerosis: a dynamic balance. Nature Reviews Immunology. 2013;13:709. doi: 10.1038/nri3520.